CHEMICAL REVIEWS

pubs.acs.org/CR

Review

Fluids and Electrolytes under Confinement in Single-Digit Nanopores

Narayana R. Aluru, Fikret Aydin, Martin Z. Bazant, Daniel Blankschtein, Alexandra H. Brozena, J. Pedro de Souza, Menachem Elimelech, Samuel Faucher, John T. Fourkas,* Volodymyr B. Koman, Matthias Kuehne, Heather J. Kulik, Hao-Kun Li, Yuhao Li, Zhongwu Li, Arun Majumdar, Joel Martis, Rahul Prasanna Misra, Aleksandr Noy, Tuan Anh Pham, Haoran Qu, Archith Rayabharam, Mark A. Reed, Cody L. Ritt, Eric Schwegler, Zuzanna Siwy, Michael S. Strano,* YuHuang Wang,* Yun-Chiao Yao, Cheng Zhan, and Ze Zhang

Cite This: *Chem. Rev.* 2023, 123, 2737−2831

Read Online

ACCESS | Metrics & More | Article Recommendations

ABSTRACT: Confined fluids and electrolyte solutions in nanopores exhibit rich and surprising physics and chemistry that impact the mass transport and energy efficiency in many important natural systems and industrial applications. Existing theories often fail to predict the exotic effects observed in the narrowest of such pores, called single-digit nanopores (SDNs), which have diameters or conduit widths of less than 10 nm, and have only recently become accessible for experimental measurements. What SDNs reveal has been surprising, including a rapidly increasing number of examples such as extraordinarily fast water transport, distorted fluid-phase boundaries, strong ion-correlation and quantum effects, and dielectric anomalies that are not observed in larger pores. Exploiting these effects presents myriad opportunities in both basic and applied research that stand to impact a host of new technologies at the water−energy nexus, from new membranes for precise separations and water purification to new gas permeable materials for water electrolyzers and energy-storage devices. SDNs also present unique opportunities to achieve ultrasensitive and selective chemical sensing at the single-ion and single-molecule limit. In this review article, we summarize the progress on nanofluidics of SDNs, with a focus on the confinement effects that arise in these extremely narrow nanopores. The recent development of precision model systems, transformative experimental tools, and multiscale theories that have played enabling roles in advancing this frontier are reviewed. We also identify new knowledge gaps in our understanding of nanofluidic transport and provide an outlook for the future challenges and opportunities at this rapidly advancing frontier.

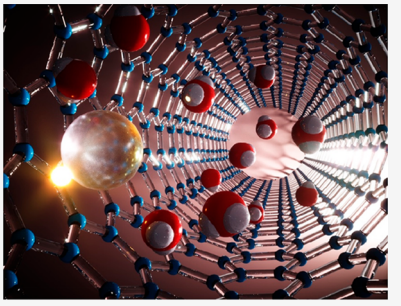

CONTENTS

Received: March 11, 2022
Published: March 10, 2023

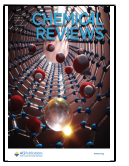

https://doi.org/10.1021/acs.chemrev.2c00155
Chem. Rev. 2023, 123, 2737−2831

1. INTRODUCTION AND SCOPE

Nanopores feature prominently in mass-transport processes in many important natural systems and industrial applications, often provide critical contributions to energy efficiency, and even define the functionality of systems and applications. Confined fluids and electrolyte solutions in nanopores often behave in ways that deviate from the predictions of simple, classical scaling theories. Such deviations are particularly significant in the narrowest of such pores, called single-digit nanopores (SDNs), which have diameters or conduit widths of less than 10 nm. Molecular simulations and existing theories, whether continuum or atomistic, often cannot adequately quantify or qualitatively describe these exotic effects in SDNs. Examples of such phenomena include slip-flow enhancement, in which the narrowest of nanopores demonstrate higher mass-transport rates than do their wider counterparts,[1,2] non-Gibbs−Thomson phase behavior, in which fluid phase boundaries in SDNs are distorted compared to their bulk fluid counterparts,[3,4] and highly nonlinear, correlative ion-transport effects that are not observed in nanopores with even slightly larger dimensions.[5] Research in this area of nanofluidics has become increasingly active, as it has become clear that experimental observations have deviated substantially from theoretical predictions or understanding. This review aims to provide continuity with past scholarship in each of these areas, with a view toward addressing and extending the frontier scientific questions of nanoconfined fluids.

Specifically, these observations point to several interesting research directions. Understanding some of the detailed, molecular-scale mechanisms that cause these deviations from classical fluid- and ion-flow models could lead to new paradigms for enhancing fluid flows,[6] developing novel precision separations and selectivity mechanisms,[7] or even conceptualizing alternative ways to store information.[8] Such advances in turn could lead to new opportunities for developing materials platforms for enhanced water purification,[9] critical materials separation and harvesting,[7] enhanced bioelectronic interfaces,[10] and low-energy nanofluidic computing.[11]

In a previously published perspective article, we identified seven critical knowledge gaps (KGs) in mass transport through SDNs.[12] In this review, we will summarize the progress that has been made in understanding nanofluidic phenomena in SDNs, with a focus on confinement effects. Studies across the same types of SDNs with varying overall length scales have proven instructive for understanding broader trends in confined nanofluidics. The carbon nanotube (CNT) literature is an example in this regard. Several studies over the past two decades observed that protons can play an important role as charge carriers in SDNs. In aqueous electrolyte solutions and under an applied electrical bias, protons were found to dominate the ion current through 0.5-mm-long carbon nanotubes.[13] Consistent with this observation, a decrease in the solution pH leads to an increase in proton conductance.[13,14] Rapid proton transport was further confirmed in experiments on short (∼10 nm) CNT porins.[15] In particular, proton-transport rates of single-file water ($4.2\ Å^2\ ps^{-1}$) were confirmed to exceed those in bulk water (0.4

https://doi.org/10.1021/acs.chemrev.2c00155
Chem. Rev. 2023, 123, 2737−2831

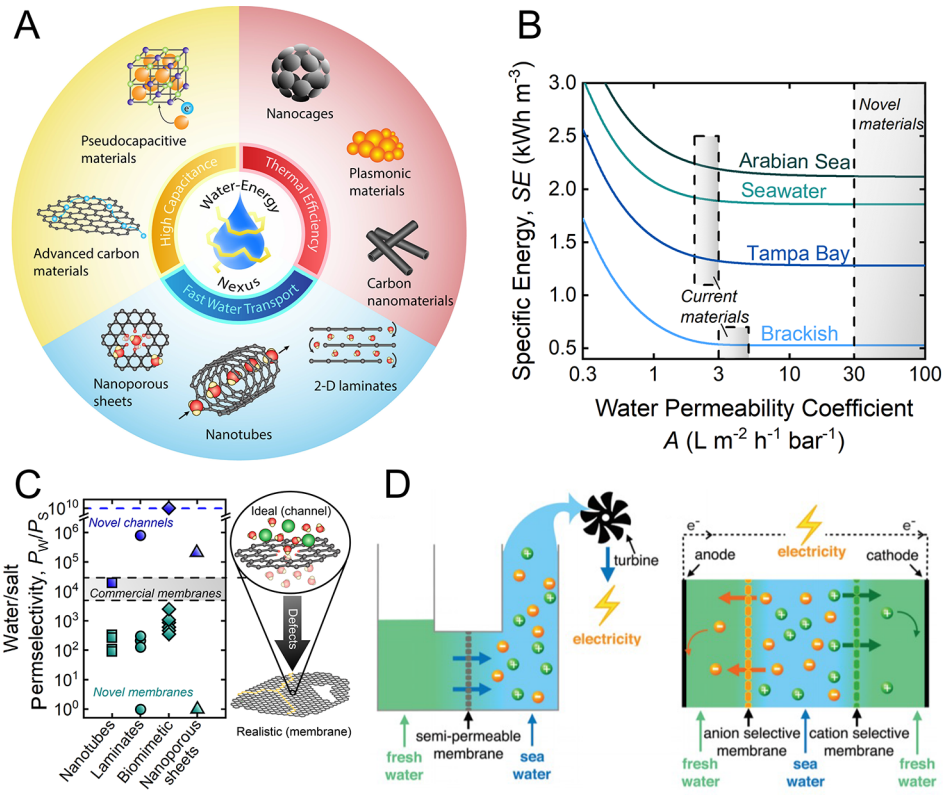

Figure 1. Nanomaterial-based membranes at the water−energy nexus. (A) Nanomaterial archetypes and their potential energy-saving properties have motivated the extensive use of such materials in next-generation desalination membranes. Adapted from ref 32. Copyright 2020 Royal Society of Chemistry under CC BY 3.0 license (https://creativecommons.org/licenses/by/3.0/). (B) Specific energy (SE) requirements for the desalination of various saline feedwaters with respect to membrane water permeability. The shaded gray regions highlight the marginal improvement in desalination energy consumption offered by increased water permeability from novel nanomaterials as compared to state-of-the-art polymeric materials. Adapted from ref 32. Copyright 2020 Royal Society of Chemistry under CC BY 3.0 license (https://creativecommons.org/licenses/by/3.0/). (C) The water−salt permselectivity (P_W/P_S) achievable with novel nanomaterials, novel material-based membranes, and current commercial membranes. The symbols represent experimental data, the gray shaded region indicates the range of selectivities achievable with current commercial membranes, and the blue dashed line represents the theoretically attainable selectivity for novel nanochannels. Adapted from ref 32. Copyright 2020 Royal Society of Chemistry under CC BY 3.0 license (https://creativecommons.org/licenses/by/3.0/). (D) Osmotic energy harvesting from pressure-retarded osmosis (left) and reverse electrodialysis (right). Both processes involve the mixing of fresh water and highly saline seawater across selective membranes. The resulting water or ion fluxes can be used to generate or capture electricity, respectively. Reproduced with permission from ref 36. Copyright 2019 Royal Society of Chemistry.

Å^2 ps^{-1}),[15] in agreement with the prediction of an enhanced Grotthuss mechanism.[16] Proton conduction is found to be similarly important for water confined in slit pores, although monolayer water in 3.4-Å-thick slit pores has a smaller transport rate than in CNT porins, possibly due to the formation of a proton-ordered ice phase.[17]

As another example, electrically sealing a nanopore has proven more challenging than it might seem. Although lipid bilayers naturally provide gigaohm membrane resistances, placing a nanopore in a solid medium does not usually result in electrical insulation of comparable quality. Polymers and SiO_2 at the 10-μm thickness level cannot block an electric field as effectively as a lipid bilayer can. This problem is especially relevant for CNTs, the sealing of which into membrane materials has been rarely verified.

Additionally, strong cation selectivity is a consistent characteristic of ion transport through electrically neutral, small-diameter CNTs. This phenomenon was first demonstrated through Coulter blocking in 0.5-mm-long CNTs, in which cations suppress the proton flux.[13,18] No pore blocking events due to anions were observed. It was proposed that anions are rejected by negative charges of carboxylate groups at the CNT pore mouths.[19,20] Strong cation selectivity was also observed in sub-1-nm diameter CNT porins at neutral pH. Interestingly, cation selectivity could be reversed by changing the solution pH to 3.0,[1] but the exact mechanism of such a reversal is still being debated.[1,21]

Recent trends have also seen SDNs used in diverse applications such as energy storage, including nanofluidic channels formed by reconstruction of cellulose fibers induced by copper ions. Such systems can achieve scalable and versatile ion-conducting matrices with ordered nanofluidic channels capable of transporting Li^+ ions. Solid-state electrolytes based on such systems show high Li^+ conductivity suitable for battery applications.

Materials science has enabled the production of nanopores with 3D order to translate nanopore physics to macroscopic fluxes. In this regard, metal organic frameworks (MOFs) have inspired the development of several other rationally designed nanoporous materials, given the realization that vertices need not be inorganic. Covalent organic frameworks (COF) are one important, emerging example.

The proliferation of 2D materials, those forming strong in-plane bonds and weak out-of-plane interactions, has also formed

https://doi.org/10.1021/acs.chemrev.2c00155
Chem. Rev. 2023, 123, 2737−2831

the basis for important nanofluidic systems. The preparation of monocrystalline graphene has motivated the field of experimental 2D crystal materials science, including new types of planar and membrane channels.

Advances in modeling tools have significantly accelerated understanding, particularly at the molecular level, for fluids within SDNs. There is generally a trade-off of higher fidelity modeling to capture forces accurately, at the expense of computationally affordable methods that ensure sufficient time or length scales are accessible to capture the relevant phenomena. Quantum simulations, force-field-based MD simulations, and continuum modeling have all been used to address problems in SDNs and the limitations imposed by this trade-off.

Future directions for SDNs are summarized at the end of the review, and broadly focus on the addition of new perturbative forces that are enabled by this next generation of channels. Conducting walls, for example, open up new opportunities to control fluid and ion flow independently of the channel fluid itself. Mechanically compliant channel walls allow new experiments involving oscillatory perturbation capable of probing critical time scales within channels. Such systems will undoubtedly highlight new gaps in our knowledge of fluids at the extremes of physical confinement.

1.1. Applications

The unique electrochemical and transport properties of SDNs, and the possibility of tuning the interactions of molecules with the entrances and walls of SDNs, have inspired scientists to use such nanoporous materials in a variety of applications, including, but not limited to, separations, energy storage, and sensing. This section describes some of the applications of membranes with a random network of SDNs, as well as of individual precision nanostructures, that motivate the need to understand the fundamental chemistry and physics of fluids in SDNs.

1.1.1. Water−Energy Nexus. Population growth and the rapid industrialization of global communities have imposed unprecedented pressures on Earth's natural resources, particularly due to increased water and energy demands.[22,23,66] Severe interim water scarcity, which affects two-thirds of the global population each year,[24,67] has necessitated the exploitation of unconventional water sources, such as seawater and brackish groundwater, that require treatment before use.[23,25] Water desalination presents an auspicious opportunity for augmenting the fresh water supply and alleviating water stress in many regions.[26] However, water−salt separation is inherently energy intensive.[26] Although strides in renewable energy have been made over the past decade, we are still highly dependent on nonrenewable sources to supply our energy demands.[22] Extraction or conversion of these nonrenewable sources, such as shale gas and crude oil, also consume considerable amounts of water.[22,27] As such, the availabilities of water and energy are intricately interdependent.

The inextricable link between water production and energy generation, termed the water−energy nexus, presents unique challenges when addressing global demands for these resources.[28,71] For water production, minimizing the energy demand is imperative. This goal requires separation materials (e.g., membranes) with highly permeable and selective pores.[29,30] A myriad of novel materials have been explored in an effort to develop the next generation of nanofluidic membranes (Figure 1A).[9] Although current polymeric membranes have adequate water permeability and already operate at energy efficiencies near the thermodynamic minimum, (Figure 1B),[26,31,69,75] novel nanofluidic materials with superior water−salt selectivity or single-species selectivity could significantly improve the overall process efficiency of desalination by eliminating the need for additional separation passes, post-treatment steps, and remineralization of product water.[32,33] To achieve this goal, bottom-up synthesis is a promising approach to create highly selective nanofluidic channels on a robust support matrix to avoid introducing the fabrication-induced defects that are inherent in top-down synthetic techniques. Fabrication-induced defects can severely limit the selectivity and overall separation performance of novel nanofluidic channels incorporated in membranes (Figure 1C).[32] The development of highly selective channels requires molecular-level design techniques, for which a fundamental understanding of confinement effects is paramount.[12,33]

The harvesting of osmotic energy, or so-called blue energy, has been explored to address energy demands. This technique, in which electricity is produced by mixing solutions of varying salinity (Figure 1D), is rather inefficient when implemented with conventional membrane materials.[34,35,77,78] However, the emergence of unique transport phenomena in novel nanofluidic materials has renewed interest in this research area, as recent experiments have realized a predicted three to six orders-of-magnitude increase in osmotic power generation over conventional materials.[36] This estimate has recently been challenged by a theoretical analysis that suggests that concentration polarization presents a severe limitation to this type of energy harvesting.[37] Nevertheless, the potential for novel nanofluidic materials to enable clean and efficient osmotic energy generation has elicited widespread optimism.

1.1.2. Energy Storage. As society moves away from fossil fuels, energy storage and delivery are becoming ever more critical for economic development, driving the research investment in new materials for batteries and supercapacitor technologies, in which the unique physics of ion transport under confinement in SDNs provides opportunities to enhance performance. Adding nanofluidic materials, such as CNTs, to the battery electrolyte has been shown to be beneficial for a range of applications, although the precise mechanisms of such enhancements remains unclear.[38] For example, addition of multiwalled carbon nanotubes (MWCNTs) was shown to the improve discharge capacity of flow batteries.[39,40] Researchers have exploited transport efficiency in SDN channels to enhance electrochemical capacitance in solid-state supercapacitors by using tungstate-anion-linked polyamide materials that create an intrinsic water-filled network of nanofluidic channels that are suitable for use with both liquid and gel electrolytes.[41]

SDNs also provide an opportunity to design efficient solid-state electrolytes, which could potentially provide superior energy density and improved safety characteristics as compared to the liquid electrolytes used in the current generation of batteries.[42] An interesting example, demonstrated recently by Hu and co-workers, used nanofluidic channels formed by reconstruction of cellulose fibers induced by copper ions to create a scalable and versatile ion-conducting matrix with ordered nanofluidic channels that are capable of transporting Li^+ ions.[43] Solid-state electrolytes based on this reconstructed cellulose matrix show high Li^+ conductivity, and their wide range of electrochemical stability renders these materials suitable for a range of battery applications.

1.1.3. Chemical and Biological Separations. Nanopores are ideal model systems for the detection of single objects,

https://doi.org/10.1021/acs.chemrev.2c00155
Chem. Rev. 2023, 123, 2737−2831

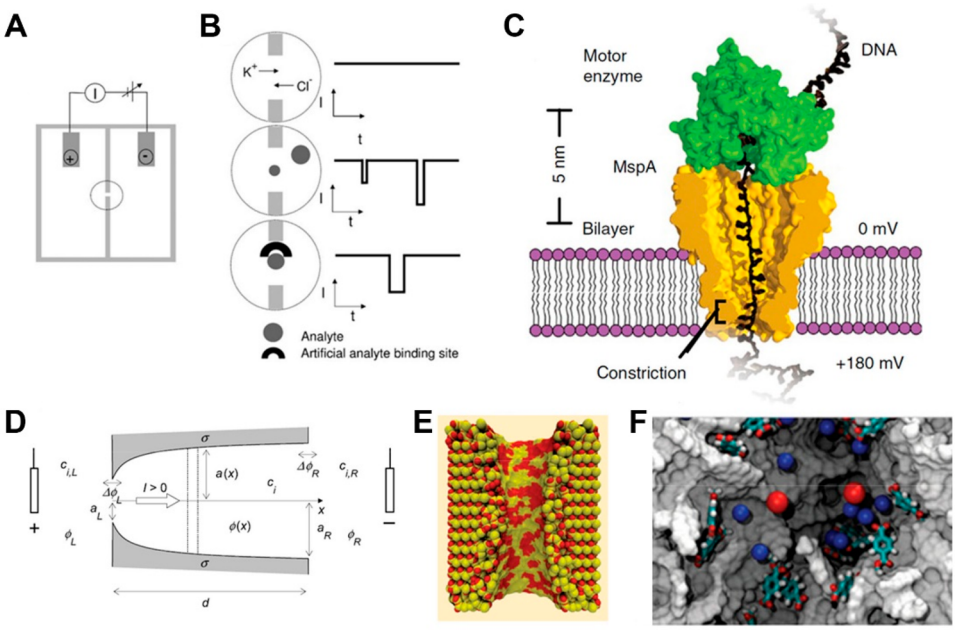

Figure 2. Single nanopores for DNA sequencing, and as a model system for understanding ionic and molecular transport under nanoconfinement. The fundamentals of the resistive-pulse technique, including (A) a schematic of a conductivity cell containing a single nanopore and (B) the ion-current signal through an empty nanopore, and through a nanopore with an object that causes a transient current decrease. The object can pass through without binding to the pore walls, or can bind transiently to recognition groups on the pore walls. (A,B) Reproduced with permission from ref 68. Copyright 2010 Royal Society of Chemistry. (C) The biological pore formed by *Mycobacterium smegmatis* porin A equipped with DNA polymerase can ratchet DNA through the pore one base at a time. Reproduced with permission from ref 58. Copyright 2015 Springer Nature. (D) Continuum modeling of transport through nanopores considers the pore geometry, surface charge properties, and ionic concentrations; the modeling is based on the Poisson−Nernst−Planck and Navier−Stokes equations. Reproduced with permission from ref 69. Copyright 2008 IOP Science. Atomistic models of (E) silica and (F) polymer nanopores. Adapted from ref 70. Copyright 2009 Institute of Electrical and Electronics Engineers.

including ions, molecules, and particles.[44−84] A large surface-to-volume ratio makes nanopores extremely sensitive to the small changes of volume caused by the presence of a molecule and/or changes in pore-wall properties.

One of the most prominent applications of single-pore sensing has been the sequencing of DNA.[48−50] This application demonstrates the crucial importance of nanoconfinement and the ability to tune the effective opening and length of the pore. DNA detection and sequencing using the resistive-pulse technique (Figure 2A) is based on the fact that the passage of a single DNA molecule through a pore causes a transient change in the current, which is called a pulse or an event.[51,52] The amplitude and duration of such events provide information about the molecular width and length (Figure 2B). The first nanopore used in such experiments, α-hemolysin from *Staphylococcus aureus*, is wide enough to allow single-stranded DNA to pass through, but is too narrow to let double-stranded DNA to enter.[51] Notably, similar behavior was demonstrated in DNA transport through 1.5 nm diameter CNT pores.[53] Early experiments also revealed that the nanoconstriction between the DNA molecule and the α-hemolysin channel allows the orientation of the DNA to be determined as the strand enters the pore. The translocation time of a DNA strand entering the pore with its 5′ end differs from that of a DNA strand that enters from its 3′ end.[51] Resistive-pulse experiments with DNA molecules also demonstrated that to recognize and differentiate all bases, it is necessary to extend the passage time and to shorten the sensing zone, such that only one base occupies the pore volume at a time.[54,55] DNA sequencing was successfully demonstrated with asymmetric nanopores equipped with a molecular motor that ensures ratcheting of the DNA molecule one base at a time (Figure 2C).[56−58] These results stimulated subsequent efforts to sequence proteins, and significant progress has already been made in this area.[59] Ellison and co-workers also demonstrated that CNT pores can pass amino acids, producing current blockades that reflect molecular volumes.[60] Nanopores have also been used to sense small molecules, and even ions.[44,61] However, the detailed description of transport of complex biological molecules is beyond the scope of this review.

Nanopores with well-defined physical and chemical structures can help us to understand the structure/function relationships of porous materials for a wide variety of applications, including ion separations.[30] If the separation is based on charge, as occurs in nanofiltration membranes, single pores can be used to probe the influence of the diameter, length, shape, and surface charge density of the pore, as well as of the magnitude of the pressure difference, on salt rejection.[62,63] These geometrical and electrochemical parameters can be modeled by a continuous approach using the Poisson−Nernst−Planck and Navier−Stokes equations (Figure 2D). How the atomistic details of the structure of a nanopore structure impact transport characteristics can also be explored using molecular dynamics (MD) simulations (Figure 2E,F).[64−67] Synergistic experimental and modeling efforts can provide an understanding of transport properties, and can allow for optimization of pore properties for ion transport and separation. Single nanopores have also been decorated with a variety of recognition systems that enable the investigation of how tuning the properties of the pore walls can enhance molecular separation and sensing.[44]

https://doi.org/10.1021/acs.chemrev.2c00155
Chem. Rev. 2023, 123, 2737−2831

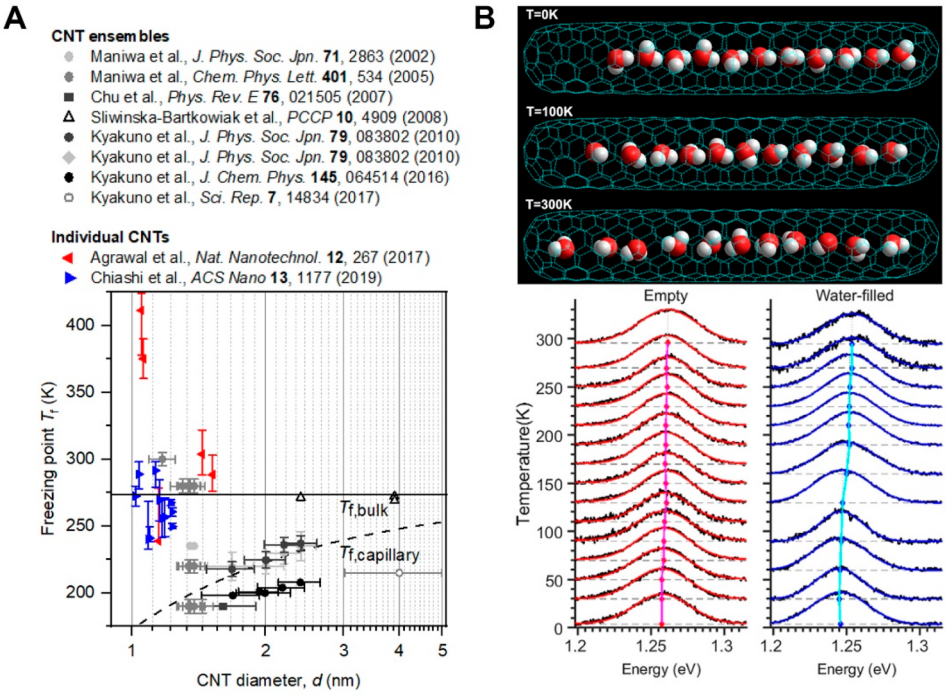

Figure 3. Water in carbon nanotubes. (A) Freezing point of water in CNTs as measured using X-ray diffraction (circles),[38,39,44−46] neutron scattering (squares),[47] differential scanning calorimetry (upward-pointing triangles),[48] nuclear magnetic resonance (diamonds),[44] Raman spectroscopy (left-pointing triangles),[40] and photoluminescence spectroscopy (right-pointing triangles).[41] The black dashed line indicates the Gibbs−Thomson behavior of water as extrapolated from measurements in glass capillaries.[49] (B) Quasiphase transitions of water arranged in a single-file manner inside (6,5) CNTs observed via changes in the photoluminescence emission energy (bottom). The quasiphases differ in the average relative orientation of the water dipole moments, as can be seen in the MD snapshot (top). Reproduced with permission from ref 99. Copyright 2017 American Physical Society.

1.2. Experimental Observations that Deviate from Simple Classical Scaling Theories

1.2.1. Liquid Dynamics and Transport. The enhanced transport of a liquid through a nanopore can be described via a slip length or flow enhancement, either of which describes the increase in volumetric flux relative to Hagen−Poiseuille flow.[71] In general, slip length varies nonmonotonically with nanopore diameter, and depends on the atomic structure of the liquid−solid interface in ways that deviate from classical theories and assumptions from fluid mechanics, such as the no-slip boundary condition.

Diameter-dependent flow enhancement in CNTs has been speculated to exist, and has therefore been the subject of modeling, for many years.[72,73] The most definitive experimental measurements of this phenomenon were made using isolated CNTs[74,75] and 2D van der Waals heterostructures.[76] Bocquet and co-workers observed pressure-driven slip flow in 20−100 nm diameter CNTs and boron nitride nanotubes (BNNTs) through measurement of a Landau−Squire jet in a scanning electron microscope (SEM).[75] Boya, Geim, and co-workers observed unexpectedly fast flow in 2D graphene slit pores with gravimetry measurements performed over the course of hours.[76] Although flow enhancement in CNTs increases dramatically as the diameter decreases from 100 to 20 nm,[75] the monotonic trend does not generally continue into the single-digit regime of nanomaterials, as has been shown by work in CNTs[74] and slit pores.[76] Instead, changes in the confining diameter result in different fluid structures with widely varying transport rates, even for changes in the diameter on the Ångstrom scale. These experimental studies[75,76] represent the state-of-the-art in the measurement of water dynamics inside well-characterized nanofluidic systems, although the work of Bocquet and co-workers[75] was in pores wider than SDNs, and the work of Geim and co-workers[76] was in an array of well-characterized nanopores rather than in a single nanopore. As shown most clearly in CNTs,[75] flow enhancement depends on both the dimensions and the chemical nature of the confining channel. For instance, CNTs show enhanced flow, whereas BNNTs do not. The very notions of slip flow and flow enhancement have been questioned recently,[77] although these concepts remain in widespread use as a means of comparing nanofluidic transport performance and classical theory. Despite these exciting developments, dynamic experimental measurements inside isolated SDN systems are scarce, and slip flow inside SDNs can be considered a knowledge gap in nanofluidics.[12] Progress toward understanding how fluid flow varies with nanopore size and liquid−solid interfacial properties is crucial for the engineering of membranes and devices with enhanced flow performance.

1.2.2. Structures. Confinement of fluids inside SDNs leads to phases and molecular organizations that are not observed in the bulk. Fluid−wall interactions and the geometry of the confinement impose spatial variations in fluid density that become more pronounced as the pore size shrinks. In the small end of the SDN range, the constraints become so severe that molecules assume unusual packing configurations.[78] Consequently, the molecular packing density in the SDN range varies nonmonotonically with pore size.[79] This phenomenon has been observed using density-gradient ultracentrifugation coupled with optical spectroscopy,[80] as well as by independent fluorescence[81,82] and Raman measurements.[83] Using SDNs to stabilize unique molecular organizations and phases,[82,83] and to

https://doi.org/10.1021/acs.chemrev.2c00155
Chem. Rev. 2023, 123, 2737−2831

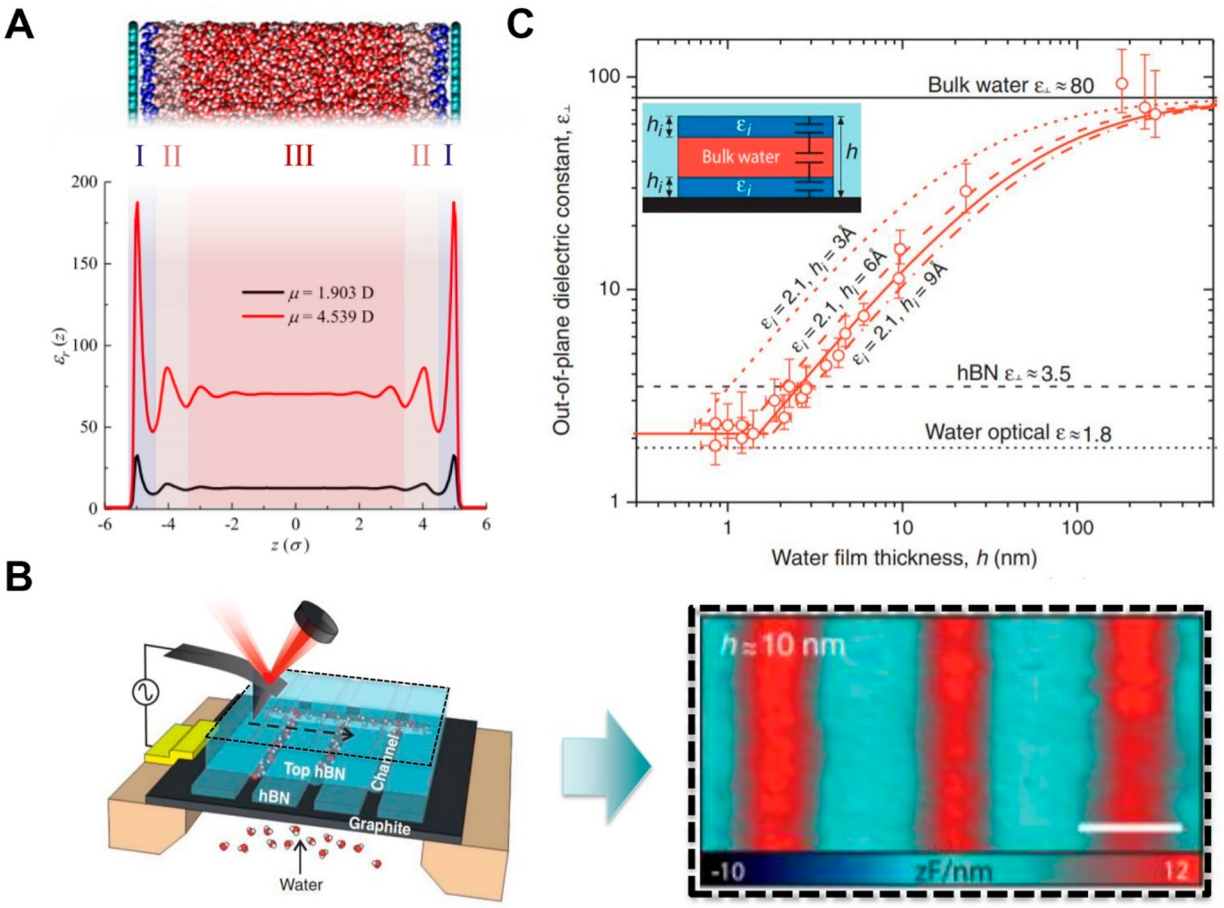

Figure 4. Decrease in the dielectric constant of confined water. (A) Three-dimensional rendering of hierarchically layered water between two graphene surfaces (top) and the influence of such layering on the dielectric permittivity profiles of water according to the Langevin dipole model with dipole moments (μ) of 1.903 and 4.539 D inside a capacitor channel that is 12 molecular diameters wide (bottom). Reproduced with permission from refs 130 (top) and 131 (bottom), respectively. Copyrights 2013 American Chemical Society and 2018 American Physical Society, respectively. (B) Schematic illustration of a nanofluidic device fabricated for scanning dielectric microscopy (left), used to perform high-resolution capacitance measurements of water in confined nanoslits (right). The channels were insulated with hexagonal boron nitride (hBN), with graphite as the ground electrode. The three-layer assembly covers an opening in a silicon nitride membrane (light brown) that allows the device to fill with water. The atomic force microscopy tip serves as the top electrode. The topographic capacitance image on the right was obtained by applying an AC tip voltage of 4 V at 1 kHz. Reproduced with permission from ref 132. Copyright 2018 American Association for the Advancement of Science. (C) Dependence of the dielectric constant of water confined in the nanoslits on the slit height h. The symbols are the experimental data, and the red curves are the modeled dielectric constants. The capacitance model (see inset) uses a dielectric constant of 2.1 for interfacial water, and averages the dielectric constant of bulk and interfacial waters in the channel. Reproduced with permission from ref 132. Copyright 2018 American Association for the Advancement of Science.

catalyze reactions,[84−86] has enabled key recent developments in nanopore technology.

In small enough pores, a regime that is characterized by unique collective properties, molecules assume a single-file arrangement.[87] There is also growing evidence that a molecule can adapt its configuration to enter such a tight nanopore.[88] Molecular sieving may occur when two species compete for a nanopore that is larger than the molecules, as is discussed later in this review for the case of *n*-hexane and cyclohexane in CNTs.

1.2.3. Phase Transitions and Melting-Point Shifts. Confinement can alter the phase behavior of a fluid in many ways. Phases without a bulk analogue may occur, phase boundaries can be distorted, the order of a phase transition can change, and new traits such as solid/liquid criticality[89−91] can emerge. Generally, phase-transition parameters are found to depend on the pore diameter. A monotonic dependence on the pore diameter is expected for pores with large enough diameters. For example, the melting point T_m of a substance is depressed with respect to that of its bulk counterpart to an extent that increases with decreasing pore size. The freezing point T_f of the corresponding liquid can be depressed to an even greater extent, due to confinement-induced supercooling, so T_m is a better indicator of the true phase boundary, but here we will use the two interchangeably. This behavior, which is described by the Gibbs−Thomson equation, is routinely observed in experiments on pores with large enough diameters.[4,92,93]

As the pore diameter becomes comparable to the size of the confined molecules, trends in phase-transition parameters can deviate substantially from such continuum thermodynamic estimates. A strongly nonmonotonic dependence on pore diameter can exist in this size realm, because the details of the confining medium determine the organization of the confined fluid, and potentially the configurations of its molecules. For example, it has been predicted that the maximization of the number of hydrogen bonds causes confined water to form exotic ice phases in slit pores[90,94] and cylindrical pores.[89] Con-

https://doi.org/10.1021/acs.chemrev.2c00155
Chem. Rev. 2023, 123, 2737−2831

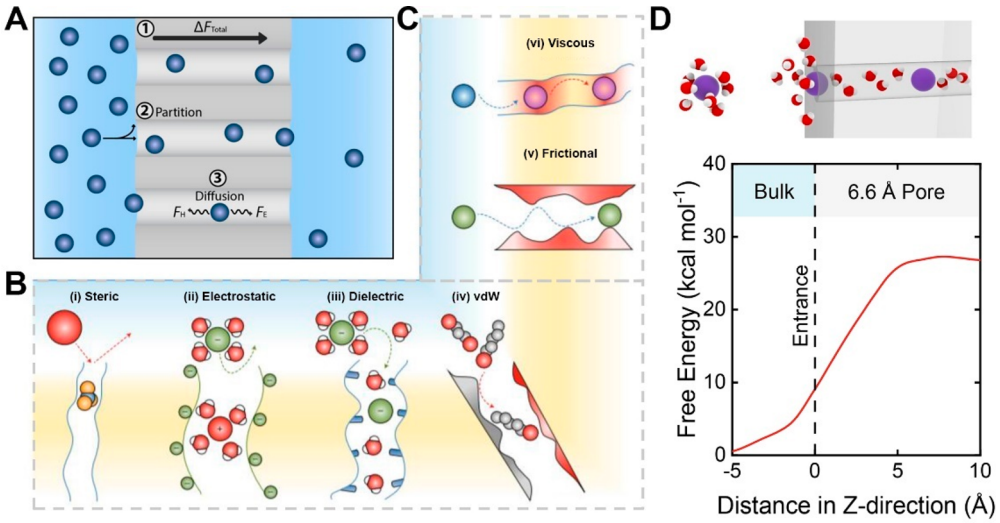

Figure 5. Factors influencing ion transport and permeability in SDNs. (A) Schematic illustration of solutes permeating SDNs from a high-concentration reservoir (left) to a low-concentration reservoir (right) due to (1) the net external driving force across the cell (ΔF_{Total}), which is based on a chemical potential difference in this case; (2) the ability to partition into the nanochannels; and (3) the net impact on solute diffusivity by hindrance forces (F_H) or enhancement forces (F_E) experienced inside the nanochannels. Schematic illustrations of elementary interactions that influence the ability of a solute to (B) partition into and (C) diffuse across SDNs. Mechanisms that can impede or enhance a solute partitioning from bulk water to an extremely confined environment include (i) steric hindrance imposed by solute size and shape; (ii) electrostatic repulsion; (iii) dielectric effects, such as partial dehydration; and (iv) van der Waals (vdW) forces. Mechanisms that can influence the rate of solute diffusion include (v) frictional forces, which can be experienced due to physical collisions with the inner walls of the nanochannel; and (vi) viscous forces from the formation and breakage of bonds between the solute and nanochannel wall. Reproduced with permission from ref 33. Copyright 2020 Springer Nature. (D) 3D rendering (top) and the energetic penalty (bottom) of a fluoride ion dehydrating from bulk water into an SDN as a function of the distance Z from the pore entrance. Data (bottom) taken and adapted from ref 145. Copyright 2012 John Wiley & Sons.

sequently, the melting point of water in CNTs has been proposed to show a strongly nonmonotonic dependence on CNT diameter.[95] Although early studies on such systems observed non-Gibbs−Thomson behavior, with evidence for ice-like phases above room temperature, the distribution of CNT diameters in the samples studied obscured the fine details of the behavior.[96,97] Recent experiments on individual CNTs have revealed a strongly nonmonotonic dependence of the apparent T_f on diameter (Figure 3A).[3,98] Strano and co-workers reported values for an effective T_f between −30 and 140 °C for CNTs with diameters between 1.05 and 1.52 nm.[3] Experimental methods capable of resolving the nuanced pore-diameter dependence of confined fluid phase behavior remain scarce at present, but are required to advance our understanding of this phenomenon.

Simulations suggest that the liquid/solid transition of water in CNTs is either first-order or continuous, depending on the pore diameter and the external pressure.[89,95] In some CNTs, water is even predicted to display solid−liquid criticality, i.e., indistinguishability between solid and liquid phases.[89,91] In addition to these drastic deviations from bulk behavior, phenomena that are more subtle can be encountered. For example, Ma and co-workers observed continuous changes in the photoluminescence spectrum of narrow CNTs containing a single-file chain of water molecules (Figure 3B). This behavior was interpreted to be indicative of quasiphase transitions, i.e., transitions between different states of average relative orientation of water dipole moments in the chain.[99] The broadened nature of these transitions can be understood to be a consequence of finite-size effects, as phase transitions are infinitely sharp only for systems in the thermodynamic limit.[100] The extent to which fluids in the narrowest SDNs may or may not be considered to be in this limit is an interesting topic for further study.

1.2.4. Changes in the Local Dielectric Constant. The polarizability of a solvent describes the response to an external electric field, and is often quantified by the solvent's permittivity (i.e., dielectric constant) relative to vacuum (ε_r). The dielectric response determines the strength of solvent-mediated intermolecular forces.[101] Given that solvents such as water are ubiquitous in fluidic systems, the electric polarizability of solvents has vast implications for phenomena such as macromolecular interactions and dynamics,[7102−104] ion solvation,[105] and confined transport.[5,106,107] A host of theoretical treatments have been pursued to understand these phenomena in aqueous media,[105,108] often assuming a bulk dielectric constant for water. Although this assumption is often reasonable for macroscopic processes, recent simulations and experimental findings have shown that the assumption can break down for interfacial processes and reactions.[109−113]

Reorientation and inductive polarization effects from the hierarchical layering of water at an interface greatly reduce the effective radial dielectric constant,[109−113] resulting in "'electrically dead water." This layering is common to many materials surfaces, and can also be induced by the electric fields close to a charged surface,[114−116] by surface hydrogen bonding,[110] or by confinement effects.[117] As such, interfacial water molecules exhibit electric properties that can be drastically different from those of their bulk counterparts (Figure 4A).[118] This phenomenon that has captured the interest of researchers for decades.[118−120] Interest in such dielectric phenomena has only increased in recent years, as novel transport and reaction phenomena continue to be discovered in nanofluidic systems,[5,106,107,121,122] in which the extremely large surface-to-volume ratio accentuates the influence of interfacial water molecules.[71,123,124]

https://doi.org/10.1021/acs.chemrev.2c00155
Chem. Rev. 2023, 123, 2737−2831

Previous experimental insights into confinement-induced dielectric phenomena came from broadband dielectric spectroscopy studies of nanoporous crystals,[125] zeolite powders,[126] and polymeric membranes,[127,128] among other materials. Capacitance measurements on these large nanofluidic systems demonstrated a roughly order-of-magnitude decrease in the local dielectric constant of confined water. More recently, solid-state nanofluidic devices have enabled the precise measurement of the local permittivity via scanning dielectric microscopy (Figure 4B).[129] In this study, the average radial dielectric constant of the water-filled nanochannels scaled from ∼80 to 2.1 as the water film thickness decreased from roughly 100 to 1 nm (Figure 4C).[129] The lowest dielectric constant presumably represents the permittivity of interfacial water. Notably, the change in the average permittivity of the water film was ascribed to the change in the fraction of interfacial water molecules compared to the total amount of water in the channel. This fraction approaches unity as the channel becomes sufficiently small, in which case all water molecules interact with the surface. This notion remains uncertain, however, as previous simulations have demonstrated that surfaces can regulate dipolar fluctuations, and thus the dielectric constant of water, at up to tens of nanometers of separation.[130] Nonetheless, confinement-induced dielectric phenomena present interesting challenges for classical theories of intermolecular interactions in confined aqueous environments, as well as exciting opportunities for improving our understanding of nanofluidic transport and reactions.

1.2.5. Ion Permeability. Ion transport in nanofluidic systems has been studied extensively,[33,133−136] as this phenomenon is central to a wide array of fundamental biological and engineering processes. At its core, ion transport can be broken down into three factors (Figure 5A). First, an external force (ΔF) is necessary to drive transport. For ions, transport is generally driven by an electrochemical potential gradient across the nanochannel. Advective forces associated with solvent movement can also drive ion transport. However, advection is usually minimal in SDNs.[137] Second, the concentration of ions in the external solution determines the ability of ions to partition into the confined environment (Figure 5B). Third, a number of intrapore diffusion forces act on the ions to alter their mobility (Figure 5C).[136] The second and third factors can generally be represented by the ion-partition coefficient (K_i) and the hindered/enhanced diffusivity (D_i), respectively, the product of which defines the intrinsic ionic permeability (P_i) in the nanochannel.[138] The total ion flux (J_i) across the length of the nanochannel (L) is then defined as $J_i = P_i\,\Delta F/L$.

In channels that are tens of nm in diameter, the vast majority of the solvent remains bulk-like,[117,124,139,140] and ion interactions with the channel walls and channel entrance are minimal. Thus, the ionic concentration and mobility in such large channels are similar to those in the bulk solution. In the SDN range, however, interactions with the nanochannel become prominent, and substantial changes in the ionic permeability may occur.[12,137] Collectively, entrance/exit and intrapore diffusion interactions govern ion transport within such nanochannels. The relative importance of these two types of interactions varies from system to system, and is dependent upon factors such as the size and chemistry of both the nanochannel and the ion.

The concentration of ions in SDNs usually differs from that in the corresponding bulk solution. This phenomenon is, in large part, a result of electrostatic interactions involving the charge and solvation of an ion.[1,75,141,142] Entry into strong confinement usually necessitates deformation of, or partial to complete shedding of, an ion's solvation shell (Figure 5D), a phenomenon that is termed dehydration. Simulations suggest that significant energetic penalties are experienced when an ion dehydrates to enter a confined environment (Figure 5D).[143−146] Pairing of these insights with recent experimental evidence[17,147−149] has led to the increasingly accepted picture that dehydration is a governing mechanism for ion transport that is akin to the behavior of ion-selective biological channels.[150,151] Although dehydration likely plays a universal role in ion transport, SDNs with significant ion−wall interactions tend to exhibit diffusion-limited transport.[138,152,153] However, there have been reports of anomalous ion transport in hydrophilic SDNs, in which ion diffusivity is enhanced rather than hindered.[154] This behavior was attributed to the existence of highly ordered water within the nanochannels, and is one of many examples that highlight the substantial knowledge gaps in our understanding of ion transport under extreme confinement.[12]

2. EXPERIMENTAL PLATFORMS

In this section, we review model SDN systems and characterization tools that enable quantitative studies in nanofluidics. Later sections focus on emerging phenomena at the nanoscale and on effects of confinement. Although many SDNs have only recently become accessible experimentally for precision transport measurements, there is a long history of studies on a diverse array of nanoporous materials with dimensionality ranging from 3D to 0D. We will discuss examples of SDNs that can serve as precision model systems for probing liquids and electrolyte solutions under confinement. For the characterization techniques, we go beyond those that are currently used for SDNs exclusively, also reviewing a variety of techniques applicable to nanomaterials, foreseeing that these techniques or their variations will be extended to SDNs in the near future.

2.1. Model Systems

2.1.1. 3D Nanoporous Materials. By convention, the dimensionality of nanoporous materials is defined as the number of dimensions that are not constrained to be on the nanoscale. Thus, a 3D nanoporous material would appear to be an oxymoron. The term 3D is actually used to denote nanoporous materials that are composed of pores that are interconnected, either regularly or randomly, in 2D or 3D networks. This class of materials can further be broken into the subcategories of powdered and monolithic materials. Some powdered "3D" materials are actually 1D within individual grains, but the random orientations of the grains can make the materials appear to be 3D as far as many experimental techniques are concerned. We will therefore discuss such powdered materials within this subsection as well.

2.1.1.1. (i) Powdered 3D Nanoporous Materials. Powdered nanoporous materials can be divided further into hard and soft categories. We will begin by discussing the former of these, which includes the class of nanoporous material that has been known and studied for by far the longest: zeolites. The term zeolite, which means "boiling stone," was coined in 1756 by A. F. Cronstedt, who observed that the mineral stilbite exhibits reversible hydration.[155] There are many naturally occurring zeolites, such as faujasite, the structure of which[156] is shown in Figure 6A. Many synthetic zeolites have been inspired by these minerals, such as ZSM-5, the structure of which[157] is shown in Figure 6B.

https://doi.org/10.1021/acs.chemrev.2c00155
Chem. Rev. 2023, 123, 2737−2831

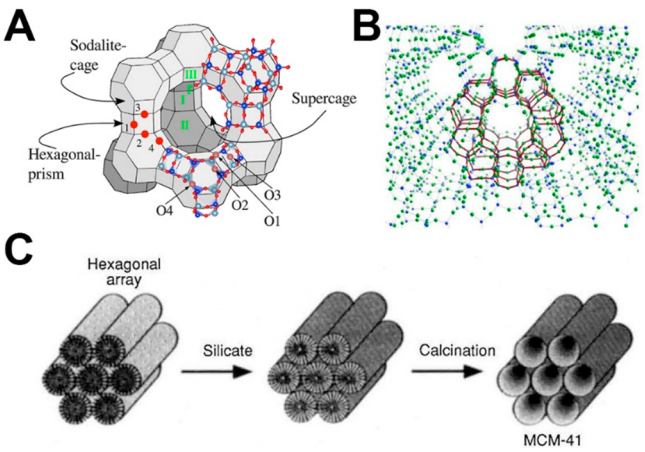

Figure 6. Representative "hard" 3D nanoporous materials. (A) Schematic of the microscopic structure of faujasite, a naturally occurring zeolite. The pore diameter is 7.8 Å, and the inner cavity diameter is 12 Å. Reproduced with permission from ref 156. Copyright 2015 American Chemical Society. (B) Schematic of the microscopic structure of the synthetic zeolite ZSM-5. The channel diameter is on the order of 5.5 Å. Adapted from ref 157. Copyright 2010 Multidisciplinary Digital Publishing Institute under CC BY 3.0 license (http://creativecommons.org/licenses/by/3.0/). (C) Schematic of the preparation of MCM-41 mesoporous glass. Reproduced with permission from ref 158. Copyright 1992 Springer Nature.

There are dozens of types of naturally occurring zeolites, most of which have cavities that are 15 Å or less in diameter and are separated by channels that are 8 Å or less in diameter.[159] The cavities may be connected in 1D chains or 2D or 3D networks.[160] Although naturally occurring zeolites have many uses in applications such as ion exchange,[161] selective adsorption,[162] and heterogeneous catalysis,[163] the small channel diameters are also a hindrance to mass transport. Thus, efforts to create synthetic zeolites, and their analogues, began in the 1840s and continue to this day.[164] The vast majority of work up to the last few decades focused on hydrothermal synthesis.[164] This synthetic method enables somewhat larger pore sizes to be attained in zeolites and related materials than do other approaches, but mass transport remains an issue.

The disparity in the dimensions between the channels and cavities in zeolites limit the use of these materials in fundamental studies of nanoconfined liquids. From an applications standpoint, the mass-transport issue has been addressed to some extent by creating zeolitic materials that also contain mesopores, but the greater pore-diameter heterogeneity makes these systems poorly suited for use with most experimental techniques for studying confined liquids.[159] Continued progress in inorganic materials with open frameworks has helped to drive further extension of the pore size range attainable in zeolite-like materials,[165] but has not been a major factor in advancing the study of nanoconfined liquids to date. Zeolites with tunable size of the constituent channels can, however, help determine different methods for ion−ion separation and desalination based on steric interactions.[166]

The templated synthesis of highly uniform nanoporous materials[158,167] represented a major step forward for the study of nanoconfined liquids. A notable material in this category is MCM-41.[158,168] As shown in Figure 6C, a surfactant is used to create a regular hexagonal array of cylindrical micelles. The addition of tetramethylammonium silicate leads to the formation of silica walls between the cylinders. Calcination is used to remove the organic material, leaving a powdered material composed of highly uniform, cylindrical silica pores. The use of templates that are more complex enables the creation of uniform 2D and 3D nanoporous powdered materials.[167] MCM-41 was also used to probe behavior of liquids at extreme confinement, as shown for phase changes and dynamics of nanoconfined acetonitrile.[169]

The past two decades have also seen a revolution in the synthesis of soft powdered nanoporous materials, which was spurred by the development of metal−organic frameworks (MOFs).[170,171] Here we use "soft" to indicate that these classes of materials have a significant organic content rather than to denote any specific mechanical properties. Indeed, conventional MOFs do not, for instance, typically undergo swelling in solvents, although variants have been developed that do exhibit such behavior.[172]

MOFs are rationally designed materials that are typically composed of vertices defined by metal atoms that are interconnected by rigid organic molecules through metal−oxygen−carbon bridges. The structure of a representative example, $[Cu_3(\text{benzene-1,3,5-tricarboxylate})_2(H_2O)_3]_n$, is shown in Figure 7A.[173] This particular material has cubic symmetry, featuring pores with a diameter on the order of 10 Å. One of the great advantages of such materials is that the pore size and topology can be controlled via the geometry around the metal centers and the length of the organic linkers. Although a major focus of applications of MOFs has been on gas adsorption, these materials can also be of great value in the understanding of confined liquids. There has been a growing interest in applying MOFs as nanofluidic systems. MOFs with sub-1 nm pore

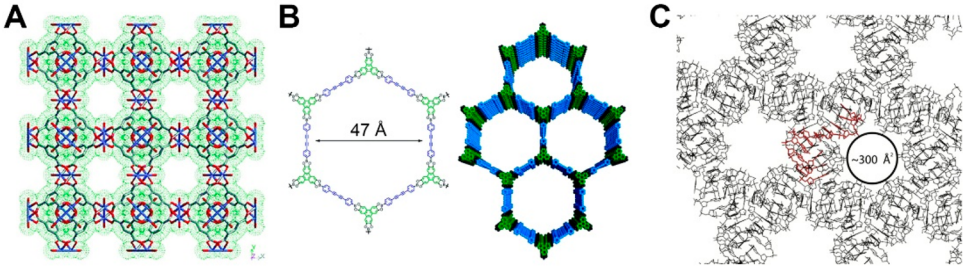

Figure 7. Representative "soft" 3D SDN materials. (A) Schematic of the structure of $[Cu_3(\text{benzene-1,3,5-tricarboxylate})_2(H_2O)_3]_n$. The pore diameter is 10 Å. Reproduced with permission from ref 173. Copyright 1999 American Association for the Advancement of Science. (B) Schematic of a covalent organic framework created via the condensation of 4,4′-diphenylbutadiynebis(boronic acid) with 2,3,6,7,10,11-hexahydroxytriphenylene. Adapted from ref 178. Copyright 2011 American Chemical Society. (C) Schematic of a 3D DNA lattice. The pore diameter is on the order of 17 Å. Adapted from ref 179. Copyright 2004 Elsevier.

https://doi.org/10.1021/acs.chemrev.2c00155
Chem. Rev. 2023, 123, 2737−2831

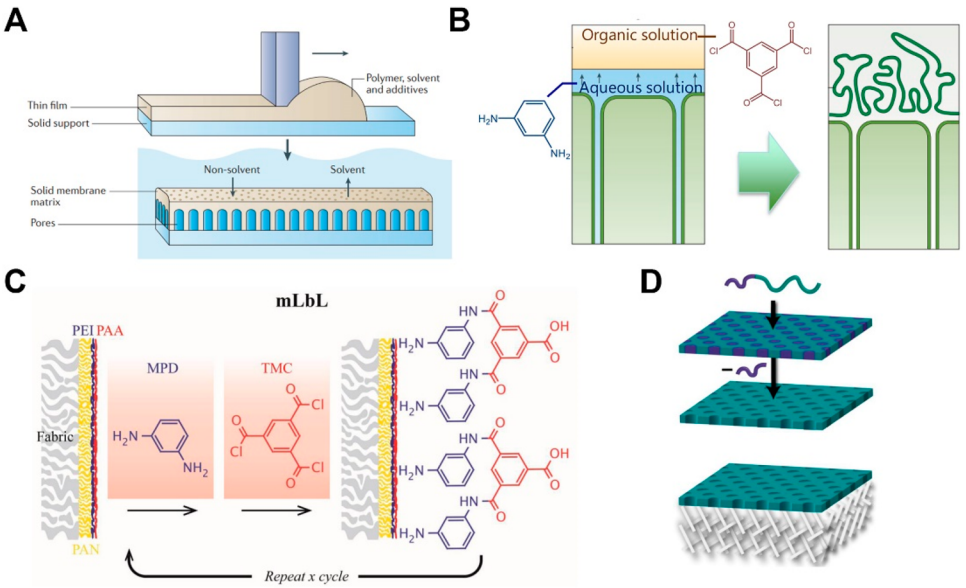

Figure 8. Methods for synthesizing nanoporous polymer membranes. (A) Schematic diagram of phase inversion by nonsolvent-induced phase separation to form asymmetric membranes. A solution consisting of polymer, solvent, and desired additives is cast onto a solid support to form a thin film (top). The film is then immersed in a nonsolvent to induce phase separation, leaving behind a solid membrane matrix (bottom). (B) Schematic diagram of interfacial polymerization to form thin-film composite membranes. A porous support embedded with an aqueous diamine solution is placed in contact with a nonaqueous organic solution containing trimesoyl chloride. The amine group diffuses to the water−organic interface (left), reacting with trimesoyl chloride to form a dense polyamide film with a ridge-and-valley structure (right). (C) Schematic illustration of nanoporous thin films formed via mLbL deposition. Dissolved reactants are deposited, dried, and rinsed sequentially for the desired number of cycles for controlled film growth. (D) Schematic representation of a cylinder-forming, diblock, copolymer thin film and the corresponding nanoporous thin film (green) obtained after selectively etching the minority microphase domains (purple) (top). This nanoporous film can be used to form a selective composite membrane with a porous support (bottom). (A,B) Reproduced with permission from ref 9. Copyright 2016 Springer Nature. (C) Reproduced with permission from ref 195. Copyright 2013 John Wiley & Sons. (D) Adapted from ref 196. Copyright 2010 American Chemical Society.

diameters have been used as a template to study fast conduction of fluoride ions[174] and alkali metal ions,[175] and for the preparation of other ion selective membranes.[176] Ion selectivity of these materials also led to the design of MOF-based osmotic power generation systems.[177]

MOFs spurred the development of several other rationally designed nanoporous materials, given the realization that the vertices need not be inorganic. The most important class of these materials is covalent organic frameworks (COFs).[180] The vertices in COFs are purely organic, allowing for more conformational flexibility than in MOFs. A representative COF structure is shown in Figure 7B.[178] This particular material has a pore diameter of 47 Å, illustrating the flexibility offered by the judicious choice of linkers. The majority of applications of COFs remain in the adsorption of gases, but the ability to create pores with larger diameters offers new opportunities for the study of nanoconfined liquids as well. COFs have already been shown to be promising materials for probing ionic conduction at the nanoscale[181] and in separation systems.[182]

An alternative strategy for the creation of regular, soft nanoporous materials is the self-assembly of DNA, as shown in Figure 7C.[179] The pore size and geometry in such materials can be programmed by the DNA sequence. These materials are suited for studies of the properties of nanoconfined aqueous mixtures that leave the pore structure intact.

2.1.1.2. (ii) Monolithic 3D Nanoporous Materials. Powdered nanoporous materials are well suited for some types of studies of nanoconfined liquids, but do not work well for others. Monolithic nanoporous materials, which are typically composed of silicate glasses, are well suited for performing studies using techniques such as optical spectroscopies, scattering, and dilatometry. The external surface area (i.e., the surface area not related to the pores) is orders of magnitude smaller for monolithic materials than for powders, which can greatly simplify the interpretation of experimental results. Furthermore, although powdered materials cannot be converted into uniform monoliths, monolithic materials can easily be converted to powders. On the other hand, the pores of typical monolithic materials are neither completely uniform nor entirely monodisperse, which creates a different set of experimental challenges.

There are two main classes of monolithic nanoporous glasses: reconstructed glasses[183] and sol−gel glasses.[184] Reconstructed glasses, the most common of which is known by the trade name Vycor, are based on the discovery that soft alkali borosilicate glasses, when heated above their annealing point but below their deformation temperature, undergo spinodal decomposition into one phase that contains the alkali and borate and a second phase that is predominantly silica.[185] The former phase can be etched away using acid, leaving the silica phase. The resultant nanoporous glass can then be fired to lock in its structure.

A typical Vycor glass sample has a porosity on the order of 28%, with an average pore diameter of 50 Å.[183] Different pore sizes can be obtained by varying the details of the heat treatment.[186] The pore diameter distribution is generally within ±10% of the average.[186] Because the pores are created by etching of the borate-rich phase, the void space is interconnected, and can therefore be filled with liquid. The fact that the pores are much smaller than the wavelength of visible light means that a piece of clean Vycor has high optical quality and is generally indistinguishable from a piece of solid glass. Vycor can also be polished to optical flatness if desired. Vycor has long been used as a model system to understand the structure of

https://doi.org/10.1021/acs.chemrev.2c00155
Chem. Rev. 2023, 123, 2737−2831

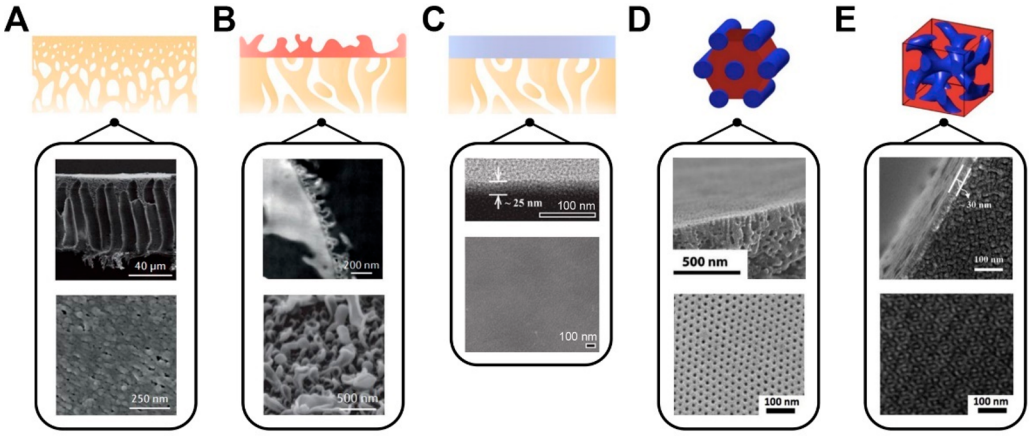

Figure 9. Porous structures of polymer membranes. (A) Illustration of phase inversion asymmetric membrane (top). SEM cross-sectional (middle) and topographic (bottom) images of a phase-inversion, asymmetric membrane (bottom). (B) Schematic of a thin-film composite membrane formed via interfacial polymerization (top). TEM cross-sectional (middle), and SEM topographic (bottom) images of a hand-cast polyamide thin film composite membrane. The SEM image is at a 45° viewing angle. (C) Illustration of a nanoporous thin film composite membrane formed via molecular, layer-by-layer (mLbL) deposition (top). TEM cross-sectional (middle) and SEM topographical (bottom) images of a 15-layer mLbL polyamide membrane. (D) Representative images of a cylindrical microstructure used in the fabrication of nanoporous membranes from block polymer templates (top). SEM cross-sectional (middle) and topographic (bottom) images of membranes fabricated using polyisoprene-*b*-polystyrene-*b*-poly(4-vinylpyridine) triblock polymers. (E) Representative image of a gyroid microstructure used in the fabrication of nanoporous membranes from block copolymer templates (top). SEM cross-sectional (middle) and topographic (bottom) images of membranes fabricated using a 1,2-PB-*b*-PDMS block copolymer precursor. (A–C) Illustrations are adapted from ref 200. Copyright 2022 American Association for the Advancement of Science. (A) Middle panel adapted from ref 201. Copyright 2011 Elsevier. Bottom panel adapted from ref 29. Copyright 2016 American Chemical Society. (B) Middle panel adapted from ref 202. Copyright 2015 American Chemical Society. Bottom panel adapted from ref 203. Copyright 2015 American Chemical Society. (C) Middle and bottom panels adapted from ref 195. Copyright 2013 John Wiley & Sons. (D,E) Illustrations adapted from ref 204. Copyright 2015 John Wiley & Sons. (D) Middle and bottom panels adapted from ref 205. Copyright 2014 Elsevier. (E) Middle and bottom panels adapted from ref 206. Copyright 2011 American Chemical Society.

water in nanoconfinement. One interesting finding is that the nanoconfinement-induced decrease in the number of hydrogen bonds per molecule compared to the bulk water.[187] In another study, Vycor was used to understand the step-like process of water freezing and the existence of pronounced dynamical heterogeneity of nanoconfined water.[188]

Sol–gel glasses are created via wet chemistry. The first step in the process is generally a relatively rapid acid- or base-catalyzed hydrolysis of an alkoxy precursor, such as tetraethylorthosilicate (TEOS).[189] The product of the hydrolysis (silicic acid, in the case of TEOS) undergoes condensation to form relatively uniform, spherical sol particles. The sol particle diameter can be controlled, via the conditions during the condensation, to be anywhere from a few nanometers to a micrometer or more. After this stage, a slow gelation process is initiated, often by a change in pH. During gelation, the sol particles slowly cross-link and reform, eventually creating a tortuous network of roughly cylindrical pores. The solvent is gradually evaporated during this stage, usually over the course of a month or more. The resultant materials can then be fired in a furnace to create xerogel monoliths with a porosity as high as 50% or more. The pore sizes of sol–gel monoliths are more readily controlled than those of reconstructed glasses. The pore diameter is determined by the gelation conditions and can range from 20 Å or less to 100 Å or more. The width of the pore-diameter distribution in sol–gel glasses that have been made carefully is similar to that of Vycor, i.e., on the order of ±10%.

As is the case for reconstructed glasses, sol–gel monoliths with small enough pores look indistinguishable from solid glass, and can be polished to optical flatness. Although the sol–gel glasses that have been used to study confined liquids are most often silicates, sol–gel precursors can involve any of a wide range of other elements. Maintaining high optical quality relies upon the initial condensation process occurring in a controlled manner, which presents a limitation for elements with highly labile alkoxides. A potential disadvantage of sol–gel monoliths for applications in polarization sensitive optical spectroscopies is strain birefringence, which is nearly impossible to avoid. That being said, it is generally possible to identify regions that are free of strain birefringence, particularly for the application of optical spectroscopies that depend upon transmission of a coherent beam, as opposed to scattering.

2.1.1.3. (iii) Polymer Membranes. Polymer membranes provide a multipore platform for studying thermodynamics and the kinetics of mass transport under confinement. The pore diameters of polymer membranes can range from ∼0.2 nm to over 100 nm.[29,190,191] The highly tunable nature of polymeric materials allows for the study of confined transport under designed chemical and steric environments. Polyamide and cellulosic materials have been the most studied polymeric membrane materials, due to the widespread usage of these polymers in desalination and water-purification processes.[192,193] However, nanoporous membranes can be synthesized with a broad range of polymer chemistries.[194] Here, we classify polymer membranes by the method used for their synthesis: phase inversion (Figure 8A), interfacial polymerization (Figure 8B), molecular, layer-by-layer (mLbL) deposition (Figure 8C), or self-assembly (Figure 8D). These synthetic approaches result in distinct porous structures that range from discrete and ordered pores to free-volume voids, each of which has its own advantages and disadvantages.

Phase-inversion membranes are fabricated via controlled precipitation of a thin film from a dissolved polymer.[197,198] There are a number of techniques that are used to create phase-

https://doi.org/10.1021/acs.chemrev.2c00155
Chem. Rev. 2023, 123, 2737–2831

inversion membranes, but nonsolvent-induced phase separation, or "immersion precipitation," is the most common approach. Phase inversion can produce membranes with asymmetric structures that have a thin, selective, nanoporous outer layer and a microporous underlying structure (Figure 9A). The membrane morphology is dictated by the nature of the solvent and nonsolvent, and the type and concentration of the polymer.[198] Cellulose acetate is a commonly used for phase inversion.[193,199] The primary benefit of phase-inversion membranes for studying confined transport is chemical continuity. In other words, the chemistry of the polymer in the nanoporous selective layer is the same as that of the underlying microporous support structure, making chemical interactions more predictable. Conversely, the gradual transition from small to large pores in phase-inversion membranes results in polydisperse steric environments. Discerning the pore-size distribution and the diffusion length is consequently difficult.[200]

Ultrathin polymer films can be formed via the polymerization of reactive monomers at the interface between two immiscible solvents.[192] This technique is most frequently employed to form polyamide membranes, with a diamine and acyl chloride as the reactants. By polymerizing directly above a porous support layer, which imparts mechanical integrity, a thin-film composite structure is formed (Figure 9B). Depending on the exact monomers used, these polymer membranes can have distinct diffusion thicknesses that can be characterized by transmission electron microscopy (TEM).[107,207] The small thickness of the selective layer relative to the support layer can complicate the characterization of the nanopores. Isolating the selective layer by dissolving the support layer in a polar solvent enables more precise characterization of the selective layer's molecular structure.[192,208] For example, electron tomography and wide-angle X-ray scattering can be used to capture the density distribution and orientation of an isolated selective layer's polymer network, respectively.[209,210] Solvent-induced isolation of the selective layer can, however, modify the polymer network, sometimes producing undesired effects.[210−212] A critical disadvantage for studying confined transport in films formed via interfacial polymerization is physical and chemical heterogeneity,[33,209,213,214] which lead to spatial heterogeneity in transport.

Nanoporous mLbL films are formed by the deposition of molecular layers through the reaction of alternating pendant functional groups (Figure 9C).[215] Polyamide is the most widely used polymer for thin mLbL films. However, the use of other polymers, such as polyurea and polyimide,[216,217] has also been explored. To avoid defect formation, nonporous substrates are typically used as the support layer when depositing mLbL thin films.[215,218] Polymer thin films formed via mLbL deposition were designed to overcome the limitations discussed above for conventional interfacial polymerization membranes.[195,215] Films prepared via mLbL methods boast chemical homogeneity,[219] and their thickness, topology, and local chemical composition are controllable at monomer length scales.[195] Additionally, mLbL deposition is not limited to specific solvents, thus broadening the chemistries that can be integrated into the nanoporous film.[220,221] The primary disadvantages of using mLbL films to study nanofluidics are the need for automation of the synthesis to obtain practical film thicknesses,[218] and the formation of defects[195] when depositing on a porous substrate for filtration experiments. The latter issue can be resolved by using an ultrathin interlayer atop the porous support to prevent unwanted penetration of reactive monomers,[195] or can be avoided altogether by measuring transport in the mLbL film atop a nonporous support with a load relaxation test, such as poroelastic relaxation indentation.[222]

Polymer membranes can also be fabricated via molecular self-assembly, in which chemically distinct molecular segments partition into thermodynamically defined microphases (Figure 9D,E). A wide range of microphase patterns[223] can be used to dictate the nanoporous structure of these films, with hexagonally packed cylindrical and bicontinuous gyroid morphologies being the most relevant.[204] Reactive small molecules[224] and block copolymers[196,204] are the two predominant classes of self-assembly materials for polymer membranes. Typically, discrete pores are formed by the selective removal or shrinkage of material from the self-assembled structures.[9] The properties of self-assembled polymer membranes can be tuned precisely.[196,204] In contrast to kinetically dictated processes such as phase inversion or interfacial polymerization, equilibrium-driven self-assembly can produce nearly uniform pore diameter distributions.[225] Although self-assembled films offer molecular-level control of the nanoporous environment, the requirement for thermodynamic stability limits the structures that can be created and the chemistries that can be employed.[9]

2.1.1.4. (iv) Single Nanopores in Polymer and Solid-State Films. The porous systems discussed above feature high porosity. Membranes that that contain a single nanopore have also been created.[226−229] Such single-nanopore membranes are ideal for exploring structure−function relationships, because the transport properties measured can be correlated directly to a single nanopore of known geometry and chemistry. Polymer films were one of the first templates used to create single-nanopore membranes. Single-polymer nanopore membranes have been prepared using the track-etching technique, in which irradiation with individual, energetic heavy ions (~2 GeV of total kinetic energy) is followed by wet chemical etching.[230,231] The process of etching defines the nanopore geometry, and cylindrical, conical, double-conical, and cigar-shaped nanopores can be prepared.[232−234] We note that the same approach of using energetic, heavy ions can also be applied to the preparation of membranes containing up to ~10^9 pores per cm^2, leading to porosities that are orders of magnitude lower than that of the polymer membranes described above. The fabrication of polymer membranes with openings as small as 1 nm has recently been demonstrated.[235] The track-etching technique is also applicable to preparing nanopores in mica,[236] glass,[237] and silicon nitride.[238]

One of the most frequently used methods of preparing single nanopores is drilling using TEM[239] or a focused ion beam (FIB).[240] The advantages of these fabrication tools are the abilities to image the nanopores during fabrication and to probe the nanopores' topography using electron tomography.[241] TEM and FIB have been used to prepare single nanopores in silicon nitride, graphene, and MoS_2.[239,242,243] Another advantage of these fabrication approaches is the ability to drill nanopores in desired locations, and even to preparate nanopore arrays, as can be accomplished using helium-ion-microscope milling. Nanopores with opening diameters down to ~1 nm have been reported. The exquisite control of pore openings with sub-1 nm precision has been demonstrated in 2D materials, such as through the electrochemical removal of individual atoms in MoS_2 films,[244] and by inducing defect nucleation centers in graphene.[245]

Recently, an inexpensive method of single nanopore fabrication has been developed based on dielectric breakdown

https://doi.org/10.1021/acs.chemrev.2c00155
Chem. Rev. 2023, 123, 2737−2831

of silicon nitride films under the influence of high electric fields.[246] This method does not require access to large-scale facilities, and was proposed as an outreach experiment to introduce the concept of nanopores to the general public.[247]

2.1.2. 2D Slits and Channels. *2.1.2.1. (i) 2D Silica Channels.* Modern nanofabrication methods enable the creation of nanofluidic channels of well-defined geometries. The planar character makes these nanofluidic channels an attractive alternative to nanopores when access to the interior of the channel is required, for instance, for imaging, or for electrochemical characterization and gating. Several fabrication strategies have been explored to fabricate channels in silica. For example, Cao et al.[248] used nanoimprint lithography and nonuniform SiO_2 sputtering deposition to fabricate nanochannels with widths as small as 10 nm, although the cross sections of these channels were not uniform at the smallest scales. Mao and Han[249] were able to create 20-nm channels by reactive ion etching or a wet etching of silicon or glass, followed by sealing the channels with another glass surface using fusion bonding or an anodic bonding process (Figure 10). Stein et al.[250] fabricated 70-nm-high channels using a simple, timed-etch process, providing a versatile system in which to study surface charge modifications.

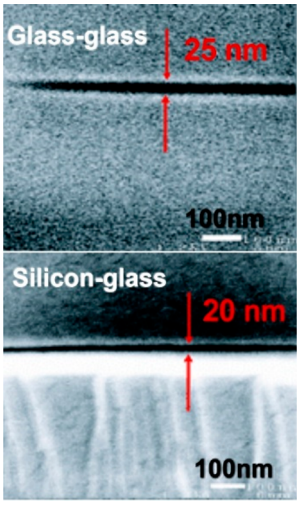

Figure 10. Nanofluidic channels formed by etching glass or silicon, followed by bonding with another flat surface. Adapted from ref 249. Copyright 2005 Royal Society of Chemistry.

Silica channels can also be prepared through sacrificial-layer approaches,[251] although initial attempts suffered from channel collapse from residual stress and from capillary forces during the drying process. Those initial obstacles were solved by a "bond-followed-by-etch" process that, in addition, facilitates integration of the device with gate electrodes (Figure 11).[252] Sacrificial Cr strips are first deposited on a SiO_2 substrate, and then are covered by another SiO_2 layer. At this stage of the fabrication process, gate electrodes are introduced to enable additional control of ion and fluid flow (Figure 11). After bonding the device with a microfluidic polydimethylsiloxane (PDMS) stamp, the Cr strips are etched away, exposing nanofluidic channels with a height that can be as little as a few nanometers.

Nanofluidic channels with heights as small as 2 nm have been prepared using precision reactive ion etching through standard semiconductor manufacturing processes (Figure 12).[253] At this length scale, steric forces (such as hydration forces in water) and

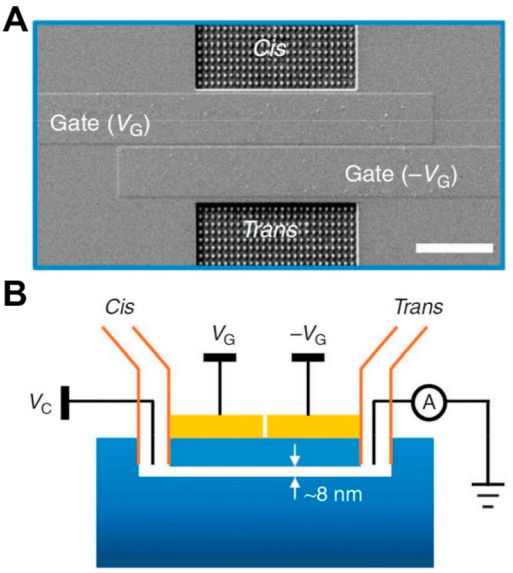

Figure 11. Solid-state nanofluidic channels fabricated by a "bond-followed-by-etch" processing. (A) Top view of a nanofluidic system consisting of multiple nanofluidic channels showing fluid inputs and outputs (cis and trans). The "dots" on these regions are posts that support the overlying PDMS and prevent it from collapsing. The nanochannels lie under the gates. Note that multiple gate structures can be employed. (B) A schematic cross-section of the device indicating the nanofluidic channels and the gates. Adapted from ref 252. Copyright 2011 Springer Nature.

van der Waals forces can become important. As discussed below, the interplay among these multiple interactions in this size regime has been shown to give rise to new transport properties such as increased ionic mobility.

2.1.2.2. (ii) 2D Pores with Stacked Slits. The development of experimental techniques for the exfoliation of monocrystalline graphene[254] effectively launched the field of experimental, 2D crystal materials science. One of the numerous examples of 2D crystal research developed over the years is van der Waals (vdW) heterostructures (Figure 13A).[255−257] These heterostructures are formed by stacking 2D crystals atop one another and allowing the vdW forces between adjacent crystals to hold the stack together. The original purpose of forming such heterostructures was the precision tailoring and synthesis of artificial materials that may exhibit properties that differ from those of the isolated 2D crystals. This initial work inspired the design of novel devices, including atomically smooth, 2D nanofluidic channels.[76]

Like many other nanofluidic devices, 2D nanochannels formed by vdW stacking (Figure 13B) require a mechanical support (e.g., silicon nitride membrane) for assembly. A rectangular hole is etched in the support, and then sealed with a thick "bottom" crystal (10 to 50 nm) via dry transfer techniques,[258] which are also used during the fabrication of precise 2D nanopores.[259] A "spacer" crystal, which defines the nanochannel height, is prepared by micromechanical cleavage[254] on a separate silicon wafer. The height of the spacer crystal depends on the number of monolayers of which the spacer is composed. As such, the height of the spacer can be tuned to the atomic height of the monolayer, which, for example, is 0.34 nm for graphene. The spacer crystal is then patterned by lithographic and etching techniques to create an array of equispaced parallel strips (i.e., channels) prior to transferring

https://doi.org/10.1021/acs.chemrev.2c00155
Chem. Rev. 2023, 123, 2737−2831

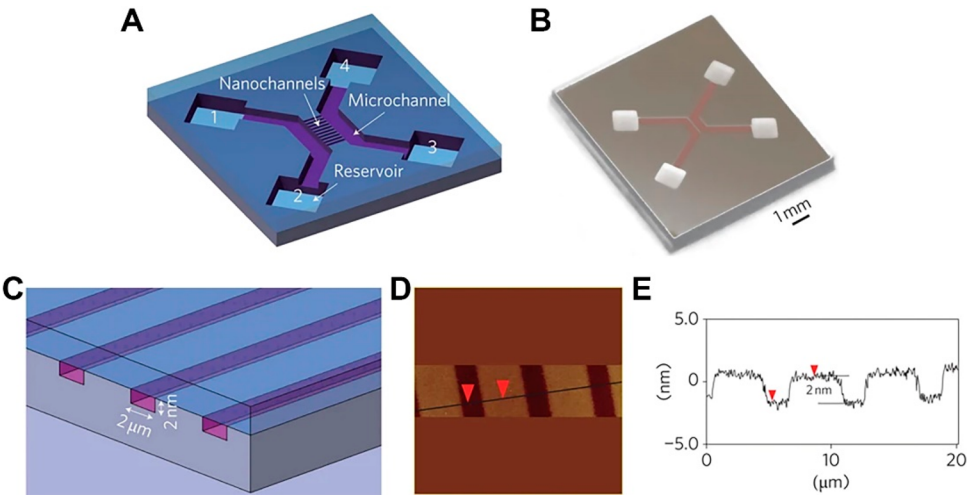

Figure 12. (A) Schematic of a nanofluidic system with 2-nm-high channels and four reservoirs. The top layer is a transparent Pyrex die and the bottom layer is a silicon die. (B) Bonded 2-nm nanochannel device with a Pyrex substrate on top. The channels are 1 cm long, 500 μm wide, and 60 μm deep, and the reservoirs are 2 mm × 2 mm through-holes. The color of the channels arises from the underlying, 500-nm-thick, thermal oxide layer. (C) Schematic of three nanochannels. (D) AFM image of three nanochannels after surface oxidation. Each device consists of ten 140-μm-long, 2-μm-wide, and 2-nm-deep silica nanochannels. (E) Cross-sectional analysis of the AFM image. The wafer and channel wall exhibit the same surface roughness (R_a ≈ 0.2 nm). Adapted from ref 253. Copyright 2010 Springer Nature.

onto the bottom crystal of the device. The device is then etched from the bottom, using the rectangular hole of the silicon nitride membrane as a mask, and is subsequently sealed with a thick (150 to 200 nm) "top" crystal. The resulting device (Figure 13C) can be used for precise studies of confined mass-transfer phenomena (Figure 13D).

Recent work on these vdW-assembled nanochannels has aimed at improving the success rate and reliability of the devices.[17,76,129,147,260,261] A few notable improvements are (i) brief exposure of the bottom crystal to an oxygen plasma to ensure atomic smoothness;[261] (ii) etching channel extremities after depositing a gold cap to prevent the top crystal from blocking the nanochannels at the edges;[147] and (iii) increased top crystal thickness to prevent sagging into the nanochannels.[17,57] These developments enabled vdW-assembled nanofluidic devices to attain confinement at the single-atom level (0.34 nm), which was originally not thought to be possible.[76]

Nanofluidic devices formed by vdW assembly offer a variety of benefits over conventional 2D nanochannels. The most noteworthy advantage is atomic-scale tunability (Figure 14A). In contrast to the single-atom-level confinement achievable by vdW assembly, conventional 2D nanochannels are limited to channel openings of ∼2 nm due to surface roughness limitations inherent in the deposition step.[154] Furthermore, vdW-assembled devices are promising platforms for studying nanofluidic transport across emerging materials, as the field has witnessed the synthesis of over a dozen new types of 2D crystals in the last 15 years.[255] Uniform channels with precise geometries enable the isolation of variables and transport phenomena that are often obscured in more complex and heterogeneous systems, such as 2D lamellar membranes, which possess nonuniform interlayer spacings and alignments, and are often plagued by macroscopic defects (Figure 14B–D).[172,262−264,] The absence of irregularities, such as defects, also enables the development of realistic simulations to complement and interpret experiments (Figure 14E).

2.1.3. 1D Materials Platforms. *2.1.3.1. (i) Carbon Nanotubes.* CNTs are 1D systems with precisely defined nanopores. CNTs can be single-walled, double-walled, or multiwalled (>2 walls),[266−268] but their pore sizes and transport properties are mainly governed by the innermost tube, which generally behaves in this context as a single-walled CNT (SWCNT). For this reason, when discussing the transport properties in this review, we will refer to CNTs by the diameter of the innermost tube, unless stated otherwise.

SWCNTs offer unique opportunities for probing molecules and ions under confinement. A single-walled CNT can be viewed as a graphene sheet rolled up along a chiral vector, described by $\vec{C} = n\vec{a}_1 + m\vec{a}_2 \equiv (n, m)$, in which $\vec{a}_1$ and $\vec{a}_2$ are the lattice unit vectors of the graphene sheet (Figure 15A). As a result of this graphitic structure, CNTs are relatively chemically inert and exhibit excellent mechanical properties, with a Young's modulus on the TPa scale.[269] Additionally, SWCNTs feature atomically smooth channels with a precisely defined pore diameter, d, that depends on the nanotube chirality (n,m). Although it was not realized until recently that other effects, such as pore−molecule interactions,[88] also play a role in determining the diameter of a nanopore, we can still provide a useful estimate of the pore diameter by subtracting the carbon-atom diameter from the carbon nucleus-to-nucleus diameter of the SWCNT. That is, $d \cong \frac{a_{c-c}\sqrt{3(m^2+n^2+nm)}}{\pi} - 2r_C$, where a_{c-c} is the carbon−carbon bond length and r_C is the van der Waals diameter of an sp^2-bonded carbon atom, which is 0.335 nm based on the interlayer spacing in graphite (Figure 15B).

CNTs are typically synthesized as a mixture of different structures, and thus different pore diameters. However, separation techniques, including density gradient ultracentrifugation (DGU),[270−272] gel chromatography,[273,274] aqueous two-phase extraction (ATPE), as well as extraction based on DNA,[275] polymers,[276,277] or small molecules,[278−280] have been developed to sort nanotubes by diameters and types. In a few cases, it has even been possible to purify single-chirality CNTs (Figure 15C). The CNT nanopores can be made accessible by opening the nanotube ends oxidatively. Figure 15D−G shows a high-resolution TEM image of SWCNTs with a diameter of 0.81 nm, which encapsulate and stabilize the infamously sponta-

https://doi.org/10.1021/acs.chemrev.2c00155
Chem. Rev. 2023, 123, 2737−2831

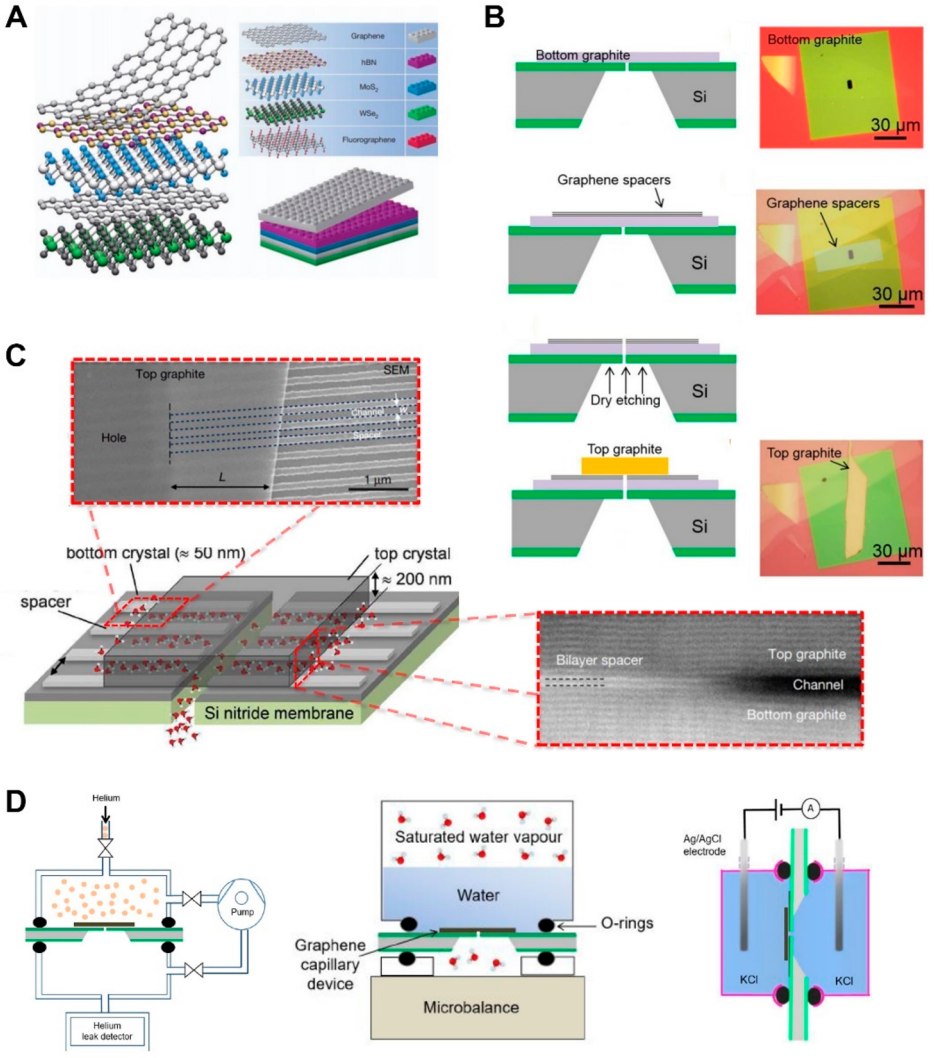

Figure 13. 2D nanofluidic devices fabricated by van der Waals assembly. (A) Schematic of 2D heterostructures formed by vdW assembly, analogous to stacked Lego blocks (bottom right). Adapted from ref 255. Copyright 2013 Springer Nature. (B) Schematic of the fabrication procedure for forming 2D nanofluidic devices by vdW assembly (left), with accompanying optical images in natural colors (right). Adapted from refs 76 and 17. Copyrights 2016 Springer Nature and 2019 American Association for the Advancement of Science, respectively. (C) 3D schematic rendering of a 2D nanofluidic device accompanied by a topographic SEM image (top) and a cross-sectional, high-annular, dark-field image of the edge of the channel (right). Adapted from refs 76 and 17. Copyrights 2016 Springer Nature and 2019 American Association for the Advancement of Science, respectively. (D) Schematics of devices for precise measurement of mass-transfer phenomena of gases (left), solvents (center), and ions (right). Adapted from refs 76 and 17. Copyrights 2016 Springer Nature and 2019 American Association for the Advancement of Science, respectively.

neously combustible P_4.[281] SWCNTs with appropriate pore diameters have also been exploited as nanoscale reactors for stereoselective synthesis[282−284] and as porous membranes for the selective transport of ions[2,19,285,286] and gas molecules.[287]

SWCNTs feature unique electronic structures that are determined by the chirality, and can be classified into three groups according to Mod $(n - m, 3) = 0$, 1, and 2. Mod 0 SWCNTs are metallic, with a continuous density of states (DOS) at the Fermi energy, whereas MOD 1 and MOD 2 SWCNTs are semiconducting, exhibiting chirality-dependent transition energies between the van Hove singularities (E_{ii}). Due to these energy levels, SWCNTs display photoluminescence (PL) from the E_{11} transition when excited by light resonant with the E_{22} transition (Figure 15H). Weisman and co-workers have mapped these transitions for many SWCNTs based on absorption and photoluminescence spectroscopy, assigning specific (n,m) structural indices.[288,289] The peak position of the E_{11} transition has been demonstrated to be sensitive to the interior nanopore environment.[80,290−292] This property can be used for detecting encapsulation and transport inside SWCNTs.[88]

In addition to the optical properties that arise from the van Hove singularities, SWCNTs are also Raman active, and have been well characterized via Raman spectroscopy (Figure 15I). Similar to graphene, SWCNTs show a signature G^+ band at ∼1591 cm^{-1} and G^- band at ∼1518 cm^{-1}. These bands arise from longitudinal (parallel to the nanotube axis) and transverse (perpendicular to the nanotube axis) sp^2 carbon displacements, respectively.[293] The incorporation of defects and disorder in the graphitic structure results in the appearance of the D band at ∼1350 cm^{-1}, which is induced by the vibrational mode of sp^3 hybridized carbons. Strong vibrations are also observed at a lower frequency, in the so-called radial breathing modes (RBMs), which correspond to the expansion and contraction of the CNT.[294] The frequency of the RBM band is correlated to the CNT diameter, and can provide information about the

https://doi.org/10.1021/acs.chemrev.2c00155
Chem. Rev. 2023, 123, 2737−2831

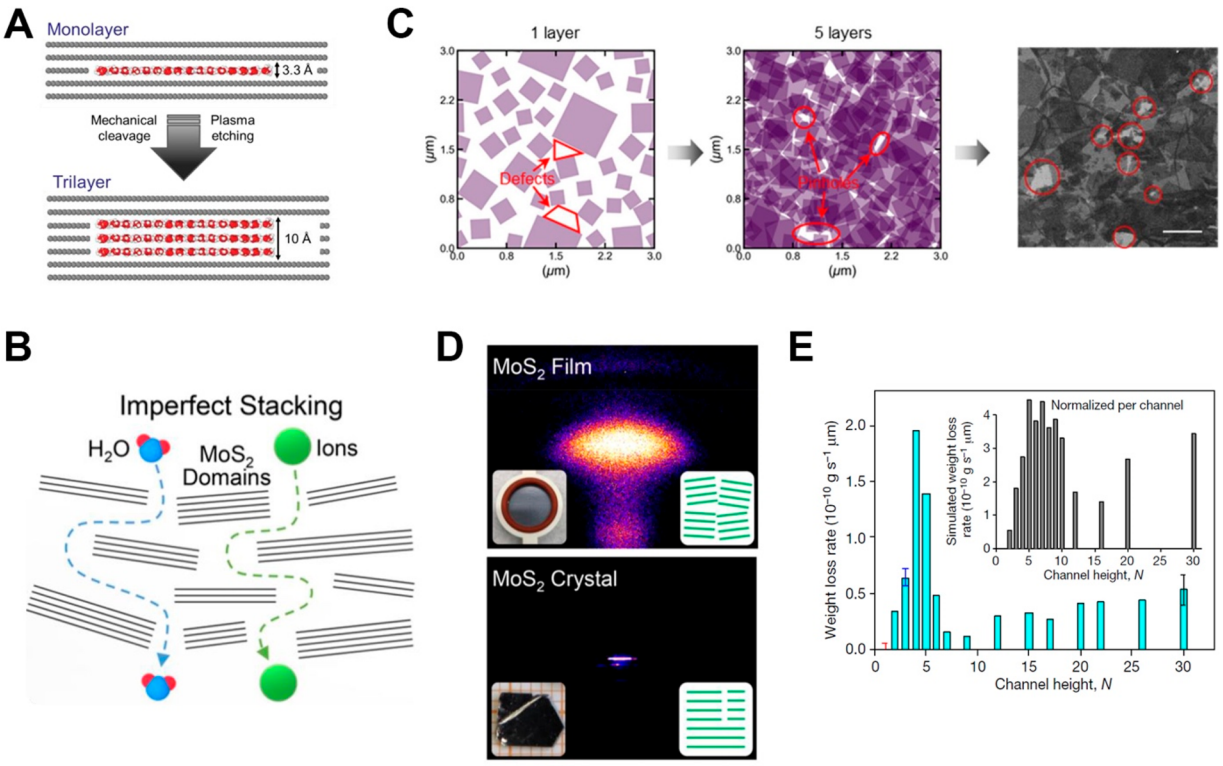

Figure 14. Advantages of 2D nanofluidic devices over 2D lamellar membranes. (A) Illustration of the Å-scale tunability of 2D nanofluidic devices, in which the channel height can be tuned by adjusting the thickness of the spacer crystal via mechanical cleavage and plasma-etching techniques. (B) Illustration of the influence of macroscopic defects and nonuniform crystal alignment on transport across 2D lamellar membranes. Such imperfections lead to irregular levels of confinement, making it difficult to separate nanoconfined transport phenomena from defect-driven artifacts. Adapted from refs 264 and 265. Copyrights 2020 American Chemical Society and 2017 Springer Nature, respectively. (C) The presence of macroscopic defects in randomly deposited 2D nanomaterial layers (left) leads to the formation of interconnected defects or "pinholes" in multilayer lamellar membranes (middle and right), resulting in low mass-transfer resistance. The purple shaded flakes are based on Monte Carlo simulations of 2D lamellar membranes, whereas the gray shaded flakes are from topographic SEM imaging of a few-layer 2D lamellar graphene oxide membrane. Adapted from refs 264 and 265. Copyrights 2020 American Chemical Society and 2017 Springer Nature, respectively. (D) 2D X-ray diffraction (XRD) pattern of a lamellar MoS_2 membrane (left) and crystal (right). The membrane shows a meridional arc-like pattern, indicative of a tendency of the nanosheets to imperfectly align parallel to the surface. Alternatively, the crystal exhibits a shortened belt in the 2D XRD pattern, suggesting large MoS_2 grains with near-perfect planar orientations. Adapted from refs 264 and 265. Copyrights 2020 American Chemical Society and 2017 Springer Nature, respectively. (E) Relationship between the water transport (represented as weight loss rate) and channel height (N) for simulated (gray bars) and experimental 2D nanofluidic channels (bottom). Experimental 2D nanofluidic data were from vdW-assembled graphene devices. Adapted from ref 76. Copyright 2016 Springer Nature.

endohedral environment. For example, Cambre et al. observed trapped water molecules in SWCNTs by comparing the RBM shifts of water-filled and empty nanotube samples.[295] Agrawal et al. subsequently demonstrated the ability to analyze phase transitions of water encapsulated inside SWCNTs via shifts in the RBMs.[3] Raman scattering can thus be used as a tool to detect filling of the nanotube pores.

There are different approaches for using CNTs as nanofluidic platforms. For example, CNTs in suspension may be filled with the surrounding solvent and investigated by means of optical spectroscopy[296] or analytical density gradient ultracentrifugation.[80] Although filling CNTs in suspension enables the deduction of the properties of the confined fluid by comparing the response of empty vs filled nanotubes of the same chirality, this approach is ill-suited for investigations of nanofluidic transport. The main platforms currently being used to study transport in CNTs are summarized in section 5.2.

2.1.3.2. (ii) Boron Nitride Nanotubes. Like CNTs, BNNTs feature 1D, tubular nanopores. A single-walled BNNT can be viewed as a rolled-up sheet of hexagonal boron nitride (h-BN) (Figure 16A). The chemical composition of boron and nitrogen can be confirmed by electron energy-loss spectroscopy (EELS), as shown in Figure 16B. BNNTs possess a Young's modulus of ~1 TPa.[298] Additionally, BNNTs can be composed of multiple nested nanotubes (Figure 16C).[299] BNNTs also have Raman signatures that can potentially be used to probe the nanopores. The Raman signatures include RBMs at 200−700 cm^{-1}, which arise from expansion and contraction vibrations similar to those of SWCNTs, the sp^3 hybridized BN bonding mode at 1292 cm^{-1}, which is similar to the D band of SWCNTs, and the counter-phase B−N vibration from the rolled up BN sheet at 1366 cm^{-1} (Figure 16D,E). As is the case for CNTs, BNNTs feature atomically smooth interior channels. Figure 16F shows a double-walled BNNT with an inner tube diameter of ~0.9 nm with α-sexithiophene encapsulated in a single-file manner.[300]

The major challenge of using BNNTs lies in their structural heterogeneity, as there is no method that can sort BNNTs by their specific structure. However, unlike SWCNTs, all BNNTs are insulators, presenting a contrasting system with distinctly different surface interactions and chemistry for studying confinement effects. Some of these distinctions have been revealed in experiments on individual, albeit large-diameter,

https://doi.org/10.1021/acs.chemrev.2c00155
Chem. Rev. 2023, 123, 2737−2831

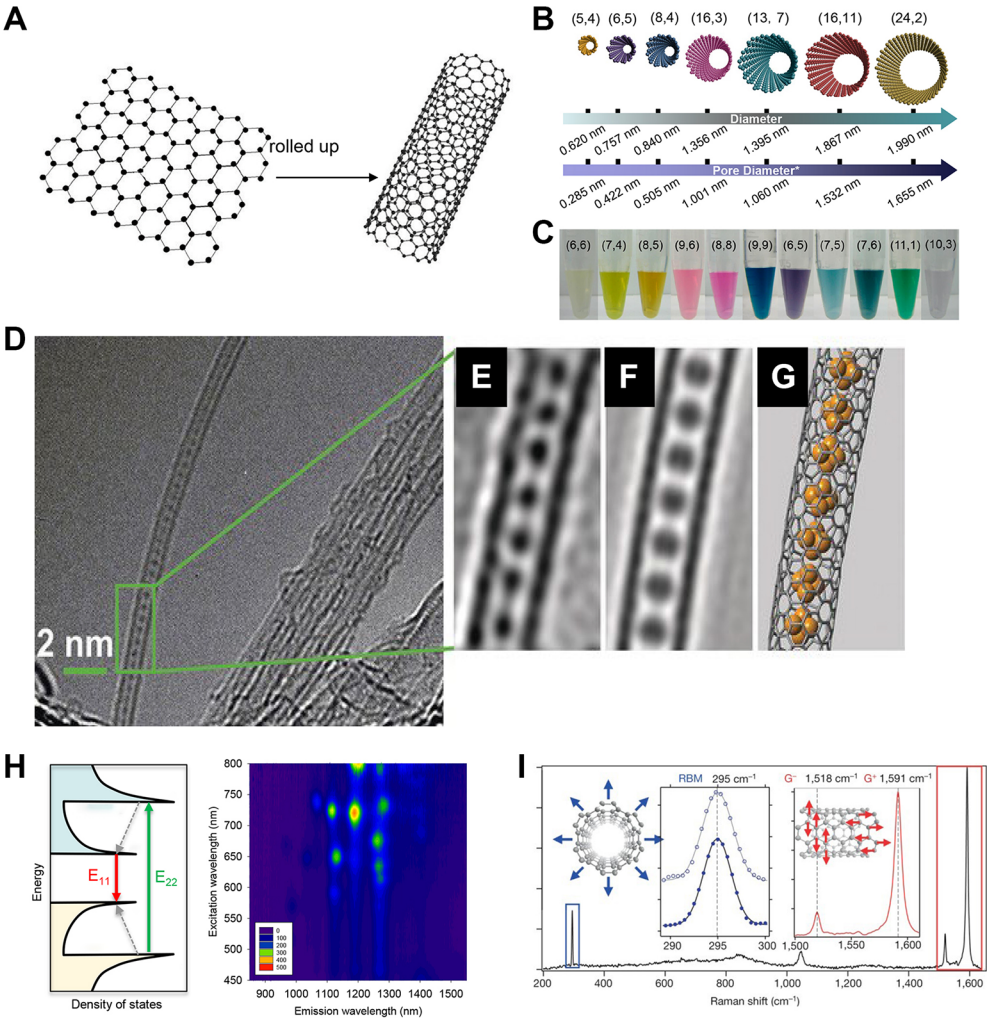

Figure 15. CNTs as tunable nanopores. (A) Schematic illustration of a SWCNT rolled up from a slice of graphene. (B) The carbon-nucleus-to-carbon-nucleus diameter and van der Waals pore size of each SWCNT correlated with the (n,m) chirality. (C) Photographs of aqueous solutions of single-chirality (n,m)-SWCNTs that are stabilized by a surfactant and DNA as individualized particles in water. Adapted from ref 275. Copyright 2016 American Chemical Society. (D) High-resolution TEM (HRTEM) image of a SWCNT filled with a string of P_4 molecules. (E) Noise-filtered HRTEM image of the region highlighted in D. (F) Simulated HRTEM image. (G) The corresponding atomic structure of P_4 molecules encapsulated within a SWCNT. Adapted from ref 281. Copyright 2017 Wiley-VCH. (H) Excitonic transitions of a semiconducting SWCNT and the corresponding photoluminescence excitation map of a mixture of multiple nanotube chiralities. (I) Raman spectrum of an individual SWCNT. The insets show further details regarding the narrow RBM peak at 295 cm^{-1} and the splitting of the G band into a G^+ component at 1,591 cm^{-1} and a G^- component at 1518 cm^{-1}. Adapted from ref 297. Copyright 2014 Springer Nature.

BNNTs, which are used as nanocapillaries.[75,301] Efforts have also been made to fabricate BNNT membranes for nanofluidic studies.[302]

2.1.4. 0D Nanoporous Materials. In zero-dimensional (0D) nanoconfinement, there is no external access to a confined liquid. Accordingly, the majority of approaches to 0D confinement of liquids rely upon self-assembly, and the confining medium is therefore soft. The most prevalent 0D confining medium for liquids is reverse micelles.[305,306] Reverse micelles in some cases can be accessible with spectroscopic tools, which, when combined with highly tunable size of the micelles, allows one to probe properties of the confined liquid in great detail.

A conventional micelle is composed of a surfactant bilayer that encapsulates an aqueous solution. The surrounding solvent is also aqueous, which makes distinguishing the spectroscopic properties of the confined population of water challenging at best. As shown in Figure 17, a reverse micelle is composed of a monolayer of surfactant encapsulating an aqueous pool.[306] The hydrophobic tails of the surfactant molecules point outward, and so the surrounding solvent can be nonpolar, e.g., an alkane. The benefit of this situation is that the solvent can be spectroscopically distinct from the aqueous pool, allowing for a range of different spectroscopic techniques to be employed to study the confined liquid.[306] The diameter of reverse micelles can range from a few nanometers to tens of nanometers or more, and is determined by the ratio of water to surfactant, which is denoted w_0. The diameters of reverse micelles of a specific composition w_0 are generally quite monodisperse.

One issue with reverse micelles is that the surfactant head groups are charged. Thus, not only must the surfactants be accompanied by counterions, but the environment inside of a reverse micelle is also heterogeneous. These factors can influence the behavior of the encapsulated liquid, which in some cases makes it difficult to isolate the effects that confinement has on the confined aqueous solution.

https://doi.org/10.1021/acs.chemrev.2c00155
Chem. Rev. 2023, 123, 2737−2831

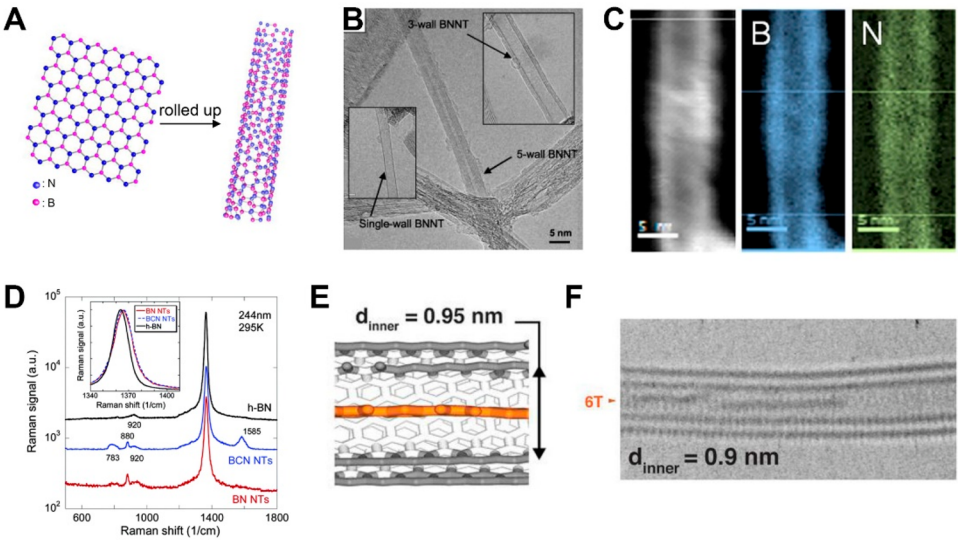

Figure 16. Boron nitride nanotubes. (A) Schematic illustration of a BNNT as a rolled-up cylinder of h-BN. Nitrogen: blue atoms. Boron: purple atoms. (B) A zero-loss, energy-filtered image of a BNNT, and the corresponding EELS elemental maps. Adapted from ref 303. Copyright 2014 American Chemical Society. (C) High-resolution TEM images of BNNTs. Adapted from ref 299. Copyright 2009 IOP Science. (D,E) Raman spectroscopy of h-BN and BNNTs in the (D) low and (E) high energy regimes. (D,E) Adapted from ref 304. Copyright 2014 IOP Science. (F) High-resolution TEM images of α-sexithiophene molecules inside a BNNT with an inner tube diameter of 0.9 nm. Adapted from ref 300. Copyright 2020 Wiley-VCH.

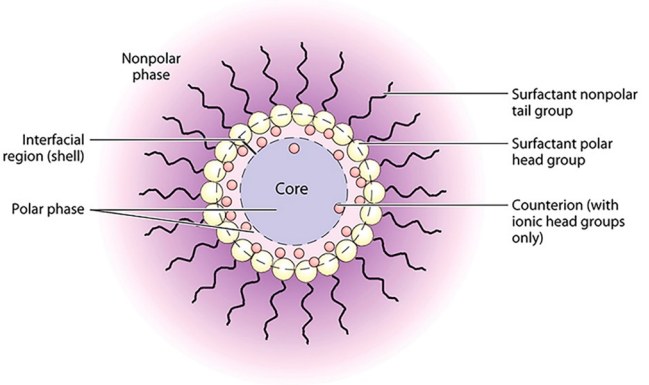

Figure 17. Schematic of a reverse micelle. The nonpolar phase is typically an alkane solvent, and the core of the micelle is an aqueous solution. The diameter of the core is controlled via the ratio of water to surfactant, w_0. Adapted from ref 306. Copyright 2009 Annual Reviews.

2.2. Characterization Tools

2.2.1. Calorimetry, from DSC to Scattering to Raman Spectroscopy. *2.2.1.1. (i) Measuring Thermodynamic Properties.* We begin by considering experimental techniques that can be used to measure the thermodynamic properties of nanoconfined liquids. Nanoconfinement can have a profound effect on a broad range of thermodynamic observables, such as the heat capacity, the coefficient of thermal expansion, the vapor pressure, and phase-transition temperatures of a liquid. The ability to measure changes in these properties can provide crucial insights into how nanoconfined liquids differ from bulk liquids, and how these differences affect transport at the nanoscale.

One classic technique for studying thermal expansion and phase transitions in nanoconfined liquids is dilatometry. In this method, the volume of a substance is studied during a dynamic process, such as a chemical reaction or a temperature change. In the case of nanoconfined liquids, dilatometry is best suited for use in monolithic confining media. Providing that expansion or contraction can be assumed to be isotropic, it is sufficient to measure the temperature dependence of a single dimension of a monolith containing a confined liquid. Some of the earliest research in this vein of nanoconfined liquids was performed by Hodgson and McIntosh, who studied the length of Vycor monoliths filled with water[307,308] and benzene[308] as a function of temperature. As shown in Figure 18A, upon cooling, the length of a water-saturated Vycor monolith decreased down to a temperature of approximately −25 °C before increasing. For the bulk liquid, expansion commences at 4 °C. Thus, confinement in Vycor leads to a substantial depression of the freezing point of water. Upon heating from low temperature, the transition from contraction to expansion occurs at approximately −10 °C. This hysteresis was found to be reproducible over many heating and cooling cycles, and was suggested to be evidence that the confined liquid does not freeze or melt at a single, well-defined temperature.[307]

Another readily monitored thermodynamic observable is vapor pressure. If a nanoconfined liquid freezes at a different temperature than the corresponding bulk liquid, then confinement must change the vapor pressure of the liquid relative to that of the bulk. One can alternatively think about this pressure difference as arising from capillary forces, although these two viewpoints are not entirely identical. In principle, vapor-pressure measurements can be made if the nanoconfining medium is either a powder or a monolith; the very fact that the vapor pressure of the confined liquid is less than that of the bulk liquid helps to prevent the presence of liquid between grains. However, close contacts between grains may confine some liquid as well. Conversely, if the nanopores are not entirely uniform, the narrowest portions (bottlenecks) may dominate the vapor pressure. Monoliths, which have an orders-of-magnitude smaller exterior surface area than do powders, can be particularly susceptible to this phenomenon.

A representative set of measurements of the vapor pressure of benzene inside of a Vycor monolith[307] is shown in Figure 18B. The hysteresis in vapor pressure between cooling and heating is often a hallmark of pore bottlenecks. In cooling, the vapor

https://doi.org/10.1021/acs.chemrev.2c00155
Chem. Rev. 2023, 123, 2737−2831

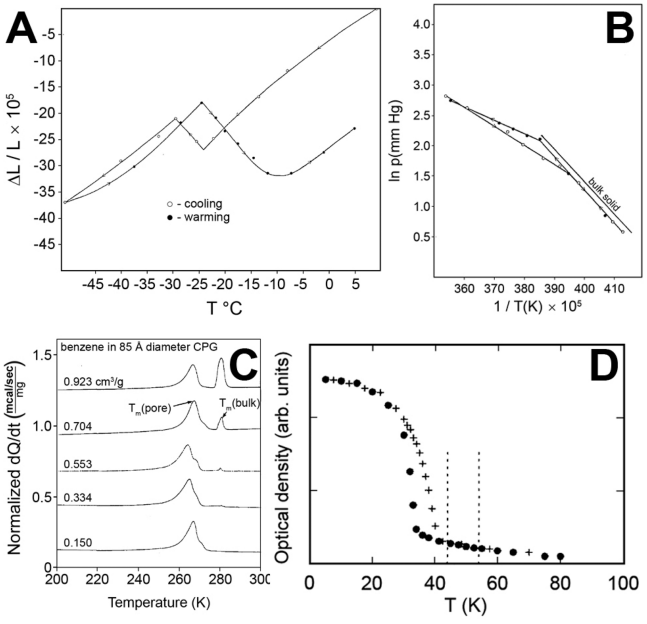

Figure 18. Classic thermodynamic measurements on the phase transitions of liquids in nanoporous materials. (A) Dilatometry experiments on water confined in Vycor glass. Adapted from ref 309. Copyright 1960 Canadian Science Publishing. (B) Vapor-pressure experiments on benzene confined in Vycor glass. Adapted from ref 309. Copyright 1960 Canadian Science Publishing. (C) Differential scanning calorimetry on benzene confined in powdered, controlled-pore glasses. Adapted from ref 310. Copyright 1990 American Institute of Physics. (D) Optical absorption as a function of temperature for oxygen confined in Vycor glass with a 44 Å pore diameter. The circles represent data obtained during cooling and the crosses data obtained during heating. The dashed vertical lines denote the bulk freezing transition at 54.4 K and the $\gamma-\beta$ solid transition at 43.8 K. Adapted from ref 311. Copyright 1987 American Physical Society.

pressure decrease is dominated by the first regions of the sample in which the liquid condenses, i.e., bottlenecks. On the other hand, upon warming, the vapor pressure in a closed system can be dominated by the confining regions with access to the exterior that have the highest vapor pressure, i.e., the largest pores. Thus, vapor-pressure data can give information about the confining regions in a material with both the highest and lowest vapor pressures.

Another traditional technique for measuring thermodynamic properties in nanoconfined liquids is differential scanning calorimetry (DSC). DSC measures the rate of change of the heat released by a material upon cooling or the rate of change of the heat involved in warming. Warming is useful for studying the melting of confined crystals and glasses,[310] whereas cooling can be used to study freezing and vitrification.[312] Cooling data may yield different phase-transition temperatures than do warming data, because liquids can often supercool more readily in confinement than in the bulk. The temperature-scan rate can also play a role in the observed phase-transition temperatures, particularly in cooling experiments. Indeed, the glass-transition temperature is itself dependent upon the cooling rate.

Figure 18C shows DSC heating curves for benzene at different loadings in powdered, controlled-pore silicate glass (a type of reconstructed glass) with an average pore diameter of 85 Å.[310] In this case, the surfaces of the glass were functionalized with a hydrophobic monolayer to facilitate filling of the sample with the liquid. It is evident from these data that benzene melts at a considerably lower temperature in nanopores than in the bulk. There is clearly an excess of liquid at the highest loadings, resulting in a second melting peak that arises from the unconfined benzene.

As discussed above, monolithic confining materials enable the use of spectroscopic techniques that would be impossible to use in powders. An example of such a spectroscopic application is shown in Figure 18D.[311] In this experiment, liquid oxygen was confined in a Vycor monolith with an average pore diameter of 44 Å. Optical absorption was used to monitor the confined oxygen, as there is known to be a significant increase in the optical density upon freezing of this liquid. The circles in this figure denote data that were obtained during cooling, and the crosses denote data that were obtained during warming. The difference between the two curves is clear evidence that confined oxygen can be supercooled when confined in Vycor. Both the freezing and melting transitions occur at temperatures well below the bulk freezing point of 54.4 K (the rightmost dashed vertical line) and the temperature of the bulk $\gamma-\beta$ phase transition at 43.8 K (the leftmost dashed vertical line).

Beyond the classic thermodynamic techniques discussed above, advances in both experimental methods and confining materials have enabled sophisticated new approaches for probing the thermodynamic properties of nanoconfined liquids. There are too many such techniques to cover here, but we will discuss some representative examples.

There are many different nuclear magnetic resonance (NMR) methods that can be used to study the thermodynamic properties of confined liquids.[188,313−316] One theme common to many of these techniques is that line shapes change dramatically when the liquid dynamics slow down, such as happens in a freezing transition. For instance, Figure 19A shows deuterium NMR data obtained from D_2O confined in a Vycor monolith with a 109 Å average pore diameter.[188] At high temperature, the NMR spectrum is composed of a single narrow feature, as expected for this liquid. This single feature persists well below the bulk freezing point of 277 K, but broadens as the temperature is reduced and the liquid viscosity increases. Spectral features that would be expected for a solid begin to appear at 253 K, and increase in intensity as the temperature is lowered further. The intensity of the central liquid peak simultaneously decreases. A small, liquid-like peak remains even at 193 K. These spectra, which match well with simulations (Figure 19B), suggest that the confined D_2O does not freeze at a single temperature, but rather that freezing occurs on a layer-by-layer basis.[188]

A property that is notably absent from the above discussion is density. Although density is a fundamental property of liquids, the measurement of the density of nanoconfined liquids remains an outstanding challenge, both in experiments and simulations.[317,318] The determination of density relies upon knowing both a number of molecules and a volume. One approach to this problem in nanoconfinement is to use Gurvich's rule,[319] which states that the density of a confined liquid matches that of the corresponding bulk liquid under the same thermodynamic conditions. However, it is quite clear from the oscillatory density profiles observed in simulations that this rule is highly approximate in SDNs. From a practical experimental perspective, the volume available to a confined liquid is generally not well-known, as the confining medium may include inaccessible regions. Thus, determining the volume of the nanoporous material itself is not sufficient to define a unique density of a liquid that is confined within this medium. From the standpoint

https://doi.org/10.1021/acs.chemrev.2c00155
Chem. Rev. 2023, 123, 2737−2831

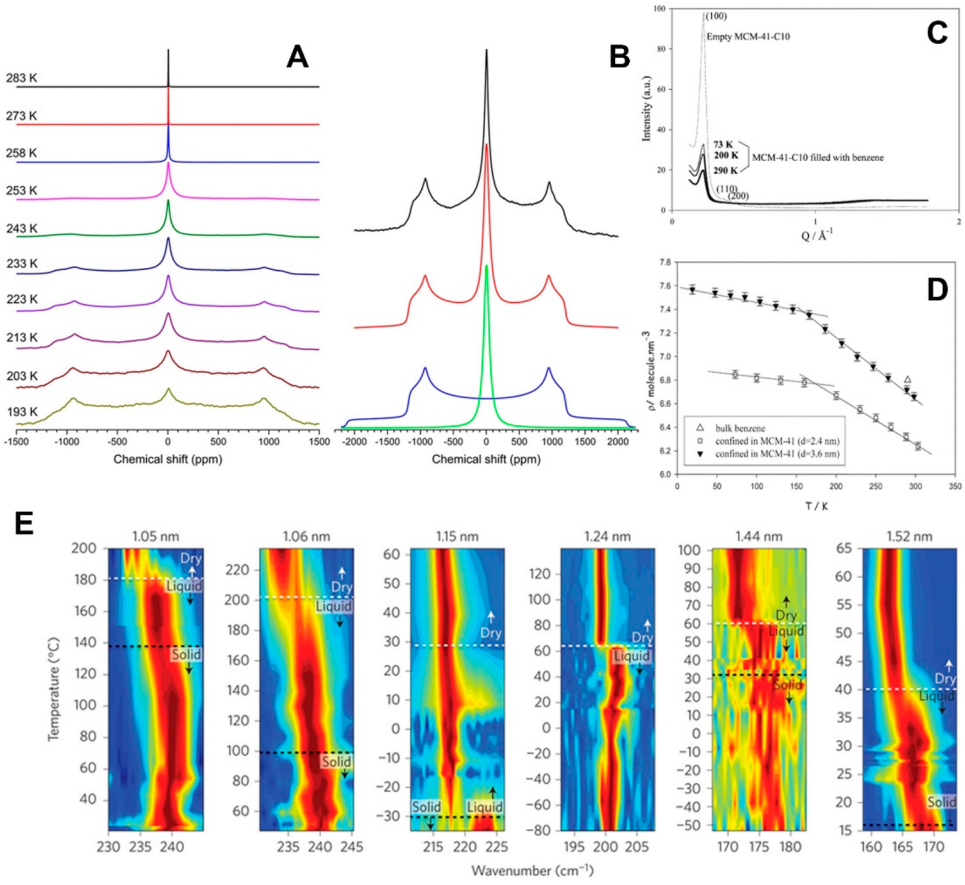

Figure 19. Spectroscopic measurements on the phase transitions of liquids in nanoporous materials. (A) ^{2}H NMR spectra and (B) simulated spectra of D_2O confined in Vycor glass. The sharp central feature arises from liquid water and the broad feature arises from ice. Adapted from ref 188. Copyright 2020 Springer Nature. (C) Neutron-scattering Bragg peaks and (D) densities inferred from such data for benzene confined in MCM-41 materials. Adapted from ref 313. Copyright 2006 American Chemical Society. (E) The radial breathing mode frequencies of water-filled CNTs of different diameters as a function of temperature. Adapted from ref 3. Copyright 2017 Springer Nature.

of simulations, although it is straightforward to calculate a density profile of a nanoconfined liquid, there is no rigorous means of determining the point at which such a profile should be terminated to calculate the average density of that liquid. Thus, the development of experimental methods that allow for the unambiguous determination of the density of nanoconfined liquids remains a key challenge in the field.

An example of an advanced technique that can be used to obtain information regarding the density of nanoconfined liquids is shown in Figure 19C.[313] This figure shows small-angle neutron-scattering data at the (100) Bragg peak for an MCM-41 sample with a 24 Å pore diameter, both empty and filled with benzene at a range of different temperatures. The filled material exhibits considerably less neutron scattering because the scattering contrast is decreased by the confined liquid. In this simplest picture, the scattered intensity depends only on the square of the difference between the product of the density and scattering length of the two media.[313]

Figure 19D shows the temperature-dependent density determined for benzene confined in pores with 24- and 36-Å diameters based on this neutron contrast-matching technique. The change in slope at low temperature was suggested to indicate the glass-transition temperature of the confined liquid.[313] However, as with other methods, the above caveats apply for the contrast-matching method. Indeed, the calculated densities for the smaller pores in Figure 19D are well below the spinodal for benzene, indicating that a liquid could not exist under these conditions. Thus, a more sophisticated method is likely required for interpreting these sorts of data, which may be due in part to the existence of volume that is inaccessible to the confined liquid.

Some precision nanomaterials offer the opportunity to probe the thermodynamic properties of nanoconfined liquids based on the observable properties of the confining medium itself. As an example, shown in Figure 19E are temperature-dependent Raman spectra of the RBMs of water-filled, individual CNTs of various diameters.[3] The RBM is highly sensitive to the mechanical properties of the confined water. Thus, as denoted in Figure 19E, there is a clear change in the RBM frequency when the confined water undergoes a phase transition or dewets the nanotube. The phase-transition temperatures exhibit considerable variation over nanotubes whose diameters vary over a range of less than 5 Å. Some of the apparent phase transitions occur at temperatures that vary considerably from those of the bulk liquid.

2.2.1.2. (ii) Measuring Dynamic Properties. The influence that nanoconfinement has on liquid dynamics is every bit as important as the influence it has on thermodynamics. The translational and orientational dynamics of a nanoconfined liquid are generally slower than those in the corresponding bulk liquid, although there are exceptions to this rule. The dynamics are furthermore generally spatially heterogeneous. As a rough

https://doi.org/10.1021/acs.chemrev.2c00155
Chem. Rev. 2023, 123, 2737−2831

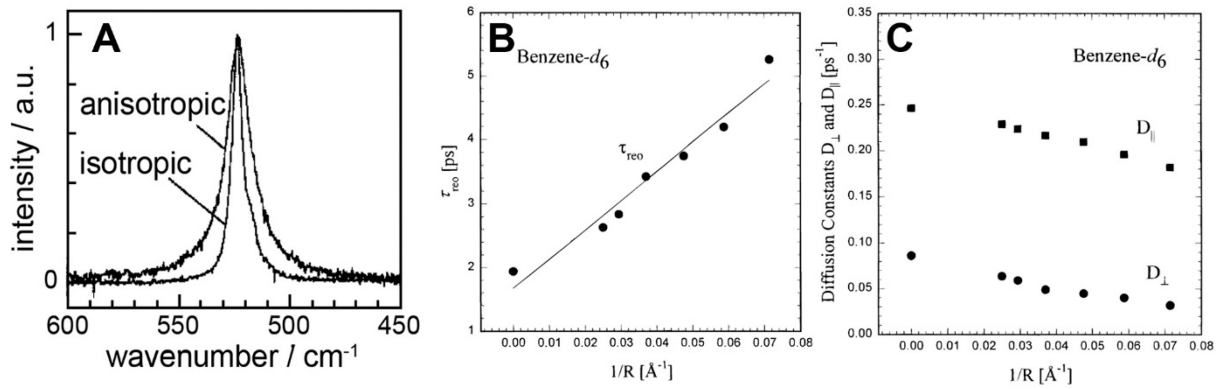

Figure 20. Orientational dynamics of nanoconfined liquids studied with spontaneous Raman spectroscopy. (A) Anisotropic (depolarized) and isotropic Raman line shapes for the C−I stretch in methyl iodide confined in a silica sol−gel monolith with a 40 Å pore diameter. Adapted from ref 322. Copyright 2000 John Wiley & Sons. (B) Orientational correlation times and (C) orientational diffusion constants for spinning and tumbling for benzene-d_6 confined in silica sol−gel glasses. Adapted from ref 323. Copyright 1996 American Chemical Society.

rule of thumb, molecules near pore walls tend to exhibit the slowest dynamics, whereas those in pore centers have faster dynamics, and in large enough pores may behave like molecules in the bulk liquid. Here we review some of the most popular experimental techniques for studying the dynamics of nanoconfined liquids.

2.2.1.2.1. Spontaneous Raman Spectroscopy. Polarization-selective spontaneous Raman spectroscopy[320] can provide a substantial amount of information regarding vibrational and molecular dynamics. The most common polarization configuration for spontaneous Raman spectroscopy, which is often denoted VH (for vertical excitation polarization and horizontal detection polarization), is used to collect the "depolarized" spectrum.[320,321] The depolarized spectrum is dependent on how the polarizability in one direction is influenced by excitation perpendicular to that direction, and is sensitive to the vibrational lifetime, vibrational dephasing, and molecular reorientation.

The counterpart to the depolarized Raman spectrum is the isotropic Raman spectrum, which measures the direction-independent change in the polarizability following polarized excitation. The isotropic spectrum is insensitive to reorientation, but is still influenced by vibrational relaxation and dephasing. The depolarized and isotropic portions of the polarizability are independent of one another, and together they represent the entire polarizability tensor.[320,321]

There are inherent challenges in the experimental measurement of the isotropic Raman spectrum, so it is more common to measure the depolarized Raman spectrum and the polarized (VV) Raman spectrum. The latter is a linear combination of the depolarized and isotropic Raman spectra, and so can be used together with the depolarized Raman spectrum to determine the isotropic Raman spectrum.[321]

Because spontaneous Raman spectroscopy is an optical technique, the use of this method to study nanoconfined liquids requires monoliths of high optical quality. The existence of strain birefringence in these materials can present a challenge for determining the isotropic Raman spectrum. Nevertheless, with sufficient care such experiments are possible. As an example, shown in Figure 20A are the depolarized and isotropic Raman spectra for the C−I stretch of methyl iodide confined in a silica sol−gel monolith with an average pore diameter of 40 Å.[322] The fact that the isotropic spectrum is so much narrower than the depolarized spectrum is a clear indication that orientational dynamics contribute strongly to the depolarized spectrum, i.e., that the time scales for vibrational relaxation and dephasing are not substantially shorter than the orientational correlation time.

Parts B and C of Figure 20 illustrate the type of information that can be extracted from the spontaneous Raman spectroscopy of nanoconfined liquids.[323] Figure 20B shows the average orientational correlation time for benzene-d_6 in sol−gel monoliths as a function of pore curvature (i.e., the inverse of the pore radius). These data indicate that reorientation becomes increasingly inhibited as the pore size becomes smaller. By monitoring different vibrational modes of benzene, it was further possible to determine the orientational diffusion constants along the 6-fold axis (spinning) and perpendicular to the 6-fold axis (tumbling).[323] As shown in Figure 20C, both of these diffusion constants decrease with increasing confinement. Because tumbling requires a greater hydrodynamic volume than does spinning, the fractional change in the diffusion constant for tumbling as the pore size decreases is considerably greater than that for spinning.

2.2.1.2.2. Nuclear Magnetic Resonance. Many different NMR techniques that have been used to probe the dynamics of nanoconfined liquids.[324−328] Here we discuss one representative example. The deuterium spin−lattice relaxation time, T_1, in a liquid is inversely proportional to the orientational correlation time of the molecules.[329] Thus, rapid orientational dynamics lead to slow spin−lattice relaxation, and vice versa. Figure 21A is an Arrhenius plot of the orientational diffusion constants of toluene-d_1 in the bulk liquid (squares) and confined in sol−gel glasses with an average pore diameter of 62 Å (circles).[329] The open symbols are data for orientational diffusion about the methyl axis, and the solid symbols are data for orientational diffusion about the two axes perpendicular to the methyl group. As expected, the orientational diffusion constants are smaller in confinement than in the bulk liquid. Interestingly, the aspect ratio of the diffusion tensor is larger in confinement than in the bulk liquid,[329] which suggests that some motions are more inhibited than others at the pore walls.

Spin−lattice relaxation occurs on a time scale (0.01−10 s in this system) that is much longer than that of orientational relaxation (approximately 1 ps to tens of ps in this system). Thus, on the time scale of spin−lattice relaxation, the confined molecules can be assumed to have sampled all dynamic environments statistically, which is consistent with only a single spin−lattice relaxation time being observed. Similar results have been observed in NMR studies of other van der Waals liquids,

https://doi.org/10.1021/acs.chemrev.2c00155
Chem. Rev. 2023, 123, 2737−2831

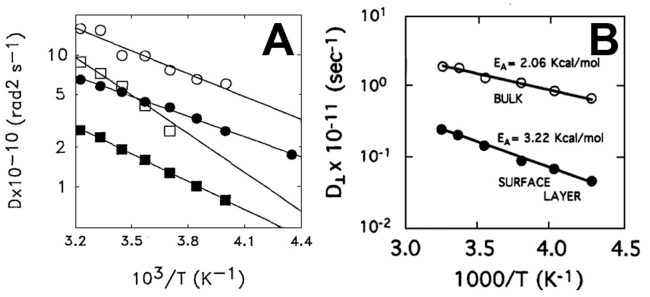

Figure 21. Orientational dynamics of nanoconfined liquids studied with NMR spectroscopy. (A) Orientational diffusion constants, determined by deuterium NMR, for toluene-d_1 parallel to the methyl axis (open symbols) and perpendicular to the methyl axis (solid symbols). The circles are for the bulk liquid and the squares for the liquid confined in silica sol−gel glasses with a 62 Å pore diameter. Adapted from ref 329. Copyright 1991 American Institute of Physics. (B) Orientational diffusion constant perpendicular to the molecular axis of acetonitrile-d_3 in the bulk-like and surface populations confined in silica sol−gel glasses, as determined by NMR. The thickness of the surface layer was assumed to be two molecular diameters. Adapted from ref 331. Copyright 1993 American Chemical Society.

which led to the development of the two-state fast-exchange (TSFE) model for analyzing such data.[330] The underlying idea of this model is that in large enough pores (i.e., those with diameters greater than a few molecular lengths), there are two distinct dynamic populations of molecules. The molecules in the pore centers are presumed to exhibit bulk-like dynamics, whereas those at the pore surfaces exhibit inhibited dynamics.

Within the TSFE model, if one knows the thickness of the surface layer and the pore diameter, then the orientational correlation time at the surface can be determined. There is no a priori method of determining the thickness of the surface layer based on NMR measurements, but a reasonable approximation that is often used is two molecular diameters.[331] Based on these assumptions, Zhang and Jonas used NMR data to estimate the temperature dependence of the orientational correlation time for tumbling in the surface layer of acetonitrile confined in sol−gel glasses. Figure 21B shows an Arrhenius plot of their results and a comparison to the bulk liquid.[331] Based on these data, the activation energy for reorientation is roughly 50% greater for the surface population than in the bulk liquid. We will revisit this picture below.

2.2.1.2.3. Optical Kerr Effect Spectroscopy. In optical Kerr effect (OKE) spectroscopy,[332−334] a linearly polarized ultrafast pulse is used to create a birefringence in an optically transparent liquid by inducing a slight alignment of molecules along the direction of the polarization. The alignment is based on the most polarizable axis of the molecules, which is why this process induces birefringence in the medium. The birefringence is probed by a second laser pulse that arrives at a variable delay time after the first pulse. The probe pulse is polarized at 45°, and encounters an analyzer polarizer following the sample that is set to pass light polarized at −45°. Thus, if there is no birefringence, then no probe light passes through the analyzer. By measuring the leakage through the analyzer as a function of the delay time

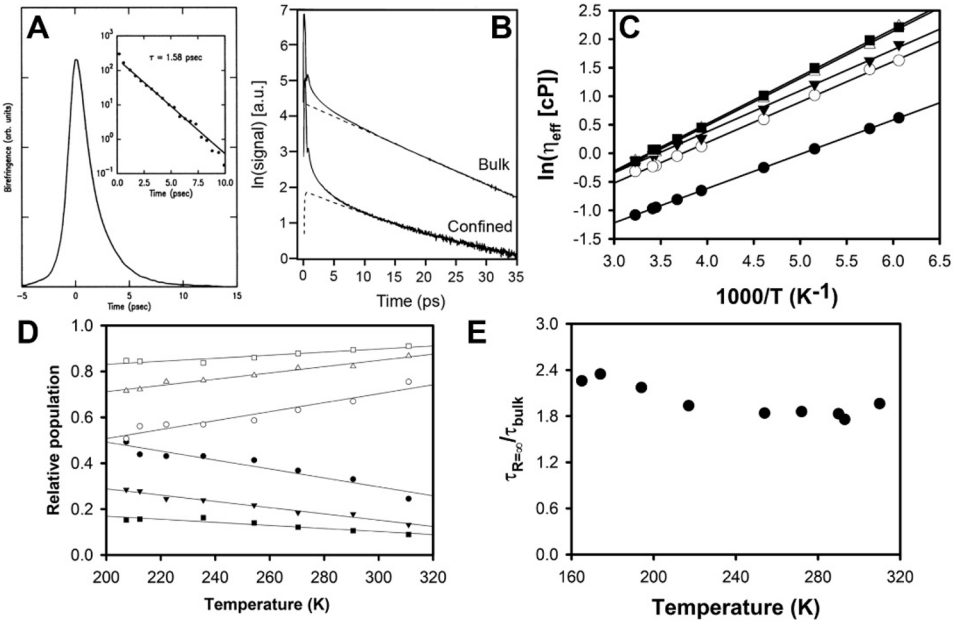

Figure 22. Orientational dynamics of nanoconfined liquids studied with optical Kerr effect spectroscopy. (A) Orientational dynamics of carbon disulfide confined in a sol−gel glass with a 44 Å pore diameter. Adapted from ref 335. Copyright 1986 American Physical Society. (B) Semilogarithmic plot of the OKE decays from CS_2 in the bulk and confined in sol−gel glasses with an average pore diameter of 24 Å. The dashed lines are fits to a component that relaxes on the same time scale as the bulk liquid and a second component with inhibited orientational dynamics. Adapted from ref 336. Copyright 1997 American Chemical Society. (C) Arrhenius plot of the viscosity of CS_2 in the bulk (solid circles) and the effective viscosity at the surfaces of silica pores with average diameters of 45 Å (open circles), 28 Å (solid triangles), 25 Å (open triangles), and 21 Å (solid squares). Adapted from ref 337. Copyright 1999 American Chemical Society. (D) Relative surface (solid symbols) and bulk-like (open symbols) populations of methyl iodide in silica pores with diameters of 83 Å (squares), 42 Å (triangles), and 24 Å (circles). Adapted from ref 338. Copyright 1998 American Chemical Society. (E) Temperature dependence of the ratio of the extrapolated orientational correlation time of CS_2 at a flat silica surface to that in the bulk. The fact that the ratio is always near 2 indicates that this component of reorientation is inhibited due to hydrodynamic volume effects. Adapted from ref 337. Copyright 1999 American Chemical Society.

https://doi.org/10.1021/acs.chemrev.2c00155
Chem. Rev. 2023, 123, 2737−2831

between the two pulses, the dynamics of the return of the liquid to its isotropic orientational state can be determined. Here we will focus on the portion of the decay that arises from collective orientational relaxation, which occurs on a time scale of a few ps and longer.

OKE spectroscopy is a form of depolarized, stimulated Raman spectroscopy, and is the time-domain analogue of low-frequency spontaneous Raman (also known as Rayleigh-wing) spectroscopy. However, the fact that OKE spectroscopy is coherent (i.e., that the signal propagates in a unique direction, along the probe beam, rather than over a broad range of angles) confers significant benefits for the study of liquids confined in monolithic porous glasses. The most important of these advantages is that a small region of the sample can be probed, which typically makes it possible to avoid strain birefringence entirely.

Warnock, Awschalom, and Shafer pioneered the use of OKE spectroscopy to study nanoconfined liquids.[335] Shown in Figure 22A are data they collected on carbon disulfide confined in a sol−gel monolith with a 44 Å pore diameter. Due to the pulse length and laser instability, these authors were not able to identify a statistically significant difference in orientational diffusion between the confined liquid and the bulk liquid in this case, although they did observe such a difference for the more strongly wetting liquid nitrobenzene.[335] With the advent of Ti:sapphire lasers, which have shorter pulses and greater stability than the laser used by Warnock, Awschalom, and Shafer, it became possible to obtain OKE data with higher time resolution and greater dynamic range. As shown in Figure 22B, there is a second, slower collective orientational diffusion component in CS_2 confined in nanoporous sol−gel glasses.[336] The overall decay can be fit with a biexponential function. One exponential decay time matches that of the bulk liquid, and presumably arises from molecules in the pore centers. The second decay is significantly slower, and thus is assumed to arise from molecules at the pore surfaces.

Because OKE spectroscopy can directly measure the diffusive orientational decay time of surface molecules, it is possible to use temperature-dependent studies to measure the activation energy for surface reorientation without any assumptions (cf. Figure 22B). An example of such a determination is shown for CS_2 in Figure 22C, both in the bulk and confined in sol−gel monoliths with average pore diameters ranging from 21 to 45 Å.[337] The quantity plotted here is the "effective" viscosity, which is calculated by multiplying the bulk viscosity at the same temperature by the ratio of the surface orientational correlation time to the bulk orientational correlation time. This picture assumes that the only factor leading to inhibition of orientational relaxation at the pore surfaces is an increase in viscosity. However, as shown in Figure 22C, the activation energy is virtually identical at the pore surfaces and in the bulk. A wide range of studies suggest that, for van der Waals liquids, this behavior is the rule, rather than the exception. The difference between the bulk viscosity and the effective surface viscosity therefore lies almost entirely in the magnitude of the Arrhenius prefactor, which calls into question whether the inhibition of surface reorientation is really due to a change in viscosity. We will return to this question below.

There is information not only in the time constants of this type of biexponential OKE decay for a confined liquid, but also in the amplitudes of the components. The amplitudes can be related directly to the fractions of bulk-like and surface molecules. An example of such an analysis is shown in Figure 22D[338] for methyl iodide confined in sol−gel monoliths with average pore diameters of 83 Å (squares), 42 Å (triangles), and 24 Å (circles). The bulk-like population is denoted with open symbols, and the surface population with solid symbols. As expected, the smaller the pore diameter, the larger the fractional surface population. The surface population also grows with decreasing temperature, a phenomenon that is common to all confined van der Waals liquids that have been studied with this technique.[339] Note that given the pore diameter and the fractional surface population, it is possible to calculate the thickness of the surface layer.

Liquids that do not have specific interactions with pore surfaces generally exhibit surface orientational relaxation rates that depend on the pore diameter. In particular, the smaller the pore diameter, the more inhibited the surface reorientation. The dependence of the surface relaxation time on pore curvature can provide insights into the mechanism of inhibition. Imagine, for instance, a liquid composed of cylindrical molecules that lie flat on the pore surfaces. Reorientation about an axis along the pore surface normal should be increasingly inhibited as the pore diameter decreases. Reorientation about an axis perpendicular to both the pore surface normal and the long molecular axis should be slower than in the bulk liquid due to an increase in the hydrodynamic volume required, but the rate of this motion should not be dependent on the pore radius. To distinguish between these two effects, the surface orientational correlation time can be plotted as a function of pore curvature. Such plots are typically linear until the pore diameter becomes only a few molecular lengths, and so by extrapolation it is possible to determine the orientational correlation time at a flat surface. Figure 22E shows the ratio of the orientational correlation time at a flat surface to that of the bulk liquid across the entire liquid temperature range of CS_2.[337] To within error, this ratio is 2, which corresponds to the expected ratio of hydrodynamic volumes for reorientation of a surface molecule about an axis parallel to the surface and a molecule that reorients freely in the bulk. This model demonstrates how reorientation can be inhibited at pore surfaces without invoking an increase in viscosity.

OKE spectroscopy has also revealed that specific interactions with the pore surfaces can have a substantial influence on the orientational dynamics of a confined van der Waals liquid. For instance, hydrogen bonds made between the pore walls and the liquid typically live for much longer than an orientational correlation time, which has a strong influence on surface relaxation, both for the hydrogen-bonded molecules and their neighbors.[340,341] Exchange into the bulk-like portion of the confined liquid can further become an important orientational relaxation mechanism for those neighbors.[340,341] The dynamics of liquids with intermolecular hydrogen bonds can be even more complex.[342]

2.2.1.2.4. Dielectric Spectroscopy. In dielectric spectroscopy,[343] an oscillating electric field is applied to a sample, and the frequency-dependent loss and/or phase shift are measured. Dielectric loss gives direct information regarding the individual and collective molecular dynamics of the sample. There are a number of challenges in applying dielectric spectroscopy to nanoconfined liquids, perhaps the greatest of which is that there is a limit to the maximum frequency that can be generated and measured. For this reason, the nanoconfined liquids that dielectric spectroscopy is most often used to study are highly viscous, either due to substantial intermolecular hydrogen bonding or to being significantly supercooled (or both).[344] For

https://doi.org/10.1021/acs.chemrev.2c00155
Chem. Rev. 2023, 123, 2737−2831

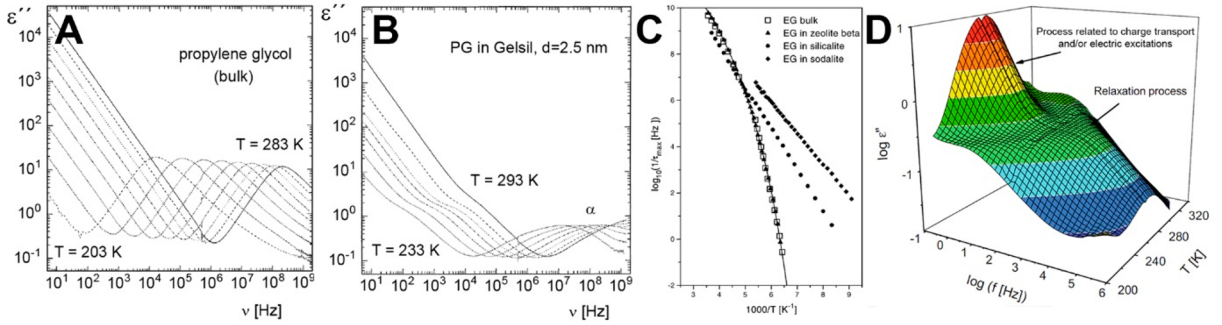

Figure 23. Dynamics of nanoconfined liquids studied using dielectric spectroscopy. Temperature-dependent dielectric loss for propylene glycol (A) in the bulk and (B) confined in silica sol−gel glasses an with average pore diameter of 25 Å. The data show clear evidence for slow relaxation at pore surfaces and a depressed glass-transition temperature. Adapted from ref 345. Copyright 1998 IOP Publishing. (C) Arrhenius plot based on dielectric relaxation data for ethylene glycol confined in zeolites. The ethylene glycol loses much of its collective behavior in silicalite and sodalite, which have pore diameters of 5.3 and 2.8 Å, respectively. In zeolite β, which has a pore diameter of 7.6 Å, the dielectric relaxation dynamics resemble those of the bulk liquid. Adapted from ref 347. Copyright 1999 American Physical Society. (D) Temperature-dependent dielectric loss data for water in aluminum containing MCM-41 with a pore diameter of 46 Å. A slow surface relaxation process is observed. Adapted from ref 348. Copyright 2008 Springer.

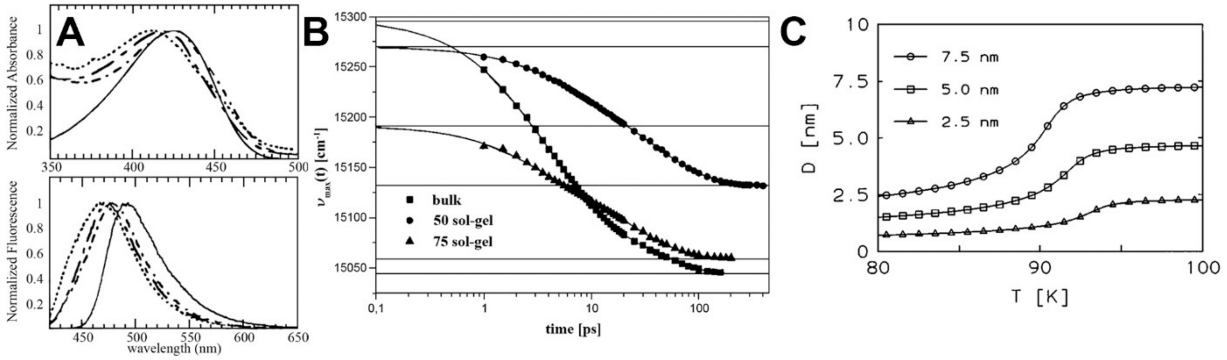

Figure 24. Solvation in nanoconfined liquids. (A) Absorption (top) and fluorescence (bottom) spectra of coumarin 343 in water in the bulk (solid lines) and in lecithin reverse micelles with water-to-surfactant ratios (w_0) of 4.8 (dotted lines), 5.8 (long dash−dotted lines), and 6.8 (short dash−dotted lines). Adapted from ref 353. Copyright 1998 American Chemical Society. (B) Dynamic Stokes shift data for solutions of Nile blue in ethanol in the bulk (squares) and sol−gel glasses with 50 Å (circles) and 75 Å (triangles) average pore diameters. Nanoconfinement influences both the magnitude and dynamics of the solvation process. Adapted from ref 354. Copyright 2001 American Institute of Physics. (C) Temperature dependence of the diameter of the bulk-like populations of liquid 2-methyltetrahydrofuran confined in silica sol−gel glasses with average pore diameters of 75 Å (circles), 50 Å (squares), and 25 Å (triangles), as measured by the triplet solvation dynamics of quinoxaline. Adapted from ref 355. Copyright 1996 American Physical Society.

the same reason, these studies are often conducted at low temperatures.

Dielectric loss spectra for bulk propylene glycol, a glass-forming liquid, are shown in 10 K increments from 283 to 203 K in Figure 23A.[345] The high-frequency peak shows that the rate of the fast dynamics slows by over 4 orders of magnitude over this temperature range. The red-shifting of this peak arises from the increase of viscosity in the liquid as it is cooled toward its glass-transition temperature of 168 K.[346] When the same liquid is confined in sol−gel glasses with an average pore diameter of 25 Å, the dielectric loss spectrum changes substantially,[345] as shown in Figure 23B. The fast relaxation component is of lower magnitude than in the bulk liquid, but is also shifted to higher frequency, suggesting a reduction in the glass-transition temperature. A shoulder also appears on the power-law portion of the decay at lower frequencies. This new feature is attributed to molecules with inhibited dynamics at the pore surfaces. Thus, this system exhibits both faster and slower dynamics than does the bulk liquid.

Dielectric spectroscopy can also be performed on powdered samples containing confined liquids. As an example, Figure 23C shows an Arrhenius plot of the peak dielectric loss rate in the high-frequency peak for ethylene glycol in the bulk and confined in different zeolites.[347] In zeolite β, which has a pore diameter of 7.6 Å, the peak of the dielectric loss tracks that of the bulk liquid, exhibiting classic Vogel−Fulcher−Tamman[349] behavior, with different limiting linear regions at low and high temperature. On the other hand, in silicalite and sodalite, which have pore diameters of 5.3 and 2.8 Å, respectively, the relaxation follows Arrhenius behavior.[347] These observations led to the conclusion that in the latter two zeolites, ethylene glycol no longer acts as a liquid.

Figure 23D shows temperature-dependent dielectric loss spectra for water in aluminum-containing MCM-41, in this case with a pore diameter of 46 Å.[350] Remarkably, the temperature-dependent shift of the high-frequency peak is nonmonotonic. In this case, the authors concluded that the temperature dependence of the spectra represents a competition between orientational fluctuations in the confined liquid and the formation of defects that allow for faster-than-expected water dynamics.[350]

2.2.1.2.5. Solvation. Solvation, as probed by static and time-resolved absorption and emission spectroscopy, can provide detailed information about the local solvent environment and dynamics around the probe molecule.[351,352] Most dye molecules

https://doi.org/10.1021/acs.chemrev.2c00155
Chem. Rev. 2023, 123, 2737−2831

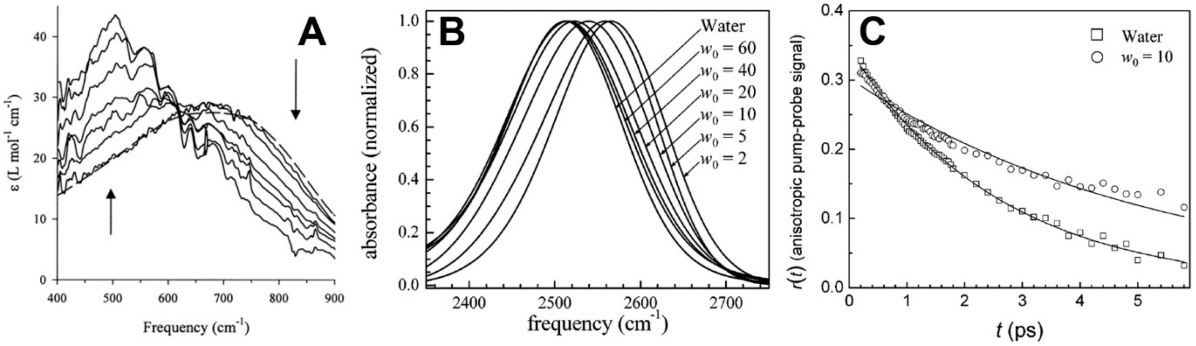

Figure 25. Infrared spectroscopy of nanoconfined liquids in reverse micelles. (A) Far-IR absorption of water in the bulk (dashed line) and in aerosol−OT reverse micelles with water-to-surfactant ratios ranging from 40 to 1 (in the directions of the arrows). These data illustrate that nanoconfinement has a strong effect on the librational modes of water. Adapted from ref 358. Copyright 2001 American Chemical Society. (B) IR spectra of the OD stretch and orientational anisotropy decays for 5% HOD in H_2O in the bulk and confined in reverse micelles of different water-to-surfactant ratios and (C) time-dependent orientational anisotropy in the bulk and in reverse micelles with a water-to-surfactant ratio of 10. Adapted from ref 359. Copyright 2006 American Chemical Society.

are solvatochromic to some extent, which is to say that their absorption spectrum depends on the nature of the solvent, and particularly its polarity. As an example, the top panel of Figure 24A shows absorption spectra of coumarin 343 in bulk water and in lecithin reverse micelles of different water-to-surfactant ratios.[353] The smaller the value of w_0, the more blue-shifted the absorption spectrum, suggesting that the solvent environment becomes less polar as the size of the reverse micelles decreases.

Fluorescence spectroscopy introduces an additional degree of sensitivity to the nature of the solvent, particularly when the charge distribution of the fluorescent molecule is different in the ground and excited states. When a molecule is excited, the solvent reorganizes to accommodate the new charge distribution. This reorganization also acts to destabilize the ground state, leading to what is known as a Stokes shift between the absorption and fluorescence peaks. The bottom panel of Figure 24A shows the fluorescence spectra corresponding to the absorption spectra in the top panel.[353] The shifts in the fluorescence spectra are greater than those in the absorption spectra. The overall shift between absorption and fluorescence decreases with increasing confinement, which is again consistent with the polarity of the solvent decreasing as the reverse micelles become smaller.

There is additional, rich information in the dynamics of the solvation process. Solvent reorganization occurs over a time period that depends on factors such as the viscosity of the solvent and the size of the solvent molecules. In confinement, additional aspects of the system, such as the pore size and the preferred environment of the fluorescent molecules (i.e., the pore centers or the pore walls), can also influence the solvation time. Solvation dynamics can be monitored by measuring the fluorescence spectrum as a function of time following excitation, in a technique called time-dependent fluorescence Stokes shift (TDFSS) spectroscopy. As an example, Figure 24B shows the time-dependence of the fluorescence peak of Nile blue in ethanol in the bulk and confined in sol−gel glasses with average pore diameters of 50 and 75 Å.[354] The magnitude of the fluorescence shift is greater in the bulk than in confinement, suggesting that confinement reduces the solvent polarity. Interestingly, the shift is somewhat greater in 50 Å pores than in 75 Å pores, which may be indicative of complex confinement effects that will be discussed below.

A limitation of TDFSS experiments is that they are only capable of monitoring dynamics over time scales on which fluorescence can be observed, typically up to a few ns to tens of ns. To monitor solvent dynamics on longer time scales, phosphorescence Stokes shifts can be used. Triplet states have lifetimes that can range up to seconds or more, so phosphorescence allows access to dynamics on an entirely different range of time scales than does fluorescence. As an example, Streck, Mel'nichencko, and Richert used triplet solvation to study the dynamics of supercooled 2-methyltetrahydrofuran confined in sol−gel monoliths with average pore diameters of 25, 50, and 75 Å.[355] They observed that one component of the phosphorescence decay showed little to no shift with time, whereas a second component did shift. The former component was related to molecules at the pore surfaces, and the latter to molecules in the pore centers. Based on the magnitudes of the two decay portions, the authors were able to determine the effective diameter of the bulk-like population as a function of pore diameter and temperature, as shown in Figure 24C.[355]

There are some caveats to be considered when applying solvation to the study of nanoconfined liquids.[356] The distribution of locations of luminescent molecules is important. Without knowledge of whether the molecules partition to the pore surfaces, to the bulk-like portion of the solvent, or are distributed statistically for a given confining medium and solvent, it can be difficult to interpret solvation data. Furthermore, a typical assumption in analyzing solvation data is that the response is linear, i.e., the motions that contribute to solvation dynamics are the same ones that occur at equilibrium. However, the fact that such studies generally use molecules with quite different charge distributions in the ground and excited states raises the possibility that the two electronic states prefer different regions of the pores. For instance, a molecule that partitions to the pore surfaces in its ground state may prefer to be in the bulk-like region of the solvent in its excited state.[356] Thus, electronic excitation may lead not only to solvent dynamics, but also to translation of the probe molecule into a completely different environment.

2.2.1.2.6. Infrared Spectroscopy. The shapes and positions of infrared (IR) absorption bands can provide useful information about the environment and dynamics of liquids, and even more information can be gained from time-resolved IR studies.[357] Most nanoconfining media have significant IR

https://doi.org/10.1021/acs.chemrev.2c00155
Chem. Rev. 2023, 123, 2737−2831

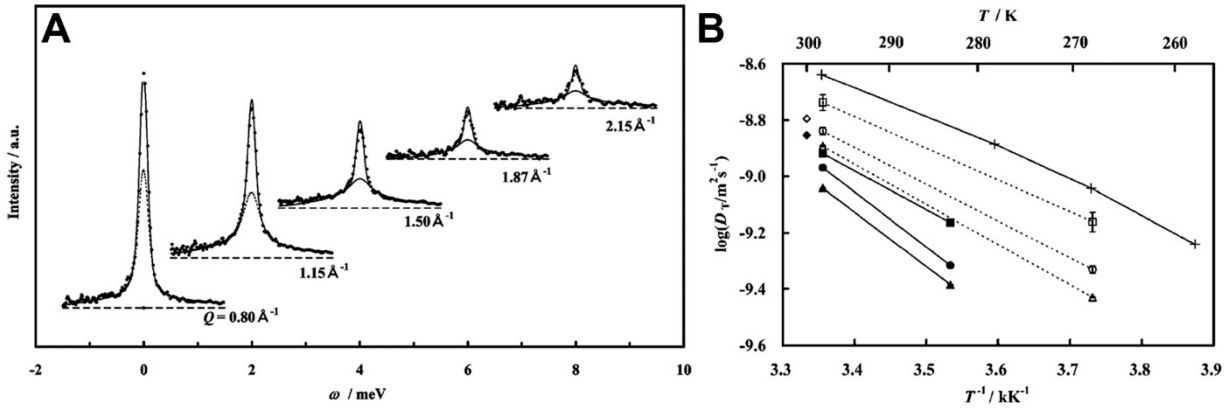

Figure 26. Probing the dynamics of nanoconfined liquids with quasi-elastic neutron scattering. (A) QENS spectra for methanol confined in MCM-41 with a 37.4 Å pore diameter. The symbols are the QENS data and the dotted, dashed, and solid lines are fits to the quasi-elastic component, the background, and the total signal. Adapted from ref 366. Copyright 2008 American Chemical Society. (B) Arrhenius plot of the translational diffusion constant determined by QENS for water in the bulk and confined in MCM-41 with 21 Å (solid symbols) and 28 Å pore diameters (open symbols). The different symbol shapes correspond to different methods of extracting the diffusion constant. Adapted from ref 367. Copyright 2005 American Chemical Society.

absorption, which can make it difficult to isolate the absorption of the confined liquid. For that reason, much of the IR work on nanoconfined liquids has focused on reverse micelles.

As a first example, Figure 25A shows THz (far-IR) absorption of bulk water and reverse micelles with different values of w_0.[358] Terahertz spectroscopy probes a spectral region for which, in this system, the absorption arises from intermolecular modes, rather than intramolecular modes. Any sort of libration (i.e., hindered translation or rotation) that changes the local dipole moment of the liquid can be observed with this spectroscopy. The bulk liquid has a librational band that peaks at approximately 700 cm^{-1}. With increasing confinement (along the arrows in Figure 25A), the bulk band decreases in intensity, and a new band builds in that peaks at approximately 500 cm^{-1}. Based on the isosbestic point at roughly 620 cm^{-1}, it was suggested that these spectra are consistent with a two-state model,[358] with the high-frequency feature corresponding to bulk-like water and the low-frequency feature corresponding to "bound" water interacting with the surfactant head groups. It is also possible that the low-frequency feature corresponds to water molecules that participate in fewer hydrogen bonds than in the bulk, which would be likely associated with a reduced librational frequency.

Mid-IR spectroscopy is also a useful means of probing the nature of nanoconfined liquids, so long as there is no spectral interference from the confining medium itself. As an example, Figure 25B shows the absorption spectrum of the O−D stretch of HOD in H_2O in reverse micelles.[359] This mode was chosen to avoid spectral overlap with the C−H stretches of the alkyl groups of the surfactants and the isooctane used as the nonpolar solvent. The spectrum shows a clear blue-shift with increasing confinement. Such a shift is known to be associated with an increase in the population of molecules that participate in a smaller number of hydrogen bonds,[360] which is again consistent with the presence of molecules at the surface of the confined water pool that are associated less strongly than in the bulk.

The dynamics of water in reverse micelles can also be probed with a range of sophisticated, time-resolved IR techniques. For instance, polarization-sensitive, pump/probe spectroscopy can be used to determine the population-relaxation and vibrational dephasing dynamics, following which the orientational anisotropy correlation function can be determined.[359] Representative data for the bulk liquid and for reverse micelles with $w_0 = 10$ are shown in Figure 25C.[359] The bulk liquid exhibits a single-exponential decay, whereas the relaxation in the confined liquid is more complex. The IR spectra and vibrational relaxation data fit correspond well to a 2-state, core−shell model, whereas orientational relaxation and spectral diffusion data (the latter determined from IR photon-echo experiments) suggest that a more complex model is required.

It is worth noting that the type of two-state or core−shell models that have been discussed throughout this section on measuring dynamic properties are often useful approximations for analyzing and understanding experimental data. However, simulations suggest that these models are at best approximate, and that the actual relationship between position and dynamic behavior in nanoconfined liquids is typically more complex.[361−363]

2.2.1.2.7. Quasi-elastic Neutron Scattering. In quasi-elastic neutron scattering (QENS),[364,365] the momentum transfer spectrum of scattered neutrons is measured, so QENS can be thought of as a type of low-frequency vibrational spectroscopy. As an example, Figure 26A shows QENS spectra and fits for methanol confined in MCM-41 with a 37.4 Å pore diameter.[366] These spectra are indicative of molecules with inhibited dynamics near the pore surfaces, in conjunction with molecules with higher mobility in the pore centers. Figure 26B shows an Arrhenius plot of the translational diffusion constant of water in the bulk and confined in MCM-41 with a pore diameter of 21 Å.[367] The different symbols correspond to different methods for extracting the translational diffusion constant, but in all cases the implied activation energy is similar in the confined liquid and in the bulk, in agreement with the results from other techniques discussed above. This technique can, for example, provide information on self-diffusion coefficient of solvents in nanoconfinement,[368] as well as on the existence of anisotropy of translational diffusion in nanochannels.[369]

2.2.1.3. (iii) Measuring Structural Properties. Nanoconfinement changes not only the thermodynamic and dynamic properties of liquids, but also the molecular organization. Although thermodynamic and dynamic measurements can be used to help infer the structural properties of liquids, it is clearly preferable to be able to probe the liquid organization directly. Unfortunately, there are few experimental techniques that can

https://doi.org/10.1021/acs.chemrev.2c00155
Chem. Rev. 2023, 123, 2737−2831

make such measurements. Most of what is known experimentally regarding the structure of confined liquids comes from studies using the surface forces apparatus (SFA).[370]

Figure 27 shows a schematic diagram of one generation of SFA.[371] The crux of this instrument is two parallel, atomically flat sheets of mica, between which can be placed a sample of a soft material. The sheets are gently curved, but in directions perpendicular to one another, such that there is a minimal contact area. The mica sheets are essentially flat and parallel in this contact region. The SFA allows the forces between the two mica sheets to be measured as a function of the distance between them, down to separations on the subnanometer scale, with sub-Ångstrom positional accuracy.[370] The variation in force with separation can reveal detailed information regarding the layering of liquids in slit pores.[372,373] Further information can be gained by exploring how the shear properties of the system depend on the distance between the mica sheets.[373,374] The mica can be functionalized with monolayers of different chemicals to tune the interactions with the liquid, and thereby the liquid's structuring. It is possible to make a wide range of other measurements as well, such as how the phase-transition temperature of a liquid depends on the separation between the mica sheets.[375]

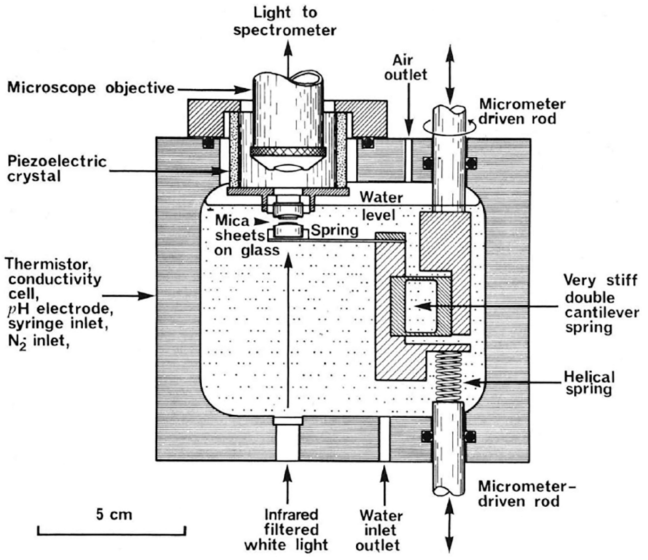

Figure 27. Schematic diagram of a surface forces apparatus. The liquid to be studied is placed between the mica sheets, the distance between which can be controlled with precision on the order of 1 Å. Adapted from ref 371. Copyright 1976 Springer Nature.

The classic sign of liquid structure in SFA data is a force profile that oscillates with the separation distance between the surfaces. For instance, long-chain alkanes tend to organize parallel to the mica surfaces. However, as seen in Figure 28, the behavior observed can also be considerably more complex.[376] This figure shows the results of SFA experiments on cyclohexane, in which the separation between the surfaces was measured during both loading and unloading (Figure 28A), and the refractive index was measured simultaneously (Figure 28B). Knowledge of the refractive index allows for the estimation of the liquid density, as shown in the scale on the right of Figure 28B. The points in these figures are connected by lines that denote the trajectory during loading and unloading. For each value of the force, a range of separations is observed, and for each separation, a range of refractive indices is observed. These observations are indicative of large-scale fluctuations in the confined liquid. Remarkably, the refractive index drops to a time-averaged value of roughly half that of the bulk liquid at a separation of slightly less than 2 nm. The large fluctuations may be an indication of a phase transition.[376]

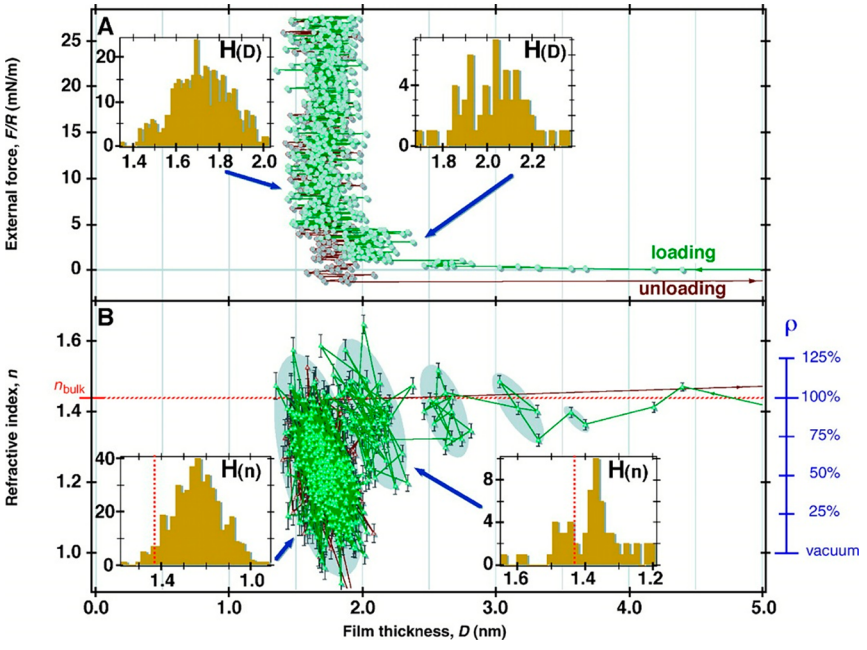

Figure 28. Simultaneous measurement of force and refractive index with a surface forces apparatus. (A) External force and (B) refractive index of cyclohexane in an extended surface forces apparatus as a function of the film thickness. Green data points are for approach, and red data points are for retraction. The density fluctuations highlighted in the histograms are considerably larger than might have been expected. Adapted from ref 376. Copyright American Association for the Advancement of Science.

https://doi.org/10.1021/acs.chemrev.2c00155
Chem. Rev. 2023, 123, 2737−2831

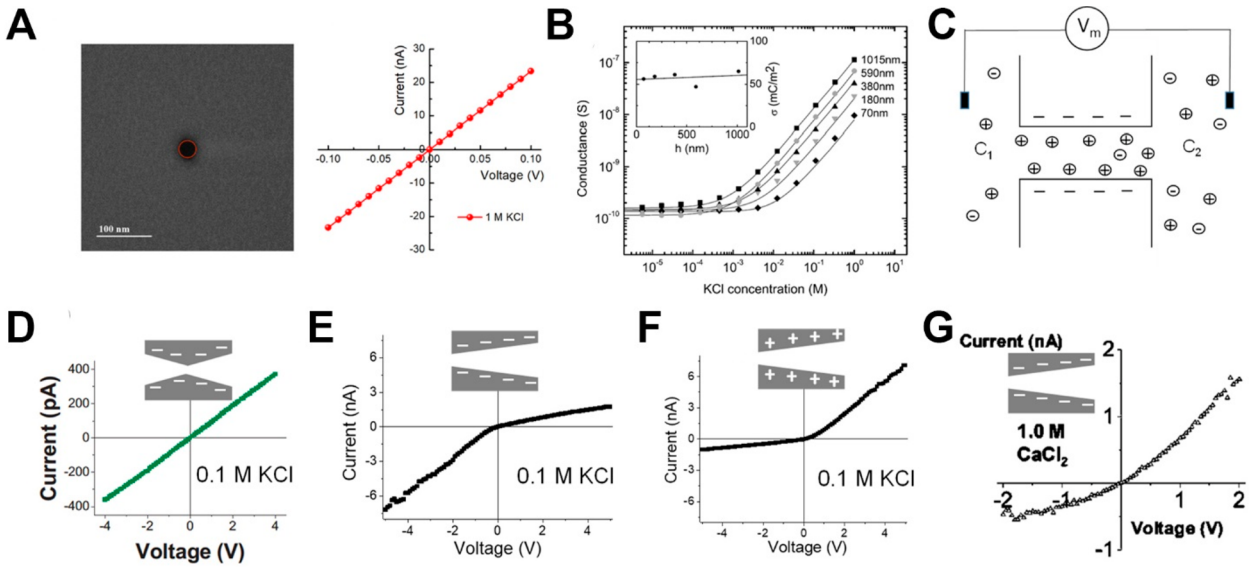

Figure 29. Ion current as a probe of the geometrical and electrochemical characteristics of single nanopores. (A) SEM image of a single nanopore prepared using FIB (left), and a corresponding current−voltage curve measured for this pore in 1 M KCl (right). Adapted from ref 402. Copyright 2020 American Chemical Society. The pore diameter, as determined by both SEM and ion-current measurements, was 32 nm. (B) Ion current measured through individual nanofluidic channels using a wide range of KCl concentrations. Adapted from ref 250. Copyright 2004 American Physical Society. Data for channels with different lengths are shown. The ion current begins to saturate when the pore length becomes comparable to the Debye screening length, allowing the surface charge of the channel to be measured (inset). (C) A scheme of the experimental setup used to probe the ion selectivity of nanopores. A nanopore is placed in contact with a concentration gradient. The established potential difference, V_m, indicates whether the pore is selective to cations or anions, and can be used to calculate transference numbers. (D) Current−voltage curve for an individual hourglass nanopore, with an effective opening of <5 nm, in 100 mM KCl. Adapted from ref 403. Copyright 2008 John Wiley & Sons. (E,F) Current−voltage curves for individual, conical nanopores with negative and positive surface charges, respectively, in 100 mM KCl. Adapted from ref 404. Copyright 2007 American Chemical Society. (G) An individual, conical nanopore with negative surface charge probed in 1 M $CaCl_2$. Adapted from ref 395. Copyright 2009 American Chemical Society. The direction of the current−voltage curve asymmetry indicates that this pore becomes effectively positively charged due to charge inversion.

2.2.2. Electrochemical Methods. In this section, we will focus on how electrochemical approaches can be used to characterize single nanopores, both synthetic and biological.[377] These approaches are applicable to nanopores in any material, including materials that cannot be easily imaged by electron microscopy.

Ion transport through single nanopores is often characterized by measuring time-dependent ion current and/or by collecting current−voltage curves. Ion current through a single pore can provide information regarding the pore diameter, the presence and polarity of surface charges, the selectivity for particular ions, and even the local ionic concentrations in the pore. Ion currents can be measured at the pA level or lower.[378] The measurement of time-dependent, ion-current signals is crucial for understanding the gating properties of biological ion channels, as well as the kinetics of the opening and closing of these pores.

Measurement of the ion current through a pore with a concentrated salt solution, such as 1 M KCl, is a common method of postfabrication characterization of synthetic nanopores and nanofluidic channels (Figure 29A). At high ionic strengths, surface charges on the pore walls are largely screened, allowing the measured current to be related to the pore geometry using an electrical analogy to a resistor.[250] This approach to sizing nanopores is rapid and nondestructive, and for some types of nanostructures provides the only means of estimating the effective diameter of the pore opening.[233] Even when nanopores are drilled by TEM or FIB, and can therefore be imaged during fabrication, electrochemical characterization is generally performed after the fabrication.[239,240] How accurate the electrochemical method is in providing information about the pore size as compared to electron microscopy remains an open issue.[379]

Recent studies described a detailed protocol for ion-current measurements that can be used to determine the diameters, and even the shapes, of pores.[380] The diameters of nanopores can also be determined using resistive-pulse measurements performed with a molecule or particle of known size. In this case, the amplitude of the measured pulses gives information regarding the pore diameter. This method can also reveal information regarding the nanopore shape.[381−383]

The surface charge in nanopores can be probed by measuring the ion current over a wide range of ionic concentrations.[250] As the bulk concentration decreases, the thickness of the electrical double layer (EDL) increases, so that a larger fraction of the pore volume is controlled by the EDL properties. Consequently, the measured ion current deviates from what would be predicted based on bulk conductivity. On the other hand, above a certain threshold concentration, the current becomes independent of the bulk concentration (Figure 29B).[250,384] This threshold concentration depends on the pore size, and corresponds to the case in which the pore radius is roughly equal to the Debye length. If the same measurement is performed with a neutral pore, a linear dependence of the current on the salt concentration is observed.

Electrochemical measurements in concentration gradients provide information on ion selectivity and the polarity of the surface charge.[377,385] When a nanopore is in contact with a salt gradient, the voltage established across the membrane (V_m in Figure 29C) reflects whether the nanopore is selective for the cation or the anion. Such measurements are often performed

https://doi.org/10.1021/acs.chemrev.2c00155
Chem. Rev. 2023, 123, 2737−2831

according to one of two protocols.[386] In the first approach, the salt concentration on one side of the nanopore is held constant, and a range of different concentrations is used on the other side. In the second approach, the magnitude of the concentration gradient is kept constant by changing the concentrations on both sides of the nanopore by the same factor. This latter method of probing ionic selectivity was used in early biophysics experiments that led to the development of the Hodgkin–Huxley action-potential model,[377] and is still used in the characterization of single channels with patch-clamp experiments.[387] The ability of a channel to differentiate between two ions of the same charge can be determined by measuring the potential difference across a channel between two reservoirs, one containing the first ion and the second containing the same concentration of the second ion. This approach is applicable both to single nanopores and porous membranes.

Due to the large surface-to-volume ratio of nanopores, ion current is sensitive to the pore geometry as well (Figure 29D,E). As an example, the current–voltage characteristics of cylindrical, conical, and hourglass-shaped nanopores are different from one another.[68] Cylindrical and hourglass nanopores with charged pore walls exhibit current–voltage curves that are linear in the low-voltage regime and saturate at higher voltages, at which the pore conductance is dominated by concentration polarization.[388] Conical nanopores were one of the first examples of an ionic rectifier.[68,389−392] Conical nanopores with negative and positive surface charges can be easily distinguished from each other by the shapes of their current–voltage curves (Figure 29E,F).

Current–voltage curves through nanopores are also sensitive to the properties of the solid–liquid interface, and especially to the surface charge density. As an example, a conical nanopore rectifies current to a degree that depends on the charge density, and if the pore walls are neutral there is no rectification at all.[393] The sensitivity of the ion current through asymmetric nanopores to the charge properties of the walls makes conical nanopores an ideal model system for probing charge inversion.[394] Charge inversion occurs when a surface that is, e.g., negatively charged in the presence of monovalent cations becomes positively charged in the presence of multivalent cations. Figure 29G shows current–voltage curves for a single conical nanopore in contact with KCl as well as $CaCl_2$.[395] Inverted current–voltage curves in the divalent salt provide evidence that the nanopore surface switches sign from negative in KCl to positive in $CaCl_2$.

The sensitivity of the transport characteristics in conical nanopores has also been used in the design of chemical sensors. To this end, pore walls and/or nanopore entrances are modified with a recognition agent that selectivity binds an analyte of interest present in the solution.[396] The analyte can be detected, and even its concentration determined, through measurements of current–voltage curves and time-dependent ion current.[397,398]

Ion current can also provide insights into the ionic concentration inside a nanopore. Ionic rectifiers transport more ions for a voltage of the polarity at which the pore volume is filled with a higher salt concentration.[68,399,400] For instance, a nanopore that has a positive surface charge tends to transport anions. If a positively charged nanopore is conically shaped, it will be filled with a higher concentration of ions when the tip of the pore is negatively biased with respect to the opposite, larger opening. This type of behavior has been verified in experiments with solutions containing a sparingly soluble salt. The concentration of the salt in the bulk solution in this case was below the solubility product. In the pore, however, the concentration was enhanced for one voltage polarity, creating nanoprecitates that temporarily blocked the ion transport.[401] The precipitates were unstable, leading to tunable ion-current oscillations.

2.2.3. Electrokinetic Methods. The experimental characterization of the electrical properties of interfaces, nanopores, and nanochannels typically requires the use of indirect, electrokinetic methods. In these techniques, nonequilibrium, thermodynamic, force–flux relationships are determined for the linear response to electrical, diffusional, and hydraulic driving forces acting on ions and the liquid solvent. Beyond the direct relationships to these driving forces (Ohm's law, Fick's law, and Poiseuille's law, respectively), the indirect relationships correspond to various linear electrokinetic phenomena, such as electro-osmotic flow, diffusion-osmosis, and streaming current, all of which are related to the pore charge.[405−425] It is important to emphasize, however, that the inferred electrical properties, such as the zeta potential and the surface charge, are model dependent, specifically requiring assumptions regarding the position of the slip plane, the ionic diffusivities, the local viscosity of the solution, the surface roughness/heterogeneity, and the permittivity of the solvent at the interface, among other considerations.[426−428] Furthermore, many of the relations that are valid for nonoverlapping EDLs are not valid for the regime of strong EDL overlap in SDNs.[429] Nevertheless, in conjunction with SFA measurements,[101] electrokinetic measurements provide the foundation for our understanding of charged interfaces, as making more direct, nondestructive observations of surface properties, electric fields, and ion concentrations is challenging at the molecular scale.

2.2.4. Transmission Electron Microscopy. Fluidic behavior inside SDNs is determined by a complex interplay among electrostatic, steric, and van der Waals interactions, as well as by solvation effects, all of which occur on molecular length scales. Understanding nanofluidic behavior in SDNs therefore requires experimental probes that offer high spatial resolution. TEM can be used to examine materials down to the atomic scale. However, this technique typically requires an environment in ultrahigh vacuum, usually below 10^{-6} mbar. In addition, the electron beam can cause damage to liquids, and has the potential to induce chemical reactions. These challenges can be overcome with cryogenic TEM (cryo-TEM) microscopy.[430−432] By vitrifying the liquid through rapid cooling, the native state of the sample is preserved, and the sample is protected from the vacuum and the electron beam. Li et al. recently used cryo-TEM to image the arrangements of discrete counterions at electrically charged liquid–solid interfaces.[433] By adding positively charged, amine-functionalized gold nanorods to aqueous solutions of phosphotungstic acid ($H_3PW_{12}O_{40}$), they captured the crowding and layering behavior of Keggin anions $[PW_{12}O_{40}]^{3-}$ at the nanorod surfaces (Figure 30A–C). Comparison between experimental observations and molecular dynamics simulations suggests that the finite ionic size (~1 nm) plays an important role in determining the nature of the layering. Furthermore, the cryo-imaging technique enabled the observation of ionic arrangements under extreme confinement. With different widths of confinement, the Keggin anions formed correlated monolayer and bilayer structures between parallel nanorods (Figure 30D,E). The cryo-TEM technique provides exciting opportunities for examining nanofluidic structures at the single-ion level, and offers a new means of validating computational and theoretical predictions.

https://doi.org/10.1021/acs.chemrev.2c00155
Chem. Rev. 2023, 123, 2737−2831

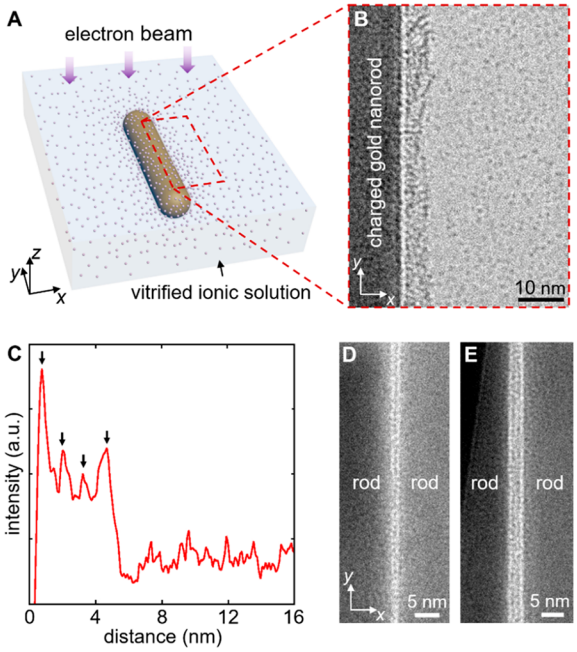

Figure 30. Cryo-TEM imaging of discrete ions and their distribution at an electrically charged, solid−liquid interface. (A) The sample consists of amine-functionalized gold nanorods embedded in an aqueous solution of phosphotungstic acid ($H_3PW_{12}O_{40}$). (B) A typical cryo-TEM image of the interface between a nanorod and the electrolyte solution (dashed region in (A)). The image contrast in the electrolyte solution is dominated by the Keggin anions, which contain multiple tungsten atoms. (C) Image-intensity profile, integrated parallel to the nanorod surface, for distances up to 16 nm from the nanorod surface. The oscillatory behavior at distances below 5 nm suggests that the Keggin anions form discrete layers at the interface. The arrows mark the positions of the concentration peaks of the Keggin anions, as obtained from molecular dynamics simulations. (D,E) Cryo-TEM images of the ionic solution confined between aggregated parallel nanorods, which show monolayer or bilayer ionic structures, depending on the confinement width. Adapted from ref 433. Copyright 2020 American Chemical Society.

Liquid cells offer another approach to imaging nanofluidic systems with TEM.[434,435] In a liquid cell, the fluid is separated from the vacuum by thin membranes, typically composed of silicon nitride or graphene, that are transparent to an electron beam (Figure 31). Liquid cells have facilitated the study of phenomena such as nanoparticle growth and dissolution with high spatial resolution.[436,437] A particular advantage of liquid-cell TEM is its ability to study dynamic processes, as sample freezing is not required. Recent studies also suggest that graphene liquid cells can reduce the radiation damage to the encapsulated materials.[438] One area of major concern in liquid cells, however, is the reactive chemical environment induced by the electron beam at room temperature. At the temperatures used in cryo-TEM, such chemical reactions are suppressed. We therefore anticipate that cryo-TEM and liquid-cell TEM will be important complements to one another in future studies of structure in nanofluidic environments.

Beyond its capabilities in high-resolution imaging, TEM has also been used in the spectroscopic characterization of nanofluidic systems via EELS. In contrast to optical spectroscopy, in which the spatial resolution is typically limited to a few hundred nanometers due to diffraction, EELS can provide subnanometer spatial resolution, which can be advantageous when studying nanofluidic systems. In one study, EELS was used to confirm the presence of water inside CNTs.[439] Another common use of EELS is in the determination of specimen thickness, in which the electron inelastic scattering mean-free-path is used in conjunction with the energy-loss spectrum to thickness with sub-10 nm resolution.[440,441] Beyond these traditional techniques, Zhang et al. recently proposed using TEM in conjunction with optical excitation to image photo-excited states with sub-nm resolution.[442] The development of improved electron detectors and TEM platforms that are more stable will enhance the spectroscopic characterization of nanofluidic systems.

2.2.5. Single-Defect Spectroscopy. Chemical defects play an important role at the nanoscale. However, it is difficult to probe the role of defects, and to quantify their impact on nanopore properties and molecular transport. Little is known regarding the role of defects in SDNs, in part because it is difficult to image these defects directly. To address this challenge, Wu et al. recently demonstrated a near-IR, spectroscopic imaging method with single-defect resolution. Figure 32A shows a schematic of the imaging system. By cooling an InGaAs detector array to −190 °C (versus the typical −80 °C), and implementing a nondestructive read-while-integrate (RWI) readout scheme, the authors were able to capture weak, near-IR fluorescence from quantum defects, also known as organic color centers (OCCs), with a signal-to-noise ratio that was improved by more than 3 orders of magnitude as compared to previous studies (Figure 32B).[443] The photoluminescence (PL) is dispersed by a volume Bragg grating system, allowing an image stack to be collected one wavelength at a time, and then reconstructed to obtain a PL spectrum for each pixel. This hyperspectral imaging capability enables simultaneous imaging

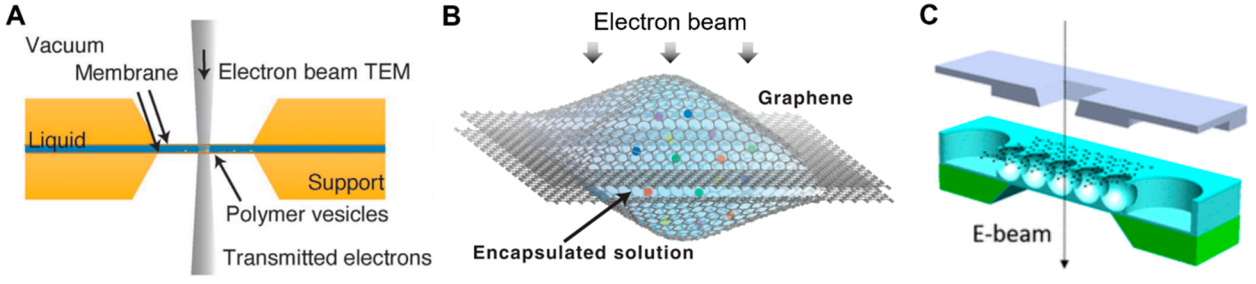

Figure 31. Experimental configurations for liquid-cell electron microscopy. (A) A liquid cell consisting of two silicon microchips supporting silicon nitride windows. Adapted from ref 434. Copyright 2020 John Wiley & Sons. (B) A graphene liquid cell, in which the solution is encapsulated between two graphene sheets. Adapted from ref 436. Copyright 2012 American Association for the Advancement of Science. (C) A monolithic, channel-type, graphene liquid-flow cell. Adapted from ref 435. Copyright 2021 American Chemical Society.

https://doi.org/10.1021/acs.chemrev.2c00155
Chem. Rev. 2023, 123, 2737−2831

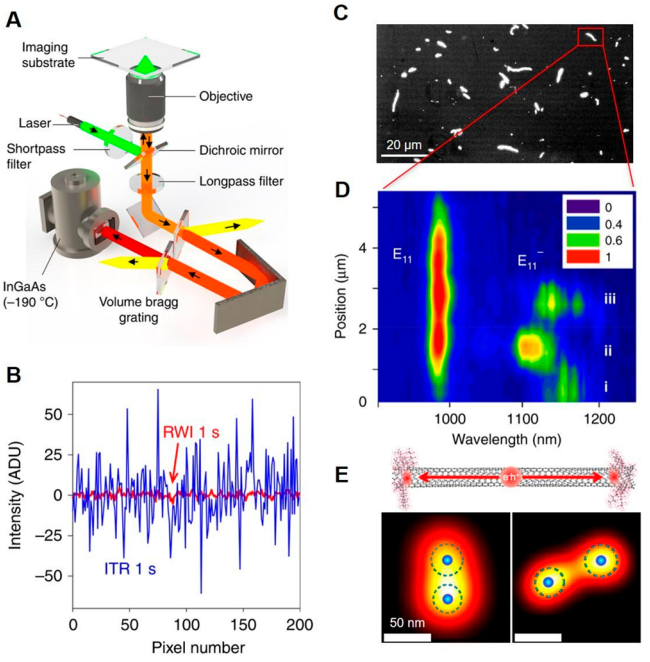

Figure 32. Super-resolved hyperspectral imaging of fluorescent defects on SWCNTs. (A) Schematic of the hyperspectral PL imaging system, which combines a volume Bragg grating for hyperspectral imaging, an InGaAs, 2D-array, NIR detector that operates at −190 °C to minimize dark current, and a nondestructive read-while-integrate (RWI) readout mode for suppression of dark current in the near-IR and reduction of read noise. (B) RWI (red) significantly depresses background signals at −190 °C. Under otherwise identical conditions, RWI exhibits a noise level that is more than an order of magnitude lower than in integrate-then-read mode (blue). (C) A hyperspectral image that contains both spatial and spectral information in each pixel, as exemplified by (D), a PL map along the length of a single (6,5)-SWCNT with three major defect sites (i, ii, iii) identified from their characteristic defect emission (labeled as E_{11}^{-}). (A−D) Adapted from ref 443. Copyright 2019 Springer Nature. (E) FUNs with OCCs at both ends. Each superlocalized defect is displayed as a two-dimensional Gaussian with a width equal to the localization precision (dotted circles). Scale bar 50 nm. Adapted from ref 445. Copyright 2018 American Chemical Society.

and spectral resolution of each defect on a SWCNT over the entire field of view (Figure 32C,D). Additionally, the distinct spectral signatures of the SWCNT and OCCs along the nanotube length allow both to be resolved spatially.

Each defect blinks stochastically, enabling superlocalization of the defect position. By analyzing the two-state nature of the stochastic PL blinking from a single defect emitting site, in conjunction with its super-resolved location, single defects can be identified optically. Figure 32E shows a super-resolution PL image of fluorescent ultrashort nanotubes ($\lesssim$40 nm) that feature OCCs implanted at both ends.[444,445] This technique thus provides a quantitative tool for characterizing single defects and their impact on nanopore properties. Single-defect detection circumvents the limitations imposed by ensemble averaging, and enables the investigation of the impact of defects on molecular transport through nanopores.

Hyperspectral imaging in single-defect spectroscopy can provide rich spectral information with high spatial resolution. For example, as discussed below in section 5.5, Qu et al. used hyperspectral imaging to capture the filling of *n*-hexane into a single (6,5)-SWCNT, which had a pore diameter of 0.42 nm.[88] Molecular filling induces strain on CNTs, and also changes the dielectric environment inside the CNT,[81,82,446] resulting in a PL shift that can be observed with high spectral and spatial resolution along the length of the CNT. This capability may open opportunities for the direct imaging of molecular filling and phase changes in SDNs with nanoscale resolution.

3. MODELING TOOLS

Many modeling tools are available to study the interfacial phenomena relevant to nanofluidics computationally. Here we will focus on applications to aqueous systems, which are both particularly important, and especially challenging, to model. These systems motivate higher-fidelity modeling to capture forces accurately, but sufficiently affordable methods are also necessary to ensure access to sufficient time and length scales to capture the relevant phenomena. The three major computational strategies used in this arena to address this trade-off are quantum simulations, force-field-based MD simulations, and continuum modeling. Modeling some properties typically requires a combination of these strategies to treat the physical phenomena of interest accurately. For example, ab initio molecular dynamics (AIMD) simulations, in which the intermolecular forces are obtained from first principles, incorporate important quantum mechanical (QM) interactions, but the high computational cost limits the length scales (sub-nm to nm) and time scales (ps) over which direct sampling can be achieved. QM interactions are required for the realistic modeling, for instance, of the properties of water at solid surfaces. However, for certain important phenomena (e.g., wetting[447] and the formation of the EDL at solid−water interfaces[448]), AIMD simulations cannot be used, due to the large length and time scales required. In such cases, lower-cost, classical MD simulations are needed. These classical models typically consist of simple analytical functional forms that are parametrized to reproduce QM properties. In classical MD simulations, however, even qualitative results can depend sensitively on the nature of the functional form of the force fields used to model the various intermolecular interactions of pure water and electrolytes at solid−water interfaces.[449,450] To overcome this challenge, system-specific intermolecular potentials of water with 2D materials, including graphene, molybdenum disulfide, and hexagonal boron nitride, have been parametrized based on quantum-chemical simulations.[451−455] Nevertheless, these force fields may not offer sufficient flexibility to describe QM phenomena, such as the polarization response of 2D materials in contact with polar solvents such as water. Thus, a recent aim has been to develop all-atom, polarizable force fields based on QM simulations, that, in addition to modeling traditional electrostatic and dispersion interactions, incorporate the variation in the charge distribution in the solid (e.g., graphene) resulting from the finite electric fields exerted by the water molecules and the ions at the solid−water interface.[447,450,456] In addition, first-principles electronic methods can provide unique insights into mechanistic understanding of nanofluidic transport in SDNs, which cannot be obtained from force-field-based MD simulations. Al-Hamdani et al.[457] used diffusion quantum Monte Carlo methods to obtain adsorption energies between water and CNTs, and Ellison et al.[60] applied DFT to investigate the energetic favorability of water at CNT defect sites. Electronic detail can be incorporated in ab initio molecular dynamics simulations to capture precise interfacial structure,[458,459] bulk phase behavior,[460] and reactive behavior at high pressures at which water can dissociate.[461,462] Furthermore, recent work by Kavokine et al.[6] suggests the

https://doi.org/10.1021/acs.chemrev.2c00155
Chem. Rev. 2023, 123, 2737−2831

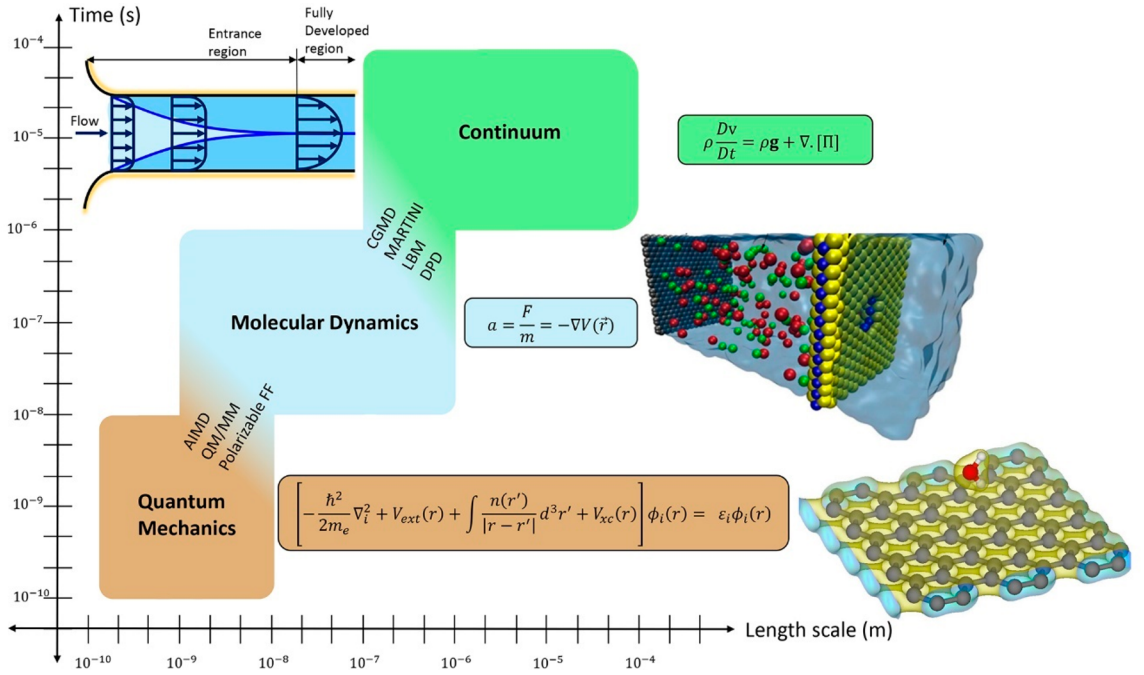

Figure 33. Methods used for the computational modeling of liquids in nanopores. Computational modeling techniques and their corresponding governing equations, mapped according to the length and time scales to which they can be applied. Methods used to bridge the gaps between the main regimes of computational modeling are also indicated in the figure. Representative figures for the methods used extensively in the study of nanofluidic phenomena are shown at the right. The lower image is from a quantum simulation of the adsorption of a water molecule on graphene, and shows the distribution of charge. The upper image above is from an MD simulation of water desalination using a porous monolayer of MoS_2.

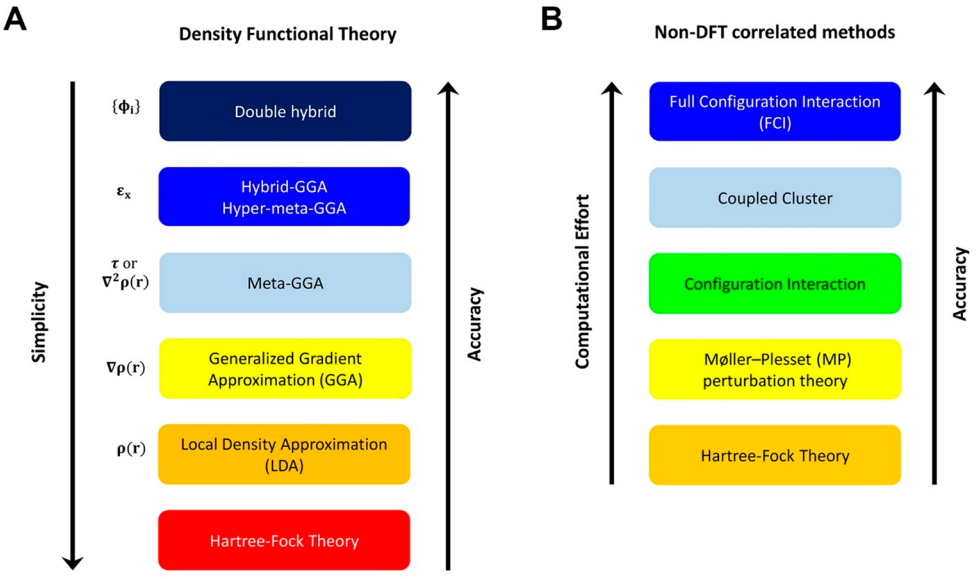

Figure 34. Trade-offs in computational methods. (A) Schematic of the trade-off between simplicity and accuracy for different implementations of DFT. The variables to the left of the techniques are discussed in the text. (B) Schematic of the trade-off between computational effort and accuracy in non-DFT correlated methods.

necessity of a proper electronic description of charge fluctuations in liquids and electron excitations in solids to explain water−carbon friction. Finally, continuum models are well suited for systems spanning mesoscale dimensions, and for which discrete effects do not play a significant role, a representative example of which is calculating the variation of the ionic conductance with concentration for electrolytes confined inside larger diameter SDNs.[429,463,464] Overall, QM AIMD and QM-derived force fields should be expected to outperform force fields that are less flexible, but if these QM techniques cannot capture the longer length and time scales needed to describe a microfluidic phenomenon, enhanced sampling or larger-scale simulations would be needed. Here, comparison to experimental observations, or across levels of theory, are both helpful in identifying whether the modeling technique is sufficiently accurate. The following subsections discuss some of the most commonly used computational methods, in increasing order of time and length scales. A

https://doi.org/10.1021/acs.chemrev.2c00155
Chem. Rev. 2023, 123, 2737−2831

schematic diagram of the methods and the time and length scales to which they can be applied is shown in Figure 33.

3.1. Quantum Methods

Several quantum methods are available for modeling nanofluidic systems. These methods range from density functional theory (DFT) to higher-order approaches, such as Møller−Plesset (MP) perturbation theory[465] and the configuration-interaction (CI) approach.[466] DFT can be applied at various levels, as depicted in Figure 34A. There is a trade-off between accuracy and complexity in DFT that depends on the form of the exchange-correlation term. Several higher-order methods that are also used in quantum simulations involve a similar trade-off, as depicted in Figure 34B.

3.1.1. Density Functional Theory. DFT[467,468] solves the Schrödinger equation using the Born−Oppenheimer approximation, in which the nuclei are assumed to be fixed, and their interactions are modeled as an external potential. The state of the system is then determined based on the wave function using[467,468]

$$\left[-\frac{\hbar^2}{2m_e}\nabla_i^2 + V_{ext}(r) + \int \frac{\rho(r')}{|r-r'|}\,d^3r' + V_{xc}(r)\right]\psi_i(r) = \varepsilon_i\psi_i(r) \tag{1}$$

where, in an N-electron system, $-\frac{\hbar^2}{2m_e}\nabla_i^2$ is the kinetic energy of the ith electron, $V_{ext}(r)$ is the potential energy due to interaction between the nuclei and the electron, the integral term is the Coulomb energy between the electrons, $V_{xc}(r)$ is the exchange-correlation potential, $\psi_i(r)$ is the wave function of the electron, and ε_i is the energy associated with the electron. The form of the exchange-correlation term ($V_{xc}(r)$) depends on the manner in which one defines the interaction energy between the electrons, as shown in Figure 34A in increasing order of accuracy. The simplest of these models is the local density approximation (LDA),[469] in which the electrons are treated as a homogeneous electron gas (HEG) with an electron density $\rho(r)$. The energy in this case is expressed as[469]

$$E_{xc}^{LDA}[\rho] = \int \rho(r)\epsilon_{xc}(\rho(r))\,dr \tag{2}$$

where $\epsilon_{xc}(\rho(r))$ is the exchange-correlation energy per electron of the HEG.

The true electron charge density is not homogeneous. To account for this inhomogeneity, the exchange-correlation term is made not just a function of $\rho(r)$, but also a function of $\nabla\rho(r)$, the gradient of the electron-charge density. This approach is called the generalized gradient approximation (GGA), and the corresponding exchange correlation energy is[470,471]

$$E_{xc}^{GGA}[\rho] = \int \rho(r)\epsilon_{xc}(\rho(r), \nabla\rho(r))\,dr \tag{3}$$

where $\epsilon_{xc}(\rho(r),\nabla\rho(r))$ is the exchange-correlation energy per electron.

A further extension to GGA is the meta-GGA,[472,473] in which the exchange-correlation energy depends on $\nabla^2\rho(r)$, the Laplacian of the electron density, in addition to $\rho(r)$ and $\nabla\rho(r)$. The exchange-correlation energy in this case can be expressed as[472,473]

$$E_{xc}^{meta\text{-}GGA}[\rho] = \int \rho(r)\epsilon_{xc}(\rho(r), \nabla\rho(r), \nabla^2\rho(r))\,dr \tag{4}$$

In some cases, the kinetic energy density $\tau(r)$ is used instead of the Laplacian of the electron density, in which case the exchange-correlation energy takes the form[472,473]

$$E_{xc}^{meta\text{-}GGA}[\rho] = \int \rho(r)\epsilon_{xc}(\rho(r), \nabla\rho(r), \tau(r))\,dr \tag{5}$$

where

$$\tau(r) = \sum_{i=1}^{N_{occ}} \frac{1}{2}|\nabla\psi_i(r)|^2 \tag{6}$$

and N_{occ} is the number of electrons in the occupied orbitals.

The next most complex approach in Figure 34A is the Hybrid-GGA method, in which a fractional contribution from the exact Hartree−Fock (HF) energy[474] is included in the calculation:

$$E_x^{HF}[\{\psi_i\}] = -\sum_{i=1}^{N_{elec}/2}\sum_{j=1}^{N_{elec}/2}\iint \frac{\psi_i^*(r)\psi_j(r)\psi_j^*(r')\psi_i(r')}{|r-r'|}\,dr\,dr' \tag{7}$$

where E_x^{HF} is the exact HF exchange functional, ψ_i, ψ_j, and ψ_i^*, ψ_j^* are the wave functions, and their complex conjugates, for the ith and jth electrons, respectively, and $\frac{1}{|r-r'|}$ is the Coulomb interaction between the two electrons. The general form of the energy-correlation term in this case is given by[475,476]

$$E_{xc} = (1-a)E_{xc}^{DFT} + aE_x^{HF} \tag{8}$$

where a is a semiempirical fitting parameter.

Methods based on DFT have been used extensively to study the properties of liquids (e.g., water) and molecules in confinement,[477,478] as well as at interfaces of materials such as metals[479−481] and graphene.[482−484] Pati et al.[477] studied the effect of water adsorption on CNTs using DFT under the GGA approximation. They found that water undergoes physisorption on CNTs, following which charge transfer occurs between the water molecule and the CNT. This process reduces the hole concentration in the nanotube, thereby reducing the nanotube's conductivity. DFT has also been used to study various electrokinetic phenomena in nanofluidic systems,[485,486] such as charge inversion and EDL formation.

3.1.2. Non-DFT/Post-Hartree−Fock Methods. The HF method discussed in the previous section is the basis for several approaches that are more sophisticated (Figure 34B), the first of which we will consider is MP perturbation theory.[465] In this method, electron correlation effects are added to the ground-state, unperturbed Hamiltonian ($\hat{H}_0$) using Rayleigh−Schrodinger perturbation theory via[487]

$$\hat{H} = \hat{H}_0 + \lambda\hat{V} \tag{9}$$

where λ is an arbitrary, dimensionless parameter, and $\hat{V}$ is a small perturbation.

The CI[466] approach is another post-HF method. In this technique, a linear variational method is used to to account for the electron correlations in solving Schrodinger's equation. The ground-state wave function Ψ is written as

$$\Psi = \sum_k c_k\psi_k \tag{10}$$

where c_k and ψ_k are the coefficient and configuration state function, respectively, of quantum state k in the expansion; the states are linear combinations of Slater determinants.[488] If the expansion above includes all possible state functions, then the

https://doi.org/10.1021/acs.chemrev.2c00155
Chem. Rev. 2023, 123, 2737−2831

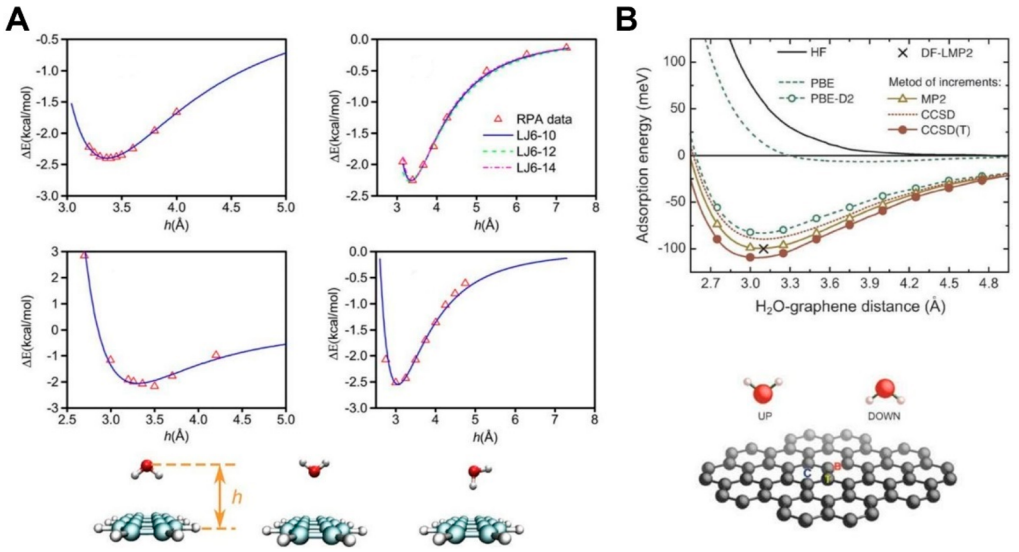

Figure 35. Studying interactions between water and graphene using electronic structure methods. (A) Lennard-Jones curves for graphene−water interactions calculated with (top left) the MP2 method,[491] (top right) the random-phase approximation,[496−498] (bottom left) DFT symmetry-adapted perturbation theory,[499,500] and (bottom right) the CC method.[489] The ab initio results are denoted with triangles, and the Lennard-Jones 6-*n* fitting curves are denoted with lines in each plot. The abscissa, *h*, is the distance between the water oxygen and the graphene plane. (B) Comparison between graphene−water interactions for the CC,[489] MP2,[491] HF,[474] and GGA methods.[501] The two orientations of the water molecule with respect to the graphene layer considered are shown at the bottom.

solution to the electronic Schrodinger's equation is exact, which is referred to as a full configuration interaction. In the coupled-cluster (CC) approach,[489] multielectron wave functions with an exponential coupled-cluster operator are used to account for the electron correlation. The ground-state wave function in this case is given by

$$\Psi = \sum_k e^{T_k} \psi_k \tag{11}$$

where T_k is the coupled-cluster operator.

MP perturbation theory[465] has been used to study the structure of water[490] and the interaction of this substance with graphene.[451] In this work, the force-field parameters characterizing the graphene−water interactions were calculated using the MP2 method.[491] The CI was first used in the accurate calculation of the excited states of water.[492] Advances in computational capabilities have enabled the use of CI to calculate the excited states of systems, such as acenes,[493] which are potential materials for organic electronics. The CC approach has been used recently to explore the adsorption of water on hBN.[494] Another previous study focused on estimating the physisorption energies of water on graphene.[495] Quantum methods ranging from DFT to CC have been extensively used to develop force fields to model the interactions between graphene and water. Such force fields are an essential component for the MD simulations that are needed to model larger systems to study macroscopic properties, such as viscosity and diffusion coefficients. Wu et al. compared the graphene−water interaction parameters calculated using higher-order quantum methods.[451] These parameters were used in multiscale methods to study the dynamics of water on graphene surfaces (Figure 35A). In similar studies, the adsorption energies of water on graphene were determined[495] using post-HF methods (Figure 35B).

3.2. Ab Initio Molecular Dynamics

In AIMD simulations, also known as Born−Oppenheimer molecular dynamics (BOMD) simulations, the nuclei are treated using classical equations of motion, and the ionic forces are calculated by solving the electronic Schrodinger equation at each time step. The electronic Schrodinger equation is solved by approximating the electron-exchange correlation energy using the LDA[469] or the GGA[470] to optimize the computational time required to propagate each time step. Because these calculations enable access to the electronic properties of the system, spectroscopic observables can be computed accurately.[502,503] Another nanofluidic application for which AIMD has been used is the diffusion of excess protons in CNTs,[16,72,504] for which the alignment, proton conduction, and time evolution of the free energy were studied.

Car−Parrinello MD (CPMD)[505] is another method that incorporates quantum interactions in MD simulations. CPMD explicitly introduces the electronic degrees of freedom as (fictitious) dynamical variables that are included in an extended Lagrangian that leads to a system of coupled equations of motion for both ions and electrons. This approach avoids the explicit electronic minimization at each time step required in AIMD. Instead, after an initial, standard electronic minimization, the fictitious dynamics keeps the electrons on the electronic ground state corresponding to each new ionic configuration visited along the trajectory, thus yielding accurate ionic forces.

3.3. Molecular Dynamics Simulations

MD is the most common simulation approach used to model nanofluidics. In MD, the atoms are defined explicitly, and the dynamics are determined by solving Newton's equations of motion numerically. The forces between atoms are calculated using interatomic potentials, which are often estimated using the quantum mechanical methods described above.

Early work on nanofluidics using MD simulations yielded a number of major predictions. MD simulations performed by Hummer et al.[87] indicated that water spontaneously fills CNTs. In CNTs with small enough inner diameters, the encapsulated water took on a single-file structure, and the hydrogen bonds exhibited 1D ordering. This study also revealed that in CNTs

https://doi.org/10.1021/acs.chemrev.2c00155
Chem. Rev. 2023, 123, 2737−2831

with small enough diameters, a water molecule forms only two hydrogen bonds, as opposed to the optimal four hydrogen bonds that most molecules make in the bulk liquid. The average lifetime of the hydrogen bonds in the confined liquids was found to be ∼5 times longer than that in the bulk. Gordillo and Martí[506] studied the hydrogen-bond network inside CNTs of various diameters. They found that as the diameter of the CNT decreases, the number of hydrogen bonds formed between water molecules also decreases. This 1D hydrogen-bonding network promotes the rapid transport of water. The source of this fast transport was examined extensively by Joseph and Aluru,[507] who evaluated water velocities for different types of nanopores, including CNTs, BNNTs, noninteracting pores, and rough CNTs. They found that OH-bond orientation and hydrogen bonding in the depletion region (where the water concentration is less than 5% of its value in the bulk) contribute to the large flow rates of water observed in CNTs. A related study of the effect of CNT chirality on the diffusivity of water was reported by Liu et al.,[508] who observed that water diffuses nearly an order of magnitude faster in armchair CNTs than in zigzag CNTs. Fast water transport through CNTs was also observed in MD simulations of osmotic flow systems by Kalra et al.,[509] who highlighted the importance of the water thermal fluctuations in CNTs with small diameters. Ma et al.[510] found that the enhancement of diffusion through CNTs arises from the coupling between the confined water molecules and the longitudinal phonon modes of the CNT. The limiting velocities explored in this study are similar to those observed experimentally. Temporal oscillations in the shear stress were observed at the water−CNT interface, corresponding to the lowest, odd-index, longitudinal phonon modes of the CNT.

3.3.1. Structure, Dynamics, and Dielectric Properties of Confined Aqueous Solutions. Since the seminal paper of Hummer et al.,[87] MD simulations have been used extensively to elucidate the organization and dynamics of liquid water confined in CNTs. Here we discuss some of the highlights of this work. MD simulations have revealed that the organization of water in CNTs displays a remarkable diversity that depends on the pore diameter, the temperature, and the pressure. For example, water molecules adopt a single-file configuration in (6,6)-SWCNTs, but as the CNT diameter increases the organization changes from ordered to disordered.[89,511] Furthermore, classical MD simulations show that, below room temperature, a new phase of high-density ice, which is characterized by stacking of *n*-membered rings in the axial direction, emerges in CNTs with sub-2 nm diameters.[512]

Several MD studies have investigated the structural properties of salt solutions in CNTs. How ion solvation is governed by the intrinsic properties of ions and nanoconfinement is not fully understood, and contradictory trends have been reported, even for simple alkali metal ions. For example, classical MD simulations using nonpolarizable force fields indicate that both K^+ and Na^+ preserve their first solvation shells, even in CNTs with a diameter as small as 10.0 Å.[513] On the other hand, simulations using polarizable force fields predict that ions in this environment will tend to be partly desolvated and reside near the solution−CNT interface.[514] First-principles simulations found that confinement effects on ion solvation may also depend on the strengths of the solvation shell and the specific interfacial interactions. For CNTs with a diameter of 14 Å, the synergy between these factors enables K^+ to be partly solvated and to reside closer to the CNT surface than do Na^+ or Li^+.[514−516] These conflicting results indicate that conclusions regarding the structure of confined aqueous solutions can be highly dependent on the specific simulation techniques and approximations used. These studies also point to the importance of including electronic effects, such as polarization and charge transfer at interfaces, to obtain a proper description of ion solvation under confinement, given the importance of interfacial phenomena.

Understanding the transport mechanism of ions and liquid water in CNTs is another outstanding challenge for simulation and modeling. The difficulty arises largely from simultaneous requirements for high accuracy and long time and length scales. Many studies have relied on classical simulations, which are more suitable for accessing the time scales relevant for transport calculations. For example, as shown in Figure 36, MD

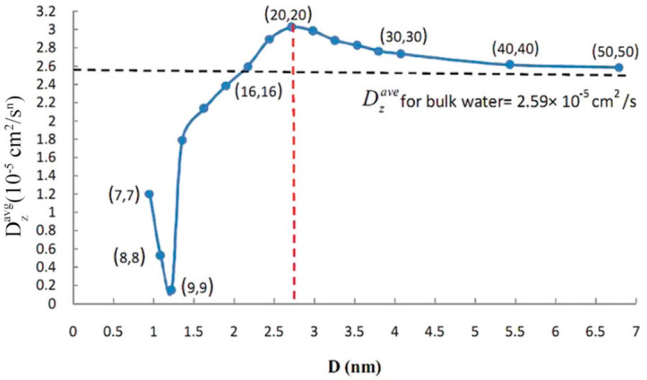

Figure 36. Variation of the average axial diffusion coefficient of water as a function of CNT diameter. The diffusion is non-Fickian for diameters of 1.5 nm and less. Adapted from ref 517. Copyright 2011 American Chemical Society.

simulations indicated that the average diffusion coefficient of water exhibits a complex dependence on the CNT diameter, and can be either larger or smaller than the corresponding bulk value.[517] This study also indicated that the axial diffusion mechanism can range from ballistic to Fickian motion, depending on the CNT diameter (Figure 36). Other MD simulation studies have explored the effect of confinement on ion diffusion, albeit with somewhat contradictory findings. For example, although some classical MD studies found that the self-diffusion of confined ions is similar to or slower than that in bulk solution,[518] other work indicated that the self-diffusion of ions can be enhanced due to partial desolvation.[519] Ion diffusion in charged CNTs was found to be slower than in neutral CNTs due to strong electrostatic interactions between the ions and the CNT surface.[520] In this regard, ion-solvation structure and ion−surface interactions appear to be important factors that affect ion transport under confinement.

Recent MD studies have also provided vital insights on the dielectric permittivity of confined water. A number of classical MD simulations have shown that water exhibits strongly anisotropic dielectric relaxation when confined in graphene nanochannels.[130] This behavior leads to an order-of-magnitude difference in the parallel and perpendicular dipolar fluctuations of water confined between graphene sheets. Such anisotropic behavior has also been observed in cylindrical confinement, including in CNTs, in which the water dielectric constant parallel to the axis of the CNT is enhanced, whereas the dielectric constant perpendicular to the CNT axis is diminished.[521] In another study, a universal scaling and reduction in the perpendicular dielectric permittivity as a

https://doi.org/10.1021/acs.chemrev.2c00155
Chem. Rev. 2023, 123, 2737−2831

function of the channel width was observed for protic and aprotic fluids confined in slit-like graphene channels.[522] This study also demonstrated that the reduction in the out-of-plane dielectric permittivity exhibits a Langevin-like behavior, which is attributed to the favorable, in-plane dipole−dipole interactions. Collectively, these studies point to a strong anisotropic behavior of dielectric properties under confinement, which in turn can play an important role in molecular transport and selectivity, as well as in chemical reactivity under nanoconfinement.

3.3.2. Incorporating Electronic Polarization Effects in MD Simulations. Due to the ability of classical MD simulations to access larger length and time scales than do AIMD simulations, the combination of MD simulations with the tools of statistical mechanics can provide essential mechanistic insights regarding the behavior of pure fluids and electrolytes, both at planar solid−water interfaces and inside SDNs. Although traditional MD force fields, such as AMBER,[523] CHARMM,[524] and OPLS-AA,[525] continue to provide useful insights and are widely used, these force fields in general neglect electronic polarization effects. These effects originate from the polarization of the charge distribution in the solid that is a consequence of the finite electric fields exerted by polar solvents, such as water, and charged species, such as ions. Further, because the electric field is a vector, both the direction and the magnitude of the local electric field felt by an atom in the solid need to be obtained based on the vectorial superposition of all the electric fields exerted by the water molecules and the ions in the system. This approach imparts a many-body nature to electronic polarization effects, which also results in a strong coupling between the ion−solid and water−solid interactions.[450]

Electronic polarization effects, which are also referred to in the literature as image−charge interactions,[526] involve intermolecular interactions that are directional in nature.[527] Therefore, in principle, these effects cannot be modeled with the scalar, pairwise-additive potentials that are used extensively in classical MD simulations. For example, as shown in Figure 37A, when

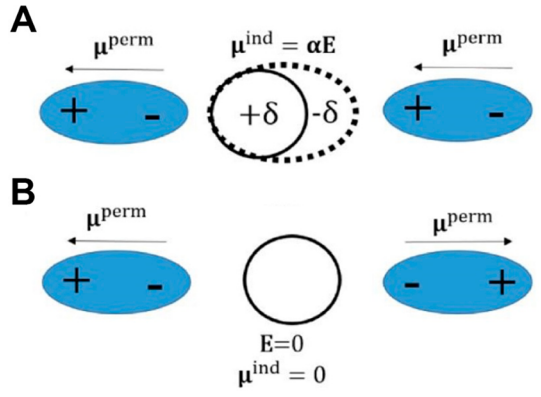

Figure 37. Schematic demonstrating the directional nature of electronic polarization interactions. In (A), the central molecule feels a finite electric field from the permanent dipoles, whereas in (B), the electric fields exerted by the permanent dipoles cancel each other such that the central molecule does not feel any net dipolar electric field.

two permanent dipoles point in the same direction, the polarizable molecule at the center feels a finite electric field, $\boldsymbol{E}$, that corresponds to the sum of the electric fields exerted by the permanent dipoles (note that bolded variables designate vectors and tensors). This field in turn contributes to the electronic polarization of the central molecule, represented by the induced dipole moment $\boldsymbol{\mu}^{ind} = \boldsymbol{\alpha}\mathbf{E}$, where $\boldsymbol{\alpha}$ is the polarizability tensor of the central molecule. On the other hand, if the permanent dipoles point in opposite directions, the electric field exerted by one dipole is canceled by that exerted by the other, such that the polarizable molecule does not feel any net external electric field with dipolar symmetry, and consequently $\boldsymbol{\mu}^{ind} = 0$, as shown in Figure 37B. This illustration demonstrates the need for self-consistent modeling of the electric fields exerted by polar molecules (e.g., water) and charged species (e.g., ions), because pairwise LJ or Coulomb potentials cannot account for the types of interactions shown in Figure 37.

Misra and Blankschtein recently developed an all-atomistic, polarizable force field[447] to model the interactions of water molecules with graphitic surfaces, using quantum-chemical simulations carried out with symmetry-adapted perturbation theory (SAPT).[499,500] The advantage of SAPT over other electronic structure theories is that, in addition to predicting the total graphene−water binding energies, this method can also decompose the binding energies into four physically meaningful contributions: electrostatics, exchange, polarization (induction), and dispersion. This decomposition is useful for predicting the polarization-energy component of the total water−graphene binding energy, which results from the water-induced electronic polarization of graphene. In the classical MD simulations carried out by Misra and Blankschtein,[447] the water−graphene polarization energy was modeled self-consistently using the classical Drude oscillator model.[528] As shown in Figure 38, every

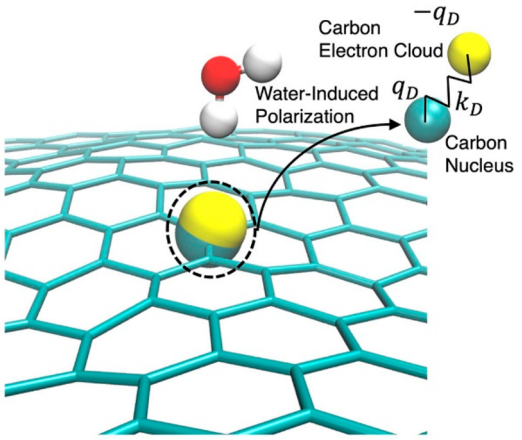

Figure 38. Schematic of the polarization of carbon atoms in graphene resulting from the electric field exerted by a water molecule. A magnified view of the polarization of the carbon atom directly facing the hydrogen atom of the water molecule is indicated by the black dashed circle (the polarizations of the other carbon atoms are not shown for clarity). The polarization of a carbon atom is modeled self-consistently using the classical Drude oscillator model, in which every carbon atom in the graphene layer is described as a Drude particle (yellow) and a Drude core (cyan). Adapted from ref 447. Copyright 2017 American Chemical Society.

carbon atom in graphene is represented as a Drude particle (DP), corresponding to the carbon electron cloud, and a Drude core (DC), corresponding to the carbon nucleus. The DP and DC for a given atom have charges of equal magnitude but opposite sign. The interactions between the DCs and DPs are modeled using the Thole dipole field tensor,[529] which can accurately reproduce the anisotropic polarizability tensor of graphene (see eqs 4−7 in ref 447), i.e., the in-plane and out-of plane polarizability components. Only two parameters are used

https://doi.org/10.1021/acs.chemrev.2c00155
Chem. Rev. 2023, 123, 2737−2831

to model the polarizability of graphene, a static dipole polarizability, α_c, and a dimensionless Thole damping parameter, a_c, the latter of which modulates the interactions between the DCs and DPs of graphene.

Electronic polarization effects induce a strong correlation between the electric fields exerted by interfacial water molecules on graphene and the orientations of these molecules, because the graphene−water polarization energy depends upon orientation.[447] The same authors also incorporated graphene−water polarization interactions in a comprehensive investigation of the water contact angle on graphite (multilayer graphene).[447] To this end, they first used the free-energy perturbation method[530] to obtain the graphite−water work of adhesion, W_{SL}, which is defined as the change in the free energy per unit area upon moving a film of water in molecular contact with graphite to an infinite distance away. As shown in parts A and B of Figure 39, W_{SL} was subsequently used to calculate the contact angle of water on graphite, θ, using the Young−Dupré equation,[531] $W_{SL} = \gamma_L(1 + \cos\theta)$, where γ_L is the surface tension of water. Further, W_{SL}, being the difference in the Helmholtz free energy (the pressure−volume work is negligible), can also be partitioned into an energetic component (ΔU_{SL}) and an entropic component ($T\Delta S_{SL}$),[447] with $W_{SL} = \Delta U_{SL} - T\Delta S_{SL}$. Their key finding was that the graphene−water polarization interactions have a more significant impact on the interfacial entropy of water than do graphene−water dispersion interactions.[447] In fact, when polarization effects are modeled self-consistently, the increase in the energetic component of W_{SL} due to graphene−water polarization interactions is canceled, to a large extent, by a concurrent increase in the entropic component. In stark contrast, the pronounced energy−entropy compensation is not observed if the graphene−water polarization energy is instead treated implicitly using an LJ potential, which underpredicts the water contact angle by ∼23° (Figure 39B). A water contact angle on graphite of 63° was calculated based on MD simulations carried out using the above polarizable force field.[447] Although graphitic surfaces are prone to hydrocarbon contamination, the simulated contact angle is in good quantitative agreement with the contact angle of 62−68° reported in the majority of recent experimental studies on pristine graphite surfaces.[532−535] All-atomistic polarizable force fields can also be used to investigate the wetting of other 2D materials, including hBN[536] and phosphorene,[537] which have polarizabilities that are similar to, or larger than, that of graphene.

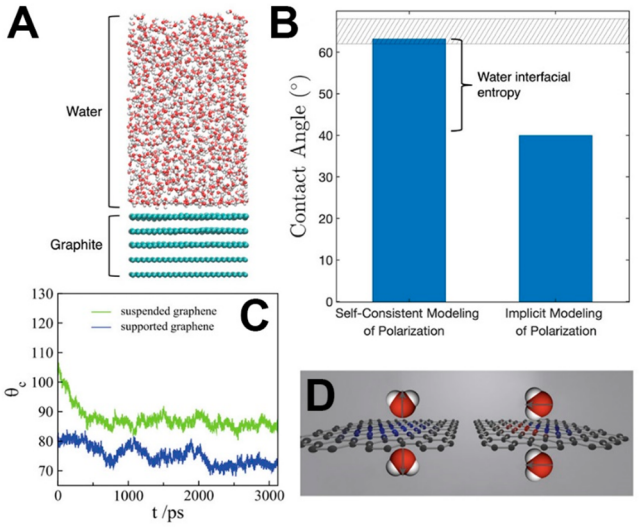

Figure 39. Understanding the role that electronic polarization effects play in dictating the wetting properties of graphitic surfaces. (A) Schematic showing the computational setup used to calculate the graphite−water work of adhesion, W_{SL}, which is then used to calculate the water contact angle on graphite based on the Young−Dupré equation. The color code used to represent the graphene layers and the water molecules is the same as that used in Figure 38. (B) The bar plots show that in comparison to the contact angle obtained using the classical Drude oscillator model to treat the graphene−water polarization energy (left), treating the graphene−water polarization energy implicitly using a LJ potential (right) predicts a contact angle that is 23° smaller.[447] The source of this difference is the pronounced influence of the graphene−water polarization interactions on the interfacial entropy of water. The dashed rectangle represents the range of recent experimental contact angle measurements on pristine graphite (see main text). (C) Contact angle of water on suspended and supported graphene layers obtained by treating the graphene layer as a conductor using the constant-potential molecular dynamics (CPMD) method. (D) Specific water orientations favored by graphene-mediated water−water interactions.[541] Neutral carbon atoms are colored in gray, and carbon atoms with positive and negative image charges are colored in blue and red, respectively. The oxygen and hydrogen atoms in the water molecule are colored in red and white, respectively. (C,D) Adapted from ref 541. Copyright 2020 American Chemical Society.

A single layer of graphene can also partially transmit van der Waals interactions by enabling intermolecular interactions between the molecules on either side of the layer; this property is referred to as partial wetting transparency.[538−540] In a recent study, Ojaghlou et al. investigated the role of electronic polarization effects and the conductivity of graphene in determining the water contact angle on, as well as the water−water interactions across, a graphene layer.[541] To this end, the authors applied the constant-potential MD method,[542] in which the charge-neutral graphene layer is maintained at a net electrostatic potential of zero, and the charges in the individual carbon atoms in the graphene layer are allowed to fluctuate in response to the electric fields exerted by the water molecules. Different combinations of water−carbon LJ potentials were used to describe the London dispersion interactions, and the variation of the water contact angle on freely suspended (a water droplet on one side only) and supported (a water droplet on one side and a water film on the other side) graphene layers were investigated. As shown in Figure 39C, the water−water interactions were found to be enhanced upon incorporation of the polarization response of the graphene layer, which resulted in a lower water contact angle on the supported graphene layer than on the suspended one. This phenomenon was attributed to specific water orientations above and below the graphene layer (Figure 39D), which enhanced the electrostatic interactions of the partial atomic charges of the hydrogen and oxygen atoms in water with the induced image charges in the graphene layer. A strong influence of polarization effects on the orientation of interfacial water molecules has been a common feature uncovered in molecular simulations of the graphene−water interface.[447,541,543]

In electrolyte solutions at solid−water interfaces, both the water and the ions have substantial electric fields that can polarize the charge distribution in a solid. The adsorption behavior of ions at graphitic surfaces has attracted attention recently because of the potential utility of graphene in energy[544−546] and membrane applications.[547,548] The Hofmeister series has been used extensively to characterize ion-specific

https://doi.org/10.1021/acs.chemrev.2c00155
Chem. Rev. 2023, 123, 2737−2831

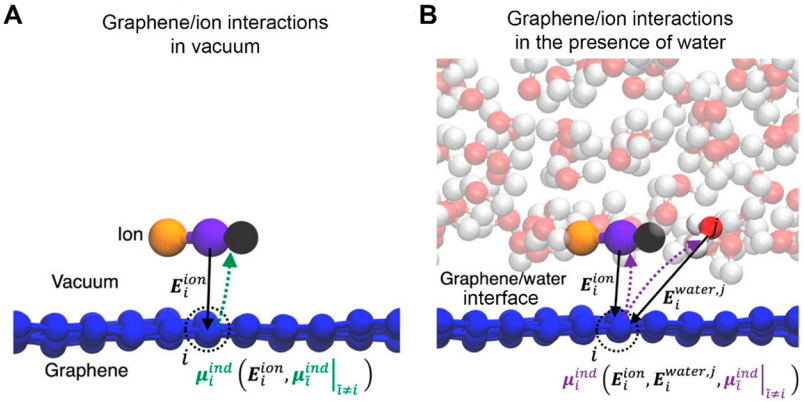

Figure 40. Comparison of the interactions of a thiocyanate ion with graphene in vacuum to those in the presence of water. (A) In vacuum, the electric field exerted on a given carbon atom by the ion is shown as a black arrow, and the electric field exerted by the induced dipole is shown as a green dashed arrow. (B) In the presence of water, the electric fields exerted on a given carbon atom by the ion and by a highlighted water molecule are shown as black arrows, whereas the electric fields of the induced dipoles are shown as purple dashed arrows. Adapted from ref 450. Copyright 2021 American Chemical Society.

effects.[549] The influence of ions in this series is ranked as SO_4^{2-} < F^- < HPO_4^{2-} < CH_3COO^- < Cl^- < Br^- < NO_3^- < I^- < ClO_4^- < SCN^-. The ions to the left of Cl^- are considered to be kosmotropic, whereas the ions to the right of Cl^- are considered to be chaotropic. Kosmotropic ions are strongly hydrated, and reduce the solubility of proteins. Chaotropic ions are weakly hydrated and increase the solubility of proteins. All-atomistic polarizable force fields derived using quantum-chemical simulations employing SAPT[450,456] were used to investigate the adsorption behavior of kosmotropic (Cl^-, F^-, and SO_4^{2-}) and chaotropic (SCN^-, NO_3^-) ions at the graphene–water interface. This work included a comparison of the free energy of adsorption of thiocyanate at the graphene–water interface with the corresponding experimental value.[550] Electronic polarization effects were found to play a major role in determining the manner in which ions interact with graphene in vacuum versus in the presence of water molecules. As shown in Figure 40A, when SCN^- interacts with a graphene layer in vacuum, the ion exerts a strong electric field that polarizes the charge distribution in the graphene layer. The resulting induced dipoles in graphene exert an electric field that interacts with the ion. In contrast, at the graphene–water interface, both the ions and the water molecules exert electric fields that polarize the graphene layer. As shown in Figure 40B, because the magnitude and direction of the induced dipole moment of each graphene carbon atom depends on the electric fields exerted by the ions and all of the water molecules in the system, the graphene–ion and graphene–water interactions are intrinsically coupled. Thus, when an ion approaches a graphene layer, there is a quantifiable change in the graphene–water interactions. Similarly, the graphene–ion interactions are modulated when a water molecule approaches the graphene layer.

Figure 41A shows the resulting binding energies of SCN^-, NO_3^-, Cl^-, F^-, and SO_4^{2-} with graphene in vacuum. For all of these ions, the graphene–ion binding energies are large and negative. This favorable binding is due to the large graphene–ion polarization energies that result from the ion-induced polarization of graphene.[456] Because the SO_4^{2-} ion is divalent, the graphene–ion polarization energy, which scales quadratically with the electric field exerted by the ion, is ~4 times larger than that of monovalent ions, resulting in a significantly larger binding energy for sulfate. Overall, the binding energies at the

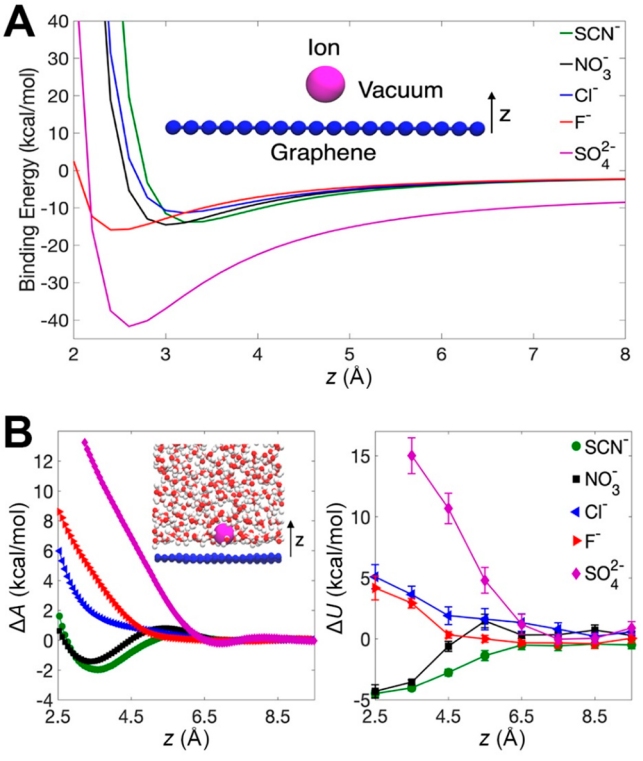

Figure 41. Energetics of ions near a graphene layer. (A) Calculated binding energies of SCN^-, NO_3^-, Cl^-, F^-, and SO_4^{2-} with a periodic graphene layer in vacuum. (B) The change in the Helmholtz free energy (left) and the potential energy (right) when each of these ions is transferred from bulk water to the graphene–water interface. The insets in (A) and (B) are schematics of an ion interacting with graphene in vacuum and in the presence of water molecules, respectively. Adapted from ref 456. Copyright 2021 American Chemical Society.

location of the minima range from −11 kcal/mol (−18 k_BT) for chloride to −42 kcal/mol (−70 k_BT) for sulfate at 300 K.

The adsorption behavior of these ions on a graphene layer in the presence of water is remarkably different than in vacuum. In water, the chaotropic ions are attracted to the graphene–water interface, whereas the kosmotropic ions are repelled. In Figure 41B, the changes in the Helmholtz free energy (ΔA) and the potential energy (ΔU) are shown as a function of the distance, z,

https://doi.org/10.1021/acs.chemrev.2c00155
Chem. Rev. 2023, 123, 2737−2831

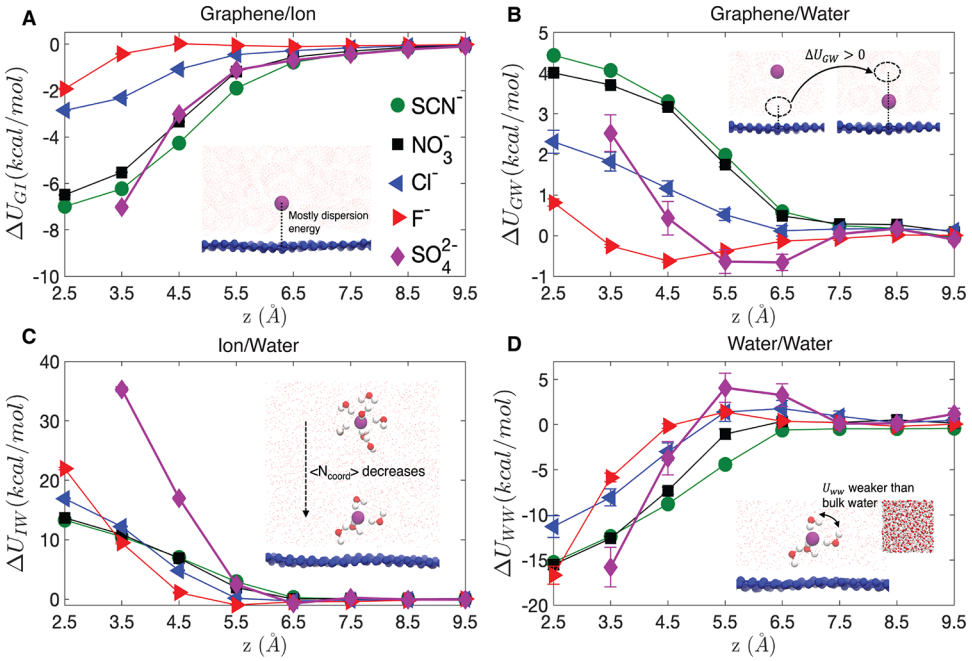

Figure 42. Energetics of transferring an ion from bulk water to the graphene−water interface. The change in the (A) graphene−ion, (B) graphene−water, (C) ion−water, and (D) water−water interactions when an ion is transferred from bulk water (z = 10 Å) to different distances at the graphene−water interface. Adapted from ref 456. Copyright 2021 American Chemical Society.

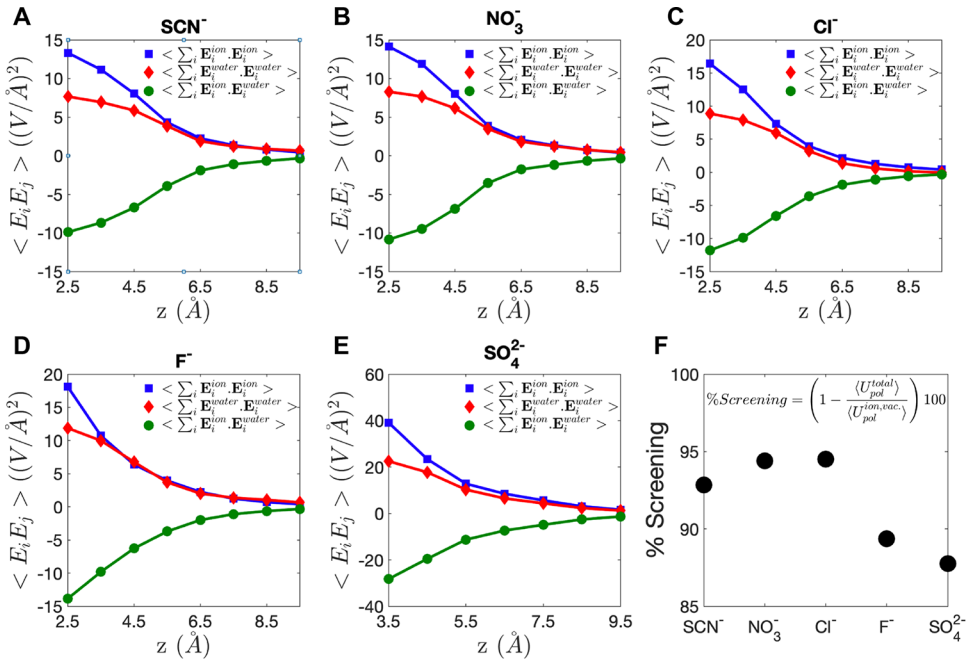

Figure 43. Dependence of the ion self-correlation function, water self-correlation function, and ion−water cross-correlation function on the distance z between the graphene layer and the center of mass of (A) SCN^-, (B) NO_3^-, (C) Cl^-, (D) F^-, and (E) SO_4^{2-}. (F) The percent screening of the total polarization energy at the graphene−water interface relative to the graphene−ion polarization energies in vacuum for the five ions investigated. Adapted from ref 456. Copyright 2021 American Chemical Society.

between the center of mass of the ion and the graphene layer. The ΔA data[450,456] are consistent with the findings of two experimental studies of the adsorption of ions at graphitic surfaces.[550,551] The simulated free energy of SCN^- adsorption at the graphene−water interface, in particular, is in quantitative agreement with spectroscopic measurements.[550] The nature of the ΔA profile can be understood qualitatively from the ΔU data, although a non-negligible entropic contribution emerges from fluctuations in the ion−water and water−water interactions.[456] The ΔU data demonstrate the critical role of interfacial water molecules in modulating the interactions of the ions with the graphene layer.

To reveal the molecular mechanism of ion adsorption at the graphene−water interface, the ΔU data were decomposed into four principal interactions: graphene−ion (ΔU_{GI}), graphene−water (ΔU_{GW}), ion−water (ΔU_{IW}), and water−water (ΔU_{WW}),

https://doi.org/10.1021/acs.chemrev.2c00155
Chem. Rev. 2023, 123, 2737−2831

as shown in Figure 42. The ΔU_{GI} data are negative, primarily because of the stabilizing London dispersion interactions between the ions and graphene, whereas the graphene−ion polarization energy, the dominant contribution to the graphene−ion binding energy in vacuum, is almost nullified in the presence of water. The negative ΔU_{GI} is partially compensated by the positive ΔU_{GW}, which results from the displacement of a few water molecules when an ion approaches a graphene layer. When an ion approaches a graphene layer from bulk water, the hydration shell shrinks, resulting in a positive change in ΔU_{IW}. Because the water−water interactions in the hydration shell are weaker than those in the bulk, ΔU_{WW} is negative.

To understand the remarkable attenuation of the polarization energy at the graphene−water interface, the graphene−ion and graphene−water polarization energies were evaluated[456] in a periodic simulation box consisting of an ion in water, both interacting with graphene. The time-averaged graphene−ion polarization energy is given by[450,456]

$$\langle U_{pol}^{ion} \rangle = -\frac{1}{2}\alpha_C^{eff}\left(\left\langle \sum_i \boldsymbol{E}_i^{ion}\cdot\boldsymbol{E}_i^{ion} \right\rangle + \left\langle \sum_i \boldsymbol{E}_i^{ion}\cdot\boldsymbol{E}_i^{water} \right\rangle \right) \tag{12}$$

where $\boldsymbol{E}_i^{ion}$ is the electric field exerted by the ion on carbon atom i, $\boldsymbol{E}_i^{water}$ is the net electric field exerted by all of the water molecules on carbon atom i, $\langle \sum_i \boldsymbol{E}_i^{ion}.\boldsymbol{E}_i^{ion} \rangle$ is the time-averaged ion self-correlation function, $\langle \sum_i \boldsymbol{E}_i^{ion}.\boldsymbol{E}_i^{water} \rangle$ is the time-averaged ion−water cross-correlation function, and $\boldsymbol{\alpha}_C^{eff}$ is the effective polarizability tensor of graphene, which incorporates the mutual interactions between the induced dipoles in graphene. The time-averaged graphene−water polarization energy is given by[450,456]

$$\langle U_{pol}^{water} \rangle = -\frac{1}{2}\alpha_C^{eff}\left(\left\langle \sum_i \boldsymbol{E}_i^{water}\cdot\boldsymbol{E}_i^{water} \right\rangle + \left\langle \sum_i \boldsymbol{E}_i^{water}\cdot\boldsymbol{E}_i^{ion} \right\rangle \right) \tag{13}$$

where $\langle \sum_i \boldsymbol{E}_i^{water}.\boldsymbol{E}_i^{water} \rangle$ is the time-averaged, water self-correlation function. The correlation functions when an ion is transferred from bulk water to various z positions at the graphene−water interface are shown in Figure 43 for SCN^-, NO_3^-, Cl^-, F^-, and SO_4^{2-}.[456]

As shown in Figure 43, when any of the five ions investigated approaches the graphene layer from bulk water, the ion and water self-correlation functions (blue and red curves) take on larger positive values, whereas the ion−water cross-correlation functions (green curves) take on larger negative values. The electric field that an ion exerts on graphene becomes larger as the ion approaches the graphene layer, as is reflected in the increase in the ion self-correlation functions as z decreases. The positive values of the water self-correlation functions (red curves) reveal, surprisingly, that when an ion approaches the graphene layer, the interfacial water structure is perturbed in such a manner that the water molecules also exert a larger electric field on graphene. The large, negative values of the ion−water cross-correlation functions (green curves) act in opposition to the positive increases in the ion and water self-correlation functions, which in turn results in a significant screening of both the graphene−ion and the graphene−water polarization energies. The negative values of the cross-correlation functions indicate that the electric fields exerted by the water molecules and the ion are out of phase with respect to each other for all five ions studied, regardless of the ionic diameter, the valency, or the nature of the solid−water interface.[456]

Comparing the system polarization energies in the presence of water molecules to those in vacuum can reveal the water-mediated screening of the polarization energies. To this end, the graphene−ion polarization energy in vacuum is given by

$$\langle U_{pol}^{ion\cdot vac} \rangle = -\frac{1}{2}\alpha_C^{eff}\left\langle \sum_i \boldsymbol{E}_i^{ion}\cdot\boldsymbol{E}_i^{ion} \right\rangle \tag{14}$$

and the total polarization energy at the graphene−water interface is given by

$$\langle U_{pol}^{total} \rangle = \langle U_{pol}^{ion} \rangle + \langle U_{pol}^{water} \rangle \tag{15}$$

The relative magnitudes of these two polarization energies indicate that more than 85% of the vacuum polarization energy is screened at the graphene−water interface, as shown in Figure 43F. Thus, the graphene−water interface dramatically attenuates the polarization energy of ions with graphene. Because the moderately negative ΔU_{GI} is largely counteracted by the positive ΔU_{GW}, the adsorption behavior of ions at the graphene−water interface is determined primarily by the interplay between ion−water and water−water interactions.

Figure 44A shows, for the five different ions, the changes in the ion−water interactions (ΔPE_{iw}), the water−water interactions (ΔPE_{ww}), and the sum of the two (ΔPE_{total}) when a

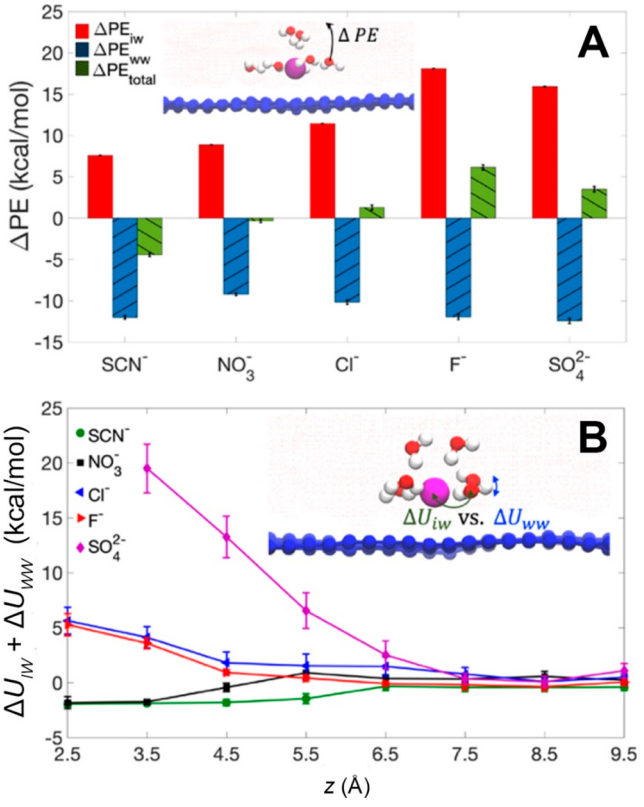

Figure 44. Energetics of the transfer of a water molecule in the first hydration shell of an ion at the graphene−water interface to bulk water. (A) ΔPE_{iw}, ΔPE_{iw}, and ΔPE_{total}. (B) The sum of ΔU_{iw} and ΔU_{ww} as a function of distance from the graphene−water interface. Adapted from ref 456. Copyright 2021 American Chemical Society.

https://doi.org/10.1021/acs.chemrev.2c00155
Chem. Rev. 2023, 123, 2737−2831

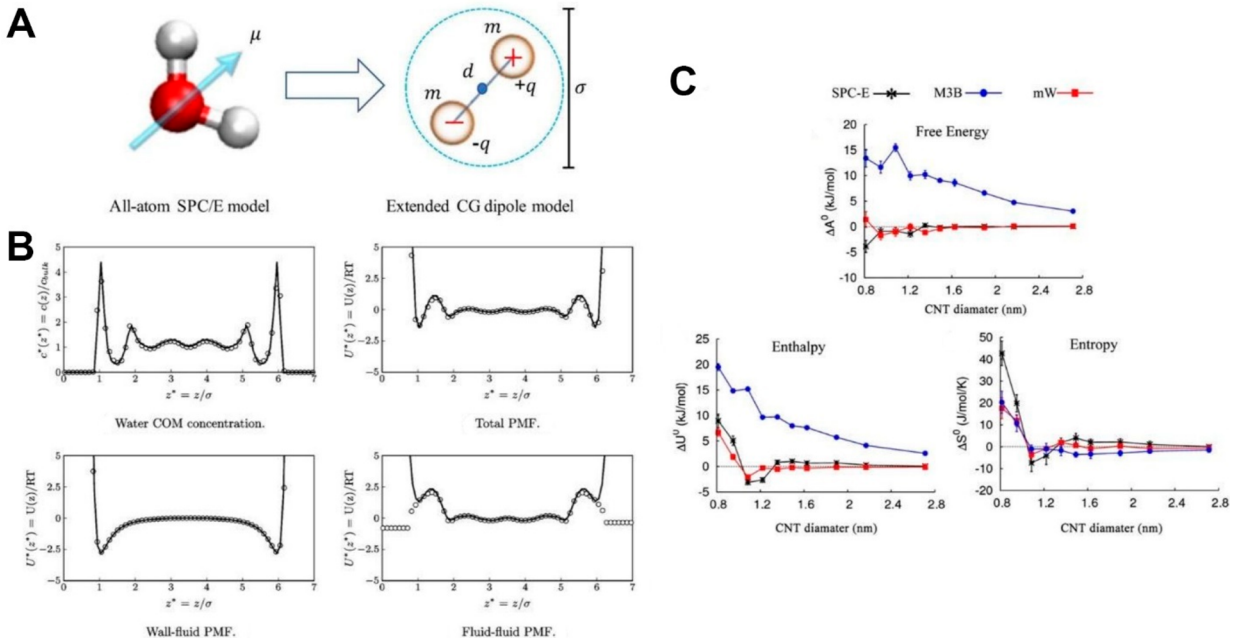

Figure 45. Coarse-graining models. (A) Topology of a coarse-grained water model. Adapted from ref 131. Copyright 2018 American Physical Society. (B) EQT predictions of the center-of-mass concentration of water and potential profiles in a 7σ graphite/water channel, where σ is the distance at which the intermolecular potential between carbon and oxygen is zero. The lines are the EQT results, and the circles are all-atom MD results. Adapted from ref 557. Copyright 2012 American Chemical Society. (C) Thermodynamics of water inside CNTs of ten different diameters using the SPC-E (black squares), M3B (blue triangles), and mW (red circles) water potentials. (top) Free energy as a function of CNT diameter. The coarse-grained mW water model tracks the SPC-E modal for the single-file, 0.8 nm CNT. The M3B model has unfavorable free energies for all CNT diameters studied. (bottom left) Enthalpy as a function of CNT diameter. The tetrahedral H bonding in the mW model gives a good match to the SPC-E results, whereas the loss of model bonding in the M3B results leads to unfavorable enthalpies for all CNT diameters. (bottom right) Entropy as a function of CNT diameter. The mW results track the SPC-E results, except for the 0.8- and 1.0-nm-diameter CNTs, for which rotational entropy is found to contribute to the total entropy by as much as 40−60% in SPC-E water. Adapted from ref 79. Copyright 2011 National Academy of Sciences.

water molecule in the first hydration shell of an ion at the graphene−water interface is transferred to bulk water.[456] Transferring a water molecule from the first hydration shell of an ion at the graphene−water interface to bulk water is favorable for chaotropic ions, but is unfavorable for kosmotropic ions. This conclusion is supported by the ΔU_{iw} and ΔU_{ww} data in Figure 44B. MD simulations at model superhydrophobic and superhydrophilic surfaces, which provide asymptotic limits for the water densities and orientations possible at any solid−water interface, demonstrate that ion-specific effects are primarily governed by an interplay between the ion−water and water−water interactions, regardless of the nature of the solid−water interface.[456]

Although the polarization energy of an ion at a planar solid−water interface is greatly reduced due to the presence of water, there are important situations in which, due to steric constraints, there are not enough water molecules to screen the polarization energy. The confined environment inside an SDN is one such example, as will be discussed in section 4.3.1. Further, for 2D materials, such as hBN and transition-metal dichalcogenides (TMDs; e.g., molybdenum disulfide), in which the electronegativity difference between the constituent atoms results in these atoms possessing permanent multipoles (e.g., boron and nitrogen atoms in hBN possess partial atomic charges), classical electrostatic interactions between the 2D material and water can also play an important role in dictating interfacial phenomena.[454,552−554] Indeed, by comparing the frictional and wetting behavior of several polar (water, ethylene glycol) and nonpolar (diiodomethane) liquids on hBN using MD simulations, Govind Rajan et al.[554] reported that the electrostatic interactions between hBN and the polar fluids can impact the fluid friction coefficient significantly, whereas the influence of these interactions on the fluid contact angle was found to be rather small. Therefore, it would be interesting to investigate how electronic polarization effects get coupled with classical electrostatics in this class of 2D materials, which includes hBN and other TMDs.

Finally, in addition to the modeling of electronic polarization effects using the classical Drude oscillator model, other approaches have also been used to describe the polarization interactions of ions and water molecules at solid−water interfaces. For example, Son and Wang used a methodology based on the implementation of the classical image-charge method in an MD framework to investigate the adsorption behavior of ions at charge-neutral and charged solid−water interfaces.[555] Machine-learning-based approaches can also be used to describe polarization interactions, as illustrated in a recent study by di Pasquale et al., who developed a neural network potential that outputs the charge distribution in the solid given the configurations of the ions and the water molecules as inputs.[556] All of these recent modeling tools introduced to describe many-body polarization effects at planar solid−water interfaces go well beyond the pairwise additive potentials typically used to describe water−solid and ion−solid interactions. It will be important to compare and contrast the results of these newly introduced modeling frameworks as applied to electrolytes confined inside SDNs, as polarization effects in these systems are expected to be more pronounced than at planar interfaces.

https://doi.org/10.1021/acs.chemrev.2c00155
Chem. Rev. 2023, 123, 2737−2831

3.4. Coarse-Graining Methods

The methods discussed in section 3.3.2 are useful in bridging the time and length scales needed for the study of nanofluidics. To study dynamic processes that occur on even longer time scales (microseconds and more), coarse-graining methods are essential to reduce the computational cost. An example of a coarse-graining method used in nanofluidics is modeling a water molecule as a dipole, instead of using an all-atom model.[131] This method (Figure 45A) accurately captures properties of the liquid that are important for nanofluidics, including the dipole−dipole fluctuations and the dielectric properties.

Coarse-graining models are able to predict a variety of other properties relevant to nanofluidics, including densities and free energies. One such model[557] (Figure 45B), which is based on empirical-potential-based quasi-continuum theory (EQT), replaces one water molecule with one particle bead. This model was developed to capture the dynamics and structure of water accurately near graphite and silicon interfaces. Some coarse-grained models are also able to capture hydrogen-bonding effects in water,[79] including accurately determining the free energies, enthalpies, and entropies of water confined in CNTs of different diameters (Figure 45C). This work compares the results using an all-atom model (SPC-E), a single-particle, two-body model (M3B), and a single-particle, three-body model (mW) for water. The force-field parameters in all of the models were adjusted to reproduce the cohesive energy and density of water at 300 K and 1 atm. The water−carbon interactions of the mW and M3B models were further adjusted to have the same interaction energy as the SPC-E model. Coarse-graining has also been successful in reproducing electrokinetic phenomena, such as charge inversion[558] and the formation of EDLs[559−561] at interfaces. A recent coarse-grained MD study by Noh et al.[562] explored the origin of the power-law dependence of ion concentration on the surface conductance that is observed in a wide variety of experimental nanofluidic systems. This power-law dependence arises due to the inability of the net charge in the solution to maintain electroneutrality, which leads to charged nanopores. In addition to models of water, coarse-graining methods describing interactions in biological systems have been developed to study dynamics at larger time and length scales. MARTINI[563] is one such force field developed for this purpose, and is currently used for most types of biological molecules, including lipids,[563] proteins,[564] and carbohydrates.[565]

Classical MD and coarse-grained MD have been able to corroborate the power-law dependence of conductivity on the ion concentration observed in various SDN experiments.[250,566,567] Extensive simulations have been performed for various diameters and lengths of SDNs to identify the physical origin of the power-law dependence.[562] In addition, length-scale studies were performed to study the transport enhancement observed in SDNs as a function of their length.[568] These large-scale simulations showed that entrance/exit effects at the mouth of the SDN contribute to the flow enhancement observed in experiments.

3.5. Continuum Methods

Nanoconfined fluids exist in a regime in which simple classical continuum descriptions, including common assumptions made in those continuum approaches, can fail.[417,427,569−572] For instance, from an electrostatic perspective, the mean-field approximation fails to describe the local correlations of ions and water at an interface,[394,573] and the dielectric profile at an interface is nonuniform and anisotropic.[574] Furthermore, at high ionic concentrations, overscreening of surface charge leads to long-range decay of alternating layers of ionic charge.[575] From a hydrodynamic perspective, properties such as the viscosity and the surface friction coefficient are strongly related to the confinement dimension.[576]

Despite the above caveats, extreme confinement does not necessarily rule out the use of continuum approaches. Treating extreme confinement requires modified continuum frameworks that seek to capture the spatial variation of transport properties and the finite size, correlated structure, and/or the specific environmental interactions of molecules.[427] Such continuum approaches have the advantage of being relatively computationally inexpensive, and may provide simple formulas for the properties of an electrolyte fluid at an interface or confined between interfaces. The simplest forms of modifications are based on the LDA, in which the steric effects of the finite size of the ions[577,578] and other short-range interactions[579] are represented in terms of the local densities of ions. Although these simple theoretical approaches can explain trends in electrochemical measurements at high ionic concentrations or high voltages, these methods cannot reproduce the formation of alternating layers of charge and mass at the interface.

To describe the impact of electrostatic correlations on EDL structure, Bazant et al. proposed a higher-order Poisson equation that can describe the phenomena of overscreening, charge inversion, and like-charge attraction.[580−583] At high ionic concentration, the effective screening length in these theories begins to increase with concentration when the Debye length becomes smaller than the ion size,[584] as demonstrated experimentally in SFA measurements.[585,586] These findings suggest that the EDLs may extend farther into the bulk at high ionic concentration than the conventional Debye length, heightening the influence of the ELD in confined systems at high ionic concentration.

Furthermore, many theoretical approaches assume that the system is a primitive model electrolyte, in which the ions exist in a structureless medium of constant dielectric constant. Solvent molecules have finite sizes, and dipole moments and respond to the local electric field. The polarization of water can be incorporated into mean-field models to capture the response to local electric fields.[587−592] Taken together, these modifications describe confined electrolyte fluids by taking correlations and finite size into account. Although these models may need parametrization and benchmarking by comparison to atomistic simulations, this approach can offer strong predictive capabilities both in and out of equilibrium.

In addition, complex, yet accurate, classical DFT describes the local electrolyte structure within the EDL in terms of integrals of the local ionic densities. Classical DFT has been applied to confined electrolytes[369,485,593−595] to explore charge inversion,[596] electrokinetic conversion efficiency,[597] charge neutrality breakdown,[598] the dynamics of concentrated electrolytes and ionic liquids,[599,600] and capacitance.[601]

4. THERMODYNAMICS UNDER CONFINEMENT

The confinement of fluids in small channels gives rise to many unusual thermodynamic phenomena. In this section, we review several key thermodynamic and related considerations that define the length scales at which fluid and ion transport begin to deviate from classical, continuum descriptions. For a more detailed discussion of these limits and the accompanying theoretical framework, we refer the reader to two reviews by Bocquet and co-workers.[71,602]

https://doi.org/10.1021/acs.chemrev.2c00155
Chem. Rev. 2023, 123, 2737−2831

4.1. How Small is Small: Confinement and Scaling Effects in SDNs

Figure 46 shows approximate size ranges over which nanoconfinement affects specific aspects of liquids and electrolyte

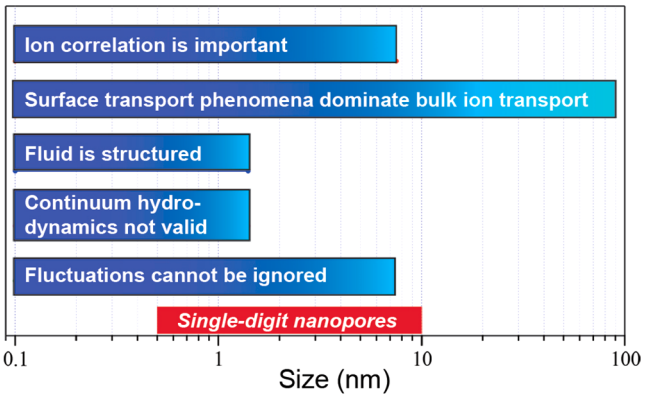

Figure 46. Length scales at which nanofluidic phenomena become important from a thermodynamic perspective. The red band indicates the SDN size range.

solutions. As a rule of thumb, a continuum thermodynamic description should begin to fail when individual fluctuations can no longer be ignored. A crude estimate of this threshold can be obtained from the size of the system at which fluctuations start to become important. Given that fluctuations scale as $\sqrt{N}$, if we somewhat arbitrarily set this fluctuation threshold at 1%, then a system with 10 000 individual molecules or fewer can no longer be considered to meet continuum predictions. As a point of reference, an ensemble of 10 000 water molecules at the density of the bulk liquid translates into a sphere having a radius of ∼6.5 nm. Alternatively, the same number of water molecules will fill a 10 nm long cylinder with a 3.1 nm radius,[603] clearly indicating that fluctuation effects are important in all SDNs.

The size threshold for the breakdown of continuum hydrodynamics can also be estimated using an argument advanced by Bocquet et al.[71] These authors suggested that this threshold is given by the size limits of the Navier−Stokes equation, which break downs when the hydrodynamic time scale defined by the kinematic viscosity becomes comparable to the molecular time scale, τ_c. The critical size, l_c, is then given by $l_c \approx \sqrt{\eta \cdot \tau_c}$ If one assumes that $\tau_c \approx 1$ ps, then this equation predicts that continuum hydrodynamics breaks down below a surprisingly small size of 1.4 nm. This threshold can be better understood if we also consider the structural changes that occur in liquids when confinement begins to approach the nanometer scale. A series of pioneering SFA experiments by Israelachvili and co-workers revealed that liquids in 2D confinement between two mica surfaces begin to show distinct layered structuring when the separation of the surfaces approaches the size of the molecules comprising the liquid.[604] For small-molecule liquids with intermolecular interactions that are not as directional as those in water, layering can appear at even longer distances.[605] In the case of 1D confinement, water in CNTs remains bulk-like for pore diameters larger than 1.4 nm; below this limit, water begins to arrange in semiordered configurations,[79] culminating in the single-file chains observed inside sub-1 nm diameter CNTs.[87] Semiordered configurations have also been reported for water in 2D confinement between two graphene sheets that are 1.4 nm apart.[606]

Similar confinement scales arise for ion-transport phenomena. Debye screening in a channel with charged walls leads to perhaps the simplest estimate of scale, i.e., when the Debye layers originating from the channel walls begin to overlap. For a 1:1 aqueous electrolyte at a physiological concentration of 150 mM, this threshold channel radius corresponds to ∼1.6 nm. A more accurate estimate[602] considers the relative contributions of the surface ion transport to the bulk transport, which is defined by the Dukhin length

$$l_{Du} = \Sigma/\rho \tag{16}$$

where Σ is the surface charge density of the channel walls and ρ is the bulk ion-charge density. Surface transport would then dominate the bulk contribution for channels narrower than l_{Du}, which could range from 1.2 nm to hundreds of nm for typical nanopore materials and electrolyte concentrations.[71] An important correction to these estimates considers slip effects at the channel boundary, which can further enhance the surface transport contribution to ion transport. In this case, the relevant parameter is the modified Dukhin length:[602]

$$l^*_{Du} = b \cdot l_{Du}/l_{GC} \tag{17}$$

where b is the slip length and l_{GC} is the Gouy−Chapman length.

Another scaling estimate is obtained by considering the ion-correlation effects that arise in small channels and nanopores. Incomplete ion screening in a channel bound by a medium with a lower dielectric constant leads to the existence of an additional electrostatic potential, which in turn can be used to define an interaction energy between two ions in the channel. For a situation in which a low-dielectric medium ($\varepsilon \approx 2$) confines a water-filled channel ($\varepsilon \approx 81$), this energy is larger than the thermal energy k_BT for channels smaller than ∼7.5 nm.

These estimates indicate that most, if not all, SDNs fall into a distinct nanofluidic regime in which the physics of ion and water transport should exhibit significant deviations from bulk descriptions, and in which phenomena such as fluid structuring, surface transport, and ion correlations are important.

4.2. Impact of Dimensionality

The properties that specify the thermodynamically stable states of a system are among the most important when studying nanofluidic systems. The sign of the free energy determines whether a process is favorable. The Helmholtz free-energy change at constant temperature is defined as $\Delta A = \Delta U - T\Delta S$. Both the internal energy and the entropy in a confined system are different from their bulk counterparts due to the influences that reduced dimensionality, surface effects, and other confinement-related phenomena have on the degrees of freedom in the system.

4.2.1. The Thermodynamics of Confined Water. As an example of the impact of dimensionality, we consider the thermodynamics of the filling of CNTs with water, which has been studied with both experiments and simulations.[79,87] Although CNTs are hydrophobic, water can fill CNT nanopores spontaneously. As discussed above, an early MD investigation showed that water molecules fill a hydrophobic, (6,6)-SWCNT by adapting a single-file configuration that allows only two hydrogen bonds per water molecule.[87] This finding appears to be counterintuitive from a thermodynamic perspective. From an energetic standpoint, the number of the hydrogen bonds per water molecule inside sub-nm diameter CNTs is generally smaller than that in the bulk, and so favorable water−water hydrogen-bond interactions in the bulk are replaced by less

https://doi.org/10.1021/acs.chemrev.2c00155
Chem. Rev. 2023, 123, 2737−2831

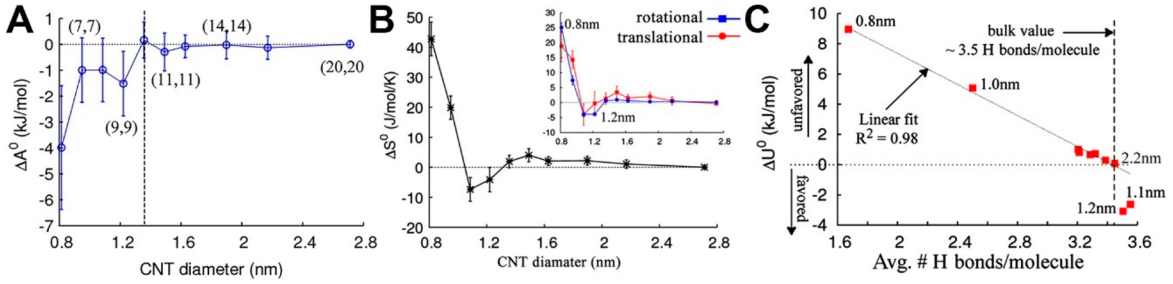

Figure 47. Thermodynamic properties of water inside CNTs. The change in (A) the Helmholtz free energy and (B) the entropy for taking water from the bulk to confinement in CNTs of different diameters. The inset in (B) shows the rotational and translational contributions to entropy as a function of CNT diameter. (C) The change in enthalpy for taking water from the bulk to confinement in CNTs as a function of the average number of hydrogen bonds per water molecule. Adapted from ref 79. Copyright 2011 National Academy of Sciences.

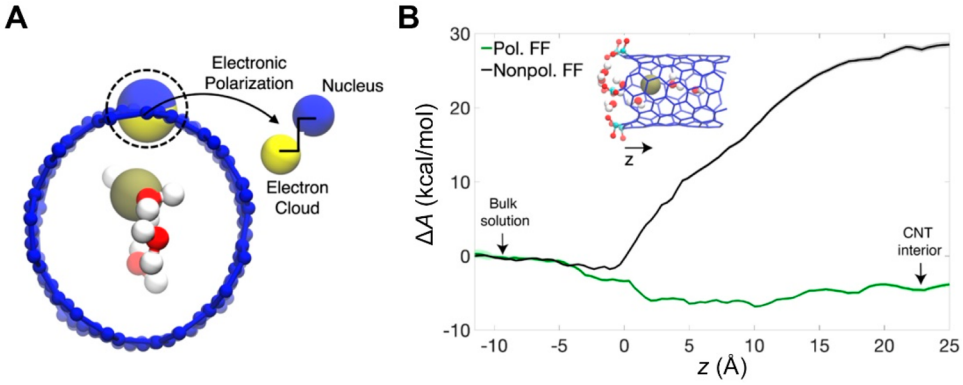

Figure 48. Transferring K^+ from the bulk into a CNT. (A) Schematic of a 0.8 nm diameter CNT (blue carbon atoms), a K^+ ion (tan), and water molecules (red and white). The electronic polarization of one carbon atom is illustrated as a displacement between the DC (blue) and the DP (yellow). The DC−DP bond of the carbon atom has been magnified by a factor of 25 for clarity. (B) The Helmholtz free-energy change when a K^+ ion is transferred from the bulk solution to depth z in the CNT. Adapted from ref 613. Copyright 2021 Massachusetts Institute of Technology.

favorable water−carbon interactions inside the CNT. From an entropic standpoint, the reduced configurational space in confinement is expected to be unfavorable compared to bulk water.

The origin of this unexpected stability of water in hydrophobic CNTs has been widely discussed in the literature. For example, MD simulations using the two-phase thermodynamics method were performed to estimate the entropy of water molecules confined in CNTs with diameters in the range of 6.9−10.8 Å.[607] The confined water molecules appeared to have a greater rotational entropy than those in the bulk.[607] Interestingly, the largest entropy difference was found for the narrowest pores studied. These simulations provided clear evidence of a more thermodynamically favorable state of water confined in narrow CNTs relative to bulk water.

As shown in Figure 47A, ΔA for transferring water from the bulk into CNTs with diameter <1.3 nm is negative.[79] Furthermore, the organization of the water depends on the CNT diameter and chirality. The filling of the CNTs, and the novel structures of the confined water, arise from both entropic and enthalpic effects under confinement. For instance, as shown in Figure 47B, the entropy of water confined in sub-1-nm-diameter CNTs is more than 30% higher than in the bulk liquid.[79] This entropy gain arises from the absence of the tetrahedral hydrogen-bonding framework that characterizes bulk water, as well as from the smaller number of hydrogen bonds per molecule. Together, these effects give the confined water higher rotational and translational entropies than the bulk liquid. An interesting exception is CNTs with 1.1- and 1.2-nm diameters, in which water forms an ice-like structure, and the entropy is lower than that of bulk water.

Figure 47C shows how ΔU for taking water from the bulk to confinement in a CNT depends on the CNT diameter. The free energy is determined primarily by the average number of hydrogen bonds per water molecule. As shown in Figure 47C, only inside the 1.1 and 1.2 nm CNTs does water make a larger number of hydrogen bonds than in the bulk due to the aforementioned ice-like structure CNTs of these diameters. For other CNT diameters, water makes fewer hydrogen bonds than in the bulk, so there is an enthalpic penalty for confinement. This type of analysis provides a general framework for studying the thermodynamics of nanofluidic systems, including the effects of parameters such as geometry, temperature, pressure.[95]

4.2.2. Effect of the Dimensionality of Confinement on the Electrostatic Screening of Ionic Charges. The electrostatic screening of ionic charges depends sensitively on the dimensionality of confinement, and is determined by the balance between entropic mixing and the electrostatic free energy.[608] In dilute bulk solutions, the ionic charges are screened at the scale of the Debye length, which depends inversely on the square root of the ionic concentration. In confinement, the balance between entropy and electrostatic interactions is altered, and depends on the dimensionality and geometry of the confinement. In 2D confinement, the effective screening length for an ionic charge, or charges, on the pore walls is longer ranged than in the bulk, but the concentration dependence remains algebraically decaying. Remarkably, in 1D confinement, the effective screening length diverges exponentially as the

https://doi.org/10.1021/acs.chemrev.2c00155
Chem. Rev. 2023, 123, 2737−2831

concentration approaches zero.[608] In many cases, the effective screening length can thus exceed the length of a nanopore, breaking the classical assumption of local electroneutrality in each cross section, and causing the integrated charge density of the pore walls not to be equal the charge within the pore.

If a pore connecting two ionic solutions is not constrained to electroneutrality, specific chemical interactions with the pore walls can dominate the ionic selectivity. The notion of electroneutrality breakdown is implicitly embedded in models of ionic conduction in 1D biological or synthetic ion channels, in which the ion transport is modeled as a chemical process that is determined by energy barriers,[1,609,610] without specific consideration of ion charges, surface charges, or electroneutrality. Furthermore, a unique ionic Coulomb blockade, in which ionic pairing leads to nonlinear conduction characteristics, has been predicted to exist in 1D channels.[5] Therefore, the dependences of charge selectivity and ionic conductance on ionic concentration are both expected to be significantly different in 1D versus 2D confinement.

4.3. Enhancement of Surface Effects in Reduced Dimensions

4.3.1. Pronounced Role of Electronic Polarization Effects on the Free Energy Barrier for Ion Transport. As discussed in section 3.3.2, electronic polarization effects can play a major role in ion-adsorption phenomena at solid−water interfaces. Nevertheless, the total polarization energy at a planar solid−water interface is screened by 85% or more due to cancellation effects resulting from the vectorial interactions of the electric fields exerted by the water molecules and ions. In contrast, inside SDNs there may not be enough water molecules to screen the electric fields exerted by the ions. For example, as shown in Figure 48A, in a CNT with a 0.8 nm diameter, water molecules and ions organize in a single-file manner. Hence, there are hardly any water molecules in the radial direction to screen the ion electric fields.

To explore the ramifications of electronic polarization effects inside SDNs, MD simulations were carried out for a system consisting of a 0.83-nm-diameter (8,4) chirality CNT embedded in a lipid bilayer. Six COO^- groups were used to mimic the negative surface charge expected at the CNT pore mouth at a physiological pH of 7.5.[1] The lipid molecules and the COO^- groups were modeled using the CHARMM36 force field.[611] The change in the Helmholtz free energy when a K^+ ion is transferred from the bulk solution to the interior of the CNT at a depth z from the CNT entrance is shown in Figure 48B. The green curve corresponds to the predictions from the polarizable force field,[447,450,456,868] and the black curve corresponds to predictions in which the electronic polarization effects are neglected and the ion−CNT and the water−CNT interactions are modeled using LJ potentials with parameters determined using geometric-mean combining rules. A K^+ ion that enters the CNT loses, on average, four to five hydration-shell water molecules.[143,612] However, the polarization stabilization more than compensates for the dehydration penalty, so that from a free-energy perspective it is favorable for K^+ to enter the CNT. The total polarization energy, which is dominated by the ion−CNT polarization energy, is estimated to be close to −25 kcal/mol in the CNT. Thus, such CNTs are expected to be permeable to K^+, in agreement with experiments.[1,13] Indeed, in a recent study,[868] electronic polarization effects are found to play a prominent role in dictating K^+ ion transport through 0.8-nm-diameter CNTs, including demonstrating a breakdown of the Nernst-Einstein relation due to two significantly different mechanisms of K^+ ion diffusion and electromigration in these channels. In contrast, the predicted free-energy profile when electronic polarization effects are neglected is strongly repulsive (see the black curve in Figure 48B) which precludes any K^+ ion transport and thereby, cannot explain the recent experimental observations of K^+ ion permeation and transport through narrow 0.8-nm-diameter CNTs. This in turn underscores the importance of incorporating polarization interactions in the modeling of electrolytes confined inside CNTs. It would be interesting to explore the significance of electronic polarization effects on electrolyte properties in other confined environments, including nanopores composed of graphene and other 2D nanomaterials.[260,548]

4.3.2. Electronic Effects in Reduced Dimensions. The electronic properties of water and other liquids can be altered significantly in SDNs. For example, first-principles simulations showed that water molecules confined in (14,0)-SWCNTs (diameter 1.1 nm) and (19,0)-SWCNTs (diameter 1.5 nm) exhibit reduced molecular dipole moments relative to the bulk value, by 9% and 7%, respectively.[516] This study also revealed important interfacial effects on the electronic properties of liquid water. For example, it was found that the dipole moment of the water molecules in the radial centers of both types of CNT remains close to that of molecules in bulk water. However, the dipole moments decreases monotonically moving away from the pore center toward the CNT wall.[516] This reduction in dipole moments under confinement is driven by the changes in the water structure at the interface, i.e., the presence of broken hydrogen bonds near the CNT wall.[614]

The collective behavior of the water dipole moments influences the dielectric environment. Close to an interface, the perpendicular component of the local dielectric constant of water may be reduced from its bulk value of $\varepsilon \approx 81$ to a value of $\varepsilon \approx 2$.[132] At an interface, the dielectric "constant" is a spatially varying tensor with different components normal to and parallel to the interface.[110,428,574,615] In the case of water, the parallel component scales with the density of the liquid, which forms layers near the interface. The normal component varies more sharply within the first few layers of liquid, and even has singularities. The water dielectric profile depends on the hydrophobicity of the interface. Early studies investigated the role of the nonlocal dielectric profile of water in bulk solutions and at interfaces.[616,617] Such solvent structuring may affect the activity of ions, not only in the bulk,[618−620] but also in confinement. Mean-field models that incorporate the polarization of solvent molecules can reproduce the response of water molecules to the electric field and ionic concentration variations near the interface,[587−592] but do not capture the full complexity of the water structuring. The impact of the dielectric profile on ionic transport in SDNs remains an important area of investigation.

Molecular polarizability is another important electronic property of liquids. First-principles simulations showed that the changes in the molecular polarizability of water molecules under confinement are more complex than those of the dipole moment.[516] For example, it was found that the polarizability of confined water generally decreases relative to that of bulk water, due to broken hydrogen bonds. However, this phenomenon is counterbalanced by a polarizability increase resulting from the interactions of the water molecules with the confining surface. In particular, the average water polarizability in a CNT with a 1.1 nm diameter, in which all the water molecules are interfacial, is

https://doi.org/10.1021/acs.chemrev.2c00155
Chem. Rev. 2023, 123, 2737−2831

enhanced by ∼3% relative to the bulk value. On the other hand, in a CNT with a 1.5-nm diameter, the average water polarizability is unchanged relative to that in the bulk.[516] In this latter case, the average molecular polarizability reflects a balance between lower polarizabilities for molecules in the center of the pore (by ∼15% relative to the bulk) and enhanced polarizabilities (by ∼23% relative to the bulk) for molecules in the interfacial region.

Several studies have shown that the vibrational properties of confined water are influenced by electronic effects at the interface between confined water and a CNT wall, including electronic charge-density fluctuations.[502,621] For example, as shown in Figure 49, it was found that the overlap of the π-

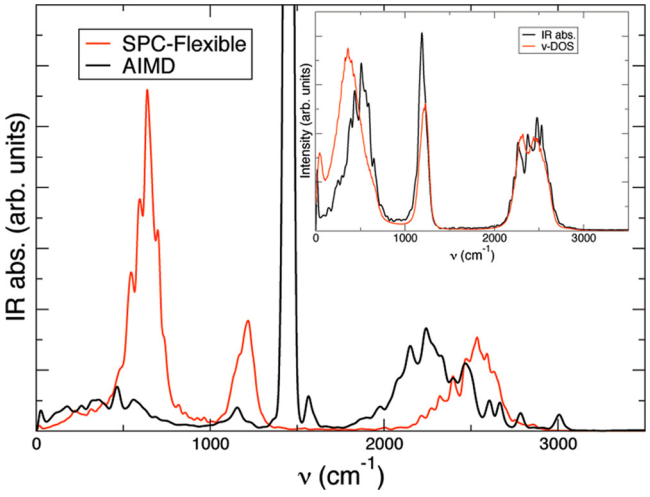

Figure 49. Effect of electronic properties on the vibrational spectrum of nanoconfined water. Comparison between the IR spectra of water confined between two graphene sheets at a distance of 1.01 nm obtained by MD simulations with classical potentials (red lines) and by AIMD (black lines). The inset shows the vibrational density of states (v-DOS, red) and the IR spectrum (black) of bulk water from classical MD simulations, illustrating the differences between the MD and AIMD arise from the treatment of collective effects in the latter technique. Reproduced with permission from ref 621. Copyright 2009 American Chemical Society.

electrons of graphene with the electronic charge density of water molecules, which is responsible for important features in IR spectra of water confined in narrow CNTs and graphene slit pores, is absent in simulations that used classical potentials.[621] Such studies point to the important effects of nanoconfinement on the electronic properties of liquid water, and the need to include these effects in next-generation force fields for the simulation of confined liquids and solutions.

4.4. Confinement Effects on Electrolytes

Confinement can have a substantial impact on the thermodynamic properties of electrolytes. Early work in colloid science identified the repulsive electrostatic disjoining pressure between like-charged surfaces which is caused by the overlap of EDLs, as the mechanism for the stability of a colloid composed of like-charged particles.[101,622,623] The success of the EDL force predictions led to the widespread application of mean-field, dilute-solution theory to describe electrolytes in confinement.[624,625] Even so, the specific properties of ions and solvent molecules under nanoconfinement can affect the pressure between surfaces, as well as other thermodynamic properties. For example, the correlated structure of multivalent ions between charged surfaces can lead to the electrostatic attraction of like-charged surfaces.[394,573,581,626] This phenomenon is responsible, for instance, for the cohesion of cement paste, in which divalent calcium ions under nanoconfinement bind the layers of a calcium−silica hydrate gel. Furthermore, layering of solvent and ions can lead to oscillating surface forces that cannot be predicted by standard EDL theories.[627] Molecular simulations and modified theoretical approaches must be employed to capture these effects.

Individual ions also experience free-energy barriers to entering a charged nanopore. Changes in the solvation structure and dielectric environment around the ions impart an energetic cost to entering a pore of molecular dimensions.[143,145,628−631] Even in a dilute electrolyte solution, an ion must shed its screening cloud to enter an SDN.[608] Ion pairing is promoted because dehydrated ions within the pore experience strong electrostatic interactions. The extent of ion pairing increases with increasing concentration.[632,633] Furthermore, ion adsorption to surfaces and association with surface groups can change the surface properties of the nanopore. This process, which depends on the ion identity and concentration, is known as charge regulation, and depends sensitively on the extent of confinement.[429,463,634−636]

MD simulations of aqueous solutions confined in SDNs generally indicate that a complex interplay between nanoconfinement and the intrinsic properties of ions determines the solvation and transport properties of confined ions. For example, first-principles simulations of LiCl and KCl solutions in a CNT with a 1.1-nm diameter showed that the Li^+ solvation shell is structurally resilient under confinement, maintaining a tight tetrahedral coordination.[516] On the other hand, K^+ and Cl^- exhibit a strong degree of desolvation relative to the bulk. The oxygen coordination of K^+ decreases from 6.8 in the bulk to 5.4 under confinement, whereas that of Cl^- decreases from 6.0 to 4.7 in a KCl solution and 5.5 in a LiCl solution. Similarly, Na^+ was found to be partly desolvated in a CNT with a 1.5-nm diameter, although the decrease in the coordination number in the first solvation shell is weaker than those of K^+ and Cl^-.[514,515] This observation is consistent with XRD experiments,[637] which showed that the hydration number of Li^+ in a CNT with a 2-nm diameter is much more bulk-like than those of larger cations.

MD simulations with classical force fields have been employed extensively to investigate ions confined inside SDNs. The use of classical force fields enables a long simulation time, which is required for a meaningful analysis of transport properties, and also affords an advantage over first-principles approaches in its ability to include or exclude various physicochemical interactions at will. For example, a recent study that combined first-principles and classical simulations of KCl and LiCl in CNTs with 1.1- and 1.5-nm diameters showed that the inclusion of both polarization and cation−π interactions is essential for the description of ion solvation under confinement, particularly for large ions (K^+ and Cl^-) with weak hydration energies.[638] This study also showed that cation−π interactions can significantly influence the transport properties of ions in CNTs, particularly for K^+, for which the simulations point to a strong correlation between ion dehydration and diffusion. For a CNT with a 1.1-nm diameter, it was found that the axial diffusion coefficients of the cation and anion in KCl are similar, in contrast to their counterparts in LiCl. This behavior arises from the strong desolvation of K^+, which leads to an enhanced coupling between the counterions. These results point to the need for an improved

https://doi.org/10.1021/acs.chemrev.2c00155
Chem. Rev. 2023, 123, 2737−2831

understanding of ion pairing in SDNs and how this pairing influences the transport of aqueous solutions in these systems.

Classical MD simulations also showed that, similar to the case for water,[517] the mechanism of ion transport can be significantly altered due to confinement effects,[638] i.e., confined ions can exhibit anomalous and anisotropic dynamic properties. For instance, the component of the ion diffusion coefficient along the axis of a CNT can be expressed as

$$D_{z,n} = \langle |z(t) - z(0)| \rangle / 2dt^n \quad (18)$$

where $z(t)$ is the axial position of the ion at time t, the dimensionality $d = 1$, and n is indicative of the mechanism of ion diffusion. In particular, $n = 0.5$, 1, and 2 correspond to single-file, Fickian, and ballistic diffusion, respectively. Simulations of a KCl solution confined in SDNs showed that the mechanism of ion transport changes from Fickian in the bulk toward the single-file diffusion limit under confinement.[638] The average value of n decreased from 0.95 in CNTs with a 1.5-nm diameter to 0.8 in CNTs with a 1.1-nm diameter. The simulations showed only small differences in the value of n for different ions in the same CNTs.

Finally, we stress that the inclusion of electronic polarization effects, such as interfacial charge transfer and polarizability, is critical for a proper description of ions confined inside SDNs, as also highlighted above. Recent studies of alkali-metal ions in narrow SDNs showed that larger cations exhibit stronger interfacial charge transfer with the nanopores, and that the charge transfer increases with increasing confinement.[639,640] This finding indicates that the point-charge approximation that is often employed in conventional MD simulations is not sufficient for capturing either the electronic effects within the EDL or the structural and dynamic properties of confined ions.

5. TRANSPORT UNDER CONFINEMENT IN SDNS

Section 2 discussed a number of the fabrication methods that enable the creation of SDN model systems. We now examine the effects of extreme confinement on fluid and ionic transport in some of these systems. Specifically, we review transport in microfabricated nanopores and nanochannels, fluidic diodes, graphene capillaries, carbon nanotubes, and polymer membranes.

5.1. Transport in Synthetic Nanopores and Nanochannels

5.1.1. Transport in Microfabricated Nanochannels. Micro- and nanofabrication techniques enable a high level of precision in the creation of nanopore systems, and can also provide the ability to control fluid and ionic transport in nanopores. The Debye length, λ_D, is inversely proportional to the square root of the ion concentration, C. In micrometer-sized channels, the Debye length is generally much smaller than the channel dimensions. The majority of the confined solution is therefore shielded from the surface charge, and experiences no electric potential. However, as shown in Figure 50, when the EDL thickness is larger than the channel size (e.g., in nanoscale channels with low ionic strength), the EDL from the two surfaces will overlap in the channel, and the potential is nonzero throughout the channel. The finite potential leads to an excess of counterions in the nanochannel interior, such that ionic concentrations in the channel differ from those in the bulk solution outside of the channel.

The enhanced concentration of counterions and decreased concentration of co-ions due to electrostatic interactions with the surface charge in a nanometer-sized channel is called the

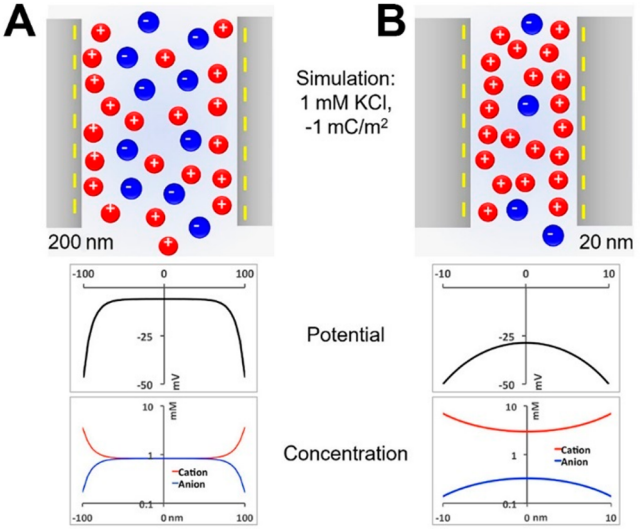

Figure 50. Ion distribution and potential profile in nanochannels. (A) A channel that is 200 nm wide and (B) a channel that is 20 nm wide. The reservoir outside the nanochannels contains a 1 mM aqueous solution of KCl. The net surface charge (the total of the native surface charge and the Stern layer charge) is held at −1 mC/m^2. Adapted from ref 385. Copyright 2015 American Chemical Society.

exclusion−enrichment effect.[641] This phenomenon depends on the Debye length, the characteristic dimension of the nanochannel, the surface potential, and the charge on the ion. Overlap of the EDLs in a channel is the basis of permselectivity.

The EDL that forms at a charged surface results in an ionic environment that is different from that in the bulk, and therefore contributes to an additional conductance mechanism known as surface conductance. Consider a negatively charged nanochannel filled with a KCl solution. The total ionic conductance G is the superposition of the bulk conductance and the surface conductance:

$$G = e(\mu_K + \mu_{Cl})C_b N_A WH/L + 2\mu_K \sigma_S W/L \quad (19)$$

Here, the first term is the bulk conductance, the second term is the surface conductance, W, L, and H are the width, length, and height of the nanochannel, respectively, μ_K and μ_{Cl} are the mobilities of the K^+ and Cl^- ions, respectively, C_b is the bulk concentration, N_A is Avogadro's number, e is the elementary charge, and σ_S is the surface charge.

Figure 51 shows ionic conductance data for a nanochannel of known width and length as a function of the ion concentration. The conductance depends linearly on the ion concentration at high concentrations, for which the bulk conductance term dominates. The value of H can be determined from the data in this regime. There is a conductance plateau in the low-concentration region, within which surface conductance dominates.[250,642] The value of σ_S can be determined from the data in this regime. The transition concentration between the two regimes is ≈1 mM. The Debye screening length at this concentration is ≈10 nm, which is half of the designed nanochannel height. The difference in the concentrations of counterions and co-ions can also be calculated from such data based on the electroneutrality requirement, and is given by $2|\sigma|/eH$.

5.1.2. Diodes. The device in Figure 51 can be thought of as a concentration-controlled resistor. As researchers investigated conductance in nanosized channels, it became clear that

https://doi.org/10.1021/acs.chemrev.2c00155
Chem. Rev. 2023, 123, 2737−2831

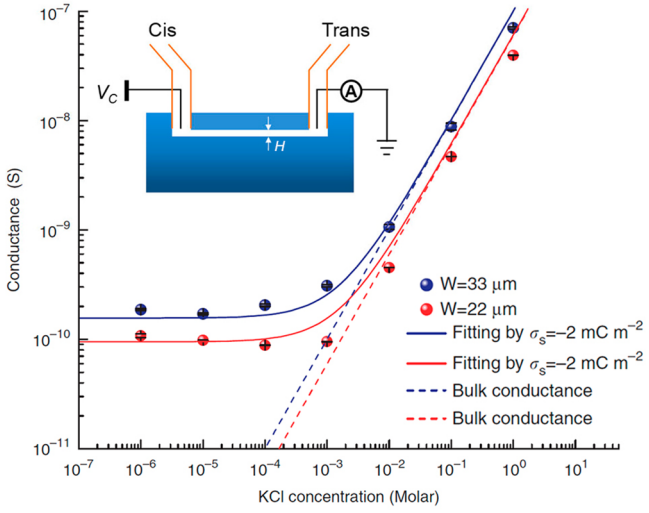

Figure 51. Ionic conductance of an array of 11 nanochannels as a function of ionic concentration. The inset is a schematic of the electrical connections. The conductance was measured for two devices fabricated using an identical process on the same wafer For the blue data points, W = 3 μm/channel · 11 channels = 33 μm, L = 100 μm, and H = 20 nm. For the red data points, W = 2 μm/channel · 11 channels = 22 μm, L = 100 μm, and H = 20 nm. The solid lines are the fitting curves, with σ_S = −2 mC/m^2. The dashed lines are the bulk conductance predictions. Adapted from ref 252. Copyright 2011 Springer Nature.

nanofluidic analogues of other electronic elements could also be created. Research on the role of surface charge in nanofluidic devices led to the design of ionic devices, such as switches and diodes,[643,644] that function by breaking the electrochemical symmetry of nanopores and nanochannels and taking advantage of surface-charge-regulated ionic transport. Asymmetry can be introduced, for example, by creating surface-charge patterns, or by using asymmetric channel shapes.

Karnik et al.[645] developed a process called diffusion-limited patterning to create nanochannels containing a junction between a positively charged zone and a neutral zone, as shown in Figure 52A. The first step in the patterning of such nanochannels is modification of the entire channel surface with biotin. The channel is then incubated with a solution containing avidin on one side, for the amount of time needed for the avidin to diffuse through half of the channel length. The region of the channel in which avidin is bound to biotin is positively charged, and the remainder of the channel is neutral. These patterned nanochannels exhibit current rectification, which is to say that the current for a voltage V of one polarity is larger than the current for voltage $-V$ (Figure 52B). In particular, the current is enhanced when the uncharged zone is at a positive potential (forward bias), and is diminished when the uncharged zone is at a negative potential (reverse bias).

Another approach to creating patterned surface charges begins with conical nanopores with surface carboxyl groups that imparted a negative charge. Surface-charge patterns can be created by introducing a solution containing an amine and an amide-coupling agent to one side of the membrane. The resulting asymmetric modification with amides is facilitated by the pore shape, which naturally induces an inhomogeneous distribution of the modifying agent in the pore,[404] and leads to the formation of a sharp junction between the modified and unmodified zones. This approach was used to fabricate a bipolar diode based on ion current (Figure 52C.[68,646] Bipolar diodes based on sub-10-nm nanopores exhibited rectification degrees above 200, even under physiological conditions.

Structural asymmetry can also be used to induce ion-current rectification in, as has been seen, for instance, in conical nanopores with homogeneous surface charge.[647] Rectification in conical nanopores was first observed by Wei et al.[389] in an experiment in which a voltage was applied across the 20-nm opening of a quartz nanopipette immersed in a low-concentration, aqueous KCl solution. Such rectifiers exhibit higher conductance when the counterions are sourced from the narrow opening and move toward the wide opening of the pore than in the opposite case, as shown in Figure 53.[648] Wei et al. attributed the asymmetry of the current−voltage behavior to the EDL at the quartz surface of the tip. They found that ion-current rectification is only observed when the tip size of the nanopipette electrode is comparable to the thickness of the diffuse double layer. It is now generally accepted that rectification requires an asymmetric EDL within the nanopore, producing an accumulation or depletion of charge-carrying ions at opposite voltage polarities.

5.1.3. Transistors and Other Devices. The transport properties of nanochannels and nanopores can also be modified by introducing gate electrodes to control the local surface

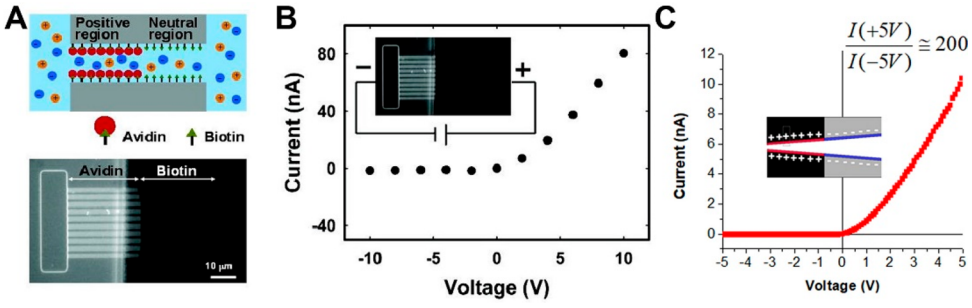

Figure 52. Nanofluidic diodes. (A) Shown at the top is a schematic of a nanofluidic diode consisting of a nanochannel containing a junction between a zone with positive surface charges due to bound avidin, and a neutral zone with no avidin. An epifluorescence image of such a nanofluidic diode is shown at the bottom left; the emission arises from fluorescently labeled avidin. The nanofluidic channels, which are 120 μm long, 4 μm wide, and ∼30 nm high, were fabricated using a sacrificial polysilicon process. The channel width was estimated from micrographs, and the channel height was estimated from conductance measurements in 1 M KCl. The scale bar 20 μm. (B) A current−voltage curve, obtained with a 10 mM KCl solution, showing ion−current rectification. (C) A current−voltage curve recorded for a 100 mM KCl solution in a nanofluidic diode created in a conical polymer nanopore with a junction between zones of opposite surface charge (inset schematic). The device exhibits strong rectification. Adapted from ref 404. Copyright 2007 American Chemical Society.

https://doi.org/10.1021/acs.chemrev.2c00155
Chem. Rev. 2023, 123, 2737−2831

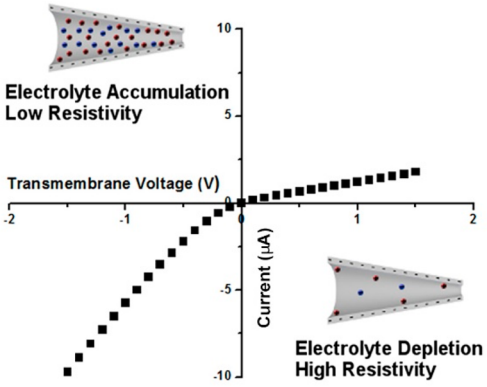

Figure 53. Representative current−voltage curve for an aqueous electrolyte in a membrane with negatively charged, conical nanopores. The rectification arises from the accumulation and depletion regions inside the pore (schematics). Adapted from ref 648. Copyright 2017 Multidisciplinary Digital Publishing Institute under CC BY 4.0 license (https://creativecommons.org/licenses/by/4.0/).

potential, thereby creating nanofluidic field-effect transistors (FETs). Fan et al. created such a device by integrating silica nanotubes with two microfluidic channels and lithographically defined gate electrodes (Figure 54).[649] In analogy to solid-state

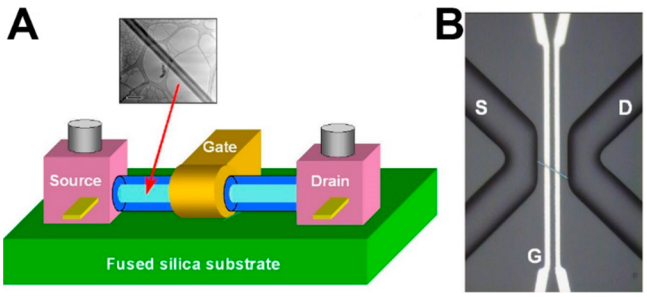

Figure 54. Nanofluidic field-effect transistor. (A) Schematic of a nanofluidic FET based on a silica nanotube with a ∼50 nm diameter. (B) An optical micrograph of the device. S = source, D = drain, and G = gate. Adapted from ref 649. Copyright 2005 American Physical Society.

FETs, the gate voltage in ionic FETs modulates the distribution of electrostatic potential inside the nanotubes, thereby modulating the concentration of charge carriers.

FETs can also be created using nanopores. As an example, Nam et al. used a membrane consisting of a 30 nm TiN metal gate layer sandwiched by two, 20 nm, Si_3N_4 dielectric films.[650] Electron-beam lithography and reactive ion etching enabled the formation of pores of a few tens of nm in diameter in these composite membranes. Atomic-layer deposition of TiO_2 was used subsequently to shrink the pore size with a highly controllable and conformal film (Figure 55). The resultant nanopore transistors had effective diameters below 10 nm, and their conductance was controlled by a gate voltage applied to the TiN layer.

Another approach to nanofluidic FETs takes advantage of asymmetric placement of the gate,[252] resulting in broken electrochemical symmetry and ion-current rectification akin to that observed previously in conical and chemically patterned nanopores.[68] Figure 56 shows a schematic of such an asymmetrically gated nanochannel device schematic, along with its current−voltage characteristics. The amount of rectification in this particular device was small, but observable. Optimization of

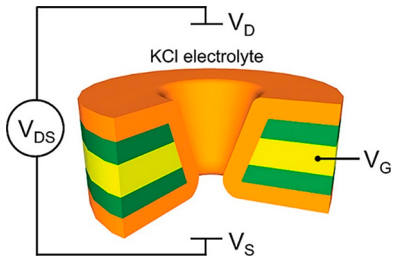

Figure 55. Schematic of a nanoporous, ionic FET. Ion transport through the nanopore is controlled by the dielectric (TiO_2, orange) and the gate electrode (TiN, yellow), which are separated by a dielectric (Si_3N_4, green). Adapted from ref 650. Copyright 2009 American Chemical Society.

the architecture through integration of two independently addressable gates, reduction of the native surface charge by chemical treatment, and reduction of the channel height led to a substantial improvement in rectification properties (Figure 57). This system exhibited ion-current rectification with a fully controllable direction, which cannot be accomplished in solid-state systems.

Another variety of nanofluidic transistor is the ionic equivalent of a semiconductor bipolar junction transistor (BJT).[650] A representative such device consists of a single, hourglass nanopore that contains two ionic diode junctions (Figure 58). The surfaces at the entrances of the pore are positively charged, whereas the middle of the pore is decorated with negatively charged carboxyl groups. The positively charged regions correspond to the emitter and the collector, whereas the negatively charged region corresponds to the gate. If the opening radius of the pore is comparable to the thickness of the EDL, then at both voltage polarities, one of the diode junctions is reversed biased, such that the device is in its closed (nonconductive) state. The conductance state of the device can be controlled chemically by changing the electrolyte concentration or the pH, as both parameters influence the surface potential of the pores, and therefore can be used to determine the extent of the depletion zone. For example, at high electrolyte concentrations, the three charged sections of the pore become less ion selective, and larger currents are observed, in analogy to the saturation of transistors.

Recently, a gated version of a nanopore BJT was realized.[652] This device exhibited amplification, but with pore lengths of hundreds of nanometers. A planar version of an ionic BJT has also been demonstrated based on microchannels filled with an ion-selective material.[653]

Following examples in biology and electronics, ionic circuits composed of multiple diodes or transistors have also been created. For instance, an ionic, full-wave rectifier was fabricated by combining four ionic diodes based on biological channels.[654] Ionic logic gates and amplifiers have also been constructed by combining ionic diodes and transistors.[652,655,656]

5.1.4. Graphene Capillaries. As discussed in section 2.2.1, within the past few years, it has become possible to use 2D materials as atomically flat and atomically precise spacers for nanofluidic systems.[76] The application of 2D materials is an elegant solution to surface-roughness issues and fabrication limitations. Figure 59A−C shows a representative device, in which a sheet of graphene is used as an atomically precise spacer, the thickness of which is determined by the number of layers of graphene. The graphene then is track-etched to create channels,

https://doi.org/10.1021/acs.chemrev.2c00155
Chem. Rev. 2023, 123, 2737−2831

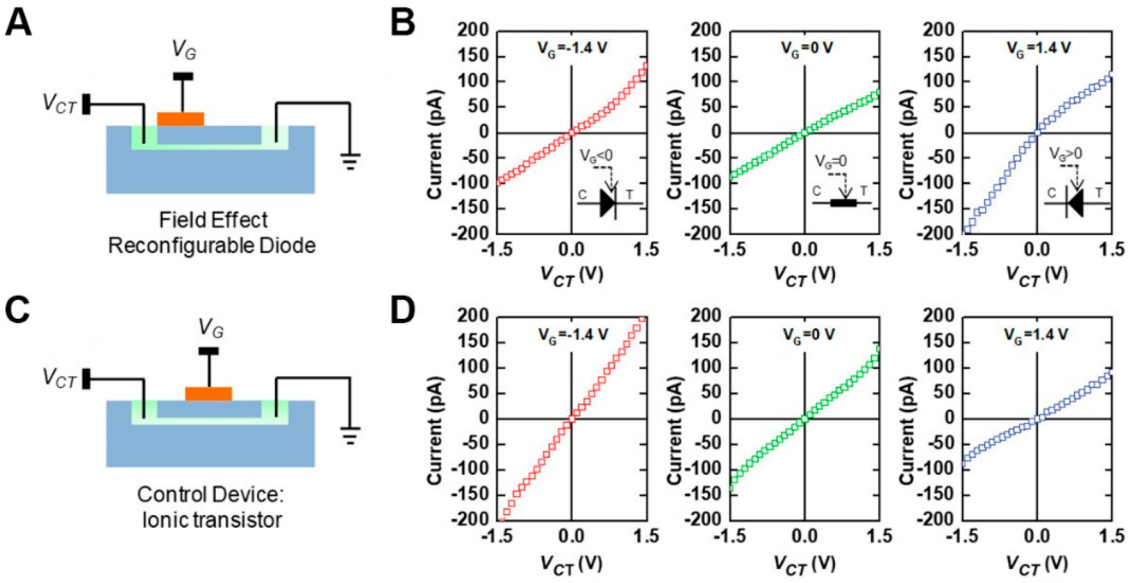

Figure 56. Current−voltage curves for a nanofluidic FET with an asymmetric gate. (A) Schematic of the FET device. (B) Current−voltage curves for devices composed of 11, 2-μm-wide channels that are 100 μm long and 20 nm high, using a 100 μM KCl solution and gate voltages as indicated. The data display a dependence on the gate voltage. The inset electronic diagrams show schematically that the forward direction is switched by transitioning from a positive gate voltage to a negative gate voltage. (C) Schematic of the control device, an ionic transistor. (D) Current−voltage curves for the control device using a 100 μM KCl solution. In this case, the gate voltage modulates the conductance, but no rectification is observed. Adapted from ref 252. Copyright 2011 Springer Nature.

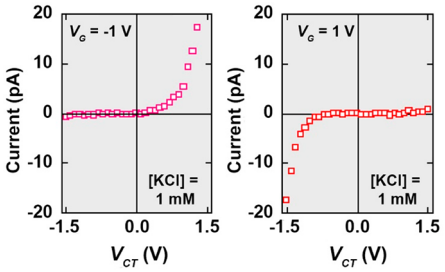

Figure 57. Rectification performance of the nanofluidic FET in Figure 56. The rectification ratios for such devices approach 100.

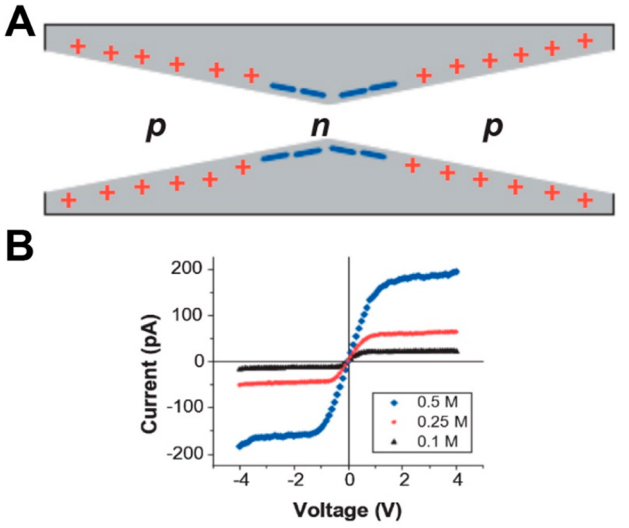

Figure 58. Nanofluidic bipolar junction transistor. (A) Schematic diagram of a nanofluidic BJT composed of an hourglass-shaped pore with negative surface charge in the narrowest region and positive surface charges in the remainder of the pore. (B) Current−voltage curves for such a device recorded at different bulk KCl concentrations. Adapted from ref 651. Copyright 2008 John Wiley & Sons.

which are cladded above and below with graphite to form capillaries.

When such a capillary is only a few layers of graphene high, the ion transport behavior differs from that of the bulk solution. The mobility of ions in capillaries of these dimensions decreases drastically, and this effect is more pronounced for larger ions. Figure 59D shows cation and anion mobility for a number of metal chlorides in the bulk and in a graphene capillary. The cation mobility in the bulk varies by a factor of ∼2. However, in confinement, the cation mobility varies by more than an order of magnitude, and decreases monotonically with the bulk hydrated diameter. This trend is a manifestation of the distortion of the cation hydration shells, which becomes progressively more energetically costly as the hydration diameter increases. The mobility of the chloride ions is ∼3 times smaller in confinement than in the bulk, regardless of cation identity, due to the interactions of these anions with the graphene. When the spacer is a single layer of graphene, total steric exclusion is observed for all cations other than protons.[17] Given the ability to tailor capillary height with sub-nm precision using different 2D materials with chip-level fabrication, this approach holds great promise for new applications of nanofluidics.

5.2. Transport in CNTs

As discussed above, CNTs are a well-defined 1D system for studying nanofluidic transport. There are two key prerequisites for studying transport through CNTs. The first prerequisite is being able to open the nanotubes, because most synthetic routes yield closed CNTs.[658−661] Strategies for opening CNTs have been pursued since the earliest days of research on these materials. The second prerequisite is being able to fill the CNTs. This issue is more subtle, as whether or not a CNT fills spontaneously depends on factors such as the CNT diameter

https://doi.org/10.1021/acs.chemrev.2c00155
Chem. Rev. 2023, 123, 2737−2831

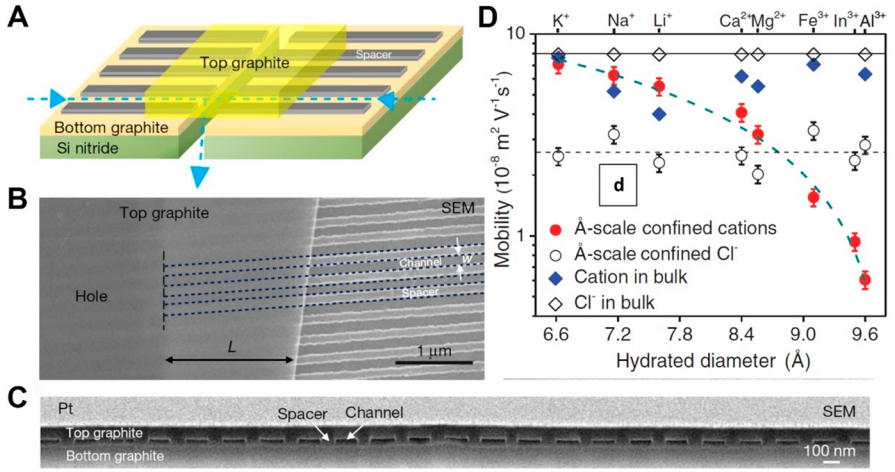

Figure 59. Graphene capillary devices. (A) Schematic of devices composed of a track-etched graphene spacer sandwiched between graphite layers, all on a SiN substrate. (B) (top view) SEM image of a representative device. The spacers are clearly seen in the area not covered by the top graphite, and can also be discerned underneath, running all the way to the trench etched in the bottom graphite. Three of the spacers are indicated by dotted lines, and the edge of the trench is denoted by the dashed line. (C) SEM image of a cross-section of another device, showing an array of capillaries with a height of ∼15 nm. Adapted from ref 76. Copyright 2016 Springer Nature. (D) Comparison of cation mobility for metal chloride solutions in the bulk and in a graphite nanochannel, as a function of the cation hydration radius. The anion mobility is lower in confinement than in the bulk, but does not depend on the cation identity. Adapted from ref 657. Copyright 2017 American Association for the Advancement of Science.

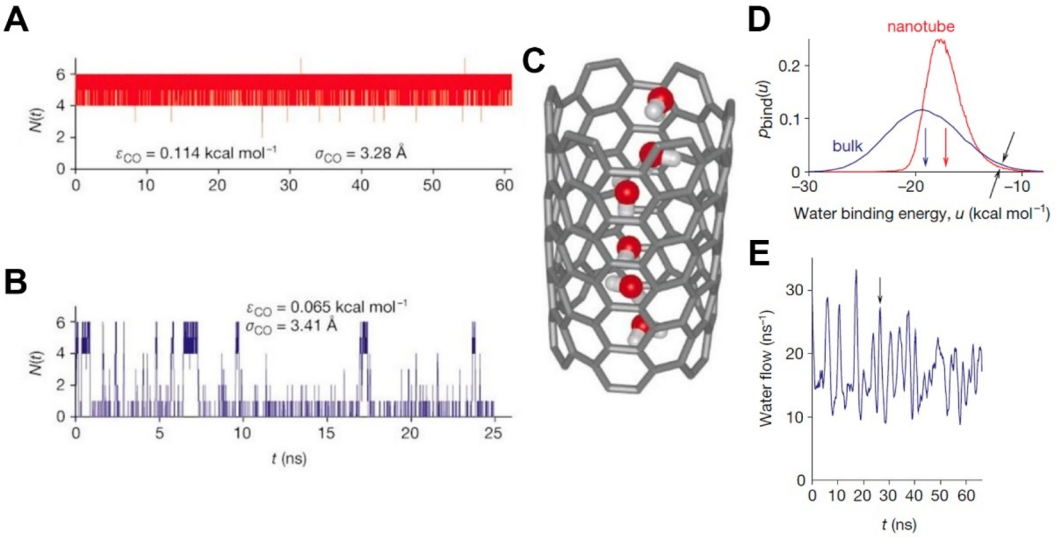

Figure 60. MD simulations of water filling a CNT. The number of water molecules inside the CNT as a function of time is plotted for (A) sp^2 carbon parameters and (B) reduced carbon/water attractions. (C) The structure of the hydrogen-bonded water chain inside the nanotube. (D) The probability distribution of binding energies for bulk water (blue) and water inside a 0.81 nm diameter CNT (red). The vertical arrows indicate the average binding energies, and the tilted black arrows indicate the region in which weakly bound states are more populated in bulk water. (E) The number of water molecules leaving the nanotube at time *t* that entered the nanotube from the other side. Adapted from ref 87. Copyright 2001 Springer Nature.

and the type of molecules to be inserted. CNTs were suggested to act as "molecular straws," capable of uptake of molecules from the liquid or gas phases.[662] Indeed, early studies reported evidence for the capillary filling of CNTs with liquid metals[658,660] and molten inorganic compounds.[663] The propensity of CNTs to fill via capillary action was analyzed in terms of wetting. Based on this analysis, fluids with a surface tension greater than ∼200 mN/m would not fill nanotubes.[664] Although the surface tension of water (72 mN/m) is below this limit, the CNT interior was widely assumed to be hydrophobic, and thus capillary filling with this important liquid was deemed unlikely. Meanwhile, studies provided evidence for the filling of CNTs by adsorption of various gases,[665,666] sparking a number of theoretical and computational studies.[667,668]

It was in this context that Hummer et al. conducted their seminal MD simulations of water confined in a CNT,[87] as was mentioned above. They simulated water in a CNT with a 0.81-nm diameter (Figure 60), and observed spontaneous and continuous filling. They also found the water conduction rate through the CNT to be on the order of 10 billion molecules per second, which is comparable to the rate in aquaporin-1 (AQP1). The water molecules in the CNT form a single-file chain (Figure 60C), with an average of ∼2 hydrogen bonds per molecule, in contrast to the ∼4 hydrogen bonds in bulk water. The hydrogen bonds in confinement were found to be longer-lived and more

https://doi.org/10.1021/acs.chemrev.2c00155
Chem. Rev. 2023, 123, 2737−2831

oriented than those in bulk water, with the OH bonds nearly aligned with the CNT axis. The strong hydrogen bonds were also found to result in burst-like conduction through the CNT (Figure 60E), via the correlated translocation of an uninterrupted water chain through the CNT within short segments of time. During each burst, water transport faces little resistance from interaction with the smooth CNT wall.

In the same year that Hummer's simulations were published, Gogotsi et al. reported an in situ TEM study that showed wetting with an aqueous substance, which mainly consisted of water, inside CNTs with larger diameters (Figure 61).[669] Their observations suggested the interior of a CNT is indeed less hydrophobic than was initially anticipated, much in line with the contact angle of water on graphite.[532] However, a more nuanced picture of the filling of CNTs with diameters in the SDN range has been proposed in which the dominant driving force varies with diameter.[79] It is now clear that CNTs can in fact spontaneously fill with a large variety of fluids,[82,290] setting the stage for studying the transport of numerous different species through CNTs.

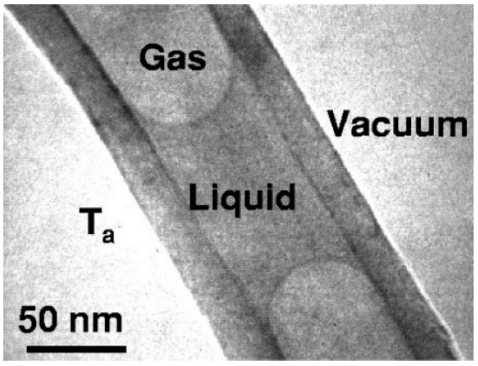

Figure 61. Liquid entrapped in a CNT. This TEM image shows liquid entrapment within a multiwalled carbon nanotube. Adapted from ref 669. Copyright 2001 American Institute of Physics.

Since the earliest experiments on mass transport through CNTs,[670] a number of different experimental platforms have been developed to probe this phenomenon. Membranes with aligned CNTs enabled the first studies that demonstrated enhanced mass flux through SDN-diameter CNTs.[2,73] These studies reported water-flow rates that were orders of magnitude larger than expected from continuum hydrodynamics (assuming Hagen–Poisseuille flow), with extracted flow velocities on the order of cm/s.[73] The enhanced mass flux was attributed to finite slip at the CNT wall, as opposed to the more common no-slip boundary condition. In other words, water molecules in the vicinity of the CNT wall are not at rest, but instead have finite velocities. The slip length is defined as the distance beyond the pore wall at which the extrapolated fluid velocity profile would come to zero, and is found to be orders of magnitude larger than the CNT diameter.[2,73] This phenomenological description, however, obscures the microscopic source of the flow enhancement, which is the low friction between the liquid and the smooth CNT wall. Flow enhancement is therefore better described using a modified friction coefficient. The wall smoothness is also believed to be responsible for observed gas flow rates in excess of Knudsen diffusion,[2] as specular collisions of molecules with the CNT wall take on increased importance. The enhanced selectivity observed in mixed-gas permeation over single-gas permeation is taken to provide independent evidence for non-Knudsen gas transport through CNT membranes.[671] Electrolyte permeation through CNTs has also been studied,[19] and cation-selective transport has been demonstrated.[13,672] Platforms for the study of transport through individual CNTs have also been developed.[18,463]

The main platforms currently being used to study transport in CNTs are summarized in Figure 62, and consist of the above-mentioned CNT membranes, arrays of ultralong CNTs, CNT porins (short CNT segments embedded in lipid-bilayer membranes), and CNT nanocapillaries. There are some key differences among these different platforms, as summarized in Table 1. In studies using any of these platforms, it is crucial to be

Table 1. Properties of the CNTs in the Major Classes of Platforms Established for Studying Transport of Species

property	CNT membranes	ultralong CNT	CNT porins	CNT nanocapillaries
number of CNTs	$10^{13}/m^2$ to $10^{15}/m^2$	1–5 mm	1–10	1
CNT length	a few μm	1–500 μm	10 nm	0.1–1 μm
CNT diameter	dependent on synthetic route	1–2 nm	sub-nm and above	tens of nm

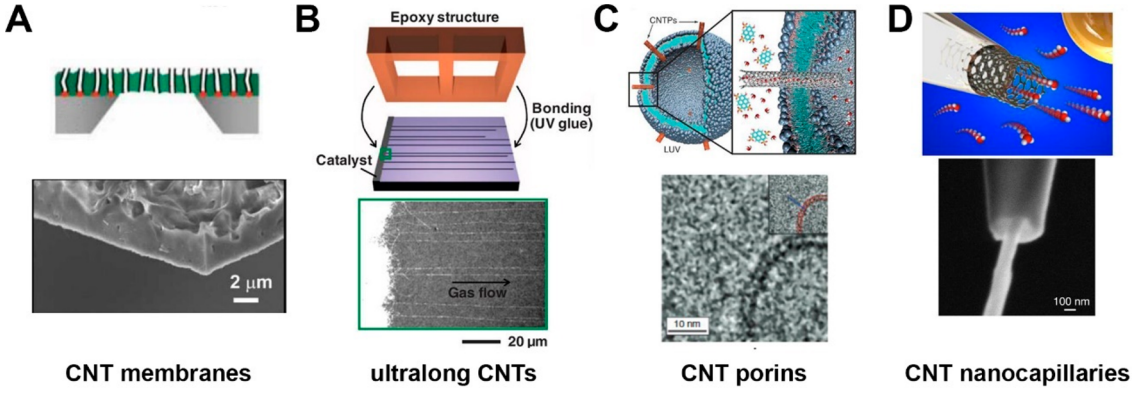

Figure 62. Experimental platforms for transport studies through CNTs. (A) CNT membranes. Adapted from ref 2. Copyright 2006 American Association for the Advancement of Science. (B) Arrays of substrate-bound CNTs. Adapted from ref 13. Copyright 2010 American Association for the Advancement of Science. (C) CNT porins. Adapted from ref 1 (top) and 53 (bottom). Copyright 2006 American Association for the Advancement of Science and 2014 Springer Nature, respectively. (D) Individual CNT nanocapillaries. Adapted from ref 75. Copyright 2016 Springer Nature.

https://doi.org/10.1021/acs.chemrev.2c00155
Chem. Rev. 2023, 123, 2737–2831

able to demonstrate the exclusion of transport through any pathway other than the CNT interior. Unlike pores drilled into impermeable, solid-state membranes,[673] it is challenging to create leak-proof seals for CNTs and other premade pores in a matrix. It is equally challenging to prove the absence of leaks; evidence for transport solely through the pore interior must be provided, with the measurement of ionic blockade currents being one of the most direct means of demonstration.[13] Additional evidence may arise from molecule−pore, interaction-induced optical signatures.[88] Defining and determining the pore size relevant for transport in these systems is another central, yet often nontrivial, task. As a few examples, size-exclusion assays have been used for CNT membranes,[2,674] vibrational spectroscopy for arrays of ultralong CNTs,[18] purified and precharacterized CNTs as starting materials for CNT porins,[1,15,53,433] and direct electron microscopy for CNT nanocapillaries.[75] Given the difficulty in preventing leaks, the CNT diameter should not be inferred from transport characteristics if the goal is to study transport. Other features that can affect transport include functional groups at the pore mouth and defects in the CNT. The characterization of the role of such features remains an experimental challenge, as does measuring the flux through CNTs at, or near, the level of individual nanotubes.

5.2.1. Aqueous Systems. We next consider water, protons, and ions, species of particular interest for transport through CNTs. As an emerging, common thread, transport characteristics depend on the CNT diameter in a nonmonotonic fashion in the few-nm to sub-nm diameter range, in which the continuum assumption breaks down. In the following, emphasis is placed on the passive transport characteristics of CNTs, but prospects of these materials as active transporters are also highlighted.

Experiments show that water enters open CNTs spontaneously for all diameters greater than or equal to the 0.55 nm diameter of (5,3)-SWCNTs.[295] Thus, water transport in all CNTs with diameters larger than the threshold set by the physical size of a water molecule seems possible. Due to confinement effects, the water transport characteristics vary with CNT diameter. Below a critical diameter of $d_{crit,sf} \approx 1$ nm, water molecules inside a CNT form a single file. Above another critical diameter $d_{crit,cont} > d_{crit,sf}$, water starts to behave in a continuum (bulk-like) manner. As d increases from the single-file limit toward the continuum limit, a sequence of distinct water ordering configurations is observed that is characterized by substantial radial density variations. The single-file ordering develops into a shell, and then into a shell with an interior file, and then into two concentric shells, and so on.[675] The larger the diameter, the more these variations blur, and the more that water (away from the pore wall) assumes its bulk ordering. Therefore, monotonic trends in water transport properties are expected for $d \geq d_{crit,cont}$, and nonmonotonic trends are expected for $d < d_{crit,cont}$. Although there is no consensus as of yet regarding the value of $d_{crit,cont}$, this diameter is likely a few times the size of a water molecule. A value of 1.39 nm has been proposed for $d_{crit,cont}$.[676]

Water transport in CNTs has been the subject of extensive experimental investigations,[1,2,73−75,677−686] most of which involved CNT membranes.[2,73,678−680,682−686] These studies investigated water flow through CNTs that were subjected to an axial pressure gradient. A common finding in such studies is that the measured water flow rates are higher than classical hydrodynamic estimates. The water flow enhancement, which is given by

$$E = Q_{measured}/Q_{no\text{-}slip} \tag{20}$$

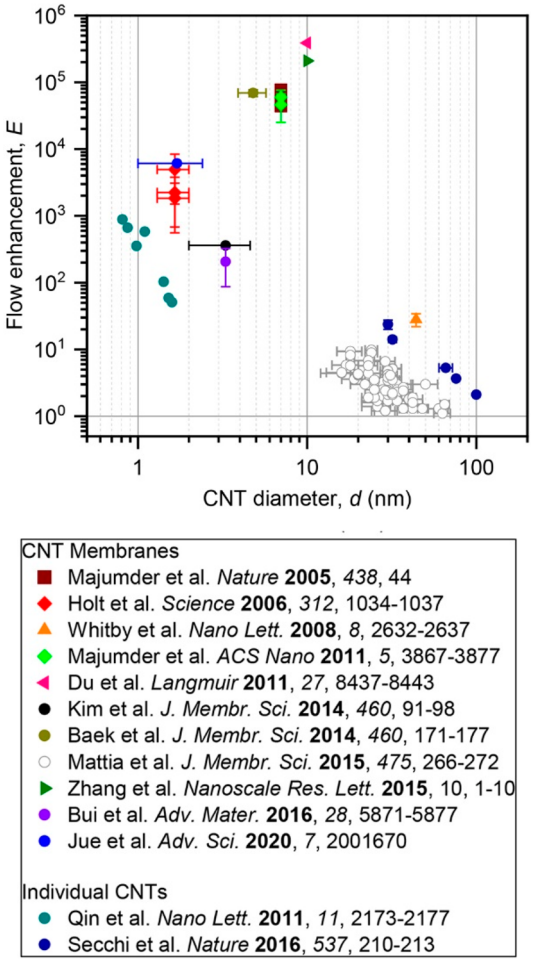

Figure 63. Flow enhancement in CNTs. Experimentally determined values for the water-flow enhancement with respect to Hagen−Poiseuille estimates.

is particularly large for CNTs with $d \leq 10$ nm, for which reported values exceed 10 000 (Figure 63).[73,679,684−686] Here, $Q_{measured}$ is the observed volumetric flow rate,

$$Q_{no\text{-}slip} = \frac{\pi R^4}{8\eta}\frac{\partial P}{\partial z} \tag{21}$$

is the volumetric flow rate estimated from the Hagen−Poiseuille equation with a no-slip boundary condition, R is the radius of the CNT, here defined from the tube center to the first carbon shell (different definitions have been used in the literature), and η is the fluid viscosity.

As discussed above, the flow enhancement has largely been attributed to reduced fluid friction at the CNT wall, which causes water molecules adjacent to the wall to acquire a finite axial velocity. A finite slip length, L_s, which is a measure of the virtual distance beyond the CNT wall at which the axial flow velocity reaches zero (Figure 64A), can be defined approximately as

https://doi.org/10.1021/acs.chemrev.2c00155
Chem. Rev. 2023, 123, 2737−2831

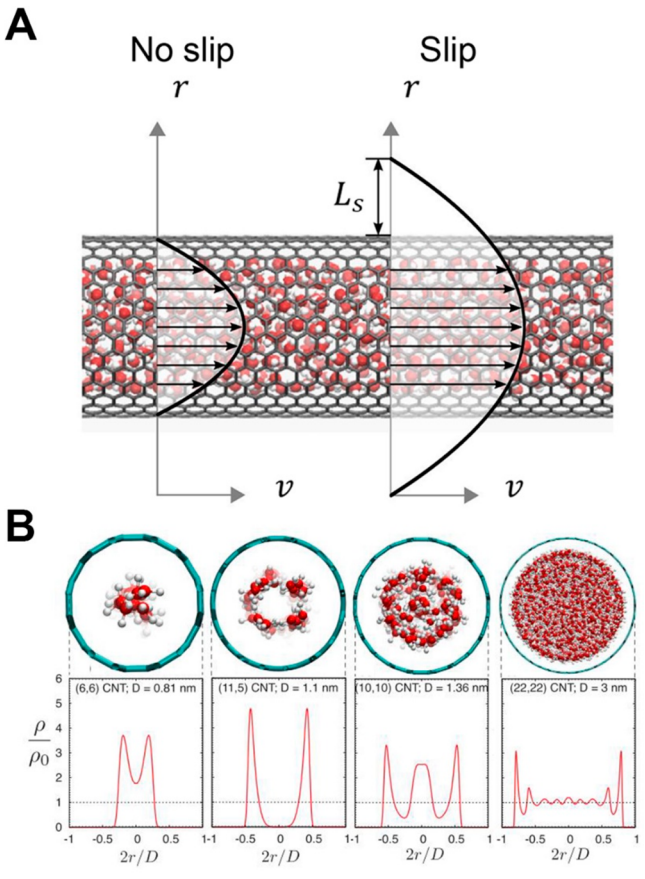

Figure 64. Water transport through CNTs. (A) Radial velocity profiles for Hagen−Poiseuille flow with no-slip (left) and slip (right) boundary conditions. (B) MD simulation results for water confined in CNTs of different diameters. The upper row shows cross sections of representative configurations, and the lower row shows radial density profiles. Here, ρ_o is the bulk density and D is the nearest-neighbor carbon-to-carbon distance. Adapted from ref 675. Copyright 2018 Elsevier.

$$L_s = \frac{v(r)}{dv/dr}\Big|_{r=R} \tag{22}$$

Here, the radial velocity profile is

$$v(r) = \frac{R^2}{4\mu}\left(1 - \frac{r^2}{R^2} + \frac{2L_s}{R}\right)\frac{\partial P}{\partial z} \tag{23}$$

Interestingly, the observed variations in the flow-enhancement factor E cannot be explained using a unique value of L_s. E is small in CNTs with large diameters and large in CNTs with small diameters (Figure 63). Reported values of L_s follow a similar trend, ranging from 17 nm for a 100-nm-diameter CNT[75] (which is comparable to the value of 30 nm reported for water slip on graphene[687]) to 53300 ± 14500 nm for a membrane composed of 7-nm-diameter CNTs.[688] The phenomenological slip-flow picture does not explain this diameter dependence of L_s, or why similar flow enhancements are not observed in boron nitride nanotubes.[75] This simple model also does not take into account the effect that confinement has on the properties of water.

Theoretical efforts have contributed to a more nuanced, microscopic description of water transport in CNTs. Although a relatively consistent picture has emerged, models so far have failed to reproduce some aspects of the available experimental data, and in particular the large flow enhancements reported for membranes composed of CNTs with diameters in the 4−10 nm range (Figure 63). Water inside CNTs displays radial density variations that are particularly pronounced in proximity to the CNT wall, and that depend on the CNT diameter (Figure 64).[506,507,687,689] The carbon−oxygen and oxygen−oxygen van der Waals interactions are believed to be responsible for this layering.[687] Water molecules adjacent to the wall form a lesser number of hydrogen bonds than do the other confined water molecules. The orientation and organization of water molecules near the wall are dictated by a potential landscape that depends on the CNT curvature and the sp^2 carbon lattice. For CNTs with large diameters, the water organization near the wall mimics the structure of the carbon honeycomb lattice.[507,687] For the smallest CNT diameters, the water organization is not correlated with the carbon lattice, because the curvature of the CNT smoothes the potential experienced by the confined water.[687,690] On the other hand, the relative orientations of water molecules are largely bulk-like in CNTs with large diameters, but are more strongly correlated in CNTs with small diameters. For CNTs with the smallest diameters, in which water takes on a single-file organization, water transport can be viewed as a collective, highly concerted ballistic motion that is mediated by long-lasting hydrogen bonds.[87,691−694]

Pressure-driven water flow in CNTs has been studied with MD simulations. The results of such simulations depend on factors such as the water model used, and so far systematic agreement between simulations and the available experimental data has not been achieved (as can be seen from a comparison of Figures 63 and 65A). Nevertheless, MD studies of pressure-driven water flow in CNTs have reached some notable conclusions. For example, the work of Thomas and McGaughey[676,687] suggests that there is a continuum-to-subcontinuum transition for water flow in CNTs at $d_{crit,cont}$ = 1.39 nm. For CNTs with $d > d_{crit,cont}$, they find continuum hydrodynamics to describe the simulated flow rates well if both the slip length and the viscosity are dependent on the diameter.[676,687] In this limit, the flow enhancement factor is expressed as[687]

$$E = (1 + 8L_s(d)/d)\eta_{bulk}/\eta(d) \tag{24}$$

where η_{bulk} is the viscosity of bulk water. As the diameter increases, $\mu(d)$ increases and $L_s(d)$ decreases, the latter following the empirical relation

$$L_s(d) = L_{s,\infty} + c/d^3 \tag{25}$$

where $L_{s,\infty} \approx 30$ nm is the slip length of water on a flat graphene surface and c is a fitting parameter.[687] Based on these equations, E is expected to decrease monotonically as d increases, as seen in Figure 65A. Such a trend has indeed been observed in measurements on individual CNTs with $d \geq 30$ nm (dark-blue data points in Figure 63).[75]

In CNTs with $d < d_{crit,cont}$, the confinement-induced structuring of water becomes important, and a continuum description is not possible.[676] Thomas and McGaughey observed a nonmonotonic dependence of E on the CNT diameter in this regime. The largest values of E were observed for the smallest CNT diameters (Figure 65A), despite the fact that the water permeability depended monotonically on d in the same regime.[676] So far, there is only one experimental study on a number of individual CNTs with $d < 2$ nm, in which a nonmonotonic trend in $E(d)$ has been observed (data points from Qin et. al in Figure 65A).[74]

https://doi.org/10.1021/acs.chemrev.2c00155
Chem. Rev. 2023, 123, 2737−2831

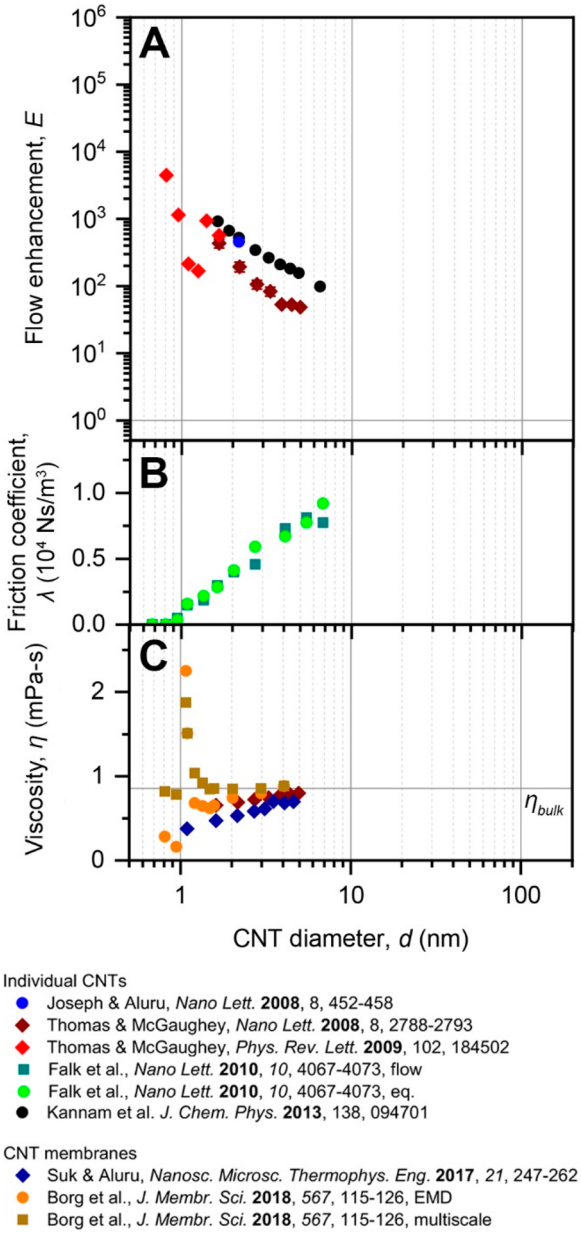

Figure 65. The dependence of key water-flow parameters on CNT diameter, based on MD simulations. (A) The flow-enhancement factor E, (B) the friction coefficient λ, and (C) the viscosity η. The data points are from MD simulations and theoretical work.

The breakdown of continuum hydrodynamics motivates an analysis in terms of the friction coefficient λ, rather than the slip length.[690] The two quantities are related via the viscosity:

$$L_s = \eta/\lambda \tag{26}$$

However, when $L_s \gg d$, the hydrodynamic permeability κ is dominated by surface effects, such that

$$\kappa = \pi d^3/16\lambda, \tag{27}$$

the friction coefficient is the physically more relevant parameter.[690] In analogy to the case made above for the slip length, λ varies with CNT curvature. The friction coefficient decreases with decreasing diameter, and is even predicted to vanish for $d < 0.8$ nm, in a phenomenon known as superlubricity (Figure 65B).[690] The curvature dependence of λ has been attributed mainly to a weakening of the water−carbon interaction as d decreases, due to an increasingly incommensurate water−carbon structure.[690] The exact origin and character of superlubricity, however, remains to be understood better.

The pressure drops at the inlet and outlet of a CNT also impart a length dependence on E. These entrance and exit losses dominate E in CNTs with lengths in the submicrometer range, but are negligible in long CNTs.[77,675,695−698] Within a continuum hydrodynamics picture, the total pressure drop can be written as[675,697,699]

$$\Delta P = 8\eta CQ/r^3 + 8\eta LQ/\pi(r^4 + 4r^3L_s) \tag{28}$$

where the first term on the right is the pressure drop due to entrance and exit losses, the second term is the pressure drop for Hagen−Poiseuille flow, r is the pore radius, and C is the loss coefficient. Equation 28 has been evaluated for 2-nm-diameter CNTs with lengths up to 2 μm, based on intensive MD simulations[697] To reduce computational cost, multiscale approaches are being explored[675] that combine MD simulations in characteristic domains (the central region of a CNT and the entrance and exit regions) with a continuum flow-resistance model to compute volumetric flow rates through laboratory-scale membranes (Figure 66A,B). Such hybrid modeling tools are valuable, particularly given that CNT membranes with areas of 60 cm^2 have now been demonstrated.[682]

It is worth noting that Hagen−Poiseuille theory can be extended by taking into account the diameter- and length-dependence of all relevant hydrodynamic properties. In an ideal extended Hagen−Poiseuille theory, there would be no enhancement factor. Heiranian and Aluru proposed such an extension, and derived the following expression for the volumetric flow rate through a CNT:[77]

$$Q = (\partial P/\partial z)\cdot\pi(r^4 + 4r^3\eta(L, r)/\lambda(L, r))/8\eta(L, r)L_{\mathrm{Dagan}} \tag{29}$$

where $L_{\mathrm{Dagan}} = L + 3\pi r/8$ characterizes the effective hydrodynamic pressure drop length.[700] Analytical expressions for the size-dependent viscosity $\eta(L,r)$ and friction coefficient $\lambda(L,r)$ have been derived,[77] each containing separate contributions from the end regions and from the bulk region of a CNT. The extended Hagen−Poiseuille theory has been gauged against MD simulations paired with Green−Kubo relations to evaluate both $\eta(L,r)$ and $\lambda(L,r)$, achieving promising agreement with a subset of data from experiments and simulations (Figure 66C).[77] The sub-nm diameter regime, however, in which single-file water transport is achieved, remains beyond the scope of this theory.

Two promising experimental routes to studying the single-file transport regime have emerged. The first approach uses individual, substrate-bound CNTs.[74] In the second approach, 10-nm-long CNT segments that are based on single-chirality-enriched CNT powders with narrow diameter distributions are embedded in lipid-bilayer membranes or vesicles to create CNT porins (Figure 67).[1,53,286] Osmotic-pressure-driven water transport through CNT porins has been studied as a function of temperature and pH, as well as in the presence of cosolvents. CNT porins with a diameter of ∼0.8 nm were found to outperform the water permeability of AQP1. Going from pH = 7.8 to pH = 3 increased permeation rates by almost an order of magnitude (Figure 67B). This phenomenon has been attributed to the protonation of the carboxyl groups that are presumed to decorate the CNT pore mouths,[1] and highlights the importance of steric and electrostatic interactions between the permeate and

https://doi.org/10.1021/acs.chemrev.2c00155
Chem. Rev. 2023, 123, 2737−2831

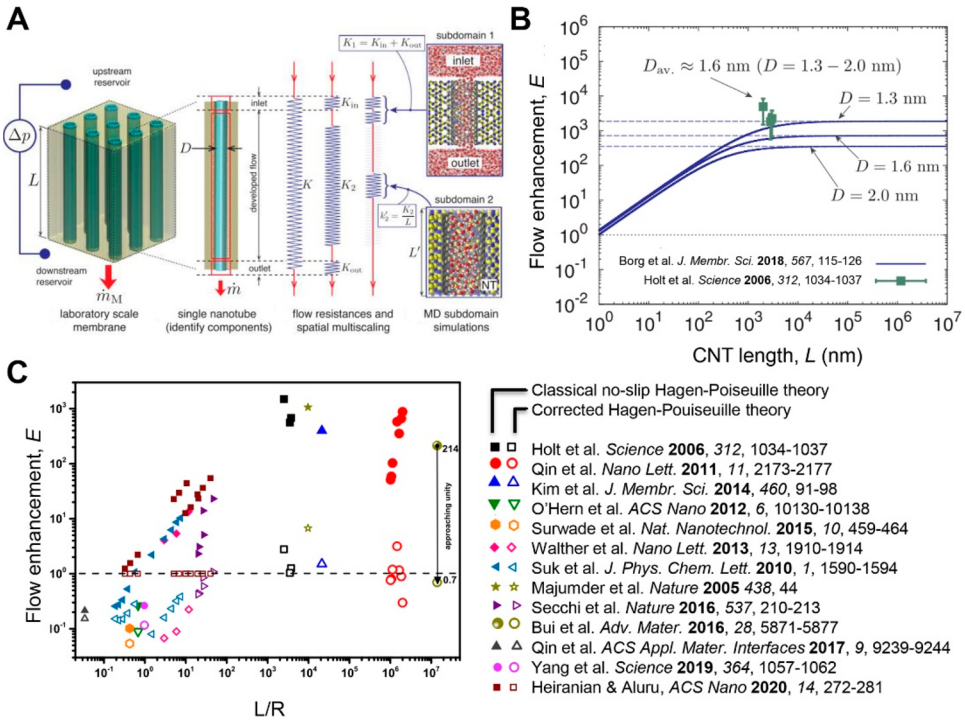

Figure 66. Flow enhancement in CNTs. (A) A multiscale flow model of pressure-driven water transport through CNTs. Adapted from ref 675. Copyright 2018 Elsevier. (B) Length- and diameter-dependent flow enhancement in pressure-driven water transport through CNTs. Adapted from ref 675. Copyright 2018 Elsevier. (C) Enhancement factors derived using the classical, no-slip Hagen−Poiseuille theory (filled symbols) and an extended Hagen−Poiseuille theory (open symbols) for different pore sizes as a function of the length to radius ratio for various experimental and computational permeation coefficients. Adapted from ref 77. Copyright 2020 American Chemical Society.

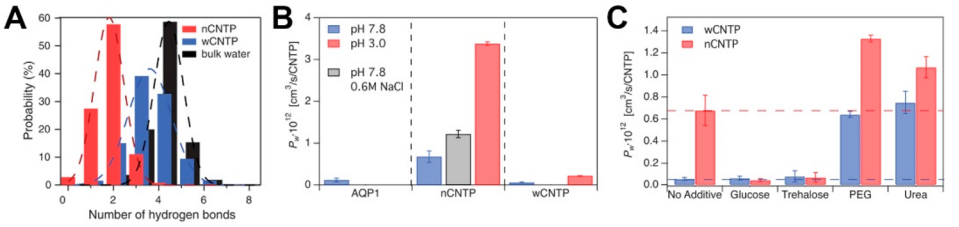

Figure 67. Water transport in CNT porins. (A) Histogram of the average number of hydrogen bonds made by a water molecule in bulk water (black) and in CNT porins with a 0.8 nm diameter (red, denoted nCNTP) and a 1.5 nm diameter (blue, denoted wCNTP), as determined from simulations. The dashed lines are Gaussian fits. (B) Water permeability values measured nCNTPs and wCNTPs at high (blue) and low (red) pH, compared to the water permeability of AQP1 measured at high pH 7.8 and the water permeability of nCNTPs measured at high pH with 0.6 M NaCl, which is chaotropic osmolyte (gray). (C) Water permeability of CNTPs measured at pH 7.8 in the presence of 150 mM concentrations of the chaotropes PEG and urea and the kosmotropes glucose and trehalose. The dashed lines indicate the permeability levels measured without additives. Adapted from ref 1. Copyright 2017 American Association for the Advancement of Science.

functional groups at the CNT entrance and exit, in particular for CNTs with narrow diameters.[612] CNT porins outperform AQP1 in water permeability, albeit at the expense of being less selective against proton transport, because of the reduced interaction between water molecules and the pore walls.[1,701] In AQP1, water molecules can form hydrogen bonds with the pore-lining residues, and undergo a dipole reorientation at the narrowest constriction. In CNT porins, water permeation is limited by only an energy barrier of ∼5.3 kcal/mol that is associated with the transition in the water organization from bulk to single-file.[286] Weakening the hydrogen-bond network in bulk water through the addition of chaotropic cosolvents, such as PEG4 or urea, facilitates the single-file formation, and thus promotes permeability (Figure 67.C). On the other hand, the addition of kosmotropic cosolvents that strengthen the H-bond network, such as glucose or trehalose, decreases the permeability (Figure 67C).[1]

5.2.2. Protons. The analysis of proton transport in CNTs began with three MD studies in 2003,[16,72,692] all of which predicted enhanced proton mobility inside CNTs as compared to the bulk, albeit with caveats. The work of Hummer and co-workers indicated that the diffusion coefficient for protons in a particular CNT is 17 Å^2/ps, as compared to the bulk diffusion constant of 0.4 Å^2/ps, but is sensitive to orientational defects of water in the 1D chain.[16] Zhu and Schulten showed that proton conduction depends on the distribution of charge within the CNT, and is particularly sensitive to charges at the pore mouth that affect the orientation of water molecules as they enter the conduit.[692] Mann and Halls focused on the stabilization of protons in CNTs by formation of an $H_9O_4^+$ complex, which led to a similar prediction of enhanced proton mobility.[72]

https://doi.org/10.1021/acs.chemrev.2c00155
Chem. Rev. 2023, 123, 2737−2831

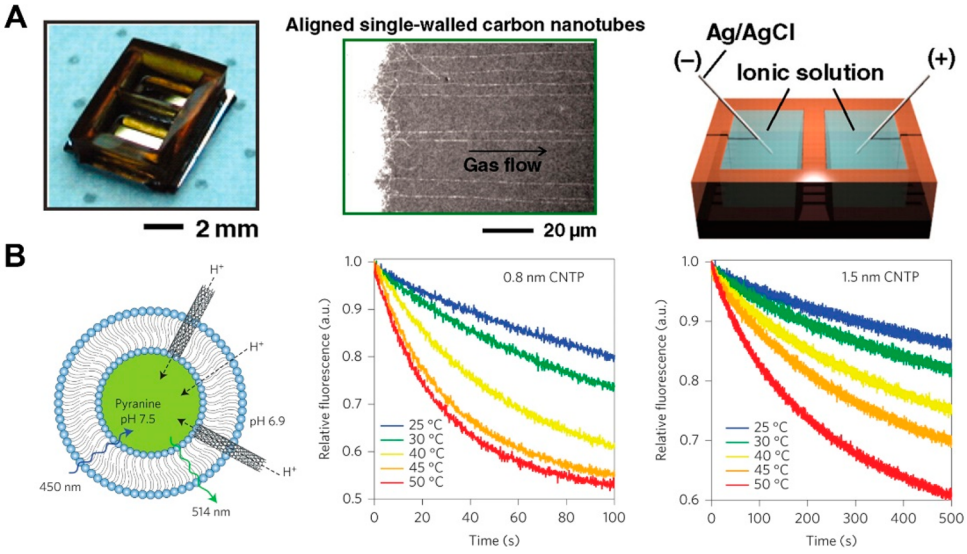

Figure 68. Experimental platforms for measuring proton diffusion inside CNTs. Proton diffusion coefficients or mobilities have been calculated from experiments in (A) isolated, substrate-bound CNTs, as adapted from ref 13. Copyright 2010 American Association for the Advancement of Science, and (B) CNT porins. Adapted from ref 15. Copyright 2016 Springer Nature.

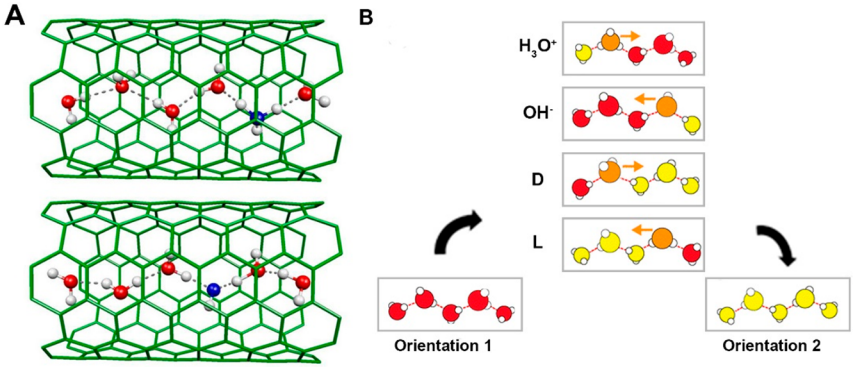

Figure 69. Mechanisms of proton transport in single-file water in CNTs. (A) MD simulation snapshots showing the translocation of a hydronium ion and a D defect through a (6,6)-SWCNT. Adapted from ref 707. Copyright 2012 American Chemical Society. (B) Schematic illustration of how translocation of a proton, a hydroxide, or a hydrogen-bonding defect changes the orientation of the hydrogen bond network in single-file water. The transport of a full proton charge requires both translocation of an ion and subsequent translocation of a D defect or an L defect. Adapted from ref 702. Copyright 2011 Royal Society of Chemistry.

These pioneering studies established several important and interrelated characteristics that have been the focus of subsequent studies of proton transport in CNTs (Figure 68). The enhanced mobility of protons inside CNTs has been a consistent theme of recent work, with an emphasis on the degree of enhancement and the dependence of this enhancement on the CNT diameter. Proton diffusion is an order of magnitude faster than water diffusion inside single-file systems.[702] Strano and co-workers provided some of the first experimental evidence for high proton mobility inside a CNT.[13,18] Experiments were performed on a system consisting of ultralong, substrate-bound CNTs that were etched and bonded to connect two fluid reservoirs (Figure 68A). Electrical measurements on this system revealed stochastic switching between high- and low-conductance states.[13,18] In CNT systems with water and electrolytes (NaCl, LiCl, and KCl), it was shown that protons were the majority charge carriers, whereas the cation identity affected the duration and conductance decrease during pore-blocking events.[13,18] The proton conductivity was estimated to be 500 S/cm, which corresponds to an ion mobility 100 times higher than that of bulk water.[13] Further experimental evidence for enhanced proton mobility came from experiments on CNT porins (Figure 68B),[15] in which proton conductance was again reduced by the addition of a larger cation, which in this case was Ca^{2+}. Enhancement of proton mobility was observed in CNT porins with an 0.8 nm diameter, but not in ones with a 1.5 nm diameter. This observation suggests that nanoscale confinement is necessary, but not sufficient, to enhance the proton flux. It is likely that single-file water chains are another required element for this enhancement.[15]

In CNTs with small diameters, proton diffusion is faster than water diffusion, due to Grotthuss-type transport. In the simplest form of the Grotthuss mechanism, proton hopping is a series of transfers among adjacent hydronium ions.[703] An area of contention is whether larger cationic clusters, including the Zundel cation ($H_5O_2^+$),[704] the Eigen cation ($H_7O_3^+$),[704] and the so-called linear $H_7O_3^+$ cation,[705] play different roles in proton transport through CNTs than in bulk water. One proposal is that proton transfer in CNTs occurs a Zundel−Zundel mechanism, rather than the Eigen−Zundel−Eigen mechanism common to bulk systems.[704] Others have suggested that there is continuous interconversion among the discrete cation structures,[705] in

https://doi.org/10.1021/acs.chemrev.2c00155
Chem. Rev. 2023, 123, 2737−2831

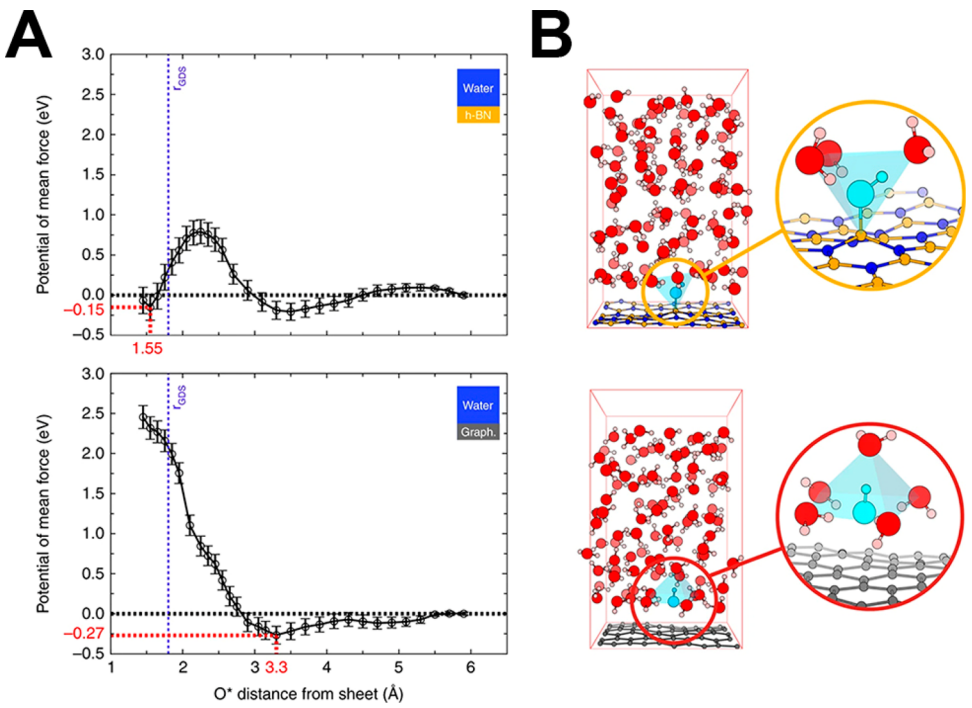

Figure 70. FPMD simulations of hydroxide adsorption at the water−hBN and water−graphene interfaces. (A) Free-energy profiles and stable configurations. Potentials of mean force of an aqueous hydroxide on BN and graphene sheets. (B) Representative configurations of the ions at the corresponding interfaces. Adapted from ref 713. Copyright 2019 Springer Nature.

essence making protons in 1D confinement act as fluxional defects, as has also been proposed to be the case for bulk water.[706] In CNTs filled with single-file water, proton transport involves the translocation of both ionic defects (hydronium and hydroxide ions) and hydrogen-bonding defects,[702] as shown in Figure 69.

Favorable alignment of water molecules within a quasi-1D chain enables enhanced proton flux. Proton transport depends not only on the overall geometry, but also on the configuration of hydrogen bonds. Proton translocation from one side of a CNT to the other is linked to reorientation of the water chain, such that 60% of the charge transfer is achieved by movement of the proton, and the other 40% arises from reorientation of the water chain back to its original state.[702] A neutral water molecule in a 1D chain generally donates one hydrogen bond and accepts one hydrogen bond.[692] In a Bjerrum defect, a neutral water molecule either donates two hydrogen bonds and accepts zero (which is known as an L defect), or accepts two hydrogen bonds and donates zero (which is known as a D defect). Bjerrum defects diffuse in the 1D chain a factor of 3 to five times more slowly than do protons, thereby reducing the proton mobility.[16] L defects are more common inside CNTs with single-file water than are D defects, because the water orientation is dictated by CNT entrance effects.[708]

Surface and mouth charges create energetic barriers for the entrance, translocation, and exit of protons from a CNT. The importance of such electrostatic interactions was demonstrated in early MD work.[692] The diffusion coefficient for protons in an uncharged, 13.4-Å-long CNT, for instance, was found to be more than twice as fast as that in a CNT with +0.25*e* charges on each end and a −0.5*e* charge in the middle.[692]

Although it is clear that enhanced proton transport requires the existence of quasi-1D water chains, and therefore only occurs in a CNT diameter range between 0.6 and 0.9 nm, the influence of the diameter within this range, not to mention that of the CNT length, remains largely unexplored. The proton diffusion coefficient in short CNTs is generally larger than that in longer CNTs.[709,710] In biological channels such as AQP1 (which suppresses proton transport) and gramacydin A (which transports protons quickly), electrostatic effects and Ångstrom-scale pinch points arising from single amino acid residues control water orientation and proton transport. Perhaps one day we will be able to engineer CNTs with this level of precision.

5.2.3. Water Dissociation and Transport. FPMD simulations showed that the dissociation free energy of water decreases by more than 15%, as compared to the bulk, when the liquid is confined between FeS layers.[711] This phenomenon was attributed to the increase in the dielectric constant in confinement. In contrast, Sirkin found that water dissociation is inhibited in (6,6)-SWCNTs.[712] In this case, the higher barrier to dissociation is attributed to the undercoordination of the hydroxide and hydronium ions in the nanotube. These studies indicate that the chemical reactivity of confined liquids is complex, and is not necessarily a monotonic function of pore diameter. Other studies have made important advances in understanding the relationship between water reactivity and transport. For instance, as shown in Figure 70, free-energy calculations indicate that both graphene and hBN can be charged through hydroxide adsorption, but that hydroxide chemisorption is stronger on hBN.[713] This observation is consistent with recent nanofluidic experiments that measured a larger negative surface charge on saline solutions in contact with BN, as compared to CNTs and planar graphitic surfaces.[463]

5.2.4. Ion Transport and Ion Selectivity in CNTs. *5.2.4.1. (i) MD Simulations.* Researchers have been interested in ion transport in CNTs since the early days of nanofluidics, because CNT pores mimic the function of biological ion channels,[1,53,714,715] and also because high intrinsic water permeability makes CNTs a promising platform for water-purification applications.[1,2,19] MD simulations have been at the

https://doi.org/10.1021/acs.chemrev.2c00155
Chem. Rev. 2023, 123, 2737−2831

forefront of these efforts. Early MD studies, which largely focused on predicting ion selectivity, provided the first window into the behavior to be expected. These studies established that a significant loss of water molecules in the ion-hydration shell (Figure 71A), as is required for permeation of ions through

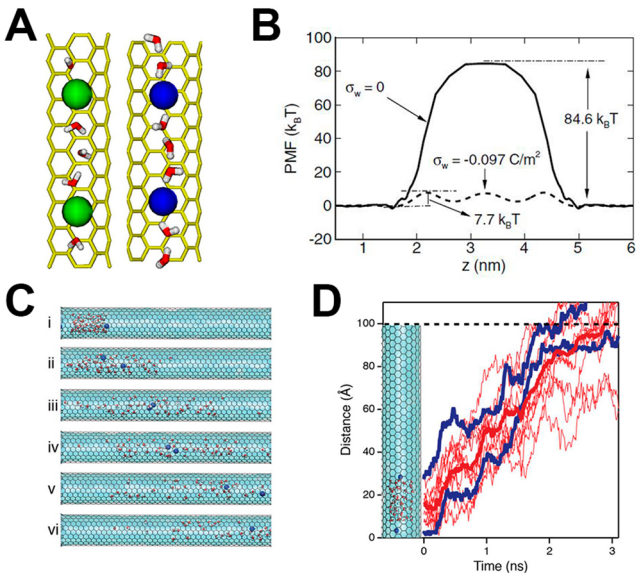

Figure 71. MD simulations of ion transport in CNTs. (A) Snapshots from simulations of (left) water and K^+ in a 0.7-nm-diameter CNT and (right) water and Cl^- in a 0.8-nm-diameter CNT. Adapted from ref 720. Copyright 2006 IOP Publishing. (B) Comparison of the energy-barrier profiles (i.e., the potential of mean force as a function of axial position) for a K^+ ion in a neutral (solid line) and a negatively charged (dashed line), 0.7-nm-diameter, 2.214-nm-long CNT. The energy barrier for K^+ transport through neutral CNTs is high, due to the partial dehydration required to enter the pore. The presence of charge along the CNT can compensate for this energetic penalty. Adapted from ref 720. Copyright 2006 IOP Publishing. (C) Sequential snapshots from an MD simulation of water and ion transport in 1.5-nm-diameter CNTs under an applied electric field, showing the same water molecules (red) and two K^+ ions (blue) as they move through the CNT from left to right. The interval between adjacent frames is 0.5 ns. Adapted from ref 464. Copyright 2019 American Chemical Society. (D) Trajectories of the ions (thick blue lines) and water molecules (thin red lines) starting from the configuration in the inset simulation snapshot. The thick red line is the average of the 11 water-molecule trajectories. Adapted from ref 464. Copyright 2019 American Chemical Society.

CNTs with sub-nm diameters, creates a large energy barrier for ion transport (Figure 71B). Peter and Hummer[716] showed that 0.8-nm-diameter CNTs reject Na^+ ions, due to the energetic penalty for stripping off the hydration shell, whereas 1.4-nm-diameter CNTs are highly permeable to these cations. Corry and co-workers reported similar results,[717] and Song and Corry[629] showed that Na^+, K^+, and Cl^- experience different dehydration energy barriers when entering CNTs with sub-nm diameters, resulting in the differential selectivity for these ions. Shao et al.[513] showed that it is energetically favorable to confine hydrated K^+ over Na^+ inside CNTs with diameters below 1.0 nm, but that the situation is reversed inside CNTs with larger diameters. Li et al.[718] predicted high K^+ selectivity over Na^+ for in CNTs with 1.1 nm diameters. This selectivity stems from the amplification of small hydration differences between the ions in the highly confined channels of CNTs.

MD simulations have also been used to explore the role that the functional groups at the ends of CNT pores play in mitigating the dehydration barriers for ion transport (Figure 71B). Aluru and co-workers showed that charges at the mouths[719] or along the walls[720] of CNTs with sub-nm diameters promote the preferential transport of counterions and significant exclusion of co-ions. Simulations by Corry[612] showed that the addition of charged groups to the entrance of a 1.1-nm-diameter CNT helps, to different degrees, to prevent the passage of Na^+ and Cl^-. Gong et al.[721] demonstrated that modified patterns of carbonyl groups along the CNT walls can further tune the hydration structure of ions, leading to controllable Na^+ or K^+ selectivity inside 1.2-nm-diameter CNTs.

MD simulations have also been used to explore ion−water coupling and ion-correlation effects in CNTs. Early MD simulations highlighted how the high slip flow at the CNT wall can lead to the enhanced coupling of ion and water fluxes, including high electroosmotic coupling during electrophoretic ion transport[36,71] and diffusioosmotic coupling during concentration-gradient-driven ion transport.[722] Large electroosmotic flows were reported in simulations by Aluru and co-workers[719,723] of 5.4-nm-diameter CNTs[723] and 2.2-nm-diameter CNTs with charged groups at the pore mouths,[719] as well as by Su et al.[724] in 1.4-nm-diameter CNTs. Yao et al.[464] showed that K^+ transport in 1.5-nm-diameter CNTs is strongly coupled with surface-charge-dependent electroosmotic flow, as shown in Figure 71C,D.

Confinement also induces unusual ion−ion coupling effects. For example, simulations by Nicholson et al.[633] and Liu et al.[725] demonstrated the formation of ion pairs in CNTs with diameters between 1.2 and 4 nm, with more pairing occurring in the nanotubes with smaller diameters. Gao et al.[726] showed that flow in 1.4-nm-diameter CNTs can undergo a transition from the passage of a continuous water chain to the transport of isolated ion−water clusters, which greatly reduces the resistance for ion transport. MD simulations have also predicted quantized ion conductance due to the layered structure of the ion hydration shell[727] and voltage-gated ion transport due to the presence of local energy barriers.[144,728]

5.2.4.2. (ii) Ion Conductance and Ion Mobility in CNTs. The development of experimental platforms for studying nanofluidic transport in CNTs (see section 2.1) has provided researchers with the opportunity to test many of the predictions described in section 5.2.4.1. Hindered transport theories[729−731] predict that as the channel size approaches that of the hydrated ions, the electrophoretic mobility will become smaller than its bulk value. The theoretically predicted conductance[732] is given by

$$G = (\mu_{K^+} + \mu_{Cl^-})\cdot N_A \cdot e \cdot C_{KCl} \cdot \left[\frac{4L_{CNT}}{\pi d_{CNT}^2} + \frac{1}{d_{CNT}}\right]^{-1} \quad (30)$$

where $\mu_{K+} = 7.62 \times 10^{-8}$ m^2/(V s) and $\mu_{Cl-} = 7.91 \times 10^{-8}$ m^2/Vs are bulk ion mobility values, C_{KCl} is the KCl concentration, e is the electron charge, d_{CNT} is the CNT diameter, L_{CNT} is the CNT length, and N_A is Avogadro's number. However, experimental data reveal a picture that is not nearly so simple. Enhanced electrophoretic ion transport has been observed in a range of experiments using platforms with different CNT lengths and diameters, although the degree of enhancement varied considerably (Figure 72).[1,53,463,464,672,728,732−735] The general trend is that the highest enhancements are observed in experiments using CNTs that are at least 20 μm long, which suggests that simple scaling relationships do not work in CNT

https://doi.org/10.1021/acs.chemrev.2c00155
Chem. Rev. 2023, 123, 2737−2831

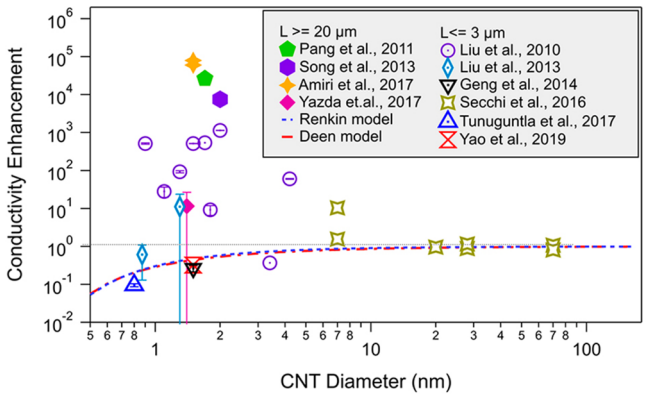

Figure 72. The conductance enhancement factor for CNTs, as compared with predictions based on bulk ion conductance. Ion conductances were measured on platforms with individual CNTs with 1.0 M KCl at neutral pH values (between 6.0 and 8.0). The experimental conductance data are from refs 1, 53, 463, 464, 672, 728, 732−735. The dashed lines indicate the predictions of hindered transport theory (blue, Renkin model;[730] red, Deen model[731]), where the Stokes size[19,737] is 0.24 nm for both K^+ and Cl^-.

pores. The ion mobility can also vary considerably from CNT to CNT. For instance, Liu et al.[732] observed that the ion conductance through individual, ultralong SWCNTs varied over nearly 4 orders of magnitude, with 20% of the measured ion conductance values being higher than the bulk conductivity, and the other 80% being either consistent with, or smaller than, the bulk value. A follow-up study from the same group showed a four-orders-of-magnitude enhancement in 20-μm-long SWCNTs with a diameter of ∼2 nm. Yazda et al.[728] also reported one-to-two-orders-of-conductance enhancement for ion transport through ultralong SWCNTs with diameters in the range of 1.2−2.0 nm. Strano and co-workers[13,18,736] observed stochastic pore blocking when individual cations partitioned into ultralong CNTs with 1.5-nm diameters. The cations obstructed an otherwise stable baseline current that was dominated by protons. The electrophoretic mobilities for K^+ and Li^+, as extracted from the ion-blockade dwell time, were 2 orders of magnitude higher than the bulk values. In contrast, Na^+ exhibited only bulk-level mobility.

Measurements on transport in shorter ($L < 5$ μm) CNTs revealed significantly smaller mobility enhancements. Hinds and co-workers[737] probed ion transport through membranes containing CNTs with an average diameter of 0.9 nm and an

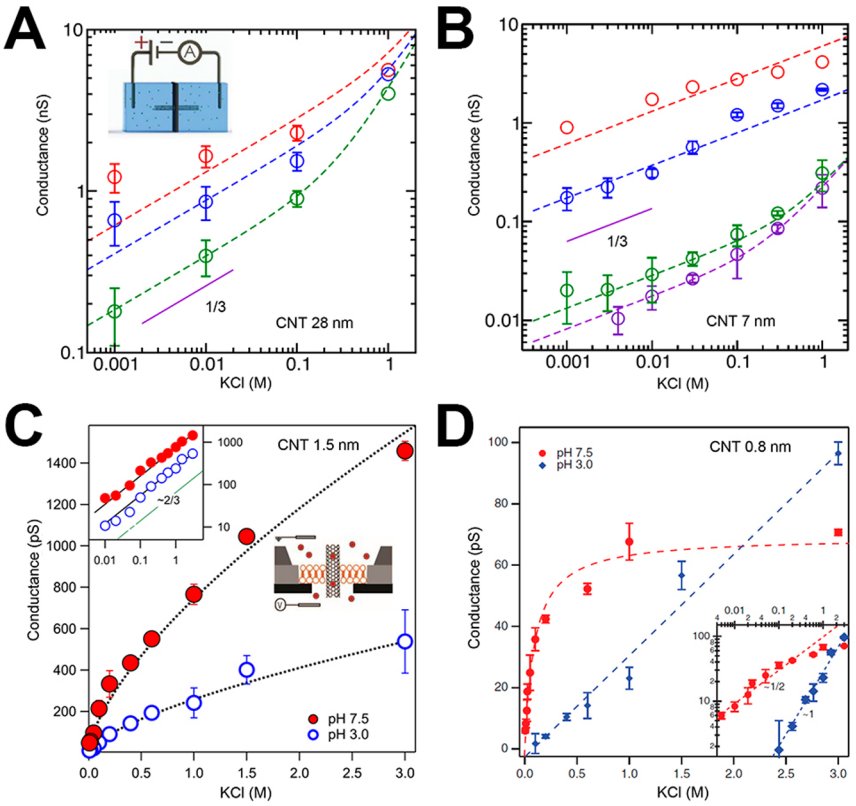

Figure 73. Scaling-law behavior for ionic transport in individual CNTs. (A) Ion conductance, measured at different pH values, as a function of KCl concentration inside single CNTs with various geometrical characteristics. The CNT diameter and length are 28 and 2000 nm, respectively, and the pH values are 6, 9, and 10, from bottom to top. The dashed lines are predictions of a surface-charge-regulated model. The inset is a schematic of the experimental setup, in which a single MWCNT is inserted into a hole and squeezed between two macroscopic fluid reservoirs. Adapted from ref 463. Copyright 2016 American Physical Society. (B) Conductance as a function of KCl concentration in CNTs with a diameter of 7 nm and a length of 3 μm at pH = 4, 6, 8, and 10, from bottom to top. The dashed lines are the predictions of a surface-charge-regulated model. Adapted from ref 463. Copyright 2016 American Physical Society. (C) The inset at right is a schematic of the experimental setup, in which a small-area lipid bilayer with a single CNT is formed over a Si_3N_4 nanopore. The left inset shows the same data plotted on a logarithmic scale. The lines are best fits of the data to a power law. Adapted from ref 464. Copyright 2019 American Chemical Society. (D) Conductance as a function of KCl concentration in CNTs at pH 3.0 and 7.5. The inset shows the data plotted on a logarithmic scale. The dashed lines are best fits to a power law. Adapted from ref 1. Copyright 2017 American Association for the Advancement of Science.

https://doi.org/10.1021/acs.chemrev.2c00155
Chem. Rev. 2023, 123, 2737−2831

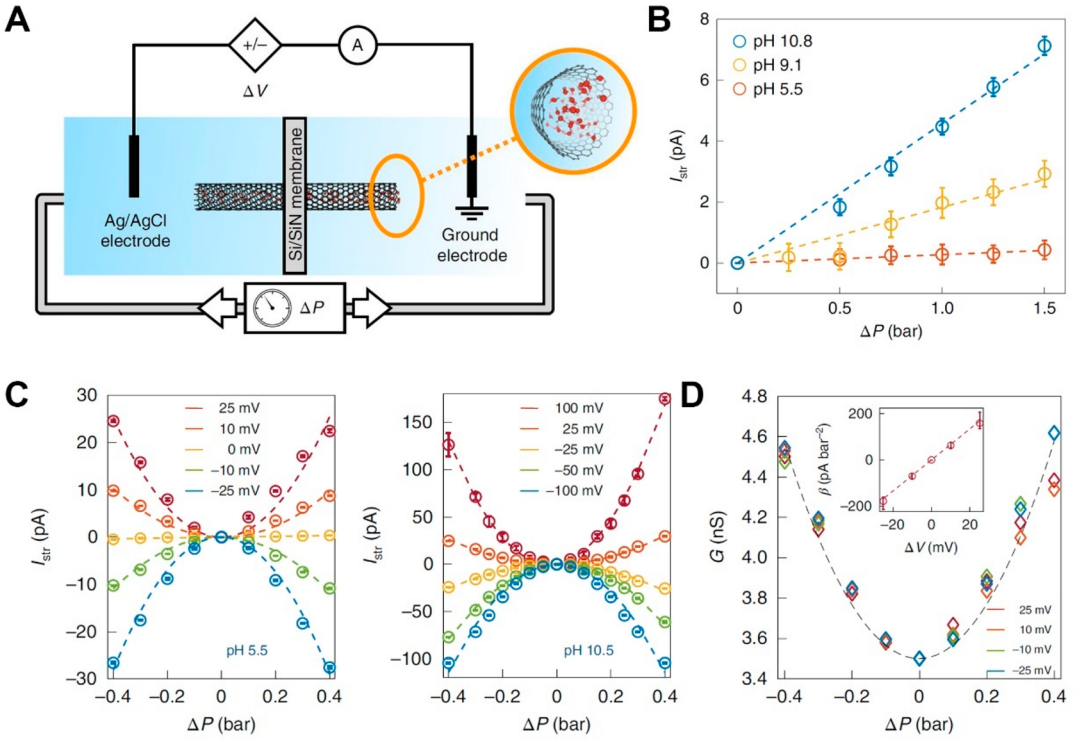

Figure 74. Mechanically activated ionic transport across SDN CNTs. (A) Schematic of a device for the measurement of pressure- and voltage-driven current through a single CNT. (B) Streaming current as a function of the pressure drop ΔP without an applied voltage ($\Delta V = 0$) at three different pH values. The dashed lines represent the best linear fits. (C) Streaming current as a function of ΔP at different values of ΔV and a pH of (left) 5.5 and (right) 10.5. The dashed lines represent the best quadratic fits. (D) The mechanosensitive conductance G as a function of ΔP for different values of ΔV at pH 5.5. The dashed line represents the best quadratic fit. The inset shows the second-order coefficient from the best parabolic fit to the data in the left panel of C as a function of ΔV. The dashed line represents the best linear fit. Adapted from ref 715. Copyright 2020 Springer Nature.

average length of 5 μm, and found that the mobilities of cations in alkali halide salts (K^+, Na^+, and Li^+) were enhanced only by a factor of 3 over bulk values. The same group observed bulk-level mobility using a similar platform with 7-nm-diameter, multiwalled CNTs.[738] Noy and co-workers probed transport in CNT porins with lengths of ∼10 nm, and observed a K^+ mobility in 1.5-nm-diameter porins that reached nearly bulk-level values.[53,464] The mobility was reduced further in 0.8-nm-diameter CNT porins.[1] These data agree well with the predictions of hindered transport models (Figure 72). Bocquet and coworkers[463] probed ion conductance in individual CNTs with lengths between 1 and 3 μm, and observed mobilities that were close to the bulk value. Liu et al.[733] measured conductance in a CNT−lipid hybrid platform with a pore length between 5 and 10 nm. They observed a surprisingly broad range of ion-conductance values. The ion conductance in the CNTs with the smallest diameters was close to the prediction of the hindered transport model, but CNTs with larger diameters exhibited a modest conductance enhancement (Figure 72).

Most of the reports on conductance enhancement have assumed that this phenomenon arises from rapid electroosmotic flow in CNTs.[672,728,732,737] However, several studies have suggested alternative mechanisms for fast ion transport, such as the breakup of single-file water chains.[726] Additionally, some reports have suggested that metallic CNTs have higher ionic conductance than do semiconducting CNTs.[732,733] The proposal that the electronic structure of CNTs can influence the fluid flow behavior still requires rigorous experimental testing.

The scaling behavior of ion conductance with concentration provides another fascinating window into confinement effects on ion transport in CNTs. Conductance is proportional to the local carrier concentration, but in nanofluidic channels the charges on the channel surface or channel entrance often cause the local ion concentration to deviate from the bulk value. Tight confinement increases the effect of such deviations on the overall ion current. Generally, such scaling relationships result in a power-law dependence of the ion conductance, G, on the bulk ion concentration. At high ionic concentrations, all of the surface charges are well screened, and the ion conductance exhibits a bulk-like, linear dependence on the salt concentration. When the channel surface carries a nonzero charge, mobile counterions can dominate the conductance at low concentrations, leading to conductance saturation. In this surface-transport regime, the power-law exponent is zero.[250] In CNT pores, physical features that include high slip flow, the absence of permanent surface charge, and the propensity for surface-charge regulation are responsible for power-law exponents that are neither zero nor unity. Power-law exponents between zero and one have been reported in CNTs with different diameters, and are routinely observed in biological channels.[739,740] Liu et al.[732] reported anomalous power-law scaling in long CNTs, with exponents ranging between 0.3 and 0.4. This scaling, as well as that observed in subsequent studies,[672,734] has been attributed to the existence of significant electroosmotic flow. A power-law exponent of ∼1/3 was reported by Secchi et al.[463] (Figure 73A,B) for transport through individual, multiwalled CNTs with diameters between 7 and 70 nm. These experiments also showed that when CNTs are replaced with BNNTs with similar

https://doi.org/10.1021/acs.chemrev.2c00155
Chem. Rev. 2023, 123, 2737−2831

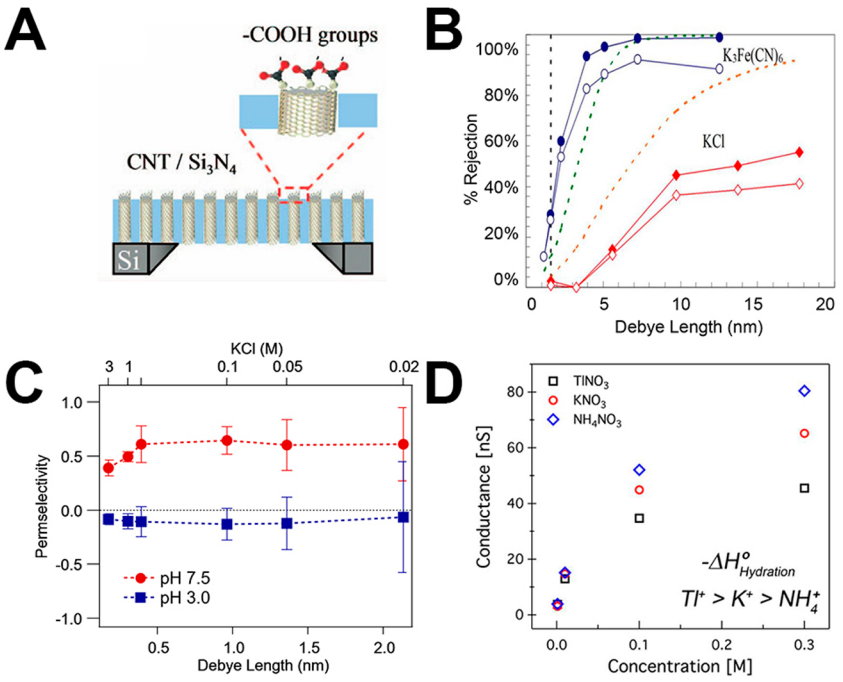

Figure 75. Ion selectivity in CNTs with diameters larger than 1 nm. (A) Schematic of aligned CNTs in a SiN_x matrix. The CNT tips feature carboxylate groups (or carboxylic acid groups, depending on the pH). The membrane thickness is 300 μm and the CNT diameters are between 0.8 and 2.6 nm. Adapted from ref 19. Copyright 2008 National Academy of Sciences. (B) The dependence of $K_3Fe(CN)_6$ (circles) and KCl (diamonds) rejection on the Debye length. The filled symbols are for anions and the open symbols are for cations. The dashed black line indicates the average CNT diameter. The dashed green and orange lines show the rejection coefficients calculated using Donnan membrane equilibrium theory for a 1:3 and a 1:1 electrolyte, respectively, with the membrane charge density set equal to 3.0 mM. Adapted from ref 19. Copyright 2008 National Academy of Sciences. (C) Permselectivity values of K^+ and Cl^- based on reversal potential measurements in 1.5-nm-diameter CNT porins, plotted as a function of the Debye length and KCl concentration at pH 7.5 (red) and 3.0 (blue). Adapted from ref 464. Copyright 2019 American Chemical Society. (D) Conductance of KNO_3, NH_4NO_3, and $TlNO_3$ solutions at various concentrations at pH 6.0 for 1.5-nm-diameter, 20-μm-long CNTs. Cations with a lower absolute value of hydration enthalpy exhibit higher conductance. Adapted from ref 735. Copyright 2017 American Chemical Society.

diameters, which carry a permanent surface charge, classic surface-conductance behavior is observed. In contrast, Amiri et al.[735] reported that the conductance of 1.5-nm-diameter CNTs exhibits a power-law exponent of ~1/2. These researchers attributed this behavior to the local electrostatic potential induced by the carboxyl groups at the channel entrance, which create a favorable co-ion exclusion environment. Tunuguntla et al.[1] invoked an analogous argument to explain a power-law exponent of 1/2 in 0.8-nm-diameter CNT porins (Figure 73D). Subsequently, Yao et al.[464] used a similar setup to establish an unusual power law exponent of ~2/3 in 1.5-nm-diameter CNT porins at both neutral and acidic pH.

These experimental efforts were accompanied by a strong push to develop realistic models of ion conductance in CNTs. Secchi et al.[463] made the assumption that CNT surfaces carry negative charge due to the adsorption of hydroxyl ions, which are then subjected to charge regulation. This assumption enabled the authors to explain the power-law exponent of 1/3 using the Gouy−Chapman model. Biesheuvel et al.[429] arrived at a similar power-law exponent using charge regulation in conjunction with a Langmuir isotherm. Uematsu et al.[741] further demonstrated the possibility of observing crossovers among different power-law exponents (0, 1/3 and 1/2) at different ion concentrations and pH values. Notably, none of these models can account for the possibility of electroosmotic coupling in CNT pores, as was considered by Manghi et al.,[742] who combined charge regulation with wall slip to model scenarios with power-law exponents of 1/2, 1/3, and 2/3. Lokesh et al.[722] reported some evidence for surface charge on CNT walls in experiments that probed diffusioosmosis in entrance-modified CNT membranes with a 2.2 nm average diameter. Noh et al.[562] have advanced an entirely different approach, suggesting that conductance-scaling behaviors arise from the breakdown of electroneutrality inside the channel due to the leakage of the surface electric potential into the reservoir. They also showed that the conductance-scaling model, which was developed based on this assumption, fits the experimental data quite well, and can explain power laws with any exponents between zero and one.

5.2.4.3. (iii) Mechanosensitive Ion Conductance in CNTs. Bocquet and co-workers[715] recently reported another interesting coupling effect in an investigation of mechanically activated ion transport across SDN CNTs (Figure 74). With no applied voltage, the streaming current through 4-nm-diameter CNTs was proportional to the applied pressure. However, when a voltage was applied, the ion conductance varied quadratically with the applied pressure. This behavior, which has some similarities to the response of biological mechanosensitive ion channels,[743,744] was attributed to a combination of pressure-dependent accumulation of ionic species in the CNTs under a voltage bias and strong electrohydrodynamic couplings originating from the ultralow friction of water on the CNT surface. In contrast, in 2D graphite slit pores with Ångstrom-scale channel heights,[260] Mouterde et al. found that the ion current was proportional to the applied pressure whether or not there was a voltage applied.

5.2.4.4. (iv) Ion Selectivity in CNTs. As discussed in section 5.2.3, MD simulations predict that the mechanism of ion

https://doi.org/10.1021/acs.chemrev.2c00155
Chem. Rev. 2023, 123, 2737−2831

selectivity in CNTs depends on the pore diameter. For sub-nm diameters, ion selectivity is dominated by size sieving and the ion dehydration energy penalty.[513,629,716−718] For somewhat larger pores, selectivity arises largely from the electrostatic interaction of ions with the CNT wall charges[719,720] or with functional groups at the nanotube ends.[612,719−721] In this latter regime, ion selectivity follows the Donnan mechanism,[745] as was shown by Fornasiero et al.[19] in membranes fabricated with a vertically aligned array of double-walled CNTs with diameters of 1−2 nm (Figure 75A,B). In this study, the ion rejection was observed to decrease significantly at Debye lengths smaller than the CNT diameter. Multivalent ions were subject to stronger rejection than were monovalent ions. Additionally, ion transport was found to be sensitive to the presence of carboxylate groups at the ends of the CNT pores. In particular, the ion rejection decreased for pH values below the pK_a of a carboxylic acid. Analogous behavior was observed by Yao et al.,[464] who measured the permselectivity of 1.5-nm-diameter CNTs at different pH values (Figure 75C). The CNTs exhibited weak cation selectivity at pH values near neutral, but became essentially nonselective at acidic pH values. Amiri et al.[735] observed cationic selectivity in 1.5-nm-diameter CNTs, which was attributed to the presence of carboxylate groups at the CNT ends. Amiri et al. also observed differential ion selectivity in these CNTs, which they attributed to the differences in ion hydration energies (Figure 75D), although the channels were wider than the hydrated sizes of the ions that they studied. This behavior may reflect the energetic penalty for altering the ion hydration state while traversing a confined hydrophobic channel, as has been observed in MD simulations.[718] A similar trend was observed by Strano and co-workers,[13,18] who found that the transport rates of alkali metal ions through 1.5-nm-diameter, ultralong SWNTs follows the order $Li^+ > K^+ > Cs^+ > Na^+$. This trend was attributed to changes in the ion hydration shells when entering the nanochannels.

Li et al.[714] investigated ion diffusion in CNT porins with a diameter of 0.8 nm and a length of 10 nm (Figure 76A). They observed strong differential selectivity among four monovalent anions, with the ion permeabilities varying by up to 2 orders of magnitude and following the Hofmeister series ($Cl^- < Br^- < I^- < SCN^-$). This behavior originates in the strong confinement of the CNT channels, which makes significant ion dehydration a requirement for permeation through these pores. This study also demonstrated that the dehydration energy is the dominant component of the energy barrier for ion transport, as neutralization of the negative charges from the CNT entrance at acidic pH values increased the anion permeability by only a small factor, and there was a strong correlation between the ion permeability and ion hydration energy. High dehydration-energy barriers also contribute to strong ion rejection in sub-1-nm CNT pores. A recent study by Li et al.[746] found the water−ion permselectivity of 0.8-nm-diameter CNT porins to be on the order of 10^5, a value that is competitive with the performance of polyamide-based water desalination membranes.[747] Even though these results are consistent with MD simulations showing high salt rejection in CNTs with small diameters,[630,748] our understanding of the ion-rejection mechanisms in these nanochannels remains incomplete. For example, electrophoretic transport measurements of KCl in 0.8-nm-diameter CNT porins[1] not only revealed that these channels are highly selective for K^+, but also showed that the energy barrier for this process is low (Figure 76B), in contrast to the high dehydration penalty observed in MD simulations.[513,629,716−718] Modeling studies that focus on the details of the interactions of ions with the CNT walls, and especially on polarization effects in this system, would help to reveal the mechanistic origins of this behavior.

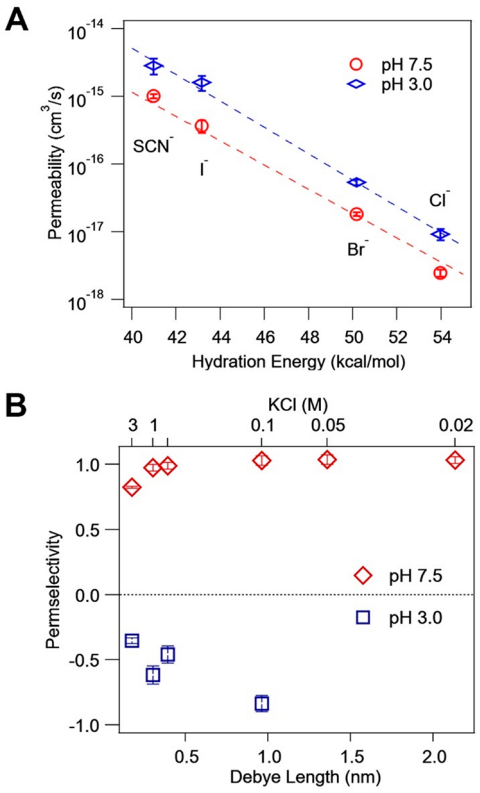

Figure 76. Ion selectivity in CNTs with sub-nm diameters. (A) Measured anion permeabilities through 0.8-nm-diameter, 10-nm-long CNT porins using a fluorescent-dye-based assay. The permeabilities of the four anions studied are plotted as a function of the first-solvation-shell hydration energy, as calculated using first-principles simulations. The dashed lines are exponential fits that are provided as a to guide the eye. Adapted from ref 714. Copyright 2020 American Chemical Society. (B) Permselectivity values for K^+ and Cl^- based on reversal potential measurements in 0.8-nm-diameter CNT porins, plotted as a function of the Debye length and KCl concentration, at pH values of 7.5 (red) and 3.0 (blue). Adapted from ref 1. Copyright 2017 American Association for the Advancement of Science.

5.3. Electrokinetic Coupling

When the EDLs screening the charge on the pore surfaces overlap in SDNs, the coupling of fluid flow and ion transport becomes especially significant.[749] In addition to the electro-diffusion of ionic species, electrokinetic transport includes fluid flow driven by electric fields (electroosmosis) and concentration gradients (diffusioosmosis).[423] Models of electrokinetic transport in the regime of overlapping EDLs build on the pioneering space-charge model of Gross and Osterle,[750] which has recently been revisited and extended[749,751] to understand electrokinetic conversion efficiency,[752] network effects,[751] and nonidealities.[753] These space-charge models typically simplify the 2D or 3D Poisson−Nernst−Planck−Stokes model to a 1D electrokinetic circuit, in which the transport coefficients for linear response are determined by the assumptions of the equilibrium EDLs and Onsager symmetry. Analytically tractable approximations for the transport characteristics are possible in these regimes. More generally, the full Poisson−Nernst−Planck−Stokes system of equations in 3D can be solved to capture nonequilibrium effects in the double layers, and to access resistance and other important quantities for comparison

https://doi.org/10.1021/acs.chemrev.2c00155
Chem. Rev. 2023, 123, 2737−2831

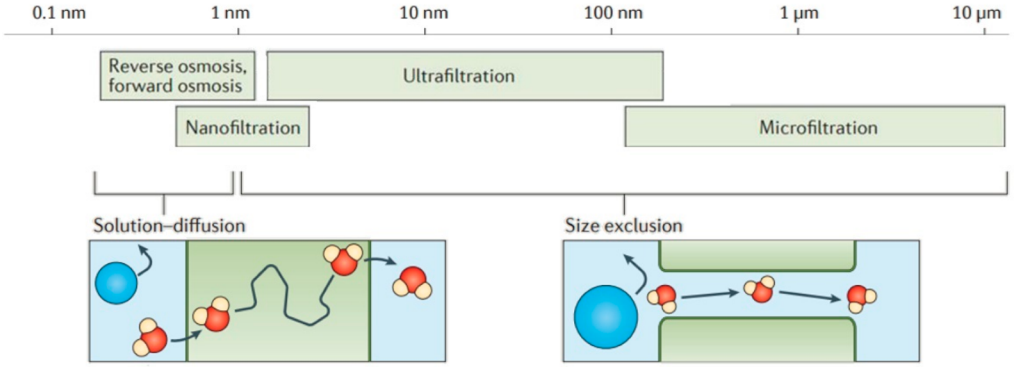

Figure 77. Comparing confinement regimes for various membrane processes. Confinement by pores <1 nm in diameter results in a transition from size-exclusion (i.e., filtration processes) to solution-diffusion (i.e., osmotic processes) transport mechanisms. Adapted from ref 9. Copyright 2016 Springer Nature.

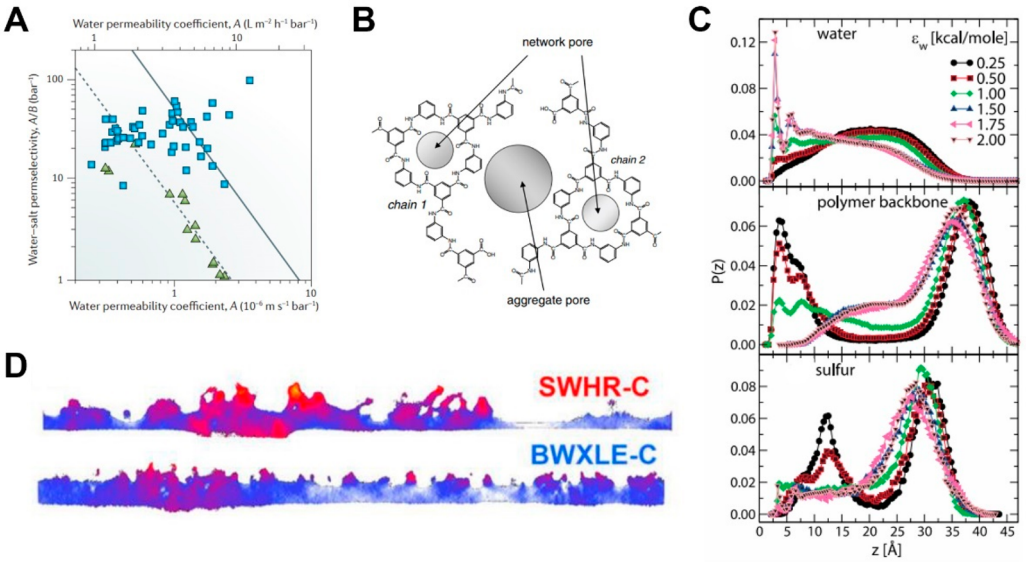

Figure 78. Inhomogeneous nature of polymer membranes. (A) Permeability/selectivity trade-off for thin-film composite (TFC) reverse osmosis (RO) membranes. The blue squares represent the permselectivity values for commercial TFC RO membranes, whereas green triangles represent the permselectivity measured for a chlorine- and caustic-treated commercial TFC RO membrane. (B) A schematic diagram of the proposed molecular structure for a highly cross-linked polyamide network, in which transport occurs across interconnected aggregate and network pores formed during interfacial polymerization. "Aggregate" pores form from the agglomeration of microscopic polymer particles during the polymerization process, whereas network pores are intrinsic to the cross-linked nature of the polymer chains. (C) Mass probability distributions of water oxygens (i), polymer backbone units (ii), and sulfur atoms (iii) as a function of depth, z, across a Nafion thin film. These results were obtained with classical molecular dynamics simulations; ε_w is a thermodynamic descriptor for the hydrophilicity of the film. (D) XZ planes of the thresholded volume of commercial TFC RO membrane tomograms with intensity displayed as a heat map. Red corresponds to higher intensity, i.e., a higher local polymer density. The intensity maps for SWHR-C and BWXLE-C suggest that the selective layers of these commercial membranes have a higher polymer density at the surface of the film. (A) Adapted from ref 9. Copyright 2016 Springer Nature. (B) Adapted from ref 771. Copyright 2011 Cambridge University Press. (C) Adapted from ref 768. Copyright 2013 American Chemical Society. (D) Adapted from ref 209. Copyright 2018 National Academy of Sciences.

to theory and MD simulations. Furthermore, to capture the rich behavior of ions in confinement, the Poisson−Nernst−Planck−Stokes model can be generalized to include nonideal effects, including coupled fluxes,[754] finite ion size,[755] and others.[427] Surface-charge-regulation reactions, both in and out of equilibrium, are important for capturing transport characteristics properly.[634]

5.4. Transport in Polymer Membranes

The development and increased implementation of polymer membranes is core to meeting future global sustainability goals.[23,194,756−758] As such, polymeric membranes represent one of the largest classes of applied 3D nanofluidic platforms. The pore diameters in polymer membranes can range from ∼0.2 nm to over 100 nm (Figure 77),[9,190,191] making these materials applicable for a host of separation processes, including those involving gases, water, solutes, and solvents. The widespread adoption of polymer membranes over other porous materials (e.g., ceramics) is largely due to the high processability and low cost associated with polymers.[9,759]

Despite decades of research on nanoporous polymer membranes, there is still much to learn. To date, the understanding of confinement effects in nanoporous polymers has been stymied by the spatial and temporal resolution limits of available measurement techniques, as well as by the complex nature of polymer physics. Transport in membranes with pores with diameters of tens of nanometers or more is sterically driven, and thus is well-described by classic Hagen−Poiseuille flow

https://doi.org/10.1021/acs.chemrev.2c00155
Chem. Rev. 2023, 123, 2737−2831

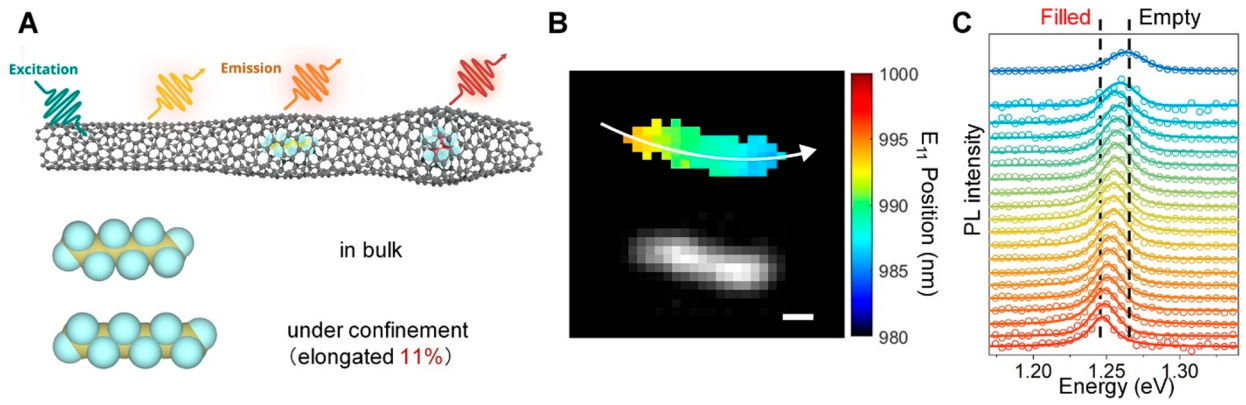

Figure 79. Filling individual CNTs with tightly fitting molecules. (A) The nanotube fluoresces at different wavelengths in response to *n*-hexane and cyclohexane. MD simulations show that *n*-hexane must stretch by nearly 11% to enter a (6,5)-SWCNT. (B) Hyperspectral PL images of a single (6,5)-SWCNT partially filled with *n*-hexane along its length. (top) PL peak position color map. (bottom) PL intensity image. Scale bar represents 500 nm. (C) PL spectra along the partially filled nanotube. Adapted from ref 88. Copyright 2021 Springer Nature.

models.[197,760] Transport in polymeric SDNs, however, is dominated by free-volume effects.[138,761] Such transport is commonly related to macroscopic transport observations using a solution-diffusion model, which employs empirically determined coefficients.[762] Although useful, this model does not provide molecular-level insight. Deciphering transport mechanisms is further complicated for membranes with pores with diameters in the 1−2 nm range, in which both diffusion and convection are important.

Elucidating confinement effects in nanoporous polymer membranes is a complex problem, due to the unique local environments in these materials. The highly interconnected networks of polymer pores often lack a discrete structure, and can sometimes be considered as voids, making it difficult to distinguish the actual level of confinement. The thermal motion of these 3D networks may further lead to coupled transport between the solvent and solute of interest.[138,194] This phenomenon results in a permeability/selectivity trade-off, in which isolating transport phenomena specific to the solute or the solvent becomes difficult (Figure 78A).[30,763,764] Polymer membranes also often possess structural and chemical inhomogeneities throughout the film that can lead to distinctly different solvent−membrane or solute−membrane interactions during transport (Figure 78B−D).[209,214,765−769] Furthermore, local changes in solvent properties due to confinement can result in electrostatic phenomena within the polymer that violate traditional mean-field theories. such as the Donnan model.[102,103,106,107] The application of transition-state theory has recently been suggested to improve our understanding of molecular-level transport phenomena in polymer membranes.[33,770] Nevertheless, there exist significant theoretical and technological hurdles that must be overcome to advance our understanding of confined transport in polymer membranes.

5.5. The Role of Molecular Configuration in Transport

A joint experimental and theoretical effort by Wang, Aluru, and co-workers demonstrated that trace amounts of *n*-hexane in liquid cyclohexane selectively fill (6,5)-SWCNTs, which have a diameter of 0.42 nm, whereas cyclohexane is excluded (Figure 79).[88] In contrast, for (8,3)-SWCNTs, which have a diameter of 0.43 nm, as well as for other CNTs with larger diameters, both *n*-hexane and cyclohexane can enter. Thus, a 0.01 nm decrease in the SDN diameter is enough to switch on selectivity. It is surprising that *n*-hexane can enter a (6,5)-SWCNT, in that the minimum cross section for an isolated *n*-hexane molecule at a local energy minimum is larger than the van der Waals inner diameter of the CNT. MD simulations revealed that *n*-hexane molecules must stretch by more than 11% to enter the pore. This stretched state is thermally accessible at room temperature.

5.6. Quantum Sieving

The transverse motion of a molecule in a nanopore should become quantized when the pore diameter is comparable to, or smaller than, the molecule's thermal de Broglie wavelength. An intriguing application of this effect is the separation of isotopes. For example, molecular deuterium and hydrogen have nearly identical sizes, and so cannot be separated using traditional molecular sieving. The concept of kinetic quantum sieving (KQS) was first proposed by Beenakker et al.[772] The zero-point energy, E_o, of a molecule confined to a pore is strongly dependent on the pore diameter, as is the molecule's interaction potential with the nanopore, ε. When $E_o > \varepsilon$, the molecule experiences an energetic barrier for transverse motion, as shown in Figure 80A. The operating principle of KQS is that because E_o is inversely dependent on the molecular mass, heavier isotopes diffuse more quickly through the pore than do lighter ones, enabling isotopic separation.

Another proposed mechanism for isotopic separation in nanopores is chemical affinity quantum sieving (CAQS).[773,774] A strong chemical affinity between an adsorbate and an adsorbent promotes preferential adsorption of some species, because E_o influences the enthalpy of adsorption. In CAQS, the lighter species diffuses more rapidly than the heavier species. Prerequisites for CAQS are that the pore size be large enough for penetration of both components and that no diffusion barrier exists inside the nanopores.[775]

Separation of H_2 and D_2 has been demonstrated via KQS and CAQS using MOFs,[776−778] COFs,[779] and zeolites.[667] Figure 80B shows the isotope selectivity for transport of D_2 over H_2 in MOFs with pore diameters between 1.9 and 4.5 Å. The preferential transport of D_2 is due to KQS. In this example, MOFs with smaller pores exhibit higher selectivity than do MOFs with larger pores, but at the cost of having lower uptake.

CNTs with tunable, sub-nm diameters are a promising platform for high-efficiency quantum sieving of isotopes. A powder composed of bundled CNTs with an average pore size of >1 nm has been demonstrated to have a transport selectivity for D_2 over H_2 by a factor of ~1.5 at 77 K.[780] Quantum sieving has

https://doi.org/10.1021/acs.chemrev.2c00155
Chem. Rev. 2023, 123, 2737−2831

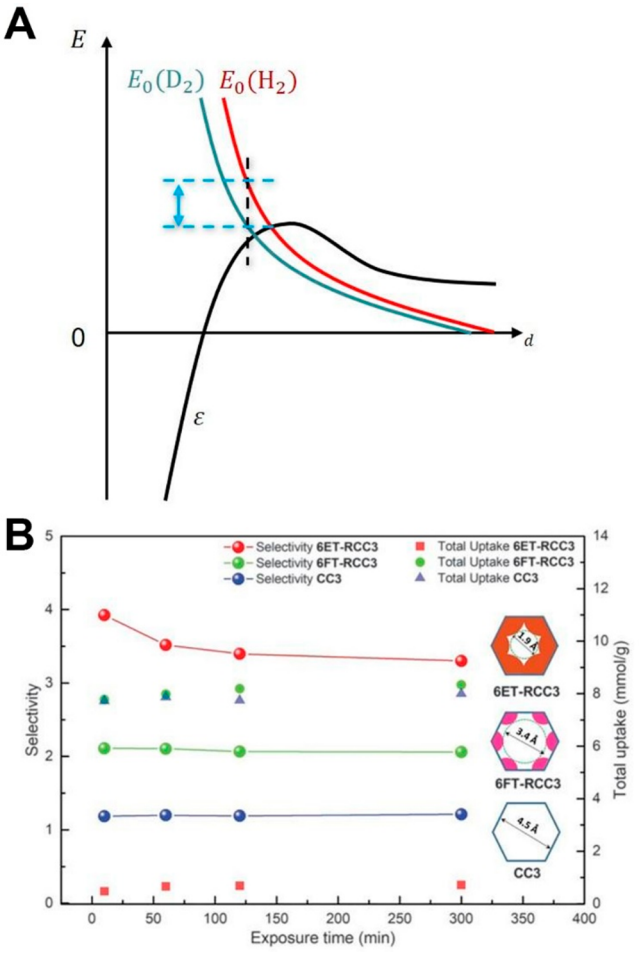

Figure 80. Quantum sieving. (A) The zero-point energy E_o of D_2 (blue curve) and H_2 (red curve) in a pore with diameter d, and the molecule–pore interaction energy approximated by a circular square well with depth ε (black curve). If $E_o > \varepsilon$, then thermal excitation is required for transport, as is the case for H_2, but not D_2, at the pore diameter indicated by the vertical dashed line. (B) D_2/H_2 selectivity and gas uptake by MOFs as a function of exposure time at 30 K. Adapted from ref 778. Copyright 2019 American Association for the Advancement of Science.

not yet been reported using CNTs with a pore diameter that is comparable to the thermal de Broglie wavelengths of H_2 and D_2, perhaps due to the structural heterogeneity of CNTs and the experimental challenges of preparing vertically aligned CNT membranes.[287,671,686,781,782] With the recent advances in the chiral sorting, solution processing, and fluorescence imaging of CNTs,[88,267,443,783] it will be exciting to revisit quantum sieving using precision CNT SDNs.

6. THE ROLE OF DEFECTS

Defects are ubiquitous in nanopores. However, the manner in which defects affect fluids and solutions confined in SDNs is largely unknown. Despite extensive studies, understanding the influence of defects on molecular transport at the nanoscale remains a significant challenge. This difficulty arises in part from the lack of in situ tools that can provide high-resolution information on defects[443] and interfaces,[784] and their impact on fluidic transport. Work in this area is at an early stage, and here we highlight the challenges and needs for further experimental and theoretical studies on the role of defects in SDNs.

Computational modeling, particularly when informed and validated by experiment, can offer insights into the key processes that underlie molecular transport in the presence of defects. For instance, MD simulations using empirical force fields have shown that the presence of carbon vacancies can disrupt the smooth and continuous potential energy landscape of CNTs, with impacts such as reducing the water-flow rate in (7,7)-SWCNTs.[785] In addition to carbon-lattice defects, the presence of bulky anionic functional groups can drastically reduce water flow in CNT membranes.[684] Simulations of water confined in (5,5)-BNNTs show that Stone–Wales defects[786] break hydrogen bonding with neighboring water due to a defect-induced dipole, resulting in both a phase transition from liquid-like to vapor-like water and high oscillatory motion of water in the axial direction of the nanotube.[786]

Recent advances in high-performance computing and computational algorithms have provided increased opportunities for using FPMD simulations to study interfacial effects on nanofluidic transport. In contrast to the case of force-field-based simulations, in FPMD simulations the energy and forces are derived self-consistently from electronic structure calculations. Although FPMD simulations are computationally expensive, and are therefore often limited to relatively small time and length scales, this technique is well suited for probing the effects of complex defects and interfacial electronic structures. As a prime example, recent studies showed that friction coefficients at the solid–liquid interface can be calculated using ab initio simulations. This work underscores the importance of surface defects and electronic structure on fluid transport. In particular, Joly et al. found that water dissociation near defective hBN and graphene sheets can lead to a significant increase in friction that is particularly sensitive to the chemical structure of the defects.[787] Tocci et al. showed that the friction of liquid water in contact with graphene and hBN differs significantly, despite similar interfacial organization (Figure 81).[788,789] The water friction coefficient on hBN is about three times larger than that on graphene, due to the greater corrugation in the BN energy landscape. Recently, Kavokine et al. derived a theory of the quantum contribution to hydrodynamic friction.[6] They demonstrated that the quantum coupling between the electronic structure in the solid and the confined water can explain the radius-dependent friction in carbon nanotubes. In addition to insulators and semiconductors, molecular simulations have also been used recently to study the effect of metallic surfaces on electrochemical interfacial properties of aqueous solutions of salts through a semiclassical Thomas–Fermi model.[790] A virtual Thomas–Fermi model was also used to investigate the phase transitions and wetting of ionic liquids near metallic surfaces.[791] Modeling of the interaction between metallic surfaces and ionic liquids has also been shown to explain the increase in the capacitance of nanoporous carbon electrodes.[792] These studies highlight the fact that the inclusion of the electronic structure of the interface is essential for the proper determination of fluidic transport properties under confinement and at water–solid interfaces.

Furthermore, an emergent class of atomistic potentials constructed from machine-learning frameworks, such as neural networks[793,794] and kernel-based methods,[795] has shown great promise in extending simulations from first-principles based approaches to larger length and time scales. These machine-learning potentials (MLPs) are trained on first-principles-derived energies and forces mapped to representations of localized atomic environments, where the learned potential

https://doi.org/10.1021/acs.chemrev.2c00155
Chem. Rev. 2023, 123, 2737–2831

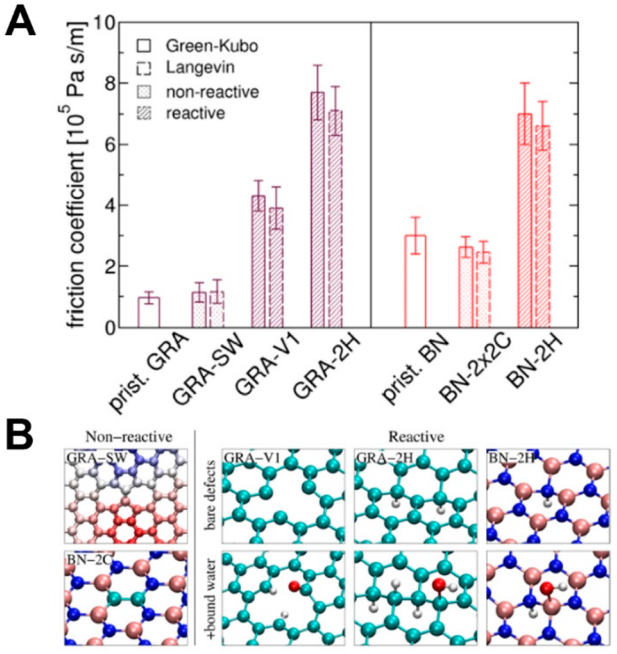

Figure 81. Friction of liquid water on contact with 2D materials. (A) Green−Kubo and Langevin estimates of the friction coefficient of water in contact with graphene (left) and hBN (right). (B) Top views of simulation snapshots of the defects introduced in graphene and boron nitride. Adapted from ref 801. Copyright 2016 American Chemical Society.

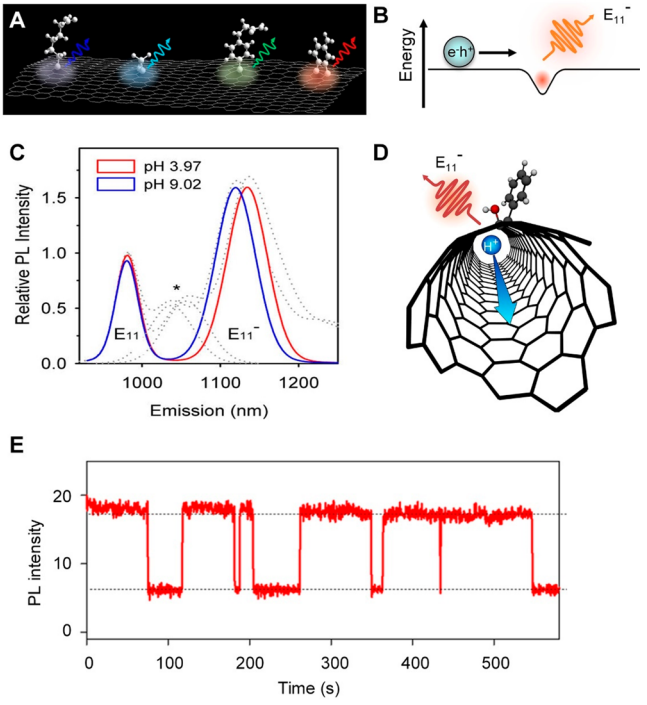

Figure 82. Defects as probes for molecular transport and confinement in SWCNT SDNs. (A) OCCs are quantum emitters that can be created by covalently attaching organic functional groups to a semiconducting host, in this case, a SWCNT. Adapted from ref 803. Copyright 2016 American Chemical Society. (B) The organic functional group induces a localized quantum well in which mobile excitons from the host semiconductor are trapped. The trapped excitons undergo radiative recombination efficiently. Adapted from ref 806. Copyright 2019 Springer Nature. (C) The E_{11}^- emission of the *N*,*N*-diethyl-4-aminobenzene-functionalized (6,5)-SWCNTs red-shifts as the pH decreases. Fits to the E_{11} and E_{11}^- emission curves (solid lines) are plotted on top of the data (dotted lines). The peaks between E_{11} and E_{11}^- (marked with an asterisk) are due to a (6,4)-SWCNT-$C_6H_4N(CH_2CH_3)_2$ impurity in solution. Adapted from ref 814. Copyright 2015 American Chemical Society. (D) Schematic of the OCC response to the endohedral transport of a proton. (E) The E_{11}^- PL intensity of a single defect as a function of time, showing a bimodal intensity that may correspond to a nearby charge temporarily trapped at the OCC site. Adapted from ref 443. Copyright 2019 Springer Nature.

energy surface can be extended and refined via active learning procedures. Such an approach is particularly well suited for systems of confined fluids in CNTs, in which there are strong electronic structure effects requiring first-principles approaches, yet long correlation lengths necessitating large-scale simulations. Several recent works[796−800] have applied MLPs to the study of confined aqueous systems, primarily focusing on the role of water phase behavior and the friction coefficient in confined environments.

Experimentally, it is difficult to probe the impact of atomic defects, because they are randomly implanted and structurally difficult to control. Organic color centers (OCCs) are a family of chemically tunable photoluminescent defects that can be covalently added to the surface of SWCNTs, and include methylene groups, alkyl chains, aryl groups, and even polymers[802−809] (Figure 82A). OCCs can be patterned using photochemical or lithographic techniques,[810−813] and can also be implanted at the pore mouth.[444,445] Such defects in the sp^2 lattice of SWCNTs create potential wells, which can locally trap E_{11} excitons that diffuse along the nanotube, resulting in red-shifted, E_{11}^- emission (Figure 82B). The wavelength and intensity of the defect PL depend on both the functional groups and the nanotube host.

OCCs respond to changes in the local chemical environment, potentially providing a spectral signature to probe the impact of defects on mass transport in SDNs. Although this application of defects remains to be explored, Kwon et al.[814] demonstrated that *N*,*N*-diethyl-4-aminobenzene OCCs respond to protons, with the defect PL red-shifting from 1117 to 1136 nm as the pH changes from 9.02 to 3.97 (Figure 82C). This spectral shift is due to the protonation of the amine moiety of the OCC. When protons are confined inside a SWCNT pore, OCCs may interact with the confined protons, resulting in PL shifts that could be used to provide information about the confinement (Figure 82D).

The PL from OCCs exhibits stochastic blinking in response to local charge fluctuations (Figure 82E). This phenomenon may provide a spectral fingerprint for the imaging of ions and molecules under confinement. Such measurements can be complemented by high-level electronic structure calculations, such as many-body perturbation theory (via the Bethe−Salpeter equation) and time-dependent DFT.[806,808,815,816] These techniques have historically been considered too computationally expensive for application to surfaces and interfaces. However, recent algorithmic developments are allowing researchers to apply these methods to larger and more realistic systems, permitting the direct treatment of solid−liquid interfaces.[817−819] This development opens the opportunity to investigate how electronic states are altered by the presence of water and solvated ions, and offers the potential of performing calculations for comparison with high-resolution experimental data.

https://doi.org/10.1021/acs.chemrev.2c00155
Chem. Rev. 2023, 123, 2737−2831

Chemical defects are predicted to play an outsized role at the nanoscale. Methods such as single-defect spectroscopy[443] allow individual luminescent chemical defects to be quantified and characterized. We anticipate that simulation techniques, used in conjunction with advanced spectroscopy and imaging techniques,[442,443,820] will help elucidate the role that defects and interfacial chemistry play in nanofluidic transport.

7. SUMMARY AND OUTLOOK

The extreme confinement of SDNs gives rise to a series of unforeseen phenomena and properties that stand to impact the efficiency and selectivity of ionic and molecular transport. Fluids in SDNs are dynamic, far from equilibrium, and extremely heterogeneous. The length and time scales for these systems are intrinsically multiscale, exhibiting rich and complicated confinement effects on the thermodynamics and fluidic transport. To understand these confinement effects, experimental platforms that build on precision model systems and transformative analytical tools have played enabling roles. Model SDN systems with tunable sub-10-nm pores, specifically tailored surface and pore-mouth chemistry, as well as intentionally incorporated atomic defects have recently become experimentally accessible. The development and use of advanced imaging and other characterization tools, such as environmental aberration-corrected TEM,[442,821,822] high resolution cryo-EM,[823] ultrafast electron diffraction imaging,[824] single defect spectroscopy,[88,443] and single ion traps,[825] are expected to transform our capabilities for probing water and ion structure in nanopores and understanding the critical roles of interfaces and defects. Theoretical tools that range from ab initio and all-atom MD calculations to continuum models are also being developed and applied to understand the intrinsically complex and intertwined phenomena concerning molecules and ions in nanopores.

Exploiting these confinement effects presents myriad opportunities for innovation and practical applications, including, but not limited to, separations, energy storage, and sensing. Ultraprecise recognition of molecules and ions, akin to that of biological channels, is considered a "holy grail" for separation processes.[33,826] For desalination, this goal would be represented by a membrane consisting of SDNs or sub-nm pores with near-perfect solute rejection that allows water molecules to pass at a reasonable rate.[827−829] Furthermore, by exploiting differences in solute size, charge, polarity, and other characteristics, SDNs and membranes can be developed for single-species selectivity[33,46] similar to that of the potassium channel, which can transport K^+ ions 10 000-fold faster than sodium ions.[60,151] These same merits also extend to solvent selectivity and biosensing, for which membranes and other SDN-based devices could be designed to differentiate between polar and nonpolar fluids for separation or flow-sensor purposes,[265,830] as well as to detect and characterize biomolecules at the single-molecule level,[831−833] and for sequencing of biomolecules.[834−836] Increasing global energy demands and societal calls for reduced reliance on fossil fuels necessitate novel approaches to energy conversion and storage. 2D nanochannels[17,154] and CNTs[13,15,837] have shown significant enhancements in proton transport over bulk diffusion, as well as complete proton selectivity in the case of Å-scale slits,[17] which are essential for highly efficient and effective fuel cells.[838] In addition to energy generation, the increased gas- and charge-storage capacities, and ultrafast ion transport offered by SDNs can improve energy technologies (e.g., batteries and capacitors). Gas storage in nanopores benefits from high surface area and strengthened local interactions with gas molecules.[665,839] Although SDN capacitance also benefits from these characteristics, electrolyte-filled SDNs can additionally store significant amounts of electrical charge within their confined EDLs.[840−842] The rapid ion transport offered by nanofluidic platforms enables improved power density that can be exploited by capacitor-based energy storage devices for faster charge delivery and longer cycle lifetime.[840,843]

7.1. The Future Outlook for SDN Transport Research

Progress in recent years toward elucidating the unique behavior of liquids in SDNs raises new questions that represent the next frontier in this field. We have identified six of these research issues/opportunities that we feel characterize key gaps between experimental observations and theoretical understanding, in addition to the seven knowledge gaps that we have reviewed and updated here.[12] These areas are:

7.1.1. Understanding Transport in Electrically Conducting SDNs. Advances in nanotechnology and nanofabrication have made possible the creation of new types of SDNs that have electrically conducting walls. These materials provide an opportunity to extend the recent understanding of nanoenhanced slip flow in SDNs to include cases in which electron momentum in the conduit wall(s) imparts momentum onto an adjacent fluid. This phenomenon constitutes a notable knowledge gap in the current literature, as the major engineering applications to date are rooted in insulating matrices. By the same token, the prevailing transport theories and associated experimental studies have involved or assumed insulating substrates. As one notable and intriguing exception, Tersoff and co-workers used a nonequilibrium Green's function simulation to show that solvated ions contained within a semiconducting SDN with a 1.34 nm diameter experience an enormous electromigrative wind-force current in which the confinement outstrips the direct force.[844] Experimental realization of this and similar confinement effects based on conductivity in the confining medium has yet to be achieved.

SDNs comprised of 2D material conduits, such as graphene bilayers, offer additional electronic handles for manipulating fluid and solvated ion phases at a conducting boundary. Graphene or transition-metal dichalcogenide bilayers in which the orientation of the two layers differs by as little as 1° can exhibit a flat electronic band structure.[845] Single electrons and holes form predictable charge-density patterns that can be manipulated by coupling to a gate electrode. This scheme provides an opportunity to manipulate fluid-entrained ions to control confinement-induced correlations.

Conducting SDNs also offer the opportunity to address longstanding issues of fundamental metrology in widely studied, insulating polymer nanopores. Many theories that relate ion sorption properties (which directly influence transport) to polymer membrane properties require knowledge of the relative permittivity of water confined within a nanopore.[106,121,846] Broadband dielectric spectroscopies enable capacitance measurements based on interfacial water, but the complex geometries of such pores requires adjustable parameters, structural assumptions, and separate modeling. These experimental shortcomings have resulted in large, and poorly understood, experimental uncertainties that we believe can be addressed with the emerging development of conducting, precision SDN conduits.

7.1.2. SDNs with Spatial Chemical Patterning. To the extent that the chemical nature of a SDN pore influences its flux

https://doi.org/10.1021/acs.chemrev.2c00155
Chem. Rev. 2023, 123, 2737−2831

and selectivity, there is considerable potential for the spatial patterning of the internal surface chemistry of the pore to enhance such properties. As an example of a problem that might be solved by spatial chemical patterning, ion-selective electrodes are powerful tools for detecting specific metals, but currently suffer from low flow.[847] One possible approach for achieving high selectivity and high flux simultaneously is to employ the chemistry already used in ion-selective electrodes at the pore entrances. Mechanistically, the patterning of surface charge leads to electrochemical symmetry breaking, from which interesting new transport properties may emerge.[252] Building on an example from nature, perhaps a precisely designed synthetic channel could recapitulate the principles of the biological K^+ channel to achieve selectivity between ions of similar size and charge. Key questions in this realm include how the interaction between ions and pore surfaces influences ion-transport behavior, and how the spacing between chemical functional groups impacts ion transport.[848]

7.1.3. SDN Transport under Temporal Forcing and Oscillations. Transport experiments, and the theory used to describe them, often assume steady state, or at least the approach to steady state. Recent experiments[13,849] and simulations[850,851] raise interesting questions regarding transport under forcing or driven fluctuations. Biological transport processes make significant use of such dynamics, whereas the use of fluctuations in technological applications is in its infancy.[850] It is known that thermal fluctuations assist the transport of oxygen into the binding pocket in hemoglobin. Structural fluctuations of biological K^+ channels have been found to be essential to ion selectivity.[852] In analogy, such fluctuations might be expected to have a substantial influence on transport and selectivity in synthetic SDNs. There is considerable mathematical work on stochastic resonance and related coherence resonances, in which electrochemical fluctuations can drive a system into ordered oscillations in flux. Stochastic resonances have been discovered in multiple biological systems, including ion channels,[853] sensory systems,[854] and the human cerebral cortex.[855]

Temporal forcing in SDNs can occur through mechanical, electrochemical, or other mechanisms. In the former case, precision SDN channels are available that allow for the study of mechanically driven temporal forcing. Recent experiments have used strain to modulate transport through 2D nanopores.[849] New transport regimes may arise when such modulation approaches characteristic time scales of the pore.[849−852] Mechanical forcing is particularly important when the same chemical environment in a nanoconstriction induces different transport properties as the pore structure undergoes thermal or oscillatory fluctuations. As an example, it would be fascinating to explore the effect that structural fluctuations have on hydrophobic gating in SDNs. As another example, it has been predicted that rigid nanopores favor condensation and wetting, whereas flexible nanopores induce evaporation, and thus the complete cancelation of the transport of water and ions.[856]

Electrochemical forcing offers the opportunity to create oscillations in new types of nanopores, nanochannels, and nanoslits. For instance, the versatility of 2D materials can be leveraged to create SDNs with channel heights from a few nm down to less than 1 nm.[17] Superimposition of surface acoustic waves on SDNs can also be used to induce new modes of transport. Driven fluctuations are expected to enhance ionic conductance, selectivity, and transport. Such systems may also enable electrochemical gating in a dynamic and fully controllable manner, which is a longstanding goal of electrokinetic transport. How the frequency of electrochemical fluctuations can influence transport is a fascinating open question.

Another interesting opportunity is the investigation of systems in which either (or both) solvent or (and) ions create organized structures at the SDN interface. Examples include bilayer-like structures created by molecules of polar, high-dipole moment solvents on polar surfaces, and spatial organization of correlated multivalent ions on charged surfaces (charge inversion).[402,433] Driven fluctuations may disturb the organization in both cases, leading to the continuous spatial and temporal reorganization of solvent and ions. The theoretical description of such dynamic systems will in turn enable the quantification of the energetics and kinetics of the interfacial organization.

7.1.4. Molecular Tunneling through Atomically Thin Membranes. Recent experiments showing proton electrokinetic transport through one-atom-thick membranes of graphene can be explained via molecular tunneling.[857] This observation opens the question of whether such molecular tunneling is a generic confinement effect, which could enable new mechanisms of transport in permselective membranes. Some computational studies have focused on low-temperature, quantum sieving based on differences on zero-point energy for isotope separation.[858] However, there is a dearth of experimental studies elucidating this effect and its applications to confined transport for species larger than protons.

7.1.5. A Universal Molecular Force Field for Fluids under Confinement. Whether a universal force field could be created to describe fluids under confinement is an open question. Such a force field would require chemical composition and dimension of the pore as the sole inputs. Although there has been interest in the development of this type of generic force field, with AMOEBA[859] as an example, this objective might in fact be unattainable. Recent theoretical developments instead suggest that a proliferation of specialized force fields is more likely to occur before any universal force field could be developed.[860] For example, even for simple systems such as solvated ions in liquid water, no generic force field has been developed to date.[861,862] The case of nanoconfinement, in which wall interactions must also be considered, remains all the more elusive. The outstanding challenge is often related to the ability to treat different interactions (e.g., water−ion, ion−pore, and water−pore) on the same footing. To this end, specialized force fields with high accuracy that incorporate many-body electronic polarization effects from first-principles have been developed for some systems. Applications have included modeling of the wetting behavior and salt ion adsorption at the graphene−water interface,[447,450,456] phase behavior of confined water,[863] and quantum friction at the water−CNT interface.[6] However, the development of force fields for more complex systems remains a challenging task. In this regard, although the development of a universal force field may currently be too ambitious, it may nevertheless be possible to construct a universal platform that combines a high-fidelity, first-principles approach and machine learning techniques[864] to tackle this challenge.

7.1.6. Chemical Reactions under Fluidic Transport Conditions within a SDN. Extreme physical confinement in an SDN influences the structure and intramolecular potential of fluid molecules and entrained reactants, such that large changes in chemical reactivity should be possible. These effects are observed experimentally at even at larger scales. For example, the detection of enzymatic reactions in nanofluidic channels has been shown to progress faster than the binding reaction at a flat

https://doi.org/10.1021/acs.chemrev.2c00155
Chem. Rev. 2023, 123, 2737−2831

surface, reaching single-enzyme sensitivity.[865] In narrow channels, the restructuring of the fluid itself can change the activation volume to either favor or disfavor certain transition states, depending upon the polarity and steric hindrance imposed by the dynamic solvent cage.[866] In this manner, fluid confinement in an SDN can select for different products than in the corresponding bulk reaction. We note that this mechanism is distinct from steric exclusion or molecular sieving. Although there has been a considerable amount of work on the role of nanopores in heterogeneous chemical catalysis,[867] new types of reactive force fields that take into account nanoconfinement may need to be developed to enable the prediction of the activation volumes, and more generally the transition state, under such transport conditions for a given chemistry.

Elucidating these knowledge gaps should enable new, energy-saving solutions for applications ranging from precision separations, to energy efficient transport solutions, to perhaps even new types of information storage and computing systems. Precision separations that would mimic, and even surpass, the accuracy and efficiency of biological separation could revolutionize water purification and chemical manufacturing. Efficient and selective transport materials could remedy shortcomings of current battery technologies, thus accelerating transition to carbon-neutral economy. Finally, new types of information storage and processing architectures based on ionics and nanofluidics that mimic brain signal processing could enable efficient computing at a fraction of the power and cost used today.

AUTHOR INFORMATION

Corresponding Authors

Michael S. Strano − *Department of Chemical Engineering, Massachusetts Institute of Technology, Cambridge, Massachusetts 02139, United States;* orcid.org/0000-0003-2944-808X; Email: Strano@mit.edu

John T. Fourkas − *Department of Chemistry and Biochemistry, University of Maryland, College Park, Maryland 20742, United States; Institute for Physical Science and Technology and Maryland NanoCenter, University of Maryland, College Park, Maryland 20742, United States;* orcid.org/0000-0002-4522-9584; Email: fourkas@umd.edu

YuHuang Wang − *Department of Chemistry and Biochemistry, University of Maryland, College Park, Maryland 20742, United States; Maryland NanoCenter, University of Maryland, College Park, Maryland 20742, United States;* orcid.org/0000-0002-5664-1849; Email: yhw@umd.edu

Authors

Narayana R. Aluru − *Oden Institute for Computational Engineering and Sciences, Walker Department of Mechanical Engineering, The University of Texas at Austin, Austin 78712 Texas, United States;* orcid.org/0000-0002-9622-7837

Fikret Aydin − *Materials Science Division, Physical and Life Science Directorate, Lawrence Livermore National Laboratory, Livermore, California 94550, United States;* orcid.org/0000-0003-3237-8043

Martin Z. Bazant − *Department of Chemical Engineering, Massachusetts Institute of Technology, Cambridge, Massachusetts 02139, United States; Department of Mathematics, Massachusetts Institute of Technology, Cambridge, Massachusetts 02139, United States;* orcid.org/0000-0002-8200-4501

Daniel Blankschtein − *Department of Chemical Engineering, Massachusetts Institute of Technology, Cambridge, Massachusetts 02139, United States;* orcid.org/0000-0002-7836-415X

Alexandra H. Brozena − *Department of Chemistry and Biochemistry, University of Maryland, College Park, Maryland 20742, United States*

J. Pedro de Souza − *Department of Chemical Engineering, Massachusetts Institute of Technology, Cambridge, Massachusetts 02139, United States;* orcid.org/0000-0003-3634-4991

Menachem Elimelech − *Department of Chemical and Environmental Engineering, Yale University, New Haven, Connecticut 06520-8286, United States;* orcid.org/0000-0003-4186-1563

Samuel Faucher − *Department of Chemical Engineering, Massachusetts Institute of Technology, Cambridge, Massachusetts 02139, United States;* orcid.org/0000-0002-2562-1079

Volodymyr B. Koman − *Department of Chemical Engineering, Massachusetts Institute of Technology, Cambridge, Massachusetts 02139, United States;* orcid.org/0000-0001-8480-4003

Matthias Kuehne − *Department of Chemical Engineering, Massachusetts Institute of Technology, Cambridge, Massachusetts 02139, United States;* orcid.org/0000-0002-5096-7522

Heather J. Kulik − *Department of Chemical Engineering, Massachusetts Institute of Technology, Cambridge, Massachusetts 02139, United States;* orcid.org/0000-0001-9342-0191

Hao-Kun Li − *Department of Mechanical Engineering, Stanford University, Stanford, California 94305, United States*

Yuhao Li − *Materials Science Division, Physical and Life Science Directorate, Lawrence Livermore National Laboratory, Livermore, California 94550, United States;* orcid.org/0000-0003-1839-0900

Zhongwu Li − *Materials Science Division, Physical and Life Science Directorate, Lawrence Livermore National Laboratory, Livermore, California 94550, United States*

Arun Majumdar − *Department of Mechanical Engineering, Stanford University, Stanford, California 94305, United States;* orcid.org/0000-0003-4226-9705

Joel Martis − *Department of Mechanical Engineering, Stanford University, Stanford, California 94305, United States*

Rahul Prasanna Misra − *Department of Chemical Engineering, Massachusetts Institute of Technology, Cambridge, Massachusetts 02139, United States;* orcid.org/0000-0001-5574-2384

Aleksandr Noy − *Materials Science Division, Physical and Life Science Directorate, Lawrence Livermore National Laboratory, Livermore, California 94550, United States; School of Natural Sciences, University of California Merced, Merced, California 95344, United States;* orcid.org/0000-0003-4924-2652

Tuan Anh Pham − *Materials Science Division, Physical and Life Science Directorate, Lawrence Livermore National Laboratory, Livermore, California 94550, United States;* orcid.org/0000-0003-0025-7263

Haoran Qu − *Department of Chemistry and Biochemistry, University of Maryland, College Park, Maryland 20742, United States;* orcid.org/0000-0003-4536-6703

Archith Rayabharam − *Oden Institute for Computational Engineering and Sciences, Walker Department of Mechanical*

https://doi.org/10.1021/acs.chemrev.2c00155
Chem. Rev. 2023, 123, 2737−2831

Engineering, The University of Texas at Austin, Austin 78712 Texas, United States; orcid.org/0000-0003-0911-2319

†**Mark A. Reed** − *Department of Electrical Engineering, Yale University, New Haven, Connecticut 06520, United States*

Cody L. Ritt − *Department of Chemical and Environmental Engineering, Yale University, New Haven, Connecticut 06520-8286, United States;* orcid.org/0000-0002-3215-1685

Eric Schwegler − *Materials Science Division, Physical and Life Science Directorate, Lawrence Livermore National Laboratory, Livermore, California 94550, United States*

Zuzanna Siwy − *Department of Physics and Astronomy, Department of Chemistry, Department of Biomedical Engineering, University of California, Irvine, Irvine 92697, United States;* orcid.org/0000-0003-2626-7873

Yun-Chiao Yao − *Materials Science Division, Physical and Life Science Directorate, Lawrence Livermore National Laboratory, Livermore, California 94550, United States; School of Natural Sciences, University of California Merced, Merced, California 95344, United States*

Cheng Zhan − *Materials Science Division, Physical and Life Science Directorate, Lawrence Livermore National Laboratory, Livermore, California 94550, United States*

Ze Zhang − *Department of Mechanical Engineering, Stanford University, Stanford, California 94305, United States;* orcid.org/0000-0002-3019-0138

Complete contact information is available at: https://pubs.acs.org/10.1021/acs.chemrev.2c00155

Author Contributions

CRediT: **Narayana R. Aluru** writing-original draft, writing-review & editing; **Fikret Aydin** writing-original draft, writing-review & editing; **Martin Z. Bazant** writing-original draft, writing-review & editing; **Daniel Blankschtein** writing-original draft, writing-review & editing; **Alexandra Brozena** writing-original draft, writing-review & editing; **J. Pedro de Souza** writing-original draft, writing-review & editing; **Menachem Elimelech** writing-original draft, writing-review & editing; **Samuel Faucher** writing-original draft, writing-review & editing; **John T. Fourkas** writing-original draft, writing-review & editing; **Volodymyr B. Koman** writing-original draft, writing-review & editing; **Matthias Kuehne** writing-original draft, writing-review & editing; **Heather J. Kulik** writing-original draft, writing-review & editing; **Hao-Kun Li** writing-original draft, writing-review & editing; **Yuhao Li** writing-original draft, writing-review & editing; **Zhongwu Li** writing-original draft, writing-review & editing; **Arun Majumdar** writing-original draft, writing-review & editing; **Joel Martis** writing-original draft, writing-review & editing; **Rahul Prasanna Misra** writing-original draft, writing-review & editing; **Aleksandr Noy** writing-original draft, writing-review & editing; **Tuan Anh Pham** writing-original draft, writing-review & editing; **Haoran Qu** writing-original draft, writing-review & editing; **Archith Rayabharam** writing-original draft, writing-review & editing; **Mark A. Reed** writing-original draft, writing-review & editing; **Cody L. Ritt** writing-original draft, writing-review & editing; **Eric Schwegler** writing-original draft, writing-review & editing; **Zuzanna S. Siwy** writing-original draft, writing-review & editing; **Michael S. Strano** writing-original draft, writing-review & editing; **YuHuang Wang** writing-original draft, writing-review & editing; **Yun-Chiao Yao** writing-original draft, writing-review & editing; **Cheng Zhang** writing-original draft, writing-review & editing; **Ze Zhang** writing-original draft, writing-review & editing.

Notes

The authors declare no competing financial interest.

†Deceased.

Biographies

Narayana Aluru received his Ph.D. from Stanford University in 1995 and was a Postdoctoral Associate at the Massachusetts Institute of Technology from 1995 to 1997. He is currently a Professor in the Oden Institute for Computational Engineering and Sciences and in the Walker Department of Mechanical Engineering at the University of Texas at Austin. He was on the faculty at the University of Illinois at Urbana−Champaign from 1998 to 2021. His research interests focus on the development of multiscale and multiphysics methods to understand physics of nanofluidics, nanoelectromechanical systems, and nanomaterials.

Fikret Aydin is currently a postdoctoral researcher in Quantum Simulation Group of Material Science Division. He received a Ph.D. in Chemical and Biochemical Engineering at Rutgers University, and a B.Sc. in Chemical and Biological Engineering at Koc University in Istanbul, Turkey. His research interests lie at the intersection of biology and chemistry. He has designed and implemented various nanoscopic and mesoscopic simulation techniques, including all-atom and coarse-grained molecular dynamics simulations, enhanced free-energy sampling techniques to study behavior of systems ranging from drug and protein molecules to synthetic/biopolymeric materials. Some of his current research topics are understanding transport and selectivity of ions under nanoscale confinement, testing accuracy of force fields for predicting ion dynamics and solvations under confinement in molecular dynamics simulations, and multiscale modeling of membrane proteins.

Martin Z. Bazant is the E. G. Roos (1944) Professor of Chemical Engineering and Mathematics and Executive Officer of the Department of Chemical Engineering at the Massachusetts Institute of Technology. After a Ph.D. in Physics at Harvard (1997), he joined the MIT faculty in Mathematics (1998) and then in Chemical Engineering (2008). He is a Fellow of the American Physical Society, the International Society of Electrochemistry, the Royal Society of Chemistry (FRSC), and winner of the 2015 Kuznetsov Prize in Theoretical Electrochemistry (ISE) and 2018 Andreas Acrivos Award for Professional Progress in Chemical Engineering (AIChE). He also serves as the Chief Scientific Advisor for Saint Gobain Ceramics and Plastics, North America.

Daniel Blankschtein is the Herman P. Meissner '29 Professor of Chemical Engineering at MIT. He received a Ph.D. in Condensed Matter Physics in 1983 from Tel-Aviv University in Israel and carried out postdoctoral studies in the Physics Department at MIT before joining the Chemical Engineering Faculty at MIT in 1986. He has 15 issued patents and has published over 230 research articles in the general subjects of molecular−thermodynamic and statistical mechanics modeling of self-assembling surfactant systems, bioseparations using two-phase aqueous micellar and polymer systems, transdermal drug delivery using ultrasound and chemical enhancers, and modeling of wetting phenomena and liquid-phase exfoliation of 2D nanomaterials using MD simulations. He has received several awards, including a Presidential Young Investigator Award, the 1996 Ebert Prize from the American Pharmaceutical Association, the 2000 Dow Corning Award from the Controlled Release Society, the 2015 Capers and Marlon McDonald Award for Excellence in Mentoring and Advising, and nine Outstanding Faculty Awards for his teaching of graduate-level Thermodynamics. He serves as advisory editor of the Marcel Dekker Surfactant Science Series. His new book, *Lectures in Classical Thermodynamics with an Introduction to Statistical Mechanics*, was published by Springer in March 2021.

https://doi.org/10.1021/acs.chemrev.2c00155
Chem. Rev. 2023, 123, 2737−2831

Alexandra H. Brozena is a Faculty Specialist at the University of Maryland, College Park. She attended Tulane University for undergraduate studies in English and Environmental Science and later received a Ph.D. in Chemistry from the University of Maryland in 2013 under the direction of Prof. YuHuang Wang. At Maryland, she studied mechanisms of covalent functionalization of carbon nanotubes with support from the Department of Energy Office of Science Graduate Fellowship. Her postdoctoral research at North Carolina State University with Prof. Greg Parsons explored metal oxide coatings on textiles via spatial atomic layer deposition.

J. Pedro de Souza is a Ph.D. candidate in the Department of Chemical Engineering at MIT. He received his B.Sc. in Chemical Engineering at the University of Texas at Austin in 2016. He works with Martin Bazant on theory and modeling of the electrical double layer and ion correlations.

Menachem Elimelech is the Sterling Professor of Chemical and Environmental Engineering at Yale University. His research focuses on membrane-based technologies at the water−energy nexus, materials for next-generation desalination and water purification membranes, and environmental applications of nanomaterials. Professor Elimelech was the recipient of numerous awards in recognition of his research contributions. Notable among these awards are the 2005 Clarke Prize for excellence in water research, election to the U.S. National Academy of Engineering in 2006, the Eni Prize for "Protection of the Environment" in 2015, and election as a foreign member to the Chinese Academy of Engineering in 2017 and the Australian Academy of Technology and Engineering in 2021. In recognition of his excellence in teaching and mentoring, he received the W. M. Keck Foundation Engineering Teaching Excellence Award in 1994, the Yale University Graduate Mentoring Award in 2004, and the Yale University Postdoctoral Mentoring Prize in 2012.

Samuel Faucher obtained a B.Sc. in Chemical Engineering from Yale University and completed his Ph.D. in Chemical Engineering at MIT in 2022. His research interests include nanofluidics of carbon nanotubes and decarbonized routes to chemical manufacturing.

John T. Fourkas is the Millard Alexander Professor of Chemistry at the University of Maryland, College Park, where he holds appointments in the Department of Chemistry and Biochemistry and the Institute for Physical Science and Technology. He received his B.Sc. and M.Sc. in Chemistry from Caltech in 1986, and his Ph.D. in Chemistry from Stanford University in 1991. His research involves applications of ultrafast, nonlinear optics in spectroscopy, imaging, and nanofabrication. The dynamics and organization of liquids in nanoconfinement and at interfaces is a longstanding interest of his research group.

Volodymyr B. Koman is a research scientist in Chemical Engineering at MIT. Dr. Koman received his Ph.D. in Photonics in 2015 from EPFL, Switzerland. He continued his research as a PostDoc at MIT under Prof. Michael Strano, supported by Swiss NSF fellowships. He is the recipient of Erasmus Mundus Photonics Scholarship and President of Ukraine Scholarship. His research interests include nanotechnology at the interface of living entities and photonics.

Matthias Kuehne is a postdoctoral researcher at MIT and will join Brown University as an assistant professor of Physics in 2023. Matthias did his doctoral studies at the Max Planck Institute for Solid State Research, for which he received a Doctorate of natural sciences (Dr. rer. nat.) from the University of Stuttgart, Germany. Matthias holds a diplome d'ingenieur from Grenoble Institute of Technology (Grenoble INP), France, as well as a diploma in Physics from Karlsruhe Institute of Technology, Germany. His group at Brown University investigates fluidic, ionic, and electronic properties of low-dimensional materials and devices.

Heather J. Kulik is an associate professor of Chemical Engineering at MIT. Prior to joining MIT as a faculty member in 2013, she completed a B.E. in Chemical Engineering at The Cooper Union in 2004, a Ph.D. in Materials Science and engineering at MIT in 2009, and postdoctoral training at Lawrence Livermore National Laboratory (2009−2010) and Stanford University (2010−2013).

Hao-Kun Li received his B.S. in Physics in 2013 from Peking University and his Ph.D. in Applied Science and Technology in 2019 from University of California, Berkeley. He then joined Majumdar's group at Stanford University as a postdoctoral researcher. His research is centered around nanomechanics.

Yuhao Li is currently a research scientist in the Physical and Life Sciences Directorate at Lawrence Livermore National Laboratory (LLNL). He joined LLNL as a postdoc in 2018 after receiving a Ph.D. in Materials Physics and Chemistry at Sun Yat-sen University in Guanghzou, China. His current research interests include exploring anomalous water/ion transport in nanoconfinement, developing biomimetic materials, and devices for desalination and membrane separation.

Zhongwu Li received his B.E. in Mechanical Engineering from China University of Mining and Technology (CUMT, China) in 2015 and his Ph.D. in Mechanical Engineering from Southeast University (SEU, China) in 2021. He was also a joint-Ph.D. student at Lawrence Livermore National Laboratory (LLNL, USA) under the supervision of Dr. Aleksandr Noy. He is currently an Assistant Professor in School of Mechatronic Engineering at CUMT, China. His current research focuses on nanofluidics in low-dimensional carbon nanochannels and their applications on iontronics, sensors, and membranes.

Arun Majumdar is the Chester Naramore Dean of the Stanford Doerr School of Sustainability, Jay Precourt Professor of Mechanical Engineering & Energy Science and Engineering, and Senior Fellow and former Director of the Precourt Institute for Energy. He is also a faculty member in the Department of Materials Science and Engineering (by courtesy) and Photon Science at SLAC. He served in the Obama administration as the Founding Director of the Advanced Research Projects Agency - Energy (ARPA-E) and as the Acting Under Secretary of Energy. He served as a Science Envoy for the US Department of State and currently serves as the Chair of the US Secretary of Energy Advisory Board. Dr. Majumdar was also the Vice President for Energy at Google and advises numerous business in the energy innovation ecosystem. He is a member of the US National Academy of Sciences, US National Academy of Engineering and the American Academy of Arts and Sciences. He received his Bachelors degree in Mechanical Engineering at the Indian Institute of Technology, Bombay in 1985 and his Ph.D. from the University of California, Berkeley in 1989.

Joel Martis is a Ph.D. candidate in the Majumdar Lab, Department of Mechanical Engineering, at Stanford University. He received his B.Tech in Mechanical Engineering from the Indian Institute of Technology Madras, India, in 2017. Joel works on using electron microcopy in novel ways to image nanopores and nanofluidic phenomena.

Rahul Prasanna Misra received his B.Tech in Chemical Engineering from the Indian Institute of Technology, Kharagpur, India, and his Master of Science in Chemical Engineering Practice (MSCEP) and Ph.D. in Chemical Engineering degrees from the Massachusetts Institute of Technology. As part of his Ph.D. under the supervision of Professor Daniel Blankschtein, he developed a multiscale framework to self-consistently model electronic polarization effects in interfacial thermodynamics and nanoscale transport phenomena. Currently, Rahul is a postdoctoral associate working with Professor Daniel

https://doi.org/10.1021/acs.chemrev.2c00155
Chem. Rev. 2023, 123, 2737−2831

Blankschtein, where his research focuses on atomistic modeling of pure water and electrolytes in nanofluidic applications.

Aleksandr Noy is a Senior Research Scientist at the Physical and Life Sciences Directorate at the Lawrence Livermore National Laboratory and an Adjunct Professor at the University of California Merced. He received his Ph.D. from Harvard University, where he developed single molecule force spectroscopy approaches for characterizing intermolecular interactions. After he came to LLNL as an E. O. Lawrence Fellow, he pivoted to bionanomaterials research and nanoscale transport studies. His current research interest center on carbon nanotube nanofluidics and the role of extreme spatial confinement on transport properties of these unique nanochannels.

Tuan Anh Pham is a staff scientist in the Quantum Simulations Group at the Lawrence Livermore National Laboratory (LLNL). He joined LLNL as a Lawrence Fellow in 2014 after receiving a Ph.D. in Physical Chemistry at the University of California, Davis. His research interests include the development and application of first-principles simulation techniques to validate, understand, and predict material properties for energy and environmental applications. These include ion batteries, supercapacitors, hydrogen production through solar-water-splitting, and water desalination. He has received numerous awards, including the LLNL Directorate Award for Excellence in Publication, LLNL Deputy Director for Science and Technology Excellence in Publication Awards, and LLNL Outstanding Mentor Award.

Haoran Qu received his B.E. in Applied Chemistry from East China University of Science and Technology (ECUST) and received his M.S. in Polymer Science from the University of Akron under the supervision of Dr. Stephen Z. D. Cheng. Currently, he is a Ph.D. student in the group of Dr. YuHuang Wang at the University of Maryland, College Park, where his research involves sp^3 quantum defects, liquid/ions under confinement of single-digit nanopores.

Archith Rayabharam is a Ph.D. student in the Aluru Lab, at the University of Illinois, Urbana—Champaign. He received his B.Tech from Indian Institute of Technology Kanpur, India, in 2017. He works on modeling various nanofluidic phenomena using ab initio simulations.

Mark A. Reed received his Ph.D. in Physics from Syracuse University in 1983, after which he joined Texas Instruments. In 1990, Mark joined Yale University, where he held the Harold Hodgkinson Chair of Engineering and Applied Science. He was chairman of the Department of Electrical Engineering from 1995 to 2001, and was the founding Associate Director of the Yale Institute for Nanoscience and Quantum Engineering. Mark's research activities have included the investigation of electronic transport in nanoscale and mesoscopic systems, artificially structured materials and devices, molecular scale electronic transport, chem/bio nanosensors, and nanoionic transport. Mark is the author of more than 200 professional publications and 6 books, has given over 75 plenary and over 400 invited talks, and holds 33 U.S. and foreign patents on quantum effect, heterojunction, and molecular devices. He was the Editor in Chief of the journal *Nanotechnology* (2009−2019), was the recent Editor-in-Chief of the journal *Nano Futures*, and holds numerous other editorial and advisory board positions. Mark has been elected to the Connecticut Academy of Science and Engineering and Who's Who in the World. His awards include; Fortune Magazine "Most Promising Young Scientist" (1990), the Kilby Young Innovator Award (1994), the Fujitsu ISCS Quantum Device Award (2001), the Yale Science and Engineering Association Award for Advancement of Basic and Applied Science (2002), Fellow of the American Physical Society (2003), the IEEE Pioneer Award in Nanotechnology (2007), Fellow of the Institute of Electrical and Electronics Engineers (2009), a Finalist for the World Technology Award (2010), and the CBA Distinguished Alumni Award (2019).

Cody L. Ritt is a Ph.D. candidate in the Elimelech Research Group, part of the Department of Chemical and Environmental Engineering at Yale University. Cody received his B.Sc. and M.Sc. in Civil Engineering from North Dakota State University, where his research focused on developing phosphate-selective sorbents for mitigation of eutrophic surface waters. At Yale, his work focuses on fundamental membrane transport and nanofluidics applied at the water−energy nexus.

Eric Schwegler is the Director of the Academic Engagement Office at Lawrence Livermore National Laboratory. He has a B.Sc. in Chemistry and Computer Science from Southwestern University and a Ph.D. in Physical Chemistry from the University of Minnesota. His research interests include combining state-of-the-art quantum simulation capabilities with large-scale computing to predict the properties of materials, including fluids confined at the nanoscale. He is a member of the Leadership Team for the Critical Materials Institute, a DOE Energy Innovation Hub, and is a Fellow of the American Physical Society

Zuzanna S. Siwy received her Ph.D. in 1997 from the Silesian University of Technology, Gliwice, Poland, and habilitation in 2004. From 2000 to 2003, she was a Fellow of the Foundation for Polish Science and the Alexander von Humboldt Foundation at the Institute for Heavy Ions Research (GSI) in Darmstadt, Germany. After conducting postdoctoral research at the University of Florida, Gainesville, in July 2005, Dr. Siwy joined the Department of Physics and Astronomy at the University of California, Irvine. In 2007, she became the Fellow of the Alfred von Sloan Foundation. In 2009, Dr. Siwy was awarded the Presidential Early Career Award for Scientists and Engineers as well as the Bessel Award from the Alexander von Humboldt Foundation. She is a Fellow of the American Physical Society, and AAAS. Her current research interests focus on using synthetic nanopores as templates for biomimetic channels as well as ionic diodes and ionic transistors.

Michael S. Strano is currently the Carbon P. Dubbs Professor in the Chemical Engineering Department at the Massachusetts Institute of Technology. He received is B.Sc from Polytechnic University in Brooklyn, NY, and Ph.D. from the University of Delaware, both in Chemical Engineering. He was a post doctoral research fellow at Rice University in the Departments of Chemistry and Physics under the guidance of Nobel Laureate Richard E. Smalley. From 2003 to 2007, Michael was an Assistant Professor in the Department of Chemical and Biomolecular Engineering at the University of Illinois at Urbana—Champaign before moving to MIT. His research focuses on biomolecule/nanoparticle interactions and the surface chemistry of low dimensional systems, nanoelectronics, nanoparticle separations, and applications of vibrational spectroscopy to nanotechnology. Michael is the recipient of numerous awards for his work, including a 2005 Presidential Early Career Award for Scientists and Engineers, a 2006 Beckman Young Investigator Award, the 2006 Coblentz Award for Molecular Spectroscopy, the Unilever Award from the American Chemical Society in 2007 for excellence in colloidal science, and the 2008 Young Investigator Award from the Materials Research Society and the 2008 Allen P. Colburn Award from the American Institute of Chemical Engineers. From 2014 to 2015, he served as member of the Defense Science Study Group and is currently an editor for the journals *Carbon* and *Protocols in Chemical Biology*. Michael was elected to the National Academy of Engineering in 2017.

YuHuang Wang is a Professor of Chemistry at the University of Maryland, College Park. He received a Ph.D. in Chemistry from Rice University in 2005 under the guidance of Richard E. Smalley and did his postdoctoral studies with Chad A. Mirkin at Northwestern University before joining the Maryland faculty in 2008. His research group focuses

https://doi.org/10.1021/acs.chemrev.2c00155
Chem. Rev. 2023, 123, 2737−2831

on the chemical physics and the synthesis of sp^3 quantum defects (also known as organic color centers) to understand and control the coupling of electrons, excitons, phonons, and spin at defects. They also develop instrumentation, methodologies, and platform technologies to address fundamental challenges in energy, biomedical, and quantum technologies.

Yun-Chiao Yao received her B.Sc. and M.Sc. in Chemistry from the National Taiwan University. In 2015, she joined Dr. Aleksandr Noy's group at the University of California, Merced, and Lawrence Livermore National Laboratory (LLNL) for graduate study. Her work focused on ionic transport through sub-2-nm carbon nanotube porins, and she received her Ph.D. in 2021.

Cheng Zhan obtained his B.Sc. degree from the University of Science and Technology of China (USTC) in 2013 and hia Ph.D. degree from the University of California, Riverside, in 2018. From 2018 to 2021, Dr. Cheng Zhan was hired as a postdoc by the Material Science Division (MSD) of the Lawrence Livermore National Laboratory (LLNL). Currently, Dr. Cheng Zhan is a Professor in the Department of Applied Physics of the Nanjing University of Science and Technology (NUST) in China. His research mainly focuses on the computational material modeling and electrochemical interface.

Ze Zhang received her Bachelor's degree from Department of Engineering Mechanics, Tsinghua University, China, in 2015. In 2021, she obtained her Ph.D. degree from Department of Mechanical Engineering, Stanford, studying electron microscopy and nanoscale heat transfer. Currently, Ze is a R&D engineer at Hisilicon.

ACKNOWLEDGMENTS

This work is supported as a part of the Center for Enhanced Nanofluidic Transport (CENT), an Energy Frontier Research Center funded by the U.S. Department of Energy, Office of Science, Basic Energy Sciences under award no. DE-SC0019112. M.K. acknowledges support by the German Research Foundation (DFG) Research Fellowship KU 3952/1-1. J.P.S. acknowledges National Science Foundation Graduate Research Fellowship under grant no. 1122374. Part of this work was performed under the auspices of the U.S. Department of Energy by Lawrence Livermore National Laboratory under Contract DE-AC52-07NA27344.

REFERENCES

(1) Tunuguntla, R. H.; Henley, R. Y.; Yao, Y. C.; Pham, T. A.; Wanunu, M.; Noy, A. Enhanced Water Permeability and Tunable Ion Selectivity in Subnanometer Carbon Nanotube Porins. *Science* **2017**, *357*, 792−796.

(2) Holt, J. K.; Park, H. G.; Wang, Y.; Stadermann, M.; Artyukhin, A. B.; Grigoropoulos, C. P.; Noy, A.; Bakajin, O. Fast Mass Transport through Sub-2-Nanometer Carbon Nanotubes. *Science* **2006**, *312*, 1034−1037.

(3) Agrawal, K. V.; Shimizu, S.; Drahushuk, L. W.; Kilcoyne, D.; Strano, M. S. Observation of Extreme Phase Transition Temperatures of Water Confined inside Isolated Carbon Nanotubes. *Nat. Nanotechnol.* **2017**, *12*, 267−273.

(4) Shimizu, S.; Agrawal, K. V.; O'Mahony, M.; Drahushuk, L. W.; Manohar, N.; Myerson, A. S.; Strano, M. S. Understanding and Analyzing Freezing-Point Transitions of Confined Fluids within Nanopores. *Langmuir* **2015**, *31*, 10113−10118.

(5) Kavokine, N.; Marbach, S.; Siria, A.; Bocquet, L. Ionic Coulomb Blockade as a Fractional Wien Effect. *Nat. Nanotechnol.* **2019**, *14*, 573−578.

(6) Kavokine, N.; Bocquet, M.-L.; Bocquet, L. Fluctuation-Induced Quantum Friction in Nanoscale Water Flows. *Nature* **2022**, *602*, 84−90.

(7) Epsztein, R.; DuChanois, R. M.; Ritt, C. L.; Noy, A.; Elimelech, M. Towards Single-Species Selectivity of Membranes with Subnanometre Pores. *Nat. Nanotechnol.* **2020**, *15*, 426−436.

(8) Robin, P.; Kavokine, N.; Bocquet, L. Modeling of Emergent Memory and Voltage Spiking in Ionic Transport through Angstrom-Scale Slits. *Science* **2021**, *373*, 687−691.

(9) Werber, J. R.; Osuji, C. O.; Elimelech, M. Materials for Next-Generation Desalination and Water Purification Membranes. *Nat. Rev. Mater.* **2016**, *1*, 16018.

(10) Zhang, A.; Lieber, C. M. Nano-Bioelectronics. *Chem. Rev.* **2016**, *116*, 215−257.

(11) Smolyanitsky, A.; Paulechka, E.; Kroenlein, K. Aqueous Ion Trapping and Transport in Graphene-Embedded 18-Crown-6 Ether Pores. *ACS Nano* **2018**, *12*, 6677−6684.

(12) Faucher, S.; Aluru, N.; Bazant, M. Z.; Blankschtein, D.; Brozena, A. H.; Cumings, J.; de Souza, J. P.; Elimelech, M.; Epsztein, R.; Fourkas, J. T.; et al. Critical Knowledge Gaps in Mass Transport through Single-Digit Nanopores: A Review and Perspective. *J. Phys. Chem. C* **2019**, *123*, 21309−21326.

(13) Lee, C. Y.; Choi, W.; Han, J. H.; Strano, M. S. Coherence Resonance in a Single-Walled Carbon Nanotube Ion Channel. *Science* **2010**, *329*, 1320−1324.

(14) Min, H.; Kim, Y.-T.; Moon, S. M.; Han, J.-H.; Yum, K.; Lee, C. Y. High-Yield Fabrication, Activation, and Characterization of Carbon Nanotube Ion Channels by Repeated Voltage-Ramping of Membrane-Capillary Assembly. *Adv. Funct. Mater.* **2019**, *29*, 1900421.

(15) Tunuguntla, R. H.; Allen, F. I.; Kim, K.; Belliveau, A.; Noy, A. Ultrafast Proton Transport in Sub-1-Nm Diameter Carbon Nanotube Porins. *Nat. Nanotechnol.* **2016**, *11*, 639.

(16) Dellago, C.; Naor, M. M.; Hummer, G. Proton Transport through Water-Filled Carbon Nanotubes. *Phys. Rev. Lett.* **2003**, *90*, 105902.

(17) Gopinadhan, K.; Hu, S.; Esfandiar, A.; Lozada-Hidalgo, M.; Wang, F. C.; Yang, Q.; Tyurnina, A. V.; Keerthi, A.; Radha, B.; Geim, A. K. Complete Steric Exclusion of Ions and Proton Transport through Confined Monolayer Water. *Science* **2019**, *363*, 145−147.

(18) Choi, W.; Ulissi, Z. W.; Shimizu, S. F.; Bellisario, D. O.; Ellison, M. D.; Strano, M. S. Diameter-Dependent Ion Transport through the Interior of Isolated Single-Walled Carbon Nanotubes. *Nat. Commun.* **2013**, *4*, 2397.

(19) Fornasiero, F.; Park, H. G.; Holt, J. K.; Stadermann, M.; Grigoropoulos, C. P.; Noy, A.; Bakajin, O. Ion Exclusion by Sub-2-Nm Carbon Nanotube Pores. *Proc. Natl. Acad. Sci. U.S.A.* **2008**, *105*, 17250−17255.

(20) Fornasiero, F.; In, J. B.; Kim, S.; Park, H. G.; Wang, Y.; Grigoropoulos, C. P.; Noy, A.; Bakajin, O. Ph-Tunable Ion Selectivity in Carbon Nanotube Pores. *Langmuir* **2010**, *26*, 14848−14853.

(21) Neklyudov, V.; Freger, V. Putting Together the Puzzle of Ion Transfer in Single-Digit Carbon Nanotubes: Mean-Field Meets Ab Initio. *Nanoscale* **2022**, *14*, 8677−8690.

(22) D'Odorico, P.; Davis, K. F.; Rosa, L.; Carr, J. A.; Chiarelli, D.; Dell'Angelo, J.; Gephart, J.; MacDonald, G. K.; Seekell, D. A.; Suweis, S.; et al. The Global Food-Energy-Water Nexus. *Rev. Geophys.* **2018**, *56*, 456−531.

(23) Shannon, M. A.; Bohn, P. W.; Elimelech, M.; Georgiadis, J. G.; Marinas, B. J.; Mayes, A. M. Science and Technology for Water Purification in the Coming Decades. *Nature* **2008**, *452*, 301−310.

(24) Mekonnen, M. M.; Hoekstra, A. Y. Four Billion People Facing Severe Water Scarcity. *Sci. Adv.* **2016**, *2*, No. e1500323.

(25) Elimelech, M. The Global Challenge for Adequate and Safe Water. *J. Water Supply Res. T* **2006**, *55*, 3−10.

(26) Elimelech, M.; Phillip, W. A. The Future of Seawater Desalination: Energy, Technology, and the Environment. *Science* **2011**, *333*, 712−717.

(27) Chavez-Rodriguez, M. F.; Nebra, S. A. Assessing Ghg Emissions, Ecological Footprint, and Water Linkage for Different Fuels. *Environ. Sci. Technol.* **2010**, *44*, 9252−9257.

(28) Schnoor, J. L. Water-Energy Nexus. *Environ. Sci. Technol.* **2011**, *45*, 5065−5065.

https://doi.org/10.1021/acs.chemrev.2c00155
Chem. Rev. 2023, 123, 2737−2831

(29) Werber, J. R.; Deshmukh, A.; Elimelech, M. The Critical Need for Increased Selectivity, Not Increased Water Permeability, for Desalination Membranes. *Environ. Sci. Technol. Lett.* **2016**, *3*, 112−120.
(30) Park, H. B.; Kamcev, J.; Robeson, L. M.; Elimelech, M.; Freeman, B. D. Maximizing the Right Stuff: The Trade-Off between Membrane Permeability and Selectivity. *Science* **2017**, *356*, eaab0530.
(31) Cohen-Tanugi, D.; McGovern, R. K.; Dave, S. H.; Lienhard, J. H.; Grossman, J. C. Quantifying the Potential of Ultra-Permeable Membranes for Water Desalination. *Energy Environ. Sci.* **2014**, *7*, 1134−1141.
(32) Patel, S. K.; Ritt, C. L.; Deshmukh, A.; Wang, Z.; Qin, M.; Epsztein, R.; Elimelech, M. The Relative Insignificance of Advanced Materials in Enhancing the Energy Efficiency of Desalination Technologies. *Energy Environ. Sci.* **2020**, *13*, 1694.
(33) Epsztein, R.; DuChanois, R. M.; Ritt, C. L.; Noy, A.; Elimelech, M. Towards Single-Species Selectivity of Membranes with Subnanometre Pores. *Nat. Nanotechnol.* **2020**, *15*, 426−436.
(34) Siria, A.; Bocquet, M. L.; Bocquet, L. New Avenues for the Large-Scale Harvesting of Blue Energy. *Nat. Rev. Chem.* **2017**, *1*, 0091.
(35) Straub, A. P.; Deshmukh, A.; Elimelech, M. Pressure-Retarded Osmosis for Power Generation from Salinity Gradients: Is It Viable? *Energy Environ. Sci.* **2016**, *9*, 31−48.
(36) Marbach, S.; Bocquet, L. Osmosis, from Molecular Insights to Large-Scale Applications. *Chem. Soc. Rev.* **2019**, *48*, 3102−3144.
(37) Wang, L.; Wang, Z.; Patel, S. K.; Lin, S.; Elimelech, M. Nanopore-Based Power Generation from Salinity Gradient: Why It Is Not Viable. *ACS Nano* **2021**, *15*, 4093−4107.
(38) Aberoumand, S.; Woodfield, P.; Shabani, B.; Dao, D. V. Advances in Electrode and Electrolyte Improvements in Vanadium Redox Flow Batteries with a Focus on the Nanofluidic Electrolyte Approach. *Phys. Rep.* **2020**, *881*, 1−49.
(39) Kim, J.; Park, H. Effect of Nanofluidic Electrolyte on the Electrochemically Enhanced Long-Term Efficiency of Vanadium Redox Flow Battery. *Energy Storage* **2019**, *1*, No. e90.
(40) Rahimi, M. A.; Molaei Dehkordi, A.; Roberts, E. P. L. Magnetic Nanofluidic Electrolyte for Enhancing the Performance of Polysulfide/Iodide Redox Flow Batteries. *Electrochim. Acta* **2021**, *369*, 137687.
(41) Xiao, K.; Yang, T.; Liang, J.; Rawal, A.; Liu, H.; Fang, R.; Amal, R.; Xu, H.; Wang, D.-W. Nanofluidic Voidless Electrode for Electrochemical Capacitance Enhancement in Gel Electrolyte. *Nat. Commun.* **2021**, *12*, 5515.
(42) Lee, S.-Y. Expanding Cellulose. *Nature Energy* **2021**, *6*, 949−950.
(43) Yang, C.; Wu, Q.; Xie, W.; Zhang, X.; Brozena, A.; Zheng, J.; Garaga, M. N.; Ko, B. H.; Mao, Y.; He, S.; et al. Copper-Coordinated Cellulose Ion Conductors for Solid-State Batteries. *Nature* **2021**, *598*, 590−596.
(44) Howorka, S.; Siwy, Z. Nanopore Analytics: Sensing of Single Molecules. *Chem. Soc. Rev.* **2009**, *38*, 2360−2384.
(45) Shi, W.; Friedman, A. K.; Baker, L. A. Nanopore Sensing. *Anal. Chem.* **2017**, *89*, 157−188.
(46) Zhang, H. C.; Tian, Y.; Jiang, L. Fundamental Studies and Practical Applications of Bio-Inspired Smart Solid-State Nanopores and Nanochannels. *Nano Today* **2016**, *11*, 61−81.
(47) Bayley, H.; Martin, C. R. Resistive-Pulse Sensing - from Microbes to Molecules. *Chem. Rev.* **2000**, *100*, 2575−2594.
(48) Wanunu, M. Nanopores: A Journey Towards DNA Sequencing. *Physics of Life Reviews* **2012**, *9*, 125−158.
(49) Branton, D.; Deamer, D. W.; Marziali, A.; Bayley, H.; Benner, S. A.; Butler, T.; Di Ventra, M.; Garaj, S.; Hibbs, A.; Huang, X.; et al. The Potential and Challenges of Nanopore Sequencing. *Nat. Biotechnol.* **2008**, *26*, 1146−1153.
(50) Deamer, D.; Akeson, M.; Branton, D. Three Decades of Nanopore Sequencing. *Nat. Biotechnol.* **2016**, *34*, 518−524.
(51) Kasianowicz, J. J.; Brandin, E.; Branton, D.; Deamer, D. W. Characterization of Individual Polynucleotide Molecules Using a Membrane Channel. *Proc. Natl. Acad. Sci. U.S.A.* **1996**, *93*, 13770−13773.
(52) DeBlois, R. W.; Wesley, R. K. Sizes and Concentrations of Several Type C Oncornaviruses and Bacteriophage T2 by the Resistive-Pulse Technique. *J. Virol* **1977**, *23*, 227−233.
(53) Geng, J.; Kim, K.; Zhang, J.; Escalada, A.; Tunuguntla, R.; Comolli, L. R.; Allen, F. I.; Shnyrova, A. V.; Cho, K. R.; Munoz, D.; et al. Stochastic Transport through Carbon Nanotubes in Lipid Bilayers and Live Cell Membranes. *Nature* **2014**, *514*, 612−615.
(54) Meller, A.; Nivon, L.; Branton, D. Voltage-Driven DNA Translocations through a Nanopore. *Phys. Rev. Lett.* **2001**, *86*, 3435−3438.
(55) Butler, T. Z.; Pavlenok, M.; Derrington, I. M.; Niederweis, M.; Gundlach, J. H. Single-Molecule DNA Detection with an Engineered Mspa Protein Nanopore. *Proc. Natl. Acad. Sci. U.S.A.* **2008**, *105*, 20647−20652.
(56) Cherf, G. M.; Lieberman, K. R.; Rashid, H.; Lam, C. E.; Karplus, K.; Akeson, M. Automated Forward and Reverse Ratcheting of DNA in a Nanopore at 5-Å Precision. *Nat. Biotechnol.* **2012**, *30*, 344−348.
(57) Noakes, M. T.; Brinkerhoff, H.; Laszlo, A. H.; Derrington, I. M.; Langford, K. W.; Mount, J. W.; Bowman, J. L.; Baker, K. S.; Doering, K. M.; Tickman, B. I.; et al. Increasing the Accuracy of Nanopore DNA Sequencing Using a Time-Varying Cross Membrane Voltage. *Nat. Biotechnol.* **2019**, *37*, 651−656.
(58) Derrington, I. M.; Craig, J. M.; Stava, E.; Laszlo, A. H.; Ross, B. C.; Brinkerhoff, H.; Nova, I. C.; Doering, K.; Tickman, B. I.; Ronaghi, M.; et al. Subangstrom Single-Molecule Measurements of Motor Proteins Using a Nanopore. *Nat. Biotechnol.* **2015**, *33*, 1073−1075.
(59) Ouldali, H.; Sarthak, K.; Ensslen, T.; Piguet, F.; Manivet, P.; Pelta, J.; Behrends, J. C.; Aksimentiev, A.; Oukhaled, A. Electrical Recognition of the Twenty Proteinogenic Amino Acids Using an Aerolysin Nanopore. *Nat. Biotechnol.* **2020**, *38*, 176−181.
(60) Ellison, M. D.; Bricker, L.; Nebel, L.; Miller, J.; Menges, S.; D'Arcangelo, G.; Kramer, A.; Drahushuk, L.; Benck, J.; Shimizu, S.; et al. Transport of Amino Acid Cations through a 2.25-Nm-Diameter Carbon Nanotube Nanopore: Electrokinetic Motion and Trapping/Desorption. *J. Phys. Chem. C* **2017**, *121*, 27709−27720.
(61) Roozbahani, G. M.; Chen, X.; Zhang, Y.; Wang, L.; Guan, X. Nanopore Detection of Metal Ions: Current Status and Future Directions. *Small Methods* **2020**, *4*, 2000266.
(62) Szymczyk, A.; Zhu, H.; Balannec, B. Ion Rejection Properties of Nanopores with Bipolar Fixed Charge Distributions. *J. Phys. Chem. B* **2010**, *114*, 10143−10150.
(63) Balannec, B.; Ghoufi, A.; Szymczyk, A. Nanofiltration Performance of Conical and Hourglass Nanopores. *J. Membr. Sci.* **2018**, *552*, 336−340.
(64) Heiranian, M.; Farimani, A. B.; Aluru, N. R. Water Desalination with a Single-Layer Mos2 Nanopore. *Nat. Commun.* **2015**, *6*, 8616.
(65) Cao, Z.; Liu, V.; Barati Farimani, A. Why Is Single-Layer Mos2 a More Energy Efficient Membrane for Water Desalination? *ACS Energy Letters* **2020**, *5*, 2217−2222.
(66) Ruan, Y.; Zhu, Y.; Zhang, Y.; Gao, Q.; Lu, X.; Lu, L. Molecular Dynamics Study of Mg2+/Li+ Separation Via Biomimetic Graphene-Based Nanopores: The Role of Dehydration in Second Shell. *Langmuir* **2016**, *32*, 13778−13786.
(67) Feng, J.; Liu, K.; Graf, M.; Dumcenco, D.; Kis, A.; Di Ventra, M.; Radenovic, A. Observation of Ionic Coulomb Blockade In nanopores. *Nat. Mater.* **2016**, *15*, 850−855.
(68) Siwy, Z. S.; Howorka, S. Engineered Voltage-Responsive Nanopores. *Chem. Soc. Rev.* **2010**, *39*, 1115.
(69) Ramírez, P.; Apel, P. Y.; Cervera, J.; Mafé, S. Pore Structure and Function of Synthetic Nanopores with Fixed Charges: Tip Shape and Rectification Properties. *Nanotechnology* **2008**, *19*, 315707.
(70) Aksimentiev, A.; Brunner, R. K.; Cruz-Chu, E.; Comer, J.; Schulten, K. Modeling Transport through Synthetic Nanopores. *IEEE Nanotechnology Magazine* **2009**, *3*, 20−28.
(71) Bocquet, L.; Charlaix, E. Nanofluidics, from Bulk to Interfaces. *Chem. Soc. Rev.* **2010**, *39*, 1073−1095.
(72) Mann, D. J.; Halls, M. D. Water Alignment and Proton Conduction inside Carbon Nanotubes. *Phys. Rev. Lett.* **2003**, *90*, 195503.

https://doi.org/10.1021/acs.chemrev.2c00155
Chem. Rev. 2023, 123, 2737−2831

(73) Majumder, M.; Chopra, N.; Andrews, R.; Hinds, B. J. Enhanced Flow in Carbon Nanotubes. *Nature* **2005**, *438*, 44−44.
(74) Qin, X.; Yuan, Q.; Zhao, Y.; Xie, S.; Liu, Z. Measurement of the Rate of Water Translocation through Carbon Nanotubes. *Nano Lett.* **2011**, *11*, 2173−2177.
(75) Secchi, E.; Marbach, S.; Niguès, A.; Stein, D.; Siria, A.; Bocquet, L. Massive Radius-Dependent Flow Slippage in Carbon Nanotubes. *Nature* **2016**, *537*, 210−213.
(76) Radha, B.; Esfandiar, A.; Wang, F. C.; Rooney, A. P.; Gopinadhan, K.; Keerthi, A.; Mishchenko, A.; Janardanan, A.; Blake, P.; Fumagalli, L.; et al. Molecular Transport through Capillaries Made with Atomic-Scale Precision. *Nature* **2016**, *538*, 222.
(77) Heiranian, M.; Aluru, N. R. Nanofluidic Transport Theory with Enhancement Factors Approaching One. *ACS Nano* **2020**, *14*, 272−281.
(78) Kolesnikov, A. I.; Zanotti, J.-M.; Loong, C.-K.; Thiyagarajan, P.; Moravsky, A. P.; Loutfy, R. O.; Burnham, C. J. Anomalously Soft Dynamics of Water in a Nanotube: A Revelation of Nanoscale Confinement. *Phys. Rev. Lett.* **2004**, *93*, 035503.
(79) Pascal, T. A.; Goddard, W. A.; Jung, Y. Entropy and the Driving Force for the Filling of Carbon Nanotubes with Water. *Proc. Natl. Acad. Sci. U.S.A.* **2011**, *108*, 11794.
(80) Cambre, S.; Wenseleers, W. Separation and Diameter-Sorting of Empty (End-Capped) and Water-Filled (Open) Carbon Nanotubes by Density Gradient Ultracentrifugation. *Angew. Chem., Int. Ed. Engl.* **2011**, *50*, 2764−2768.
(81) Streit, J.; Snyder, C. R.; Campo, J.; Zheng, M.; Simpson, J. R.; Hight Walker, A. R.; Fagan, J. A. Alkane Encapsulation Induces Strain in Small-Diameter Single-Wall Carbon Nanotubes. *J. Phys. Chem. C* **2018**, *122*, 11577−11585.
(82) Campo, J.; Cambré, S.; Botka, B.; Obrzut, J.; Wenseleers, W.; Fagan, J. A. Optical Property Tuning of Single-Wall Carbon Nanotubes by Endohedral Encapsulation of a Wide Variety of Dielectric Molecules. *ACS Nano* **2021**, *15*, 2301−2317.
(83) Faucher, S.; Kuehne, M.; Koman, V. B.; Northrup, N.; Kozawa, D.; Yuan, Z.; Li, S. X.; Zeng, Y.; Ichihara, T.; Misra, R. P.; et al. Diameter Dependence of Water Filling in Lithographically Segmented Isolated Carbon Nanotubes. *ACS Nano* **2021**, *15*, 2778−2790.
(84) Chuvilin, A.; Bichoutskaia, E.; Gimenez-Lopez, M. C.; Chamberlain, T. W.; Rance, G. A.; Kuganathan, N.; Biskupek, J.; Kaiser, U.; Khlobystov, A. N. Self-Assembly of a Sulphur-Terminated Graphene Nanoribbon within a Single-Walled Carbon Nanotube. *Nat. Mater.* **2011**, *10*, 687−692.
(85) Okazaki, T.; Iizumi, Y.; Okubo, S.; Kataura, H.; Liu, Z.; Suenaga, K.; Tahara, Y.; Yudasaka, M.; Okada, S.; Iijima, S. Coaxially Stacked Coronene Columns inside Single-Walled Carbon Nanotubes. *Angew. Chem., Int. Ed.* **2011**, *50*, 4853−4857.
(86) Fujihara, M.; Miyata, Y.; Kitaura, R.; Nishimura, Y.; Camacho, C.; Irle, S.; Iizumi, Y.; Okazaki, T.; Shinohara, H. Dimerization-Initiated Preferential Formation of Coronene-Based Graphene Nanoribbons in Carbon Nanotubes. *J. Phys. Chem. C* **2012**, *116*, 15141−15145.
(87) Hummer, G.; Rasaiah, J. C.; Noworyta, J. P. Water Conduction through the Hydrophobic Channel of a Carbon Nanotube. *Nature* **2001**, *414*, 188−190.
(88) Qu, H.; Rayabharam, A.; Wu, X.; Wang, P.; Li, Y.; Fagan, J. A.; Aluru, N. R.; Wang, Y. Selective Filling of N-Hexane in a Tight Nanopore. *Nat. Commun.* **2021**, *12*, 310.
(89) Koga, K.; Gao, G. T.; Tanaka, H.; Zeng, X. C. Formation of Ordered Ice Nanotubes inside Carbon Nanotubes. *Nature* **2001**, *412*, 802−805.
(90) Han, S.; Choi, M. Y.; Kumar, P.; Stanley, H. E. Phase Transitions in Confined Water Nanofilms. *Nat. Phys.* **2010**, *6*, 685−689.
(91) Mochizuki, K.; Koga, K. Solid-Liquid Critical Behavior of Water in Nanopores. *Proc. Natl. Acad. Sci. U.S.A.* **2015**, *112*, 8221.
(92) Christenson, H. Confinement Effects on Freezing and Melting. *J. Phys.: Condens. Matter* **2001**, *13*, R95−R133.
(93) Alba-Simionesco, C.; Coasne, B.; Dosseh, G.; Dudziak, G.; Gubbins, K. E.; Radhakrishnan, R.; Sliwinska-Bartkowiak, M. Effects of Confinement on Freezing and Melting. *J. Phys.: Condens. Matter* **2006**, *18*, R15−R68.
(94) Koga, K.; Zeng, X. C.; Tanaka, H. Freezing of Confined Water: A Bilayer Ice Phase in Hydrophobic Nanopores. *Phys. Rev. Lett.* **1997**, *79*, 5262−5265.
(95) Takaiwa, D.; Hatano, I.; Koga, K.; Tanaka, H. Phase Diagram of Water in Carbon Nanotubes. *Proc. Natl. Acad. Sci. U. S. A.* **2008**, *105*, 39−43.
(96) Maniwa, Y.; Kataura, H.; Abe, M.; Suzuki, S.; Achiba, Y.; Kira, H.; Matsuda, K. Phase Transition in Confined Water inside Carbon Nanotubes. *J. Phys. Soc. Jpn.* **2002**, *71*, 2863−2866.
(97) Maniwa, Y.; Kataura, H.; Abe, M.; Udaka, A.; Suzuki, S.; Achiba, Y.; Kira, H.; Matsuda, K.; Kadowaki, H.; Okabe, Y. Ordered Water inside Carbon Nanotubes: Formation of Pentagonal to Octagonal Ice-Nanotubes. *Chem. Phys. Lett.* **2005**, *401*, 534−538.
(98) Chiashi, S.; Saito, Y.; Kato, T.; Konabe, S.; Okada, S.; Yamamoto, T.; Homma, Y. Confinement Effect of Sub-Nanometer Difference on Melting Point of Ice-Nanotubes Measured by Photoluminescence Spectroscopy. *ACS Nano* **2019**, *13*, 1177−1182.
(99) Ma, X.; Cambré, S.; Wenseleers, W.; Doorn, S. K.; Htoon, H. Quasiphase Transition in a Single File of Water Molecules Encapsulated in (6,5) Carbon Nanotubes Observed by Temperature-Dependent Photoluminescence Spectroscopy. *Phys. Rev. Lett.* **2017**, *118*, 027402.
(100) Imry, Y. Finite-Size Rounding of a First-Order Phase Transition. *Phys. Rev. B* **1980**, *21*, 2042−2043.
(101) Israelachvili, J. N.*Intermolecular and Surface Forces*; Academic Press, 2011.
(102) Nap, R.; Gong, P.; Szleifer, I. Weak Polyelectrolytes Tethered to Surfaces: Effect of Geometry, Acid-Base Equilibrium and Electrical Permittivity. *J. Polym. Sci. B Polym. Phys.* **2006**, *44*, 2638−2662.
(103) Muthukumar, M. Theory of Counter-Ion Condensation on Flexible Polyelectrolytes: Adsorption Mechanism. *J. Chem. Phys.* **2004**, *120*, 9343−9350.
(104) Mehler, E. L.; Eichele, G. Electrostatic Effects in Water-Accessible Regions of Proteins. *Biochemistry* **1984**, *23*, 3887−3891.
(105) Marcus, Y.*Ions in Solution and Their Solvation*; John Wiley & Sons, 2015.
(106) Freger, V. Ion Partitioning and Permeation in Charged Low-T* Membranes. *Adv. Colloid Interface Sci.* **2020**, *277*, 102107.
(107) Ritt, C. L.; Werber, J.; Wang, M.; Yang, Z.; Zhao, Y.; Kulik, H. J.; Elimelech, M. Ionization Behavior of Nanoporous Polyamide Membranes. *Proc. Natl. Acad. Sci. U.S.A.* **2020**, *117*, 30191−30200.
(108) Robinson, R. A.; Stokes, R. H.*Electrolyte Solutions*; Dover Publications, 2002.
(109) Webb, T. J. The Free Energy of Hydration of Ions and the Electrostriction of the Solvent. *J. Am. Chem. Soc.* **1926**, *48*, 2589−2603.
(110) Schlaich, A.; Knapp, E. W.; Netz, R. R. Water Dielectric Effects in Planar Confinement. *Phys. Rev. Lett.* **2016**, *117*, 048001.
(111) Motevaselian, M. H.; Mashayak, S. Y.; Aluru, N. R. Extended Coarse-Grained Dipole Model for Polar Liquids: Application to Bulk and Confined Water. *Phys. Rev. E* **2018**, *98*, 052135.
(112) Schaaf, C.; Gekle, S. Spatially Resolved Dielectric Constant of Confined Water and Its Connection to the Non-Local Nature of Bulk Water. *J. Chem. Phys.* **2016**, *145*, 084901.
(113) Loche, P.; Ayaz, C.; Schlaich, A.; Uematsu, Y.; Netz, R. R. Giant Axial Dielectric Response in Water-Filled Nanotubes and Effective Electrostatic Ion-Ion Interactions from a Tensorial Dielectric Model. *J. Phys. Chem. B* **2019**, *123*, 10850−10857.
(114) Israelachvili, J. N.; Pashley, R. M. Molecular Layering of Water at Surfaces and Origin of Repulsive Hydration Forces. *Nature* **1983**, *306*, 249−250.
(115) Toney, M. F.; Howard, J. N.; Richer, J.; Borges, G. L.; Gordon, J. G.; Melroy, O. R.; Wiesler, D. G.; Yee, D.; Sorensen, L. B. Voltage-Dependent Ordering of Water-Molecules at an Electrode-Electrolyte Interface. *Nature* **1994**, *368*, 444−446.
(116) Velasco-Velez, J. J.; Wu, C. H.; Pascal, T. A.; Wan, L. W. F.; Guo, J. H.; Prendergast, D.; Salmeron, M. The Structure of Interfacial

https://doi.org/10.1021/acs.chemrev.2c00155
Chem. Rev. 2023, 123, 2737−2831

Water on Gold Electrodes Studied by X-Ray Absorption Spectroscopy. *Science* **2014**, *346*, 831−834.
(117) Cicero, G.; Grossman, J. C.; Schwegler, E.; Gygi, F.; Galli, G. Water Confined in Nanotubes and between Graphene Sheets: A First Principle Study. *J. Am. Chem. Soc.* **2008**, *130*, 1871−1878.
(118) Conway, B. E.; Bockris, J. O.; Ammar, I. A. The Dielectric Constant of the Solution in the Diffuse and Helmholtz Double Layers at a Charged Interface in Aqueous Solution. *Trans. Faraday Society* **1951**, *47*, 756−766.
(119) Chandra, A. Static Dielectric Constant of Aqueous Electrolyte Solutions: Is There Any Dynamic Contribution? *J. Chem. Phys.* **2000**, *113*, 903−905.
(120) Hubbard, J. B.; Onsager, L. J. Dielectric-Dispersion and Dielectric Friction in Electrolyte-Solutions.1. *J. Chem. Phys.* **1977**, *67*, 4850−4857.
(121) Yaroshchuk, A. E. Dielectric Exclusion of Ions from Membranes. *Adv. Colloid Interface Sci.* **2000**, *85*, 193−230.
(122) Napoli, M.; Eijkel, J. C. T.; Pennathur, S. Nanofluidic Technology for Biomolecule Applications: A Critical Review. *Lab Chip* **2010**, *10*, 957−985.
(123) Schoch, R. B.; Han, J. Y.; Renaud, P. Transport Phenomena in Nanofluidics. *Rev. Mod. Phys.* **2008**, *80*, 839−883.
(124) Hu, G. Q.; Li, D. Q. Multiscale Phenomena in Microfluidics and Nanofluidics. *Chem. Eng. Sci.* **2007**, *62*, 3443−3454.
(125) Cui, H. B.; Takahashi, K.; Okano, Y.; Kobayashi, H.; Wang, Z. M.; Kobayashi, A. Dielectric Properties of Porous Molecular Crystals That Contain Polar Molecules. *Angew. Chem., Int. Ed.* **2005**, *44*, 6508−6512.
(126) Haidar, A. R.; Jonscher, A. K. The Dielectric-Properties of Zeolites in Variable Temperature and Humidity. *Journal of the Chemical Society-Faraday Transactions I* **1986**, *82*, 3535−3551.
(127) Efligenir, A.; Fievet, P.; Deon, S.; Salut, R. Characterization of the Isolated Active Layer of a Nf Membrane by Electrochemical Impedance Spectroscopy. *J. Membr. Sci.* **2015**, *477*, 172−182.
(128) Friebe, A.; Moritz, W. Influence of Electrolyte on Electrical-Properties of Thin Cellulose-Acetate Membranes. *J. Appl. Polym. Sci.* **1994**, *51*, 625−634.
(129) Fumagalli, L.; Esfandiar, A.; Fabregas, R.; Hu, S.; Ares, P.; Janardanan, A.; Yang, Q.; Radha, B.; Taniguchi, T.; Watanabe, K.; et al. Anomalously Low Dielectric Constant of Confined Water. *Science* **2018**, *360*, 1339−1342.
(130) Zhang, C.; Gygi, F.; Galli, G. Strongly Anisotropic Dielectric Relaxation of Water at the Nanoscale. *J. Phys. Chem. Lett.* **2013**, *4*, 2477−2481.
(131) Motevaselian, M.; Mashayak, S.; Aluru, N. Extended Coarse-Grained Dipole Model for Polar Liquids: Application to Bulk and Confined Water. *Phys. Rev. E* **2018**, *98*, 052135.
(132) Fumagalli, L.; Esfandiar, A.; Fabregas, R.; Hu, S.; Ares, P.; Janardanan, A.; Yang, Q.; Radha, B.; Taniguchi, T.; Watanabe, K.; et al. Anomalously Low Dielectric Constant of Confined Water. *Science* **2018**, *360*, 1339−1342.
(133) Daiguji, H. Ion Transport in Nanofluidic Channels. *Chem. Soc. Rev.* **2010**, *39*, 901−911.
(134) Daiguji, H.; Yang, P. D.; Majumdar, A. Ion Transport in Nanofluidic Channels. *Nano Lett.* **2004**, *4*, 137−142.
(135) Guan, W. H.; Li, S. X.; Reed, M. A. Voltage Gated Ion and Molecule Transport in Engineered Nanochannels: Theory, Fabrication and Applications. *Nanotechnology* **2014**, *25*, 122001.
(136) Sparreboom, W.; van den Berg, A.; Eijkel, J. C. T. Principles and Applications of Nanofluidic Transport. *Nat. Nanotechnol.* **2009**, *4*, 713−720.
(137) Balme, S.; Picaud, F.; Manghi, M.; Palmeri, J.; Bechelany, M.; Cabello-Aguilar, S.; Abou-Chaaya, A.; Miele, P.; Balanzat, E.; Janot, J. M. Ionic Transport through Sub-10 Nm Diameter Hydrophobic High-Aspect Ratio Nanopores: Experiment, Theory and Simulation. *Sci. Rep.* **2015**, *5*, 10135.
(138) Geise, G. M.; Paul, D. R.; Freeman, B. D. Fundamental Water and Salt Transport Properties of Polymeric Materials. *Prog. Polym. Sci.* **2014**, *39*, 1−42.
(139) Suk, M. E.; Aluru, N. R. Molecular and Continuum Hydrodynamics in Graphene Nanopores. *RSC Adv.* **2013**, *3*, 9365−9372.
(140) Neek-Amal, M.; Lohrasebi, A.; Mousaei, M.; Shayeganfar, F.; Radha, B.; Peeters, F. M. Fast Water Flow through Graphene Nanocapillaries: A Continuum Model Approach Involving the Microscopic Structure of Confined Water. *Appl. Phys. Lett.* **2018**, *113*, 083101.
(141) Smeets, R. M. M.; Keyser, U. F.; Krapf, D.; Wu, M. Y.; Dekker, N. H.; Dekker, C. Salt Dependence of Ion Transport and DNA Translocation through Solid-State Nanopores. *Nano Lett.* **2006**, *6*, 89−95.
(142) Plecis, A.; Schoch, R. B.; Renaud, P. Ionic Transport Phenomena in Nanofluidics: Experimental and Theoretical Study of the Exclusion-Enrichment Effect on a Chip. *Nano Lett.* **2005**, *5*, 1147−1155.
(143) Sahu, S.; Di Ventra, M.; Zwolak, M. Dehydration as a Universal Mechanism for Ion Selectivity in Graphene and Other Atomically Thin Pores. *Nano Lett.* **2017**, *17*, 4719−4724.
(144) Samoylova, O. N.; Calixte, E. I.; Shuford, K. L. Molecular Dynamics Simulations of Ion Transport in Carbon Nanotube Channels. *J. Phys. Chem. C* **2015**, *119*, 1659−1666.
(145) Richards, L. A.; Schafer, A. I.; Richards, B. S.; Corry, B. The Importance of Dehydration in Determining Ion Transport in Narrow Pores. *Small* **2012**, *8*, 1701−1709.
(146) Suk, M. E.; Aluru, N. R. Ion Transport in Sub-5-Nm Graphene Nanopores. *J. Chem. Phys.* **2014**, *140*, 084707.
(147) Esfandiar, A.; Radha, B.; Wang, F. C.; Yang, Q.; Hu, S.; Garaj, S.; Nair, R. R.; Geim, A. K.; Gopinadhan, K. Size Effect in Ion Transport through Angstrom-Scale Silts. *Science* **2017**, *358*, 511−513.
(148) Li, Z. W.; Li, Y. H.; Yao, Y. C.; Aydin, F.; Zhan, C.; Chen, Y. F.; Elimelech, M.; Pham, T. A.; Noy, A. Strong Differential Monovalent Anion Selectivity in Narrow Diameter Carbon Nanotube Porins. *ACS Nano* **2020**, *14*, 6269−6275.
(149) Jain, T.; Rasera, B. C.; Guerrero, R. J. S.; Boutilier, M. S. H.; O'Hern, S. C.; Idrobo, J. C.; Karnik, R. Heterogeneous Sub-Continuum Ionic Transport in Statistically Isolated Graphene Nanopores. *Nat. Nanotechnol.* **2015**, *10*, 1053.
(150) Gouaux, E.; MacKinnon, R. Principles of Selective Ion Transport in Channels and Pumps. *Science* **2005**, *310*, 1461−1465.
(151) Doyle, D. A.; Cabral, J. M.; Pfuetzner, R. A.; Kuo, A. L.; Gulbis, J. M.; Cohen, S. L.; Chait, B. T.; MacKinnon, R. The Structure of the Potassium Channel: Molecular Basis of K+ Conduction and Selectivity. *Science* **1998**, *280*, 69−77.
(152) Lauger, P. Diffusion-Limited Ion Flow through Pores. *Biochim. Biophys. Acta* **1976**, *455*, 493−509.
(153) Zhou, X.; Wang, Z.; Epsztein, R.; Zhan, C.; Li, W.; Fortner, J. D.; Pham, T. A.; Kim, J.-H.; Elimelech, M. Intrapore Energy Barriers Govern Ion Transport and Selectivity of Desalination Membranes. *Sci. Adv.* **2020**, *6*, No. eabd9045.
(154) Duan, C. H.; Majumdar, A. Anomalous Ion Transport in 2-Nm Hydrophilic Nanochannels. *Nat. Nanotechnol.* **2010**, *5*, 848−852.
(155) Cronstedt, A. K. Observation and Description of an Unknown Kind of Rock to Be Named Zeolites. *Kongliga Svenska Vetenskapsakademiens Handlingar Stockholm* **1756**, *17*, 120−123.
(156) Błoński, P.; Birczyński, A.; Lalowicz, Z. T.; Datka, J.; Łodziana, Z. Structure of the Hydroxyl Groups and Adsorbed D_2o Sites in the Dx Zeolite: Dft and Experimental Nmr Data. *J. Phys. Chem. C* **2015**, *119*, 19548−19557.
(157) Yumura, T.; Hasegawa, S.; Itadani, A.; Kobayashi, H.; Kuroda, Y. The Variety of Carbon-Metal Bonds inside Cu-Zsm-5 Zeolites: A Density Functional Theory Study. *Materials* **2010**, *3*, 2516−2535.
(158) Kresge, C. T.; Leonowicz, M. E.; Roth, W. J.; Vartuli, J. C.; Beck, J. S. Ordered Mesoporous Molecular Sieves Synthesized by a Liquid-Crystal Template Mechanism. *Nature* **1992**, *359*, 710−712.
(159) Tao, Y.; Kanoh, H.; Abrams, L.; Kaneko, K. Mesopore-Modified Zeolites: Preparation, Characterization, and Applications. *Chem. Rev.* **2006**, *106*, 896−910.

https://doi.org/10.1021/acs.chemrev.2c00155
Chem. Rev. 2023, 123, 2737−2831

(160) Smith, J. V. Topochemistry of Zeolites and Related Materials. 1. Topology and Geometry. *Chem. Rev.* **1988**, *88*, 149−182.
(161) Townsend, R. P.; Coker, E. N.Ion Exchange in Zeolites. In *Studies in Surface Science Catalysis*; van Bekkum, H., Flanigen, E. M., Jacobs, P. A., Jansen, J. C., Eds.; Elsevier, 2001; Vol. *137*, pp 467−524.
(162) Dehghan, R.; Anbia, M. Zeolites for Adsorptive Desulfurization from Fuels: A Review. *Fuel Process. Technol.* **2017**, *167*, 99−116.
(163) Corma, A. State of the Art and Future Challenges of Zeolites as Catalysts. *J. Catal.* **2003**, *216*, 298−312.
(164) Cundy, C. S.; Cox, P. A. The Hydrothermal Synthesis of Zeolites: History and Development from the Earliest Days to the Present Time. *Chem. Rev.* **2003**, *103*, 663−702.
(165) Cheetham, A. K.; Ferey, G.; Loiseau, T. Open-Framework Inorganic Materials. *Angew. Chem., Int. Ed.* **1999**, *38*, 3268−3292.
(166) Dong, J.; Xu, Z.; Yang, S.; Murad, S.; Hinkle, K. R. Zeolite Membranes for Ion Separations from Aqueous Solutions. *Curr. Opin. Chem. Eng.* **2015**, *8*, 15−20.
(167) Zhao, D.; Huo, Q.; Feng, J.; Chmelka, B. F.; Stucky, G. D. Nonionic Triblock and Star Diblock Copolymer and Oligomeric Surfactant Syntheses of Highly Ordered, Hydrothermally Stable, Mesoporous Silica Structures. *J. Am. Chem. Soc.* **1998**, *120*, 6024−6036.
(168) Beck, J. S.; Vartuli, J. C.; Roth, W. J.; Leonowicz, M. E.; Kresge, C. T.; Schmitt, K. D.; Chu, C. T. W.; Olson, D. H.; Sheppard, E. W.; McCullen, S. B.; et al. A New Family of Mesoporous Molecular Sieves Prepared with Liquid Crystal Templates. *J. Am. Chem. Soc.* **1992**, *114*, 10834−10843.
(169) Kittaka, S.; Iwashita, T.; Serizawa, A.; Kranishi, M.; Takahara, S.; Kuroda, Y.; Mori, T.; Yamaguchi, T. Low Temperature Properties of Acetonitrile Confined in Mcm-41. *J. Phys. Chem. B* **2005**, *109*, 23162−23169.
(170) Yaghi, O. M.; O'Keeffe, M.; Ockwig, N. W.; Chae, H. K.; Eddaoudi, M.; Kim, J. Reticular Synthesis and the Design of New Materials. *Nature* **2003**, *423*, 705−714.
(171) James, S. L. Metal-Organic Frameworks. *Chem. Soc. Rev.* **2003**, *32*, 276−288.
(172) Schneemann, A.; Bon, V.; Schwedler, I.; Senkovska, I.; Kaskel, S.; Fischer, R. A. Flexible Metal-Organic Frameworks. *Chem. Soc. Rev.* **2014**, *43*, 6062−6096.
(173) Chui, S. S.-Y.; Lo, S. M.-F.; Charmant, J. P. H.; Orpen, A. G.; Williams, I. D. A Chemically Functionalizable Nanoporous Material $[Cu_3(Tma)_2(H_2o)_3]_N$. *Science* **1999**, *283*, 1148−1150.
(174) Li, X.; Zhang, H.; Wang, P.; Hou, J.; Lu, J.; Easton, C. D.; Zhang, X.; Hill, M. R.; Thornton, A. W.; Liu, J. Z.; et al. Fast and Selective Fluoride Ion Conduction in Sub-1-Nanometer Metal-Organic Framework Channels. *Nat. Commun.* **2019**, *10*, 2490.
(175) Zhang, H.; Hou, J.; Hu, Y.; Wang, P.; Ou, R.; Jiang, L.; Liu, J. Z.; Freeman, B. D.; Hill, A. J.; Wang, H. Ultrafast Selective Transport of Alkali Metal Ions in Metal Organic Frameworks with Subnanometer Pores. *Sci. Adv.* **2018**, *4*, No. eaaq0066.
(176) Lu, J.; Xu, H.; Yu, H.; Hu, X.; Xia, J.; Zhu, Y.; Wang, F.; Wu, H.-A.; Jiang, L.; Wang, H. Ultrafast Rectifying Counter-Directional Transport of Proton and Metal Ions in Metal-Organic Framework−Based Nanochannels. *Sci. Adv.* **2022**, *8*, No. eabl5070.
(177) Liu, Y.-C.; Yeh, L.-H.; Zheng, M.-J.; Wu, K. C.-W. Highly Selective and High-Performance Osmotic Power Generators in Subnanochannel Membranes Enabled by Metal-Organic Frameworks. *Sci. Adv.* **2021**, *7*, No. eabe9924.
(178) Spitler, E. L.; Koo, B. T.; Novotney, J. L.; Colson, J. W.; Uribe-Romo, F. J.; Gutierrez, G. D.; Clancy, P.; Dichtel, W. R. A 2d Covalent Organic Framework with 4.7-Nm Pores and Insight into Its Interlayer Stacking. *J. Am. Chem. Soc.* **2011**, *133*, 19416−19421.
(179) Paukstelis, P. J.; Nowakowski, J.; Birktoft, J. J.; Seeman, N. C. Crystal Structure of a Continuous Three-Dimensional DNA Lattice. *Chemistry & Biology* **2004**, *11*, 1119−1126.
(180) Ding, S.-Y.; Wang, W. Covalent Organic Frameworks (Cofs): From Design to Applications. *Chem. Soc. Rev.* **2013**, *42*, 548−568.
(181) Liu, L.; Yin, L.; Cheng, D.; Zhao, S.; Zang, H.-Y.; Zhang, N.; Zhu, G. Surface-Mediated Construction of an Ultrathin Free-Standing Covalent Organic Framework Membrane for Efficient Proton Conduction. *Angew. Chem., Int. Ed.* **2021**, *60*, 14875−14880.
(182) Hou, L.; Xian, W.; Bing, S.; Song, Y.; Sun, Q.; Zhang, L.; Ma, S. Understanding the Ion Transport Behavior across Nanofluidic Membranes in Response to the Charge Variations. *Adv. Funct. Mater.* **2021**, *31*, 2009970.
(183) Elmer, T. H.Porous and Reconstructed Glasses. In *Engineered Materials Handbook*, ASM International, 1992; Vol. *4*, pp 427−432.
(184) Brinker, C. J.; Scherer, G. W.*Sol-Gel Science: The Physics and Chemistry of Sol-Gel Processing*; Academic Press, 1990.
(185) Hood, H. P.; Nordberg, M. E.Treated Borosilicate Glass. US Patent 2,106,744, 1938.
(186) Shelekhin, A. B.; Pien, S.; Ma, Y. H. Permeability, Surface Area, Pore Volume and Pore Size of Vycor Glass Membrane Heat-Treated at High Temperatures. *J. Membr. Sci.* **1995**, *103*, 39−43.
(187) Thompson, H.; Soper, A. K.; Ricci, M. A.; Bruni, F.; Skipper, N. T. The Three-Dimensional Structure of Water Confined in Nanoporous Vycor Glass. *J. Phys. Chem. B* **2007**, *111*, 5610−5620.
(188) Xia, Y.; Cho, H.; Deo, M.; Risbud, S. H.; Bartl, M. H.; Sen, S. Layer-by-Layer Freezing of Nanoconfined Water. *Sci. Rep.* **2020**, *10*, 5327.
(189) Stöber, W.; Fink, A.; Bohn, E. Controlled Growth of Monodisperse Silica Spheres in the Micron Size Range. *J. Colloid Interface Sci.* **1968**, *26*, 62−69.
(190) Kosutic, K.; Kastelan-Kunst, L.; Kunst, B. Porosity of Some Commercial Reverse Osmosis and Nanofiltration Polyamide Thin-Film Composite Membranes. *J. Membr. Sci.* **2000**, *168*, 101−108.
(191) Van der Bruggen, B.; Vandecasteele, C.; Van Gestel, T.; Doyen, W.; Leysen, R. A Review of Pressure-Driven Membrane Processes in Wastewater Treatment and Drinking Water Production. *Environ. Prog.* **2003**, *22*, 46−56.
(192) Lu, X. L.; Elimelech, M. Fabrication of Desalination Membranes by Interfacial Polymerization: History, Current Efforts, and Future Directions. *Chem. Soc. Rev.* **2021**, *50*, 6290−6307.
(193) Glater, J. The Early History of Reverse Osmosis Membrane Development. *Desalination* **1998**, *117*, 297−309.
(194) Geise, G. M.; Lee, H. S.; Miller, D. J.; Freeman, B. D.; McGrath, J. E.; Paul, D. R. Water Purification by Membranes: The Role of Polymer Science. *J. Polym. Sci. B Polym. Phys.* **2010**, *48*, 1685−1718.
(195) Gu, J. E.; Lee, S.; Stafford, C. M.; Lee, J. S.; Choi, W.; Kim, B. Y.; Baek, K. Y.; Chan, E. P.; Chung, J. Y.; Bang, J.; et al. Molecular Layer-by-Layer Assembled Thin-Film Composite Membranes for Water Desalination. *Adv. Mater.* **2013**, *25*, 4778−4782.
(196) Jackson, E. A.; Hillmyer, M. A. Nanoporous Membranes Derived from Block Copolymers: From Drug Delivery to Water Filtration. *ACS Nano* **2010**, *4*, 3548−3553.
(197) Baker, R. W.*Membrane Technology and Applications*; John Wiley & Sons, 2012.
(198) Strathmann, H.; Kock, K. The Formation Mechanism of Phase Inversion Membranes. *Desalination* **1977**, *21*, 241−255.
(199) Lee, K. P.; Arnot, T. C.; Mattia, D. A Review of Reverse Osmosis Membrane Materials for Desalination-Development to Date and Future Potential. *J. Membr. Sci.* **2011**, *370*, 1−22.
(200) Ritt, C. L.; Liu, M.; Pham, T. A.; Epsztein, R.; Kulik, H. J.; Elimelech, M. Machine Learning Reveals Key Ion Selectivity Mechanisms in Polymeric Membranes with Subnanometer Pores. *Sci. Adv.* **2022**, *8*, No. eabl5771.
(201) Tiraferri, A.; Yip, N. Y.; Phillip, W. A.; Schiffman, J. D.; Elimelech, M. Relating Performance of Thin-Film Composite Forward Osmosis Membranes to Support Layer Formation and Structure. *J. Membr. Sci.* **2011**, *367*, 340−352.
(202) Lu, X. L.; Nejati, S.; Choo, Y. W.; Osuji, C. O.; Ma, J.; Elimelech, M. Elements Provide a Clue: Nanoscale Characterization of Thin-Film Composite Polyamide Membranes. *ACS Appl. Mater. Interfaces* **2015**, *7*, 16917−16922.
(203) Lu, X. L.; ARias Chavez, L. H.; Romero-Vargas Castrillon, S.; Ma, J.; Elimelech, M. Influence of Active Layer and Support Layer Surface Structures on Organic Fouling Propensity of Thin-Film

https://doi.org/10.1021/acs.chemrev.2c00155
Chem. Rev. 2023, 123, 2737−2831

Composite Forward Osmosis Membranes. *Environ. Sci. Technol.* **2015**, *49*, 1436−1444.
(204) Zhang, Y. Z.; Sargent, J. L.; Boudouris, B. W.; Phillip, W. A. Nanoporous Membranes Generated from Self-Assembled Block Polymer Precursors: Quo Vadis? *J. Appl. Polym. Sci.* **2015**, *132*, 41683.
(205) Dorin, R. M.; Phillip, W. A.; Sai, H.; Werner, J.; Elimelech, M.; Wiesner, U. Designing Block Copolymer Architectures for Targeted Membrane Performance. *Polymer* **2014**, *55*, 347−353.
(206) Li, L.; Schulte, L.; Clausen, L. D.; Hansen, K. M.; Jonsson, G. E.; Ndoni, S. Gyroid Nanoporous Membranes with Tunable Permeability. *ACS Nano* **2011**, *5*, 7754−7766.
(207) Pacheco, F. A.; Pinnau, I.; Reinhard, M.; Leckie, J. O. Characterization of Isolated Polyamide Thin Films of Ro and Nf Membranes Using Novel Tem Techniques. *J. Membr. Sci.* **2010**, *358*, 51−59.
(208) Freger, V. Swelling and Morphology of the Skin Layer of Polyamide Composite Membranes: An Atomic Force Microscopy Study. *Environ. Sci. Technol.* **2004**, *38*, 3168−3175.
(209) Culp, T. E.; Shen, Y. X.; Geitner, M.; Paul, M.; Roy, A.; Behr, M. J.; Rosenberg, S.; Gu, J.; Kumar, M.; Gomez, E. D. Electron Tomography Reveals Details of the Internal Microstructure of Desalination Membranes. *Proc. Natl. Acad. Sci. U.S.A.* **2018**, *115*, 8694−8699.
(210) Fu, Q. Y.; Verma, N.; Ma, H. Y.; Medellin-Rodriguez, F. J.; Li, R. P.; Fukuto, M.; Stafford, C. M.; Hsiao, B. S.; Ocko, B. M. Molecular Structure of Aromatic Reverse Osmosis Polyamide Barrier Layers. *ACS Macro Lett.* **2019**, *8*, 352−356.
(211) Fu, Q.; Verma, N.; Hsiao, B. S.; Medellin-Rodriguez, F.; Beaucage, P. A.; Stafford, C. M.; Ocko, B. M. X-Ray Scattering Studies of Reverse Osmosis Materials. *Synchrotron Radiat. News* **2020**, *33*, 40.
(212) Shin, M. G.; Park, S. H.; Kwon, S. J.; Kwon, H. E.; Park, J. B.; Lee, J. H. Facile Performance Enhancement of Reverse Osmosis Membranes Via Solvent Activation with Benzyl Alcohol. *J. Membr. Sci.* **2019**, *578*, 220−229.
(213) Song, X. X.; Gan, B. W.; Yang, Z.; Tang, C. Y. Y.; Gao, C. J. Confined Nanobubbles Shape the Surface Roughness Structures of Thin Film Composite Polyamide Desalination Membranes. *J. Membr. Sci.* **2019**, *582*, 342−349.
(214) Freger, V. Nanoscale Heterogeneity of Polyamide Membranes Formed by Interfacial Polymerization. *Langmuir* **2003**, *19*, 4791−4797.
(215) Johnson, P. M.; Yoon, J.; Kelly, J. Y.; Howarter, J. A.; Stafford, C. M. Molecular Layer-by-Layer Deposition of Highly Crosslinked Polyamide Films. *J. Polym. Sci. B Polym. Phys.* **2012**, *50*, 168−173.
(216) Alf, M. E.; Asatekin, A.; Barr, M. C.; Baxamusa, S. H.; Chelawat, H.; Ozaydin-Ince, G.; Petruczok, C. D.; Sreenivasan, R.; Tenhaeff, W. E.; Trujillo, N. J.; et al. Chemical Vapor Deposition of Conformal, Functional, and Responsive Polymer Films. *Adv. Mater.* **2010**, *22*, 1993−2027.
(217) Putkonen, M.; Harjuoja, J.; Sajavaara, T.; Niinisto, L. Atomic Layer Deposition of Polyimide Thin Films. *J. Mater. Chem.* **2007**, *17*, 664−669.
(218) Chan, E. P.; Lee, J. H.; Chung, J. Y.; Stafford, C. M. An Automated Spin-Assisted Approach for Molecular Layer-by-Layer Assembly of Crosslinked Polymer Thin Films. *Rev. Sci. Instrum.* **2012**, *83*, 114102.
(219) Zimudzi, T. J.; Feldman, K. E.; Sturnfield, J. F.; Roy, A.; Hickner, M. A.; Stafford, C. M. Quantifying Carboxylic Acid Concentration in Model Polyamide Desalination Membranes Via Fourier Transform Infrared Spectroscopy. *Macromolecules* **2018**, *51*, 6623−6629.
(220) Broderick, A. H.; Manna, U.; Lynn, D. M. Covalent Layer-by-Layer Assembly of Water-Permeable and Water-Impermeable Polymer Multilayers on Highly Water-Soluble and Water-Sensitive Substrates. *Chem. Mater.* **2012**, *24*, 1786−1795.
(221) Lomadze, N.; Perez, M.; Prucker, O.; Ruhe, J.; Reinecke, H. Step-and-Repeat Assembly of Molecularly Controlled Ultrathin Polyaramide Layers. *Macromolecules* **2010**, *43*, 9056−9062.
(222) Chan, E. P. Deswelling of Ultrathin Molecular Layer-by-Layer Polyamide Water Desalination Membranes. *Soft Matter* **2014**, *10*, 2949−2954.
(223) Bates, F. S.; Fredrickson, G. H. Block Copolymers - Designer Soft Materials. *Phys. Today* **1999**, *52*, 32−38.
(224) Gin, D. L.; Bara, J. E.; Noble, R. D.; Elliott, B. J. Polymerized Lyotropic Liquid Crystal Assemblies for Membrane Applications. *Macromol. Rapid Commun.* **2008**, *29*, 367−389.
(225) Hillmyer, M. A. Nanoporous Materials from Block Copolymer Precursors. *Adv. Polym. Sci.* **2005**, *190*, 137−181.
(226) Fried, J. P.; Swett, J. L.; Nadappuram, B. P.; Mol, J. A.; Edel, J. B.; Ivanov, A. P.; Yates, J. R. In Situ Solid-State Nanopore Fabrication. *Chem. Soc. Rev.* **2021**, *50*, 4974−4992.
(227) Albrecht, T. Single-Molecule Analysis with Solid-State Nanopores. *Annual Review of Analytical Chemistry* **2019**, *12*, 371−387.
(228) Xue, L.; Yamazaki, H.; Ren, R.; Wanunu, M.; Ivanov, A. P.; Edel, J. B. Solid-State Nanopore Sensors. *Nat. Rev. Mater.* **2020**, *5*, 931−951.
(229) Nehra, A.; Ahlawat, S.; Singh, K. P. A Biosensing Expedition of Nanopore: A Review. *Sens. Actuators, B* **2019**, *284*, 595−622.
(230) Fleischer, R. L.; Price, P. B.; Walker, R. M.*Nuclear Tracks in Solids: Principles and Applications*; University of California Press1975.
(231) Spohr, R.Method for Producing Nuclear Traces or Microholes Originating from Nuclear Traces of an Individual Ion. US Patent US4369370A, 1983.
(232) Apel, P. Y.; Blonskaya, I. V.; Dmitriev, S. N.; Orelovitch, O. L.; Presz, A.; Sartowska, B. A. Fabrication of Nanopores in Polymer Foils with Surfactant-Controlled Longitudinal Profiles. *Nanotechnology* **2007**, *18*, 305302.
(233) Apel, P. Y.; Korchev, Y. E.; Siwy, Z.; Spohr, R.; Yoshida, M. Diode-Like Single-Ion Track Membrane Prepared by Electro-Stopping. *Nuclear Instruments & Methods in Physics Research Section B-Beam Interactions with Materials and Atoms* **2001**, *184*, 337−346.
(234) Scopece, P.; Baker, L. A.; Ugo, P.; Martin, C. R. Conical Nanopore Membranes: Solvent Shaping of Nanopores. *Nanotechnology* **2006**, *17*, 3951−3956.
(235) Wang, P.; Wang, M.; Liu, F.; Ding, S.; Wang, X.; Du, G.; Liu, J.; Apel, P.; Kluth, P.; Trautmann, C.; et al. Ultrafast Ion Sieving Using Nanoporous Polymeric Membranes. *Nat. Commun.* **2018**, *9*, 569.
(236) Quinn, J. A.; Anderson, J. L.; Ho, W. S.; Petzny, W. J. Model Pores of Molecular Dimension: The Preparation and Characterization of Track-Etched Membranes. *Biophys. J.* **1972**, *12*, 990−1007.
(237) Rajasekaran, P. R.; Wolff, J.; Zhou, C.; Kinsel, M.; Trautmann, C.; Aouadi, S.; Kohli, P. Two Dimensional Anisotropic Etching in Tracked Glass. *J. Mater. Chem.* **2009**, *19*, 8142−8149.
(238) Vlassiouk, I.; Apel, P. Y.; Dmitriev, S. N.; Healy, K.; Siwy, Z. S. Versatile Ultrathin Nanoporous Silicon Nitride Membranes. *Proc. Natl. Acad. Sci. U.S.A.* **2009**, *106*, 21039−21044.
(239) Storm, A. J.; Chen, J. H.; Ling, X. S.; Zandbergen, H. W.; Dekker, C. Fabrication of Solid-State Nanopores with Single-Nanometre Precision. *Nat. Mater.* **2003**, *2*, 537.
(240) Li, J.; Stein, D.; McMullan, C.; Branton, D.; Aziz, M. J.; Golovchenko, J. A. Ion-Beam Sculpting at Nanometre Length Scales. *Nature* **2001**, *412*, 166.
(241) Wei, R.; Pedone, D.; Zürner, A.; Döblinger, M.; Rant, U. Fabrication of Metallized Nanopores in Silicon Nitride Membranes for Single-Molecule Sensing. *Small* **2010**, *6*, 1406−1414.
(242) Fischbein, M. D.; Drndić, M. Electron Beam Nanosculpting of Suspended Graphene Sheets. *Appl. Phys. Lett.* **2008**, *93*, 113107.
(243) Feng, J.; Liu, K.; Bulushev, R. D.; Khlybov, S.; Dumcenco, D.; Kis, A.; Radenovic, A. Identification of Single Nucleotides in Mos2 Nanopores. *Nat. Nanotechnol.* **2015**, *10*, 1070−1076.
(244) Yang, J.; Ferranti, D. C.; Stern, L. A.; Sanford, C. A.; Huang, J.; Ren, Z.; Qin, L.-C.; Hall, A. R. Rapid and Precise Scanning Helium Ion Microscope Milling of Solid-State Nanopores for Biomolecule Detection. *Nanotechnology* **2011**, *22*, 285310.
(245) Russo, C. J.; Golovchenko, J. A. Atom-by-Atom Nucleation and Growth of Graphene Nanopores. *Proc. Natl. Acad. Sci. U.S.A.* **2012**, *109*, 5953−5957.

https://doi.org/10.1021/acs.chemrev.2c00155
Chem. Rev. 2023, 123, 2737−2831

(246) Kwok, H.; Briggs, K.; Tabard-Cossa, V. Nanopore Fabrication by Controlled Dielectric Breakdown. *PLoS One* **2014**, *9*, No. e92880.
(247) Bandara, Y. M. N. D. Y.; Karawdeniya, B. I.; Dwyer, J. R. Push-Button Method to Create Nanopores Using a Tesla-Coil Lighter. *ACS Omega* **2019**, *4*, 226−230.
(248) Cao, H.; Yu, Z.; Wang, J.; Tegenfeldt, J. O.; Austin, R. H.; Chen, E.; Wu, W.; Chou, S. Y. Fabrication of 10 Nm Enclosed Nanofluidic Channels. *Appl. Phys. Lett.* **2002**, *81*, 174−176.
(249) Mao, P.; Han, J. Fabrication and Characterization of 20 Nm Planar Nanofluidic Channels by Glass-Glass and Glass-Silicon Bonding. *Lab Chip* **2005**, *5*, 837−844.
(250) Stein, D.; Kruithof, M.; Dekker, C. Surface-Charge-Governed Ion Transport in Nanofluidic Channels. *Phys. Rev. Lett.* **2004**, *93*, 035901.
(251) Turner, S. W.; Perez, A. M.; Lopez, A.; Craighead, H. G. Monolithic Nanofluid Sieving Structures for DNA Manipulation. *Journal of Vacuum Science & Technology B: Microelectronics and Nanometer Structures Processing, Measurement, and Phenomena* **1998**, *16*, 3835−3840.
(252) Guan, W.; Fan, R.; Reed, M. A. Field-Effect Reconfigurable Nanofluidic Ionic Diodes. *Nat. Commun.* **2011**, *2*, 506.
(253) Duan, C.; Majumdar, A. Anomalous Ion Transport in 2-Nm Hydrophilic Nanochannels. *Nat. Nanotechnol.* **2010**, *5*, 848−852.
(254) Novoselov, K. S.; Jiang, D.; Schedin, F.; Booth, T. J.; Khotkevich, V. V.; Morozov, S. V.; Geim, A. K. Two-Dimensional Atomic Crystals. *Proc. Natl. Acad. Sci. U.S.A.* **2005**, *102*, 10451−10453.
(255) Geim, A. K.; Grigorieva, I. V. Van Der Waals Heterostructures. *Nature* **2013**, *499*, 419−425.
(256) Ponomarenko, L. A.; Geim, A. K.; Zhukov, A. A.; Jalil, R.; Morozov, S. V.; Novoselov, K. S.; Grigorieva, I. V.; Hill, E. H.; Cheianov, V. V.; Fal'ko, V. I.; et al. Tunable Metal-Insulator Transition in Double-Layer Graphene Heterostructures. *Nat. Phys.* **2011**, *7*, 958−961.
(257) Haigh, S. J.; Gholinia, A.; Jalil, R.; Romani, S.; Britnell, L.; Elias, D. C.; Novoselov, K. S.; Ponomarenko, L. A.; Geim, A. K.; Gorbachev, R. Cross-Sectional Imaging of Individual Layers and Buried Interfaces of Graphene-Based Heterostructures and Superlattices. *Nat. Mater.* **2012**, *11*, 764−767.
(258) Withers, F.; Del Pozo-Zamudio, O.; Mishchenko, A.; Rooney, A. P.; Gholinia, A.; Watanabe, K.; Taniguchi, T.; Haigh, S. J.; Geim, A. K.; Tartakovskii, A. I.; et al. Light-Emitting Diodes by Band-Structure Engineering in Van Der Waals Heterostructures. *Nat. Mater.* **2015**, *14*, 301−306.
(259) Graf, M.; Lihter, M.; Thakur, M.; Georgiou, S.; Topolancik, J.; Ilic, B. R.; Liu, K.; Feng, J. D.; Astier, Y.; Radenovic, A. Fabrication and Practical Applications of Molybdenum Disulfide Nanopores. *Nat. Protoc.* **2019**, *14*, 1130−1168.
(260) Mouterde, T.; Keerthi, A.; Poggioli, A. R.; Dar, S. A.; Siria, A.; Geim, A. K.; Bocquet, L.; Radha, B. Molecular Streaming and Its Voltage Control in Angstrom-Scale Channels. *Nature* **2019**, *567*, 87.
(261) Keerthi, A.; Geim, A. K.; Janardanan, A.; Rooney, A. P.; Esfandiar, A.; Hu, S.; Dar, S. A.; Grigorieva, I. V.; Haigh, S. J.; Wang, F. C.; et al. Ballistic Molecular Transport through Two-Dimensional Channels. *Nature* **2018**, *558*, 420.
(262) Zhang, W.-H.; Yin, M.-J.; Zhao, Q.; Jin, C.-G.; Wang, N.; Ji, S.; Ritt, C. L.; Elimelech, M.; An, Q.-F. Graphene Oxide Membranes with Stable Porous Structure for Ultrafast Water Transport. *Nat. Nanotechnol.* **2021**, *16*, 337.
(263) Ritt, C. L.; Werber, J. R.; Deshmukh, A.; Elimelech, M. Monte Carlo Simulations of Framework Defects in Layered Two Dimensional Nanomaterial Desalination Membranes: Implications for Permeability and Selectivity. *Environ. Sci. Technol.* **2019**, *53*, 6214−6224.
(264) Lu, X.; Gabinet, U. R.; Ritt, C. L.; Feng, X.; Deshmukh, A.; Kawabata, K.; Kaneda, M.; Hashmi, S. M.; Osuji, C. O.; Elimelech, M. Relating Selectivity and Separation Performance of Lamellar Two-Dimensional Molybdenum Disulfide (Mos2) Membranes to Nanosheet Stacking Behavior. *Environ. Sci. Technol.* **2020**, *54*, 9640−9651.
(265) Yang, Q.; Su, Y.; Chi, C.; Cherian, C. T.; Huang, K.; Kravets, V. G.; Wang, F. C.; Zhang, J. C.; Pratt, A.; Grigorenko, A. N.; et al. Ultrathin Graphene-Based Membrane with Precise Molecular Sieving and Ultrafast Solvent Permeation. *Nat. Mater.* **2017**, *16*, 1198.
(266) Sun, C.-F.; Meany, B.; Wang, Y.Characteristics and Applications of Carbon Nanotubes with Different Numbers of Walls. In *Carbon Nanotubes and Graphene*, 2nd ed.; Tanaka, K., Iijima, S., Eds.; Elsevier, 2014; Chapter 13, pp 313−339.
(267) Yang, F.; Wang, M.; Zhang, D.; Yang, J.; Zheng, M.; Li, Y. Chirality Pure Carbon Nanotubes: Growth, Sorting, and Characterization. *Chem. Rev.* **2020**, *120*, 2693−2758.
(268) Shen, C.; Brozena, A. H.; Wang, Y. Double-Walled Carbon Nanotubes: Challenges and Opportunities. *Nanoscale* **2011**, *3*, 503−518.
(269) Treacy, M. M. J.; Ebbesen, T. W.; Gibson, J. M. Exceptionally High Young's Modulus Observed for Individual Carbon Nanotubes. *Nature* **1996**, *381*, 678−680.
(270) Ghosh, S.; Bachilo, S. M.; Weisman, R. B. Advanced Sorting of Single-Walled Carbon Nanotubes by Nonlinear Density-Gradient Ultracentrifugation. *Nat. Nanotechnol.* **2010**, *5*, 443−450.
(271) Arnold, M. S.; Stupp, S. I.; Hersam, M. C. Enrichment of Single-Walled Carbon Nanotubes by Diameter in Density Gradients. *Nano Lett.* **2005**, *5*, 713−718.
(272) Arnold, M. S.; Green, A. A.; Hulvat, J. F.; Stupp, S. I.; Hersam, M. C. Sorting Carbon Nanotubes by Electronic Structure Using Density Differentiation. *Nat. Nanotechnol.* **2006**, *1*, 60−65.
(273) Liu, H.; Nishide, D.; Tanaka, T.; Kataura, H. Large-Scale Single-Chirality Separation of Single-Wall Carbon Nanotubes by Simple Gel Chromatography. *Nat. Commun.* **2011**, *2*, 309.
(274) Liu, H.; Tanaka, T.; Urabe, Y.; Kataura, H. High-Efficiency Single-Chirality Separation of Carbon Nanotubes Using Temperature-Controlled Gel Chromatography. *Nano Lett.* **2013**, *13*, 1996−2003.
(275) Ao, G.; Streit, J. K.; Fagan, J. A.; Zheng, M. Differentiating Left- and Right-Handed Carbon Nanotubes by DNA. *J. Am. Chem. Soc.* **2016**, *138*, 16677−16685.
(276) Nish, A.; Hwang, J. Y.; Doig, J.; Nicholas, R. J. Highly Selective Dispersion of Single-Walled Carbon Nanotubes Using Aromatic Polymers. *Nat. Nanotechnol.* **2007**, *2*, 640−646.
(277) Graf, A.; Zakharko, Y.; Schießl, S. P.; Backes, C.; Pfohl, M.; Flavel, B. S.; Zaumseil, J. Large Scale, Selective Dispersion of Long Single-Walled Carbon Nanotubes with High Photoluminescence Quantum Yield by Shear Force Mixing. *Carbon* **2016**, *105*, 593−599.
(278) Fagan, J. A.; Haroz, E. H.; Ihly, R.; Gui, H.; Blackburn, J. L.; Simpson, J. R.; Lam, S.; Hight Walker, A. R.; Doorn, S. K.; Zheng, M. Isolation of > 1 Nm Diameter Single-Wall Carbon Nanotube Species Using Aqueous Two-Phase Extraction. *ACS Nano* **2015**, *9*, 5377−5390.
(279) Li, H.; Gordeev, G.; Garrity, O.; Reich, S.; Flavel, B. S. Separation of Small-Diameter Single-Walled Carbon Nanotubes in One to Three Steps with Aqueous Two-Phase Extraction. *ACS Nano* **2019**, *13*, 2567−2578.
(280) Shen, C.; Ma, D.; Meany, B.; Isaacs, L.; Wang, Y. Acyclic Cucurbit[N]Uril Molecular Containers Selectively Solubilize Single-Walled Carbon Nanotubes in Water. *J. Am. Chem. Soc.* **2012**, *134*, 7254−7257.
(281) Hart, M.; White, E. R.; Chen, J.; McGilvery, C. M.; Pickard, C. J.; Michaelides, A.; Sella, A.; Shaffer, M. S. P.; Salzmann, C. G. Encapsulation and Polymerization of White Phosphorus inside Single-Wall Carbon Nanotubes. *Angew. Chem., Int. Ed. Engl.* **2017**, *56*, 8144−8148.
(282) Miners, S. A.; Fay, M. W.; Baldoni, M.; Besley, E.; Khlobystov, A. N.; Rance, G. A. Steric and Electronic Control of 1,3-Dipolar Cycloaddition Reactions in Carbon Nanotube Nanoreactors. *J. Phys. Chem. C* **2019**, *123*, 6294−6302.
(283) Britz, D. A.; Khlobystov, A. N.; Porfyrakis, K.; Ardavan, A.; Briggs, G. A. Chemical Reactions inside Single-Walled Carbon Nano Test-Tubes. *Chem. Commun.* **2005**, 37−39.
(284) Allen, C. S.; Ito, Y.; Robertson, A. W.; Shinohara, H.; Warner, J. H. Two-Dimensional Coalescence Dynamics of Encapsulated Metallofullerenes in Carbon Nanotubes. *ACS Nano* **2011**, *5*, 10084−10089.

(285) Hinds, B. J.; Chopra, N.; Rantell, T.; Andrews, R.; Gavalas, V.; Bachas, L. G. Aligned Multiwalled Carbon Nanotube Membranes. *Science* **2004**, *303*, 62−65.
(286) Li, Z.; Li, Y.; Yao, Y. C.; Aydin, F.; Zhan, C.; Chen, Y.; Elimelech, M.; Pham, T. A.; Noy, A. Strong Differential Monovalent Anion Selectivity in Narrow Diameter Carbon Nanotube Porins. *ACS Nano* **2020**, *14*, 6269−6275.
(287) Labropoulos, A.; Veziri, C.; Kapsi, M.; Pilatos, G.; Likodimos, V.; Tsapatsis, M.; Kanellopoulos, N. K.; Romanos, G. E.; Karanikolos, G. N. Carbon Nanotube Selective Membranes with Subnanometer, Vertically Aligned Pores, and Enhanced Gas Transport Properties. *Chem. Mater.* **2015**, *27*, 8198−8210.
(288) Bachilo, S. M.; Strano, M. S.; Kittrell, C.; Hauge, R. H.; Smalley, R. E.; Weisman, R. B. Structure-Assigned Optical Spectra of Single-Walled Carbon Nanotubes. *Science* **2002**, *298*, 2361−2366.
(289) Weisman, R. B.; Bachilo, S. M. Dependence of Optical Transition Energies on Structure for Single-Walled Carbon Nanotubes in Aqueous Suspension: An Empirical Kataura Plot. *Nano Lett.* **2003**, *3*, 1235−1238.
(290) Campo, J.; Piao, Y.; Lam, S.; Stafford, C. M.; Streit, J. K.; Simpson, J. R.; Hight Walker, A. R.; Fagan, J. A. Enhancing Single-Wall Carbon Nanotube Properties through Controlled Endohedral Filling. *Nanoscale Horiz* **2016**, *1*, 317−324.
(291) Fagan, J. A.; Huh, J. Y.; Simpson, J. R.; Blackburn, J. L.; Holt, J. M.; Larsen, B. A.; Walker, A. R. Separation of Empty and Water-Filled Single-Wall Carbon Nanotubes. *ACS Nano* **2011**, *5*, 3943−3953.
(292) Cambre, S.; Santos, S. M.; Wenseleers, W.; Nugraha, A. R.; Saito, R.; Cognet, L.; Lounis, B. Luminescence Properties of Individual Empty and Water-Filled Single-Walled Carbon Nanotubes. *ACS Nano* **2012**, *6*, 2649−2655.
(293) Dresselhaus, M. S.; Dresselhaus, G.; Saito, R.; Jorio, A. Exciton Photophysics of Carbon Nanotubes. *Annu. Rev. Phys. Chem.* **2007**, *58*, 719−747.
(294) Dresselhaus, M. S.; Dresselhaus, G.; Saito, R.; Jorio, A. Raman Spectroscopy of Carbon Nanotubes. *Phys. Rep.* **2005**, *409*, 47−99.
(295) Cambre, S.; Schoeters, B.; Luyckx, S.; Goovaerts, E.; Wenseleers, W. Experimental Observation of Single-File Water Filling of Thin Single-Wall Carbon Nanotubes Down to Chiral Index (5,3). *Phys. Rev. Lett.* **2010**, *104*, 207401.
(296) Wenseleers, W.; Cambré, S.; Čulin, J.; Bouwen, A.; Goovaerts, E. Effect of Water Filling on the Electronic and Vibrational Resonances of Carbon Nanotubes: Characterizing Tube Opening by Raman Spectroscopy. *Adv. Mater.* **2007**, *19*, 2274−2278.
(297) Sanchez-Valencia, J. R.; Dienel, T.; Gröning, O.; Shorubalko, I.; Mueller, A.; Jansen, M.; Amsharov, K.; Ruffieux, P.; Fasel, R. Controlled Synthesis of Single-Chirality Carbon Nanotubes. *Nature* **2014**, *512*, 61−64.
(298) Arenal, R.; Wang, M. S.; Xu, Z.; Loiseau, A.; Golberg, D. Young Modulus, Mechanical and Electrical Properties of Isolated Individual and Bundled Single-Walled Boron Nitride Nanotubes. *Nanotechnology* **2011**, *22*, 265704.
(299) Smith, M. W.; Jordan, K. C.; Park, C.; Kim, J. W.; Lillehei, P. T.; Crooks, R.; Harrison, J. S. Very Long Single- and Few-Walled Boron Nitride Nanotubes Via the Pressurized Vapor/Condenser Method. *Nanotechnology* **2009**, *20*, 505604.
(300) Allard, C.; Schue, L.; Fossard, F.; Recher, G.; Nascimento, R.; Flahaut, E.; Loiseau, A.; Desjardins, P.; Martel, R.; Gaufres, E. Confinement of Dyes inside Boron Nitride Nanotubes: Photostable and Shifted Fluorescence Down to the near Infrared. *Adv. Mater.* **2020**, *32*, No. 2001429.
(301) Siria, A.; Poncharal, P.; Biance, A.-L.; Fulcrand, R.; Blase, X.; Purcell, S. T.; Bocquet, L. Giant Osmotic Energy Conversion Measured in a Single Transmembrane Boron Nitride Nanotube. *Nature* **2013**, *494*, 455−458.
(302) Casanova, S.; Mistry, S.; Mazinani, S.; Borg, M. K.; Chew, Y. M. J.; Mattia, D. Enhanced Nanoparticle Rejection in Aligned Boron Nitride Nanotube Membranes. *Nanoscale* **2020**, *12*, 21138−21145.
(303) Kim, K. S.; Kingston, C. T.; Hrdina, A.; Jakubinek, M. B.; Guan, J.; Plunkett, M.; Simard, B. Hydrogen-Catalyzed, Pilot-Scale Production of Small-Diameter Boron Nitride Nanotubes and Their Macroscopic Assemblies. *ACS Nano* **2014**, *8*, 6211−6220.
(304) Lu, J.; Ren, Q.; Sun, L.; Yu, J.; Chen, Y.; Shen, X.; Chen, Z. Temperature-Dependent Raman Spectra of Bamboo-Like Boron Nitride Nanotubes. *Applied Physics Express* **2014**, *7*, 022401.
(305) Bagchi, B.*Water in Biological and Chemical Processes: From Structure and Dynamics to Function*; Cambridge University Press, 2013.
(306) Levinger, N. E.; Swafford, L. A. Ultrafast Dynamics in Reverse Micelles. *Annu. Rev. Phys. Chem.* **2009**, *60*, 385−406.
(307) Hodgson, C.; McIntosh, R. The Freezing of Water and Benzene in Porous Vycor Glass. *Canadian Journal of Chemistry-Revue Canadienne De Chimie* **1960**, *38*, 958−971.
(308) Hodgson, C.; McIntosh, R. Note on the Detection of an Apparent Phase Transition of Adsorbed Water on Porous Vycor Glass by Measurements of Dimensional Changes. *Canadian Journal of Chemistry-Revue Canadienne De Chimie* **1959**, *37*, 1278−1280.
(309) Hodgson, C.; McIntosh, R. The Freezing of Water and Benzene in Porous Vycor Glass. *Can. J. Chem.* **1960**, *38*, 958−971.
(310) Jackson, C. L.; McKenna, G. B. The Melting Behavior of Organic Materials Confined in Porous Solids. *J. Chem. Phys.* **1990**, *93*, 9002−9011.
(311) Awschalom, D. D.; Warnock, J. Supercooled Liquids and Solids in Porous Glass. *Phys. Rev. B* **1987**, *35*, 6779−6785.
(312) Jackson, C. L.; McKenna, G. B. Vitrification and Crystallization of Organic Liquids Confined to Nanoscale Pores. *Chem. Mater.* **1996**, *8*, 2128−2137.
(313) Xia, Y.; Dosseh, G.; Morineau, D.; Alba-Simionesco, C. Phase Diagram and Glass Transition of Confined Benzene. *J. Phys. Chem. B* **2006**, *110*, 19735−19744.
(314) Tang, X.-P.; Wang, J.-C.; Cary, L. W.; Kleinhammes, A.; Wu, Y. A ^{13}c Nmr Study of the Molecular Dynamics and Phase Transition of Confined Benzene inside Titanate Nanotubes. *J. Am. Chem. Soc.* **2005**, *127*, 9255−9259.
(315) Azaïs, T.; Tourné-Péteilh, C.; Aussenac, F.; Baccile, N.; Coelho, C.; Devoisselle, J.-M.; Babonneau, F. Solid-State Nmr Study of Ibuprofen Confined in Mcm-41 Material. *Chem. Mater.* **2006**, *18*, 6382−6390.
(316) Mitchell, J.; Webber, J. B. W.; Strange, J. H. Nuclear Magnetic Resonance Cryoporometry. *Phys. Rep.* **2008**, *461*, 1−36.
(317) Ongari, D.; Boyd, P. G.; Barthel, S.; Witman, M.; Haranczyk, M.; Smit, B. Accurate Characterization of the Pore Volume in Microporous Crystalline Materials. *Langmuir* **2017**, *33*, 14529−14538.
(318) Mason, J. A.; Veenstra, M.; Long, J. R. Evaluating Metal-Organic Frameworks for Natural Gas Storage. *Chem. Sci.* **2014**, *5*, 32−51.
(319) Gurvich, L. G. On the Physico-Chemical Force of Attraction. *J. Phys. Chem. Soc. Russia* **1915**, *47*, 805−827.
(320) Gardiner, D. J.; Graves, P. R.*Practical Raman Spectroscopy.*; Springer-Verlag: Berlin, 1989; p 158.
(321) Murry, R. L.; Fourkas, J. T. Polarization Selectivity of Nonresonant Spectroscopies in Isotropic Media. *J. Chem. Phys.* **1997**, *107*, 9726−9740.
(322) Czeslik, C.; Kim, Y. J.; Jonas, J. Dynamics of Confined Methyl Iodide Studied by Raman Spectroscopy. *J. Raman Spectrosc.* **2000**, *31*, 571−575.
(323) Yi, J.; Jonas, J. Raman Study of Vibrational and Rotational Relaxation of Liquid Benzene-D_6 Confined to Nanoporous Silica Glasses. *J. Phys. Chem.* **1996**, *100*, 16789−16793.
(324) Korb, J. P.; Delville, A.; Xu, S.; Demeulenaere, G.; Costa, P.; Jonas, J. Relative Role of Surface Interactions and Topological Effects in Nuclear Magnetic Resonance of Confined Liquids. *J. Chem. Phys.* **1994**, *101*, 7074−7081.
(325) Korb, J. P.; Xu, S.; Jonas, J. Confinement Effects on Dipolar Relaxation by Translational Dynamics of Liquids in Porous Silica Glasses. *J. Chem. Phys.* **1993**, *98*, 2411−2422.
(326) Koziol, P.; Nelson, S. D.; Jonas, J. Low-Dimensional Effects on Frequency Dependence of Proton Nmr Relaxation in Liquid Cyclohexane Confined to Porous Glasses. *Chem. Phys. Lett.* **1993**, *201*, 383−386.

https://doi.org/10.1021/acs.chemrev.2c00155
Chem. Rev. 2023, 123, 2737−2831

(327) Vogel, M. Nmr Studies on Simple Liquids in Confinement. *European Physical Journal Special Topics* **2010**, *189*, 47−64.
(328) Buntkowsky, G.; Breitzke, H.; Adamczyk, A.; Roelofs, F.; Emmler, T.; Gedat, E.; Grünberg, B.; Xu, Y.; Limbach, H.-H.; Shenderovich, I.; et al. Structural and Dynamical Properties of Guest Molecules Confined in Mesoporous Silica Materials Revealed by Nmr. *Phys. Chem. Chem. Phys.* **2007**, *9*, 4843−4853.
(329) Liu, G.; Mackowiak, M.; Li, Y.; Jonas, J. Rotational Diffusion of Liquid Toluene in Confined Geometry. *J. Chem. Phys.* **1991**, *94*, 239−242.
(330) Liu, G.; Li, Y.; Jonas, J. Confined Geometry Effects on Reorientational Dynamics of Molecular Liquids in Porous Silica Glasses. *J. Chem. Phys.* **1991**, *95*, 6892−6901.
(331) Zhang, J.; Jonas, J. Nmr Study of the Geometric Confinement Effects on the Anisotropic Rotational Diffusion of Acetonitrile-D_3. *J. Phys. Chem.* **1993**, *97*, 8812−8815.
(332) Righini, R. Ultrafast Optical Kerr Effect in Liquids and Solids. *Science* **1993**, *262*, 1386−1390.
(333) Hunt, N. T.; Jaye, A. A.; Meech, S. R. Ultrafast Dynamics in Complex Fluids Observed through the Ultrafast Optically-Heterodyne-Detected Optical-Kerr-Effect (Ohd-Oke). *Phys. Chem. Chem. Phys.* **2007**, *9*, 2167−2180.
(334) Zhong, Q.; Fourkas, J. T. Optical Kerr Effect Spectroscopy of Simple Liquids. *J. Phys. Chem. B* **2008**, *112*, 15529−15539.
(335) Warnock, J.; Awschalom, D. D.; Shafer, M. W. Orientational Behavior of Molecular Liquids in Restricted Geometries. *Phys. Rev. B* **1986**, *34*, 475−478.
(336) Farrer, R. A.; Loughnane, B. J.; Fourkas, J. T. Dynamics of Confined Carbon Disulfide from 165 to 310 K. *J. Phys. Chem. A* **1997**, *101*, 4005−4010.
(337) Loughnane, B. J.; Scodinu, A.; Fourkas, J. T. Extremely Slow Dynamics of a Weakly Wetting Liquid at a Solid/Liquid Interface: Cs2 Confined in Nanoporous Glasses. *J. Phys. Chem. B* **1999**, *103*, 6061−6068.
(338) Loughnane, B. J.; Fourkas, J. T. Geometric Effects in the Dynamics of a Nonwetting Liquid in Microconfinement: An Optical Kerr Effect Study of Methyl Iodide in Nanporous Glasses. *J. Phys. Chem. B* **1998**, *102*, 10288−10294.
(339) Farrer, R. A.; Fourkas, J. T. Orientational Dynamics of Liquids Confined in Nanoporous Sol-Gel Glasses Studied by Optical Kerr Effect Spectroscopy. *Acc. Chem. Res.* **2003**, *36*, 605−612.
(340) Loughnane, B. J.; Farrer, R. A.; Fourkas, J. T. Evidence for the Direct Observation of Molecular Exchange of a Liquid at the Solid/Liquid Interface. *J. Phys. Chem. B* **1998**, *102*, 5409−5412.
(341) Loughnane, B. J.; Farrer, R. A.; Scodinu, A.; Fourkas, J. T. Dynamics of a Wetting Liquid in Nanopores: An Optical Kerr Effect Study of the Dynamics of Acetonitrile Confined in Sol-Gel Glasses. *J. Chem. Phys.* **1999**, *111*, 5116−5123.
(342) Scodinu, A.; Fourkas, J. T. Comparison of the Orientational Dynamics of Water Confined in Hydrophobic and Hydrophilic Nanopores. *J. Phys. Chem. B* **2002**, *106*, 10292−10295.
(343) Kaatze, U.; Feldman, Y. Broadband Dielectric Spectrometry of Liquids and Biosystems. *Meas. Sci. Technol.* **2006**, *17*, R17−R35.
(344) Richert, R. Dynamics of Nanoconfined Supercooled Liquids. *Annu. Rev. Phys. Chem.* **2011**, *62*, 65−84.
(345) Pissis, P.; Kyritsis, A.; Daoukaki, D.; Barut, G.; Pelster, R.; Nimtz, G. Dielectric Studies of Glass Transition in Confined Propylene Glycol. *J. Phys.: Condens. Matter* **1998**, *10*, 6205−6227.
(346) Elamin, K.; Björklund, J.; Nyhlén, F.; Yttergren, M.; Mårtensson, L.; Swenson, J. Glass Transition and Relaxation Dynamics of Propylene Glycol-Water Solutions Confined in Clay. *J. Chem. Phys.* **2014**, *141*, 034505.
(347) Huwe, A.; Kremer, F.; Behrens, P.; Schwieger, W. Molecular Dynamics in Confining Space: From the Single Molecule to the Liquid State. *Phys. Rev. Lett.* **1999**, *82*, 2338−2341.
(348) Frunza, L.; Schönhals, A.; Kosslick, H.; Frunza, S. Relaxation Processes of Water Confined to Aimcm-41 Molecular Sieves. Influence of the Hydroxyl Groups of the Pore Surface. *European Physical Journal E. Soft Matter and Biological Physics* **2008**, *26*, 379−386.
(349) Garca-Coln, L. S.; del Castillo, L. F.; Goldstein, P. Theoretical Basis for the Vogel-Fulcher-Tammann Equation. *Phys. Rev. B* **1989**, *40*, 7040−7044.
(350) Frunza, L.; Schönhals, A.; Kosslick, H.; Frunza, S. Relaxation Processes of Water Confined to Almcm-41 Molecular Sieves. Influence of the Hydroxyl Groups of the Pore Surface. *Eur. Phys. J. E* **2008**, *26*, 379−386.
(351) Barbara, P.; Kang, T.; Jarzeba, W.; Fonseca, T.Solvation Dynamics and Ultrafast Electron Transfer. In *The Jerusalem Symposia on Quantum Chemistry and Biochemistry*; Perspectives in Photosynthesis; Jortner, J., Pullman, B., Eds.; Springer Netherlands, 1990; Vol. *22*, pp 273−292.
(352) Fleming, G. R.; Cho, M. Chromophore-Solvent Dynamics. *Annu. Rev. Phys. Chem.* **1996**, *47*, 109−134.
(353) Willard, D. M.; Riter, R. E.; Levinger, N. E. Dynamics of Polar Solvation in Lecithin/Water/Cyclohexane Reverse Micelles. *J. Am. Chem. Soc.* **1998**, *120*, 4151−4160.
(354) Baumann, R.; Ferrante, C.; Deeg, F. W.; Bräuchle, C. Solvation Dynamics of Nile Blue in Ethanol Confined in Porous Sol-Gel Glasses. *J. Chem. Phys.* **2001**, *114*, 5781−5791.
(355) Streck, C.; Mel'nichenko, Y. B.; Richert, R. Dynamics of Solvation in Supercooled Liquids Confined to the Pores of Sol-Gel Glasses. *Phys. Rev. B* **1996**, *53*, 5341−5347.
(356) Thompson, W. H. Solvation Dynamics and Proton Transfer in Nanoconfined Liquids. *Annu. Rev. Phys. Chem.* **2011**, *62*, 599−619.
(357) Fayer, M. D.*Ultrafast Infrared Vibrational Spectroscopy.*; CRC Press: Boca Raton, FL, 2013; p 475.
(358) Venables, D. S.; Huang, K.; Schmuttenmaer, C. A. Effect of Reverse Micelle Size on the Librational Band of Confined Water and Methanol. *J. Phys. Chem. B* **2001**, *105*, 9132−9138.
(359) Piletic, I. R.; Moilanen, D. E.; Spry, D. B.; Levinger, N. E.; Fayer, M. D. Testing the Core/Shell Model of Nanoconfined Water in Reverse Micelles Using Linear and Nonlinear Ir Spectroscopy. *J. Phys. Chem. A* **2006**, *110*, 4985−4999.
(360) Lawrence, C. P.; Skinner, J. L. Ultrafast Infrared Spectroscopy Probes Hydrogen-Bonding Dynamics in Liquid Water. *Chem. Phys. Lett.* **2003**, *369*, 472−477.
(361) Gulmen, T. S.; Thompson, W. H. Testing a Two-State Model of Nanoconfined Liquids: Conformational Equilibrium of Ethylene Glycol in Amorphous Silica Pores. *Langmuir* **2006**, *22*, 10919−10923.
(362) Laage, D.; Thompson, W. H. Reorientation Dynamics of Nanoconfined Water: Power-Law Decay, Hydrogen-Bond Jumps, and Test of a Two-State Model. *J. Chem. Phys.* **2012**, *136*, 044513.
(363) Norton, C. D.; Thompson, W. H. Reorientation Dynamics of Nanoconfined Acetonitrile: A Critical Examination of Two-State Models. *J. Phys. Chem. B* **2014**, *118*, 8227−8235.
(364) Embs, J. P.; Juranyi, F.; Hempelmann, R. Introduction to Quasielastic Neutron Scattering. *Zeitschrift Fur Physikalische Chemie-International Journal of Research in Physical Chemistry & Chemical Physics* **2010**, *224*, 5−32.
(365) Telling, M. T. F.*A Practical Guide to Quasi-Elastic Neutron Scattering*; Royal Society of Chemistry, 2020.
(366) Takahara, S.; Kittaka, S.; Mori, T.; Kuroda, Y.; Takamuku, T.; Yamaguchi, T. Neutron Scattering and Dielectric Studies on Dynamics of Methanol and Ethanol Confined in Mcm-41. *J. Phys. Chem. C* **2008**, *112*, 14385−14393.
(367) Takahara, S.; Sumiyama, N.; Kittaka, S.; Yamaguchi, T.; Bellissent-Funel, M.-C. Neutron Scattering Study on Dynamics of Water Molecules in Mcm-41. 2. Determination of Translational Diffusion Coefficient. *J. Phys. Chem. B* **2005**, *109*, 11231−11239.
(368) Hashimoto, S.; Nakajima, K.; Kikuchi, T.; Kamazawa, K.; Shibata, K.; Yamada, T. Experimental Analysis on Dynamics of Liquid Molecules Adjacent to Particles in Nanofluids. *J. Mol. Liq.* **2021**, *342*, 117580.
(369) Hoffmann, J.; Gillespie, D. Ion Correlations in Nanofluidic Channels: Effects of Ion Size, Valence, and Concentration on Voltage- and Pressure-Driven Currents. *Langmuir* **2013**, *29*, 1303−1317.
(370) Israelachvili, J.; Min, Y.; Akbulut, M.; Alig, A.; Carver, G.; Greene, W.; Kristiansen, K.; Meyer, E.; Pesika, N.; Rosenberg, K.; et al.

Recent Advances in the Surface Forces Apparatus (Sfa) Technique. *Rep. Prog. Phys.* **2010**, *73*, 036601.
(371) Israelachvili, J. N.; Adams, G. E. Direct Measurement of Long Range Forces between Two Mica Surfaces in Aqueous Kno3 Solutions. *Nature* **1976**, *262*, 774−776.
(372) Israelachvili, J. N. Adhesion Forces between Surfaces in Liquids and Condensable Vapours. *Surf. Sci. Rep.* **1992**, *14*, 109−159.
(373) Granick, S. Motions and Relaxations of Confined Liquids. *Science* **1991**, *253*, 1374−1379.
(374) Yoshizawa, H.; Chen, Y. L.; Israelachvili, J. Fundamental Mechanisms of Interfacial Friction. 1. Relation between Adhesion and Friction. *J. Phys. Chem.* **1993**, *97*, 4128−4140.
(375) Christenson, H. K. Confinement Effects on Freezing and Melting. *J. Phys.: Condens. Matter* **2001**, *13*, R95−R133.
(376) Heuberger, M.; Zäch, M.; Spencer, N. D. Density Fluctuations under Confinement: When Is a Fluid Not a Fluid? *Science* **2001**, *292*, 905−908.
(377) Hille, B.*Ion Channels of Excitable Membranes*, 3rd ed.; Oxford University Press, 2001.
(378) Sakmann, B.; Neher, E.*Single-Channel Recording*; Springer, 2009.
(379) Smeets, R. M. M.; Keyser, U. F.; Dekker, N. H.; Dekker, C. Noise in Solid-State Nanopores. *Proc. Natl. Acad. Sci. U. S. A.* **2008**, *105*, 417.
(380) Bandara, Y. M. N. D. Y.; Nichols, J. W.; Iroshika Karawdeniya, B.; Dwyer, J. R. Conductance-Based Profiling of Nanopores: Accommodating Fabrication Irregularities. *ELECTROPHORESIS* **2018**, *39*, 626−634.
(381) Lan, W.-J.; Holden, D. A.; Zhang, B.; White, H. S. Nanoparticle Transport in Conical-Shaped Nanopores. *Anal. Chem.* **2011**, *83*, 3840−3847.
(382) Pevarnik, M.; Healy, K.; Toimil-Molares, M. E.; Morrison, A.; Létant, S. E.; Siwy, Z. S. Polystyrene Particles Reveal Pore Substructure as They Translocate. *ACS Nano* **2012**, *6*, 7295−7302.
(383) Harms, Z. D.; Mogensen, K. B.; Nunes, P. S.; Zhou, K.; Hildenbrand, B. W.; Mitra, I.; Tan, Z.; Zlotnick, A.; Kutter, J. P.; Jacobson, S. C. Nanofluidic Devices with Two Pores in Series for Resistive-Pulse Sensing of Single Virus Capsids. *Anal. Chem.* **2011**, *83*, 9573−9578.
(384) Wolf, A.; Reber, N.; Apel, P. Y.; Fischer, B. E.; Spohr, R. Electrolyte Transport in Charged Single Ion Track Capillaries. *Nuclear Instruments and Methods in Physics Research Section B: Beam Interactions with Materials and Atoms* **1995**, *105*, 291−293.
(385) Li, S. X.; Guan, W.; Weiner, B.; Reed, M. A. Direct Observation of Charge Inversion in Divalent Nanofluidic Devices. *Nano Lett.* **2015**, *15*, 5046−5051.
(386) Alcaraz, A.; Nestorovich, E. M.; Aguilella-Arzo, M.; Aguilella, V. M.; Bezrukov, S. M. Salting out the Ionic Selectivity of a Wide Channel: The Asymmetry of Ompf. *Biophys. J.* **2004**, *87*, 943−957.
(387) Obergrussberger, A.; Friis, S.; Brüggemann, A.; Fertig, N. Automated Patch Clamp in Drug Discovery: Major Breakthroughs and Innovation in the Last Decade. *Expert Opinion on Drug Discovery* **2021**, *16*, 1−5.
(388) Kim, S. J.; Wang, Y. C.; Lee, J. H.; Jang, H.; Han, J. Concentration Polarization and Nonlinear Electrokinetic Flow near a Nanofluidic Channel. *Phys. Rev. Lett.* **2007**, *99*, 044501.
(389) Wei, C.; Bard, A. J.; Feldberg, S. W. Current Rectification at Quartz Nanopipet Electrodes. *Anal. Chem.* **1997**, *69*, 4627.
(390) Hou, X.; Guo, W.; Jiang, L. Biomimetic Smart Nanopores and Nanochannels. *Chem. Soc. Rev.* **2011**, *40*, 2385.
(391) Tian, Y.; Wen, L. P.; Hou, X.; Hou, G. L.; Jiang, L. Bioinspired Ion-Transport Properties of Solid-State Single Nanochannels and Their Applications in Sensing. *ChemPhysChem* **2012**, *13*, 2455−2470.
(392) Siwy, Z. S. Ion Current Rectification in Nanopores and Nanotubes with Broken Symmetry Revisited. *Adv. Funct. Mater.* **2006**, *16*, 735.
(393) Pietschmann, J. F.; Wolfram, M. T.; Burger, M.; Trautmann, C.; Nguyen, G.; Pevarnik, M.; Bayer, V.; Siwy, Z. S. Rectification Properties of Conically Shaped Nanopores: Consequences of Miniaturization. *Phys. Chem. Chem. Phys.* **2013**, *15*, 16917.
(394) Grosberg, A. Y.; Nguyen, T. T.; Shklovskii, B. I. Colloquium: The Physics of Charge Inversion in Chemical and Biological Systems. *Rev. Mod. Phys.* **2002**, *74*, 329−345.
(395) He, Y.; Gillespie, D.; Boda, D.; Vlassiouk, I.; Eisenberg, R. S.; Siwy, Z. S. Tuning Transport Properties of Nanofluidic Devices with Local Charge Inversion. *J. Am. Chem. Soc.* **2009**, *131*, 5194−5202.
(396) Siwy, Z.; Trofin, L.; Kohli, P.; Baker, L. A.; Trautmann, C.; Martin, C. R. Protein Biosensors Based on Functionalized Conical Gold Nanotubes. *J. Am. Chem. Soc.* **2005**, *127*, 5000.
(397) Wei, R.; Gatterdam, V.; Wieneke, R.; Tampé, R.; Rant, U. Stochastic Sensing of Proteins with Receptor-Modified Solid-State Nanopores. *Nat. Nanotechnol.* **2012**, *7*, 257−263.
(398) Sexton, L. T.; Horne, L. P.; Sherrill, S. A.; Bishop, G. W.; Baker, L. A.; Martin, C. R. Resistive-Pulse Studies of Proteins and Protein/Antibody Complexes Using a Conical Nanotube Sensor. *J. Am. Chem. Soc.* **2007**, *129*, 13144−13152.
(399) Cervera, J.; Schiedt, B.; Ramirez, P. A Poisson/Nernst-Planck Model for Ionic Transport through Synthetic Conical Nanopores. *Europhys. Lett.* **2005**, *71*, 35.
(400) Guan, W. H.; Fan, R.; Reed, M. A. Field-Effect Reconfigurable Nanofluidic Ionic Diodes. *Nat. Commun.* **2011**, *2*, 506.
(401) Powell, M. R.; Sullivan, M.; Vlassiouk, I.; Constantin, D.; Sudre, O.; Martens, C. C.; Eisenberg, R. S.; Siwy, Z. S. Nanoprecipitation-Assisted Ion Current Oscillations. *Nat. Nanotechnol.* **2008**, *3*, 51−57.
(402) Lin, K.; Lin, C.-Y.; Polster, J. W.; Chen, Y.; Siwy, Z. S. Charge Inversion and Calcium Gating in Mixtures of Ions in Nanopores. *J. Am. Chem. Soc.* **2020**, *142*, 2925−2934.
(403) Kalman, E.; Vlassiouk, I.; Siwy, Z. S. Nanofluidic Bipolar Transistors. *Adv. Mater.* **2008**, *20*, 293.
(404) Vlassiouk, I.; Siwy, Z. S. Nanofluidic Diode. *Nano Lett.* **2007**, *7*, 552.
(405) Westermann-Clark, G. B.; Anderson, J. L. Experimental Verification of the Space-Charge Model for Electrokinetics in Charged Microporous Membranes. *J. Electrochem. Soc.* **1983**, *130*, 839.
(406) Elimelech, M.; Chen, W. H.; Waypa, J. J. Measuring the Zeta (Electrokinetic) Potential of Reverse Osmosis Membranes by a Streaming Potential Analyzer. *Desalination* **1994**, *95*, 269−286.
(407) Kim, K. J.; Fane, A. G.; Nystrom, M.; Pihlajamaki, A.; Bowen, W. R.; Mukhtar, H. Evaluation of Electroosmosis and Streaming Potential for Measurement of Electric Charges of Polymeric Membranes. *J. Membr. Sci.* **1996**, *116*, 149−159.
(408) Szymczyk, A.; Fievet, P.; Mullet, M.; Reggiani, J. C.; Pagetti, J. Comparison of Two Electrokinetic Methods-Electroosmosis and Streaming Potential-to Determine the Zeta-Potential of Plane Ceramic Membranes. *J. Membr. Sci.* **1998**, *143*, 189−195.
(409) Peeters, J. M. M.; Mulder, M. H. V.; Strathmann, H. Streaming Potential Measurements as a Characterization Method for Nanofiltration Membranes. *Colloids Surf. A Physicochem. Eng. Asp.* **1999**, *150*, 247−259.
(410) Childress, A. E.; Elimelech, M. Relating Nanofiltration Membrane Performance to Membrane Charge (Electrokinetic) Characteristics. *Environ. Sci. Technol.* **2000**, *34*, 3710−3716.
(411) Fievet, P.; Szymczyk, A.; Aoubiza, B.; Pagetti, J. Evaluation of Three Methods for the Characterisation of the Membrane-Solution Interface: Streaming Potential, Membrane Potential and Electrolyte Conductivity inside Pores. *J. Membr. Sci.* **2000**, *168*, 87−100.
(412) Schaep, J.; Vandecasteele, C. Evaluating the Charge of Nanofiltration Membranes. *J. Membr. Sci.* **2001**, *188*, 129−136.
(413) Walker, S. L.; Bhattacharjee, S.; Hoek, E. M. V.; Elimelech, M. A Novel Asymmetric Clamping Cell for Measuring Streaming Potential of Flat Surfaces. *Langmuir* **2002**, *18*, 2193−2198.
(414) Sbaı, M.; Fievet, P.; Szymczyk, A.; Aoubiza, B.; Vidonne, A.; Foissy, A. Streaming Potential, Electroviscous Effect, Pore Conductivity and Membrane Potential for the Determination of the Surface Potential of a Ceramic Ultrafiltration Membrane. *J. Membr. Sci.* **2003**, *215*, 1−9.

https://doi.org/10.1021/acs.chemrev.2c00155
Chem. Rev. 2023, 123, 2737−2831

(415) Kirby, B. J.; Hasselbrink, E. F., Jr Zeta Potential of Microfluidic Substrates: 1. Theory, Experimental Techniques, and Effects on Separations. *Electrophoresis* **2004**, *25*, 187−202.
(416) Lyklema, J.*Fundamentals of Interface and Colloid Science: Soft Colloids*; Elsevier, 2005.
(417) Squires, T. M.; Quake, S. R. Microfluidics: Fluid Physics at the Nanoliter Scale. *Rev. Mod. Phys.* **2005**, *77*, 977.
(418) Delgado, Á. V.; González-Caballero, F.; Hunter, R. J.; Koopal, L. K.; Lyklema, J. Measurement and Interpretation of Electrokinetic Phenomena. *J. Colloid Interface Sci.* **2007**, *309*, 194−224.
(419) Datta, S.; Conlisk, A. T.; Kanani, D. M.; Zydney, A. L.; Fissell, W. H.; Roy, S. Characterizing the Surface Charge of Synthetic Nanomembranes by the Streaming Potential Method. *J. Colloid Interface Sci.* **2010**, *348*, 85−95.
(420) Morikawa, K.; Mawatari, K.; Kato, M.; Tsukahara, T.; Kitamori, T. Streaming Potential/Current Measurement System for Investigation of Liquids Confined in Extended-Nanospace. *Lab Chip* **2010**, *10*, 871−875.
(421) Saini, R.; Garg, A.; Barz, D. P. J. Streaming Potential Revisited: The Influence of Convection on the Surface Conductivity. *Langmuir* **2014**, *30*, 10950−10961.
(422) Mugele, F.; Bera, B.; Cavalli, A.; Siretanu, I.; Maestro, A.; Duits, M.; Cohen-Stuart, M.; Van Den Ende, D.; Stocker, I.; Collins, I. Ion Adsorption-Induced Wetting Transition in Oil-Water-Mineral Systems. *Sci. Rep.* **2015**, *5*, 10519.
(423) Squires, T. M. Particles in Electric Fields. *Fluids, Colloids and Soft Materials: An Introduction to Soft Matter Physics* **2016**, 59−79.
(424) Lucas, R. A.; Lin, C.-Y.; Siwy, Z. S. Electrokinetic Phenomena in Organic Solvents. *J. Phys. Chem. B* **2019**, *123*, 6123−6131.
(425) Collini, H.; Li, S.; Jackson, M. D.; Agenet, N.; Rashid, B.; Couves, J. Zeta Potential in Intact Carbonates at Reservoir Conditions and Its Impact on Oil Recovery During Controlled Salinity Waterflooding. *Fuel* **2020**, *266*, 116927.
(426) Dukhin, S. S. Non-Equilibrium Electric Surface Phenomena. *Adv. Colloid Interface Sci.* **1993**, *44*, 1−134.
(427) Bazant, M. Z.; Kilic, M. S.; Storey, B. D.; Ajdari, A. Towards an Understanding of Induced-Charge Electrokinetics at Large Applied Voltages in Concentrated Solutions. *Adv. Colloid Interface Sci.* **2009**, *152*, 48−88.
(428) Bonthuis, D. J.; Netz, R. R. Unraveling the Combined Effects of Dielectric and Viscosity Profiles on Surface Capacitance, Electro-Osmotic Mobility, and Electric Surface Conductivity. *Langmuir* **2012**, *28*, 16049−16059.
(429) Biesheuvel, P. M.; Bazant, M. Z. Analysis of Ionic Conductance of Carbon Nanotubes. *Phys. Rev. E* **2016**, *94*, 050601.
(430) Dubochet, J. The Physics of Rapid Cooling and Its Implications for Cryoimmobilization of Cells. *Methods Cell Biol.* **2007**, *79*, 7−21.
(431) Henderson, R. Overview and Future of Single Particle Electron Cryomicroscopy. *Arch. Biochem. Biophys.* **2015**, *581*, 19−24.
(432) Fernandez-Leiro, R.; Scheres, S. H. Unravelling Biological Macromolecules with Cryo-Electron Microscopy. *Nature* **2016**, *537*, 339−346.
(433) Li, H. K.; Pedro de Souza, J.; Zhang, Z.; Martis, J.; Sendgikoski, K.; Cumings, J.; Bazant, M. Z.; Majumdar, A. Imaging Arrangements of Discrete Ions at Liquid-Solid Interfaces. *Nano Lett.* **2020**, *20*, 7927−7932.
(434) Wu, H.; Friedrich, H.; Patterson, J. P.; Sommerdijk, N.; de Jonge, N. Liquid-Phase Electron Microscopy for Soft Matter Science and Biology. *Adv. Mater.* **2020**, *32*, No. 2001582.
(435) Park, J.; Koo, K.; Noh, N.; Chang, J. H.; Cheong, J. Y.; Dae, K. S.; Park, J. S.; Ji, S.; Kim, I. D.; Yuk, J. M. Graphene Liquid Cell Electron Microscopy: Progress, Applications, and Perspectives. *ACS Nano* **2021**, *15*, 288−308.
(436) Yuk, J. M.; Park, J.; Ercius, P.; Kim, K.; Hellebusch, D. J.; Crommie, M. F.; Lee, J. Y.; Zettl, A.; Alivisatos, A. P. High-Resolution Em of Colloidal Nanocrystal Growth Using Graphene Liquid Cells. *Science* **2012**, *336*, 61−64.
(437) Ye, X.; Jones, M. R.; Frechette, L. B.; Chen, Q.; Powers, A. S.; Ercius, P.; Dunn, G.; Rotskoff, G. M.; Nguyen, S. C.; Adiga, V. P.; et al. Single-Particle Mapping of Nonequilibrium Nanocrystal Transformations. *Science* **2016**, *354*, 874−877.
(438) Keskin, S.; de Jonge, N. Reduced Radiation Damage in Transmission Electron Microscopy of Proteins in Graphene Liquid Cells. *Nano Lett.* **2018**, *18*, 7435−7440.
(439) Naguib, N.; Ye, H.; Gogotsi, Y.; Yazicioglu, A. G.; Megaridis, C. M.; Yoshimura, M. Observation of Water Confined in Nanometer Channels of Closed Carbon Nanotubes. *Nano Lett.* **2004**, *4*, 2237−2243.
(440) Rice, W. J.; Cheng, A.; Noble, A. J.; Eng, E. T.; Kim, L. Y.; Carragher, B.; Potter, C. S. Routine Determination of Ice Thickness for Cryo-Em Grids. *J. Struct. Biol.* **2018**, *204*, 38−44.
(441) Hwang, J.; Daiguji, H. Ion Transport in Sub-10 Nm Nanofluidic Channels: Synthesis, Measurement, and Modeling. *Isr. J. Chem.* **2014**, *54*, 1509−1518.
(442) Zhang, Z.; Rayabharam, A.; Martis, J.; Li, H.-K.; Aluru, N. R.; Majumdar, A. Prospects for Sub-Nanometer Scale Imaging of Optical Phenomena Using Electron Microscopy. *Appl. Phys. Lett.* **2021**, *118*, 033104.
(443) Wu, X.; Kim, M.; Qu, H.; Wang, Y. Single-Defect Spectroscopy in the Shortwave Infrared. *Nat. Commun.* **2019**, *10*, 2672.
(444) Li, Y.; Wu, X.; Kim, M.; Fortner, J.; Qu, H.; Wang, Y. Fluorescent Ultrashort Nanotubes from Defect-Induced Chemical Cutting. *Chem. Mater.* **2019**, *31*, 4536−4544.
(445) Danne, N.; Kim, M.; Godin, A. G.; Kwon, H.; Gao, Z.; Wu, X.; Hartmann, N. F.; Doorn, S. K.; Lounis, B.; Wang, Y.; et al. Ultrashort Carbon Nanotubes That Fluoresce Brightly in the near-Infrared. *ACS Nano* **2018**, *12*, 6059−6065.
(446) Silvera-Batista, C. A.; Wang, R. K.; Weinberg, P.; Ziegler, K. J. Solvatochromic Shifts of Single-Walled Carbon Nanotubes in Non-polar Microenvironments. *Phys. Chem. Chem. Phys.* **2010**, *12*, 6990−6998.
(447) Misra, R. P.; Blankschtein, D. Insights on the Role of Many-Body Polarization Effects in the Wetting of Graphitic Surfaces by Water. *J. Phys. Chem. C* **2017**, *121*, 28166−28179.
(448) Bazant, M. Z.; Thornton, K.; Ajdari, A. Diffuse-Charge Dynamics in Electrochemical Systems. *Phys. Rev. E* **2004**, *70*, 021506.
(449) Kavokine, N.; Netz, R. R.; Bocquet, L. Fluids at the Nanoscale: From Continuum to Subcontinuum Transport. *Annu. Rev. Fluid Mech.* **2021**, *53*, 377−410.
(450) Misra, R. P.; Blankschtein, D. Ion Adsorption at Solid/Water Interfaces: Establishing the Coupled Nature of Ion-Solid and Water-Solid Interactions. *J. Phys. Chem. C* **2021**, *125*, 2666−2679.
(451) Wu, Y.; Aluru, N. R. Graphitic Carbon-Water Nonbonded Interaction Parameters. *J. Phys. Chem. B* **2013**, *117*, 8802−8813.
(452) Heiranian, M.; Wu, Y.; Aluru, N. R. Molybdenum Disulfide and Water Interaction Parameters. *J. Chem. Phys.* **2017**, *147*, 104706.
(453) Wu, Y.; Wagner, L. K.; Aluru, N. R. Hexagonal Boron Nitride and Water Interaction Parameters. *J. Chem. Phys.* **2016**, *144*, 164118−164118.
(454) Sresht, V.; Govind Rajan, A.; Bordes, E.; Strano, M. S.; Pádua, A. A. H.; Blankschtein, D. Quantitative Modeling of Mos 2 -Solvent Interfaces: Predicting Contact Angles and Exfoliation Performance Using Molecular Dynamics. *J. Phys. Chem. C* **2017**, *121*, 9022−9031.
(455) Govind Rajan, A.; Strano, M. S.; Blankschtein, D. Ab Initio Molecular Dynamics and Lattice Dynamics-Based Force Field for Modeling Hexagonal Boron Nitride in Mechanical and Interfacial Applications. *J. Phys. Chem. Lett.* **2018**, *9*, 1584−1591.
(456) Misra, R. P.; Blankschtein, D. Uncovering a Universal Molecular Mechanism of Salt Ion Adsorption at Solid/Water Interfaces. *Langmuir* **2021**, *37*, 722−733.
(457) Al-Hamdani, Y. S.; Nagy, P. R.; Zen, A.; Barton, D.; Kállay, M.; Brandenburg, J. G.; Tkatchenko, A. Interactions between Large Molecules Pose a Puzzle for Reference Quantum Mechanical Methods. *Nat. Commun.* **2021**, *12*, 3927.
(458) Ruiz-Barragan, S.; Munoz-Santiburcio, D.; Marx, D. Nano-confined Water within Graphene Slit Pores Adopts Distinct Confinement-Dependent Regimes. *J. Phys. Chem. Lett.* **2019**, *10*, 329−334.

https://doi.org/10.1021/acs.chemrev.2c00155
Chem. Rev. 2023, 123, 2737−2831

(459) Cicero, G.; Grossman, J. C.; Schwegler, E.; Gygi, F.; Galli, G. Water Confined in Nanotubes and between Graphene Sheets: A First Principle Study. *J. Am. Chem. Soc.* **2008**, *130*, 1871−1878.
(460) Kapil, V.; Schran, C.; Zen, A.; Chen, J.; Pickard, C. J.; Michaelides, A. The First-Principles Phase Diagram of Monolayer Nanoconfined Water. *Nature* **2022**, *609*, 512.
(461) Hosseini, E.; Zakertabrizi, M.; Habibnejad Korayem, A.; Carbone, P.; Esfandiar, A.; Shahsavari, R. Mechanical Hydrolysis Imparts Self-Destruction of Water Molecules under Steric Confinement. *Phys. Chem. Chem. Phys.* **2021**, *23*, 5999−6008.
(462) Coudert, F.-X.; Boutin, A.; Fuchs, A. H. Open Questions on Water Confined in Nanoporous Materials. *Commun. Chem.* **2021**, *4*, 106.
(463) Secchi, E.; Niguès, A.; Jubin, L.; Siria, A.; Bocquet, L. Scaling Behavior for Ionic Transport and Its Fluctuations in Individual Carbon Nanotubes. *Phys. Rev. Lett.* **2016**, *116*, 154501.
(464) Yao, Y. C.; Taqieddin, A.; Alibakhshi, M. A.; Wanunu, M.; Aluru, N. R.; Noy, A. Strong Electroosmotic Coupling Dominates Ion Conductance of 1.5 Nm Diameter Carbon Nanotube Porins. *ACS Nano* **2019**, *13*, 12851−12859.
(465) Møller, C.; Plesset, M. S. Note on an Approximation Treatment for Many-Electron Systems. *Phys. Rev.* **1934**, *46*, 618.
(466) Sherrill, C. D.; Schaefer, H. F. The Configuration Interaction Method: Advances in Highly Correlated Approaches. *Adv. Quantum Chem.* **1999**, *34*, 143−269.
(467) Kohn, W.; Sham, L. J. Self-Consistent Equations Including Exchange and Correlation Effects. *Phys. Rev.* **1965**, *140*, A1133.
(468) Kohn, W.; Sham, L. Quantum Density Oscillations in an Inhomogeneous Electron Gas. *Phys. Rev.* **1965**, *137*, A1697.
(469) Kohn, W. Density-Functional Theory for Excited States in a Quasi-Local-Density Approximation. *Phys. Rev. A* **1986**, *34*, 737.
(470) Perdew, J. P.; Chevary, J. A.; Vosko, S. H.; Jackson, K. A.; Pederson, M. R.; Singh, D. J.; Fiolhais, C. Atoms, Molecules, Solids, and Surfaces: Applications of the Generalized Gradient Approximation for Exchange and Correlation. *Phys. Rev. B* **1992**, *46*, 6671.
(471) Langreth, D. C.; Mehl, M. Beyond the Local-Density Approximation in Calculations of Ground-State Electronic Properties. *Phys. Rev. B* **1983**, *28*, 1809.
(472) Adamo, C.; Ernzerhof, M.; Scuseria, G. E. The Meta-Gga Functional: Thermochemistry with a Kinetic Energy Density Dependent Exchange-Correlation Functional. *J. Chem. Phys.* **2000**, *112*, 2643−2649.
(473) Becke, A. D. A New Mixing of Hartree-Fock and Local Density-Functional Theories. *J. Chem. Phys.* **1993**, *98*, 1372−1377.
(474) Fischer, C. F.*Hartree−Fock Method for Atoms: A Numerical Approach.*; John Wiley & Sons, 1977.
(475) Perdew, J. P.; Ernzerhof, M.; Burke, K. Rationale for Mixing Exact Exchange with Density Functional Approximations. *J. Chem. Phys.* **1996**, *105*, 9982−9985.
(476) Becke, A. D. Density-Functional Thermochemistry. Iii. The Role of Exact Exchange. *J. Chem. Phys.* **1993**, *98*, 5648−5646.
(477) Pati, R.; Zhang, Y.; Nayak, S. K.; Ajayan, P. M. Effect of H2o Adsorption on Electron Transport in a Carbon Nanotube. *Appl. Phys. Lett.* **2002**, *81*, 2638−2640.
(478) Sung, D.; Hong, S.; Kim, Y.-H.; Park, N.; Kim, S.; Maeng, S. L.; Kim, K.-C. Ab Initio Study of the Effect of Water Adsorption on the Carbon Nanotube Field-Effect Transistor. *Appl. Phys. Lett.* **2006**, *89*, 243110.
(479) Kovalenko, A.; Hirata, F. Self-Consistent Description of a Metal-Water Interface by the Kohn-Sham Density Functional Theory and the Three-Dimensional Reference Interaction Site Model. *J. Chem. Phys.* **1999**, *110*, 10095−10112.
(480) Schnur, S.; Groß, A. Properties of Metal-Water Interfaces Studied from First Principles. *New J. Phys.* **2009**, *11*, 125003.
(481) Carrasco, J.; Hodgson, A.; Michaelides, A. A Molecular Perspective of Water at Metal Interfaces. *Nat. Mater.* **2012**, *11*, 667−674.
(482) Ma, J.; Michaelides, A.; Alfè, D.; Schimka, L.; Kresse, G.; Wang, E. Adsorption and Diffusion of Water on Graphene from First Principles. *Phys. Rev. B* **2011**, *84*, 033402.
(483) Freitas, R.; Rivelino, R.; Mota, F. d. B.; De Castilho, C. Dft Studies of the Interactions of a Graphene Layer with Small Water Aggregates. *J. Phys. Chem. A* **2011**, *115*, 12348−12356.
(484) Wehling, T. O.; Lichtenstein, A. I.; Katsnelson, M. I. First-Principles Studies of Water Adsorption on Graphene: The Role of the Substrate. *Appl. Phys. Lett.* **2008**, *93*, 202110.
(485) Gillespie, D.; Khair, A. S.; Bardhan, J. P.; Pennathur, S. Efficiently Accounting for Ion Correlations in Electrokinetic Nanofluidic Devices Using Density Functional Theory. *J. Colloid Interface Sci.* **2011**, *359*, 520−529.
(486) Yu, Y.-X.; Wu, J.; Gao, G.-H. Density-Functional Theory of Spherical Electric Double Layers and Z Potentials of Colloidal Particles in Restricted-Primitive-Model Electrolyte Solutions. *J. Chem. Phys.* **2004**, *120*, 7223−7233.
(487) Schrödinger, E. Quantisierung Als Eigenwertproblem. *Annalen der physik* **1926**, *385*, 437−490.
(488) Slater, J. C. The Theory of Complex Spectra. *Phys. Rev.* **1929**, *34*, 1293.
(489) Čížek, J. On the Correlation Problem in Atomic and Molecular Systems. Calculation of Wavefunction Components in Ursell-Type Expansion Using Quantum-Field Theoretical Methods. *J. Chem. Phys.* **1966**, *45*, 4256−4266.
(490) Xantheas, S. S. Ab Initio Studies of Cyclic Water Clusters (H2o)N, N = 1−6. Iii. Comparison of Density Functional with Mp2 Results. *J. Chem. Phys.* **1995**, *102*, 4505−4517.
(491) Head-Gordon, M.; Pople, J. A.; Frisch, M. J. Mp2 Energy Evaluation by Direct Methods. *Chem. Phys. Lett.* **1988**, *153*, 503−506.
(492) Winter, N. W.; Goddard, W. A.; Bobrowicz, F. W. Configuration Interaction Studies of the Excited States of Water. *J. Chem. Phys.* **1975**, *62*, 4325−4331.
(493) Bettinger, H. F.; Tönshoff, C.; Doerr, M.; Sanchez-Garcia, E. Electronically Excited States of Higher Acenes up to Nonacene: A Density Functional Theory/Multireference Configuration Interaction Study. *J. Chem. Theory Comput.* **2016**, *12*, 305−312.
(494) Gruber, T.; Liao, K.; Tsatsoulis, T.; Hummel, F.; Grüneis, A. Applying the Coupled-Cluster Ansatz to Solids and Surfaces in the Thermodynamic Limit. *Phys. Rev. X* **2018**, *8*, 21043.
(495) Voloshina, E.; Usvyat, D.; Schütz, M.; Dedkov, Y.; Paulus, B. On the Physisorption of Water on Graphene: A Ccsd(T) Study. *Phys. Chem. Chem. Phys.* **2011**, *13*, 12041−12047.
(496) Bohm, D.; Pines, D. I. A Collective Description of Electron Interactions. I. Magnetic Interactions. *Phys. Rev.* **1951**, *82*, 625.
(497) Pines, D.; Bohm, D. A Collective Description of Electron Interactions: Ii. Collective Vs Individual Particle Aspects of the Interactions. *Phys. Rev.* **1952**, *85*, 338.
(498) Bohm, D.; Pines, D. A Collective Description of Electron Interactions: Iii. Coulomb Interactions in a Degenerate Electron Gas. *Phys. Rev.* **1953**, *92*, 609.
(499) Szalewicz, K. Symmetry-Adapted Perturbation Theory of Intermolecular Forces. *Wiley Interdisciplinary Reviews-Computational Molecular Science* **2012**, *2*, 254−272.
(500) Parker, T. M.; Burns, L. A.; Parrish, R. M.; Ryno, A. G.; Sherrill, C. D. Levels of symmetry adapted perturbation theory (SAPT). I. Efficiency and performance for interaction energies. *J. Chem. Phys.* **2014**, *140*, 094106.
(501) Perdew, J. P.; Burke, K.; Ernzerhof, M. Generalized Gradient Approximation Made Simple. *Phys. Rev. Lett.* **1996**, *77*, 3865.
(502) Sharma, M.; Donadio, D.; Schwegler, E.; Galli, G. Probing Properties of Water under Confinement: Infrared Spectra. *Nano Lett.* **2008**, *8*, 2959−2962.
(503) Marzari, N.; Vanderbilt, D. Maximally Localized Generalized Wannier Functions for Composite Energy Bands. *Physical Review B - Condensed Matter and Materials Physics* **1997**, *56*, 12847−12865.
(504) Clark, J. K.; Paddison, S. J. Ab Initio Molecular Dynamics Simulations of Water and an Excess Proton in Water Confined in Carbon Nanotubes. *Phys. Chem. Chem. Phys.* **2014**, *16*, 17756−17769.

https://doi.org/10.1021/acs.chemrev.2c00155
Chem. Rev. 2023, 123, 2737−2831

(505) Laasonen, K.; Pasquarello, A.; Car, R.; Lee, C.; Vanderbilt, D. Car-Parrinello Molecular Dynamics with Vanderbilt Ultrasoft Pseudopotentials. *Phys. Rev. B* **1993**, *47*, 10142.
(506) Gordillo, M. C.; Martí, J. Hydrogen Bond Structure of Liquid Water Confined in Nanotubes. *Chem. Phys. Lett.* **2000**, *329*, 341−345.
(507) Joseph, S.; Aluru, N. R. Why Are Carbon Nanotubes Fast Transporters of Water? *Nano Lett.* **2008**, *8*, 452−458.
(508) Liu, Y. C.; Shen, J. W.; Gubbins, K. E.; Moore, J. D.; Wu, T.; Wang, Q. Diffusion Dynamics of Water Controlled by Topology of Potential Energy Surface inside Carbon Nanotubes. *Phys. Rev. B* **2008**, *77*, 125438.
(509) Kalra, A.; Garde, S.; Hummer, G. Osmotic Water Transport through Carbon Nanotube Membranes. *Proc. Natl. Acad. Sci. U.S.A.* **2003**, *100*, 10175−10180.
(510) Ma, M.; Grey, F.; Shen, L.; Urbakh, M.; Wu, S.; Liu, J. Z.; Liu, Y.; Zheng, Q. Water Transport inside Carbon Nanotubes Mediated by Phonon-Induced Oscillating Friction. *Nat. Nanotechnol.* **2015**, *10*, 692−695.
(511) Joseph, S.; Mashl, R. J.; Jakobsson, E.; Aluru, N. Electrolytic Transport in Modified Carbon Nanotubes. *Nano Lett.* **2003**, *3*, 1399−1403.
(512) Bai, J.; Su, C. R.; Parra, R. D.; Zeng, X. C.; Tanaka, H.; Koga, K.; Li, J. M. Ab Initiostudies of Quasi-One-Dimensional Pentagon and Hexagon Ice Nanotubes. *J. Chem. Phys.* **2003**, *118*, 3913−3916.
(513) Shao, Q.; Zhou, J.; Lu, L.; Lu, X.; Zhu, Y.; Jiang, S. Anomalous Hydration Shell Order of Na^+ and K^+ inside Carbon Nanotubes. *Nano Lett.* **2009**, *9*, 989−994.
(514) Pham, T. A.; Mortuza, S. M. G.; Wood, B. C.; Lau, E. Y.; Ogitsu, T.; Buchsbaum, S. F.; Siwy, Z. S.; Fornasiero, F.; Schwegler, E. Salt Solutions in Carbon Nanotubes: The Role of Cation-Π Interactions. *J. Phys. Chem. C* **2016**, *120*, 7332−7338.
(515) Kulik, H. J.; Schwegler, E.; Galli, G. Probing the Structure of Salt Water under Confinement with First-Principles Molecular Dynamics and Theoretical X-Ray Absorption Spectroscopy. *journal of physical chemistry letters* **2012**, *3*, 2653−2658.
(516) Rozsa, V.; Pham, T. A.; Galli, G. Molecular Polarizabilities as Fingerprints of Perturbations to Water by Ions and Confinement. *J. Chem. Phys.* **2020**, *152*, 124501.
(517) Barati Farimani, A.; Aluru, N. R. Spatial Diffusion of Water in Carbon Nanotubes: From Fickian to Ballistic Motion. *J. Phys. Chem. B* **2011**, *115*, 12145−12149.
(518) Tang, Y. W.; Chan, K.-Y.; Szalai, I. Structural and Transport Properties of an Spc/E Electrolyte in a Nanopore. *J. Phys. Chem. B* **2004**, *108*, 18204−18213.
(519) Peng, J.; Cao, D.; He, Z.; Guo, J.; Hapala, P.; Ma, R.; Cheng, B.; Chen, J.; Xie, W. J.; Li, X. Z.; et al. The Effect of Hydration Number on the Interfacial Transport of Sodium Ions. *Nature* **2018**, *557*, 701−705.
(520) Kong, J.; Bo, Z.; Yang, H.; Yang, J.; Shuai, X.; Yan, J.; Cen, K. Temperature Dependence of Ion Diffusion Coefficients in Nacl Electrolyte Confined within Graphene Nanochannels. *Phys. Chem. Chem. Phys.* **2017**, *19*, 7678−7688.
(521) Mondal, S.; Bagchi, B. Water in Carbon Nanotubes: Pronounced Anisotropy in Dielectric Dispersion and Its Microscopic Origin. *J. Phys. Chem. Lett.* **2019**, *10*, 6287−6292.
(522) Motevaselian, M. H.; Aluru, N. R. Universal Reduction in Dielectric Response of Confined Fluids. *ACS Nano* **2020**, *14*, 12761−12770.
(523) Wang, J. M.; Wolf, R. M.; Caldwell, J. W.; Kollman, P. a.; Case, D. a. Development and Testing of a General Amber Force Field. *J. Comput. Chem.* **2004**, *25*, 1157−1174.
(524) Brooks, B. R.; Brooks, C. L.; Mackerell, A. D.; Nilsson, L.; Petrella, R. J.; Roux, B.; Won, Y.; Archontis, G.; Bartels, C.; Boresch, S.; et al. Charmm: The Biomolecular Simulation Program. *J. Comput. Chem.* **2009**, *30*, 1545−1614.
(525) Jorgensen, W. L.; Maxwell, D. S.; Tirado-Rives, J. Development and Testing of the Olps All-Atom Force Field on Conformational Energetics and Properties of Organic Liquids. *J. Am. Chem. Soc.* **1996**, *118*, 11225−11236.
(526) Jackson, J. D.*Classical Electrodynamics*; John Wiley & Sons, 2012.
(527) Stone, A.*The Theory of Intermolecular Forces*; Oxford University Press Oxford, 2013.
(528) Lamoureux, G.; Roux, B. t. Modeling Induced Polarization with Classical Drude Oscillators: Theory and Molecular Dynamics Simulation Algorithm. *J. Chem. Phys.* **2003**, *119*, 3025−3039.
(529) Thole, B. T. Molecular Polarizabilities Calculated with a Modified Dipole Interaction. *Chem. Phys.* **1981**, *59*, 341−350.
(530) Zwanzig, R. W. High-Temperature Equation of State by a Perturbation Method. I. Nonpolar Gases. *J. Chem. Phys.* **1954**, *22*, 1420−1426.
(531) Adam, N. K. Use of the Term 'Young's Equation' for Contact Angles. *Nature* **1957**, *180*, 809−810.
(532) Li, Z.; Wang, Y.; Kozbial, A.; Shenoy, G.; Zhou, F.; McGinley, R.; Ireland, P.; Morganstein, B.; Kunkel, A.; Surwade, S. P.; et al. Effect of Airborne Contaminants on the Wettability of Supported Graphene and Graphite. *Nat. Mater.* **2013**, *12*, 925−931.
(533) Kozbial, A.; Li, Z.; Sun, J.; Gong, X.; Zhou, F.; Wang, Y.; Xu, H.; Liu, H.; Li, L. Understanding the Intrinsic Water Wettability of Graphite. *Carbon* **2014**, *74*, 218−225.
(534) Amadei, C. A.; Lai, C.-Y.; Heskes, D.; Chiesa, M. Time Dependent Wettability of Graphite Upon Ambient Exposure: The Role of Water Adsorption. *J. Chem. Phys.* **2014**, *141*, 084709−084709.
(535) Ondarçuhu, T.; Thomas, V.; Nuñez, M.; Dujardin, E.; Rahman, A.; Black, C. T.; Checco, A. Wettability of Partially Suspended Graphene. *Sci. Rep.* **2016**, *6*, 24237.
(536) Kumar, P.; Chauhan, Y. S.; Agarwal, A.; Bhowmick, S. Thickness and Stacking Dependent Polarizability and Dielectric Constant of Graphene-Hexagonal Boron Nitride Composite Stacks. *J. Phys. Chem. C* **2016**, *120*, 17620−17626.
(537) Kumar, P.; Bhadoria, B. S.; Kumar, S.; Bhowmick, S.; Chauhan, Y. S.; Agarwal, A. Thickness and Electric-Field-Dependent Polarizability and Dielectric Constant in Phosphorene. *Phys. Rev. B* **2016**, *93*, 195428−195428.
(538) Shih, C. J.; Wang, Q. H.; Lin, S. C.; Park, K. C.; Jin, Z.; Strano, M. S.; Blankschtein, D. Breakdown in the Wetting Transparency of Graphene. *Phys. Rev. Lett.* **2012**, *109*, 176101.
(539) Shih, C. J.; Strano, M. S.; Blankschtein, D. Wetting Translucency of Graphene. *Nat. Mater.* **2013**, *12*, 866−869.
(540) Driskill, J.; Vanzo, D.; Bratko, D.; Luzar, A. Wetting Transparency of Graphene in Water. *J. Chem. Phys.* **2014**, *141*, 18C517.
(541) Ojaghlou, N.; Bratko, D.; Salanne, M.; Shafiei, M.; Luzar, A. Solvent-Solvent Correlations across Graphene: The Effect of Image Charges. *ACS Nano* **2020**, *14*, 7987−7998.
(542) Siepmann, J. I.; Sprik, M. Influence of Surface Topology and Electrostatic Potential on Water/Electrode Systems. *J. Chem. Phys.* **1995**, *102*, 511−524.
(543) Ho, T. A.; Striolo, A. Polarizability Effects in Molecular Dynamics Simulations of the Graphene-Water Interface. *J. Chem. Phys.* **2013**, *138*, 054117.
(544) Stoller, M. D.; Park, S.; Zhu, Y.; An, J.; Ruoff, R. S. Graphene-Based Ultracapacitors. *Nano Lett.* **2008**, *8*, 3498−3502.
(545) Yoo, E.; Kim, J.; Hosono, E.; Zhou, H.-s.; Kudo, T.; Honma, I. Large Reversible Li Storage of Graphene Nanosheet Families for Use in Rechargeable Lithium Ion Batteries. *Nano Lett.* **2008**, *8*, 2277−2282.
(546) Raccichini, R.; Varzi, A.; Passerini, S.; Scrosati, B. The Role of Graphene for Electrochemical Energy Storage. *Nat. Mater.* **2015**, *14*, 271−279.
(547) Cohen-Tanugi, D.; Grossman, J. C. Water Desalination across Nanoporous Graphene. *Nano Lett.* **2012**, *12*, 3602−3608.
(548) Surwade, S. P.; Smirnov, S. N.; Vlassiouk, I. V.; Unocic, R. R.; Veith, G. M.; Dai, S.; Mahurin, S. M. Water Desalination Using Nanoporous Single-Layer Graphene. *Nat. Nanotechnol.* **2015**, *10*, 459.
(549) Assaf, K. I.; Nau, W. M. The Chaotropic Effect as an Assembly Motif in Chemistry. *Angew. Chem., Int. Ed.* **2018**, *57*, 13968−13981.
(550) McCaffrey, D. L.; Nguyen, S. C.; Cox, S. J.; Weller, H.; Alivisatos, A. P.; Geissler, P. L.; Saykally, R. J. Mechanism of Ion

Adsorption to Aqueous Interfaces: graphene−water Vs. Air/Water. *Proc. Natl. Acad. Sci. U.S.A.* **2017**, *114*, 13369−13373.
(551) Luo, Z.-X.; Xing, Y.-Z.; Ling, Y.-C.; Kleinhammes, A.; Wu, Y. Electroneutrality Breakdown and Specific Ion Effects in Nanoconfined Aqueous Electrolytes Observed by Nmr. *Nat. Commun.* **2015**, *6*, 6358.
(552) Rajan, A. G.; Sresht, V.; Padua, A. A. H.; Strano, M. S.; Blankschtein, D. Dominance of Dispersion Interactions and Entropy over Electrostatics in Determining the Wettability and Friction of Two-Dimensional Mos2 Surfaces. *ACS Nano* **2016**, *10*, 9145−9155.
(553) Rajan, A. G.; Strano, M. S.; Blankschtein, D. Ab Initio Molecular Dynamics and Lattice Dynamics-Based Force Field for Modeling Hexagonal Boron Nitride in Mechanical and Interfacial Applications. *J. Phys. Chem. Lett.* **2018**, *9*, 1584−1591.
(554) Rajan, A. G.; Strano, M. S.; Blankschtein, D. Liquids with Lower Wettability Can Exhibit Higher Friction on Hexagonal Boron Nitride: The Intriguing Role of Solid-Liquid Electrostatic Interactions. *Nano Lett.* **2019**, *19*, 1539−1551.
(555) Son, C. Y.; Wang, Z. G. Image-Charge Effects on Ion Adsorption near Aqueous Interfaces. *Proc. Natl. Acad. Sci. U. S. A.* **2021**, *118*, No. e2020615118.
(556) Di Pasquale, N.; Elliott, J. D.; Hadjidoukas, P.; Carbone, P. Dynamically Polarizable Force Fields for Surface Simulations Via Multi-Output Classification Neural Networks. *J. Chem. Theory Comput.* **2021**, *17*, 4477−4485.
(557) Mashayak, S.; Aluru, N. Coarse-Grained Potential Model for Structural Prediction of Confined Water. *J. Chem. Theory Comput.* **2012**, *8*, 1828−1840.
(558) Mashayak, S.; Aluru, N. A Multiscale Model for Charge Inversion in Electric Double Layers. *J. Chem. Phys.* **2018**, *148*, 214102.
(559) Hansen, J.-P.; Löwen, H. Effective Interactions between Electric Double Layers. *Annu. Rev. Phys. Chem.* **2000**, *51*, 209−242.
(560) Turesson, M.; Jönsson, B.; Labbez, C. Coarse-Graining Intermolecular Interactions in Dispersions of Highly Charged Colloids. *Langmuir* **2012**, *28*, 4926−4930.
(561) Mashayak, S.; Aluru, N. Langevin-Poisson-Eqt: A Dipolar Solvent Based Quasi-Continuum Approach for Electric Double Layers. *J. Chem. Phys.* **2017**, *146*, 044108.
(562) Noh, Y.; Aluru, N. R. Ion Transport in Electrically Imperfect Nanopores. *ACS Nano* **2020**, *14*, 10518−10526.
(563) Marrink, S. J.; Risselada, H. J.; Yefimov, S.; Tieleman, D. P.; De Vries, A. H. The Martini Force Field: Coarse Grained Model for Biomolecular Simulations. *J. Phys. Chem. B* **2007**, *111*, 7812−7824.
(564) Monticelli, L.; Kandasamy, S. K.; Periole, X.; Larson, R. G.; Tieleman, D. P.; Marrink, S.-J. The Martini Coarse-Grained Force Field: Extension to Proteins. *J. Chem. Theory Comput.* **2008**, *4*, 819−834.
(565) López, C. A.; Rzepiela, A. J.; De Vries, A. H.; Dijkhuizen, L.; Hünenberger, P. H.; Marrink, S. J. Martini Coarse-Grained Force Field: Extension to Carbohydrates. *J. Chem. Theory Comput.* **2009**, *5*, 3195−3210.
(566) Secchi, E.; Niguès, A.; Jubin, L.; Siria, A.; Bocquet, L. Scaling Behavior for Ionic Transport and Its Fluctuations in Individual Carbon Nanotubes. *Phys. Rev. Lett.* **2016**, *116*, 154501.
(567) Shan, Y.; Tiwari, P.; Krishnakumar, P.; Vlassiouk, I.; Li, W.; Wang, X.; Darici, Y.; Lindsay, S.; Wang, H.; Smirnov, S.; et al. Surface Modification of Graphene Nanopores for Protein Translocation. *Nanotechnology* **2013**, *24*, 495102.
(568) Walther, J. H.; Ritos, K.; Cruz-Chu, E. R.; Megaridis, C. M.; Koumoutsakos, P. Barriers to Superfast Water Transport in Carbon Nanotube Membranes. *Nano Lett.* **2013**, *13*, 1910−1914.
(569) Bonthuis, D. J.; Netz, R. R. Beyond the Continuum: How Molecular Solvent Structure Affects Electrostatics and Hydrodynamics at Solid-Electrolyte Interfaces. *J. Phys. Chem. B* **2013**, *117*, 11397−11413.
(570) Koplik, J.; Banavar, J. R. Continuum Deductions from Molecular Hydrodynamics. *Annu. Rev. Fluid Mech.* **1995**, *27*, 257−292.
(571) Qiao, R.; Aluru, N. R. Ion Concentrations and Velocity Profiles in Nanochannel Electroosmotic Flows. *J. Chem. Phys.* **2003**, *118*, 4692−4701.
(572) Qiao, R.; Aluru, N. R. Charge Inversion and Flow Reversal in a Nanochannel Electro-Osmotic Flow. *Phys. Rev. Lett.* **2004**, *92*, 198301.
(573) Moreira, A. G.; Netz, R. R. Simulations of Counterions at Charged Plates. *Eur. Phys. J. E* **2002**, *8*, 33−58.
(574) Bonthuis, D. J.; Gekle, S.; Netz, R. R. Dielectric Profile of Interfacial Water and Its Effect on Double-Layer Capacitance. *Phys. Rev. Lett.* **2011**, *107*, 166102.
(575) Fedorov, M. V.; Kornyshev, A. A. Ionic Liquids at Electrified Interfaces. *Chem. Rev.* **2014**, *114*, 2978−3036.
(576) Heiranian, M.; Aluru, N. R. Nanofluidic Transport Theory with Enhancement Factors Approaching One. *ACS Nano* **2020**, *14*, 272−281.
(577) Kilic, M. S.; Bazant, M. Z.; Ajdari, A. Steric Effects in the Dynamics of Electrolytes at Large Applied Voltages. I. Double-Layer Charging. *Phys. Rev. E* **2007**, *75*, 021502.
(578) Kornyshev, A. A. Double-Layer in Ionic Liquids: Paradigm Change? *J. Phys. Chem. B* **2007**, *111*, 5545−5557.
(579) Goodwin, Z. A. H.; Feng, G.; Kornyshev, A. A. Mean-Field Theory of Electrical Double Layer in Ionic Liquids with Account of Short-Range Correlations. *Electrochim. Acta* **2017**, *225*, 190−197.
(580) de Souza, J. P.; Bazant, M. Z. Continuum Theory of Electrostatic Correlations at Charged Surfaces. *J. Phys. Chem. C* **2020**, *124*, 11414−11421.
(581) Misra, R. P.; de Souza, J. P.; Blankschtein, D.; Bazant, M. Z. Theory of Surface Forces in Multivalent Electrolytes. *Langmuir* **2019**, *35*, 11550−11565.
(582) Bazant, M. Z.; Storey, B. D.; Kornyshev, A. A. Double Layer in Ionic Liquids: Overscreening Versus Crowding. *Phys. Rev. Lett.* **2011**, *106*, 046102.
(583) Storey, B. D.; Bazant, M. Z. Effects of Electrostatic Correlations on Electrokinetic Phenomena. *Phys. Rev. E* **2012**, *86*, 056303.
(584) Cats, P.; Evans, R.; Härtel, A.; van Roij, R. Primitive Model Electrolytes in the near and Far Field: Decay Lengths from Dft and Simulations. *J. Chem. Phys.* **2021**, *154*, 124504.
(585) Lee, A. A.; Perez-Martinez, C. S.; Smith, A. M.; Perkin, S. Scaling Analysis of the Screening Length in Concentrated Electrolytes. *Phys. Rev. Lett.* **2017**, *119*, 026002.
(586) Smith, A. M.; Lee, A. A.; Perkin, S. The Electrostatic Screening Length in Concentrated Electrolytes Increases with Concentration. *J. Phys. Chem. Lett.* **2016**, *7*, 2157−2163.
(587) Abrashkin, A.; Andelman, D.; Orland, H. Dipolar Poisson-Boltzmann Equation: Ions and Dipoles Close to Charge Interfaces. *Phys. Rev. Lett.* **2007**, *99*, 077801.
(588) Prasanna Misra, R.; Das, S.; Mitra, S. K. Electric Double Layer Force between Charged Surfaces: Effect of Solvent Polarization. *J. Chem. Phys.* **2013**, *138*, 114703.
(589) Ben-Yaakov, D.; Andelman, D.; Podgornik, R.; Harries, D. Ion-Specific Hydration Effects: Extending the Poisson-Boltzmann Theory. *Curr. Opin. Colloid Interface Sci.* **2011**, *16*, 542−550.
(590) McEldrew, M.; Goodwin, Z. A. H.; Kornyshev, A. A.; Bazant, M. Z. Theory of the Double Layer in Water-in-Salt Electrolytes. *J. Phys. Chem. Lett.* **2018**, *9*, 5840−5846.
(591) Iglič, A.; Gongadze, E.; Bohinc, K. Excluded Volume Effect and Orientational Ordering near Charged Surface in Solution of Ions and Langevin Dipoles. *Bioelectrochemistry* **2010**, *79*, 223−227.
(592) Ben-Yaakov, D.; Andelman, D.; Harries, D.; Podgornik, R. Ions in Mixed Dielectric Solvents: Density Profiles and Osmotic Pressure between Charged Interfaces. *J. Phys. Chem. B* **2009**, *113*, 6001−6011.
(593) Lee, J. W.; Nilson, R. H.; Templeton, J. A.; Griffiths, S. K.; Kung, A.; Wong, B. M. Comparison of Molecular Dynamics with Classical Density Functional and Poisson-Boltzmann Theories of the Electric Double Layer in Nanochannels. *J. Chem. Theory Comput.* **2012**, *8*, 2012−2022.
(594) Härtel, A. Structure of Electric Double Layers in Capacitive Systems and to What Extent (Classical) Density Functional Theory Describes It. *J. Phys.: Condens. Matter* **2017**, *29*, 423002.
(595) Lian, C.; Su, H.; Li, C.; Liu, H.; Wu, J. Non-Negligible Roles of Pore Size Distribution on Electroosmotic Flow in Nanoporous Materials. *ACS Nano* **2019**, *13*, 8185−8192.

https://doi.org/10.1021/acs.chemrev.2c00155
Chem. Rev. 2023, 123, 2737−2831

(596) Chou, K.-H.; McCallum, C.; Gillespie, D.; Pennathur, S. An Experimental Approach to Systematically Probe Charge Inversion in Nanofluidic Channels. *Nano Lett.* **2018**, *18*, 1191−1195.
(597) Gillespie, D. High Energy Conversion Efficiency in Nanofluidic Channels. *Nano Lett.* **2012**, *12*, 1410−1416.
(598) Colla, T.; Girotto, M.; Dos Santos, A. P.; Levin, Y. Charge Neutrality Breakdown in Confined Aqueous Electrolytes: Theory and Simulation. *J. Chem. Phys.* **2016**, *145*, 094704.
(599) Qing, L.; Zhao, S.; Wang, Z.-G. Surface Charge Density in Electrical Double Layer Capacitors with Nanoscale Cathode-Anode Separation. *J. Phys. Chem. B* **2021**, *125*, 625−636.
(600) Lian, C.; Zhao, S.; Liu, H.; Wu, J. Time-Dependent Density Functional Theory for the Charging Kinetics of Electric Double Layer Containing Room-Temperature Ionic Liquids. *J. Chem. Phys.* **2016**, *145*, 204707.
(601) Yang, J.; Ding, Y.; Lian, C.; Ying, S.; Liu, H. Theoretical Insights into the Structures and Capacitive Performances of Confined Ionic Liquids. *Polymers* **2020**, *12*, 722.
(602) Kavokine, N.; Netz, R. R.; Bocquet, L. Fluids at the Nanoscale: From Continuum to Subcontinuum Transport. *Annu. Rev. Fluid Mech.* **2021**, *53*, 377−410.
(603) Noy, A.; Park, H. G.; Fornasiero, F.; Holt, J. K.; Grigoropoulos, C. P.; Bakajin, O. Nanofluidics in Carbon Nanotubes. *Nano Today* **2007**, *2*, 22−29.
(604) Israelachvili, J. Solvation Forces and Liquid Structure, as Probed by Direct Force Measurements. *Acc. Chem. Res.* **1987**, *20*, 415−421.
(605) Ding, F.; Hu, Z.; Zhong, Q.; Manfred, K.; Gattass, R. R.; Brindza, M. R.; Fourkas, J. T.; Walker, R. A.; Weeks, J. D. Interfacial Organization of Acetonitrile: Simulation and Experiment. *J. Phys. Chem. C* **2010**, *114*, 17651−17659.
(606) Zhou, K. G.; Vasu, K. S.; Cherian, C. T.; Neek-Amal, M.; Zhang, J. C.; Ghorbanfekr-Kalashami, H.; Huang, K.; Marshall, O. P.; Kravets, V. G.; Abraham, J.; et al. Electrically Controlled Water Permeation through Graphene Oxide Membranes. *Nature* **2018**, *559*, 236−240.
(607) Kumar, H.; Mukherjee, B.; Lin, S.-T.; Dasgupta, C.; Sood, A. K.; Maiti, P. K. Thermodynamics of Water Entry in Hydrophobic Channels of Carbon Nanotubes. *J. Chem. Phys.* **2011**, *134*, 124105.
(608) Levy, A.; de Souza, J. P.; Bazant, M. Z. Breakdown of Electroneutrality in Nanopores. *J. Colloid Interface Sci.* **2020**, *579*, 162−176.
(609) Almers, W.; McCleskey, E. W. Non-Selective Conductance in Calcium Channels of Frog Muscle: Calcium Selectivity in a Single-File Pore. *Journal of physiology* **1984**, *353*, 585−608.
(610) Hille, B. Ionic Channels in Excitable Membranes. Current Problems and Biophysical Approaches. *Biophys. J.* **1978**, *22*, 283−294.
(611) Vanommeslaeghe, K.; Hatcher, E.; Acharya, C.; Kundu, S.; Zhong, S.; Shim, J.; Darian, E.; Guvench, O.; Lopes, P.; Vorobyov, I.; et al. Charmm General Force Field: A Force Field for Drug-Like Molecules Compatible with the Charmm All-Atom Additive Biological Force Fields. *J. Comput. Chem.* **2010**, *31*, 671−690.
(612) Corry, B. Water and Ion Transport through Functionalised Carbon Nanotubes: Implications for Desalination Technology. *Energy Environ. Sci.* **2011**, *4*, 751−759.
(613) Misra, R. P.Multiscale Modeling of Electronic Polarization Effects in Interfacial Thermodynamics and Nanoscale Transport Phenomena. Ph.D. Dissertation. Massachusetts Institute of Technology: Cambridge, MA, 2021; https://hdl.handle.net/1721.1/140168 (accessed 2021-08-12).
(614) Cicero, G.; Grossman, J. C.; Schwegler, E.; Gygi, F.; Galli, G. Water Confined in Nanotubes and between Graphene Sheets: A First Principle Study. *J. Am. Chem. Soc.* **2008**, *130*, 1871−1878.
(615) Bonthuis, D. J.; Gekle, S.; Netz, R. R. Profile of the Static Permittivity Tensor of Water at Interfaces: Consequences for Capacitance, Hydration Interaction and Ion Adsorption. *Langmuir* **2012**, *28*, 7679−7694.
(616) Kornyshev, A. A.; Schmickler, W.; Vorotyntsev, M. A. Nonlocal Electrostatic Approach to the Problem of a Double Layer at a Metal-Electrolyte Interface. *Phys. Rev. B* **1982**, *25*, 5244.
(617) Bopp, P. A.; Kornyshev, A. A.; Sutmann, G. Static Nonlocal Dielectric Function of Liquid Water. *Phys. Rev. Lett.* **1996**, *76*, 1280.
(618) Levy, A.; Bazant, M.; Kornyshev, A. Ionic Activity in Concentrated Electrolytes: Solvent Structure Effect Revisited. *Chem. Phys. Lett.* **2020**, *738*, 136915.
(619) Kornyshev, A. A.; Sutmann, G. The Shape of the Nonlocal Dielectric Function of Polar Liquids and the Implications for Thermodynamic Properties of Electrolytes: A Comparative Study. *J. Chem. Phys.* **1996**, *104*, 1524−1544.
(620) Kornyshev, A. A. Nonlocal Screening of Ions in a Structurized Polar Liquid—New Aspects of Solvent Description in Electrolyte Theory. *Electrochim. Acta* **1981**, *26*, 1−20.
(621) Donadio, D.; Cicero, G.; Schwegler, E.; Sharma, M.; Galli, G. Electronic Effects in the Ir Spectrum of Water under Confinement. *J. Phys. Chem. B* **2009**, *113*, 4170−4175.
(622) Verwey, E. J. W. Theory of the Stability of Lyophobic Colloids. *J. Phys. Chem.* **1947**, *51*, 631−636.
(623) Derjaguin, B.; Landau, L. Theory of the Stability of Strongly Charged Lyophobic Sols and of the Adhesion of Strongly Charged Particles in Solutions of Electrolytes. *Prog. Surf. Sci.* **1993**, *43*, 30−59.
(624) Lyklema, J.; Mysels, K. J. A Study of Double Layer Repulsion and Van Der Waals Attraction in Soap Films. *J. Am. Chem. Soc.* **1965**, *87*, 2539−2546.
(625) Pashley, R. M.; McGuiggan, P. M.; Ninham, B. W.; Brady, J.; Evans, D. F. Direct Measurements of Surface Forces between Bilayers of Double-Chained Quaternary Ammonium Acetate and Bromide Surfactants. *J. Phys. Chem.* **1986**, *90*, 1637−1642.
(626) Kjellander, R.; Marčelja, S.; Pashley, R. M.; Quirk, J. P. A Theoretical and Experimental Study of Forces between Charged Mica Surfaces in Aqueous Cacl2 Solutions. *J. Chem. Phys.* **1990**, *92*, 4399−4407.
(627) Pivnic, K.; Bresme, F.; Kornyshev, A. A.; Urbakh, M. Structural Forces in Mixtures of Ionic Liquids with Organic Solvents. *Langmuir* **2019**, *35*, 15410−15420.
(628) Zwolak, M.; Lagerqvist, J.; Di Ventra, M. Quantized Ionic Conductance in Nanopores. *Phys. Rev. Lett.* **2009**, *103*, 128102.
(629) Song, C.; Corry, B. Intrinsic Ion Selectivity of Narrow Hydrophobic Pores. *J. Phys. Chem. B* **2009**, *113*, 7642−7649.
(630) Thomas, M.; Corry, B.; Hilder, T. A. What Have We Learnt About the Mechanisms of Rapid Water Transport, Ion Rejection and Selectivity in Nanopores from Molecular Simulation? *Small* **2014**, *10*, 1453−1465.
(631) Abraham, J.; Vasu, K. S.; Williams, C. D.; Gopinadhan, K.; Su, Y.; Cherian, C. T.; Dix, J.; Prestat, E.; Haigh, S. J.; Grigorieva, I. V.; et al. Tunable Sieving of Ions Using Graphene Oxide Membranes. *Nat. Nanotechnol.* **2017**, *12*, 546.
(632) Wander, M. C. F.; Shuford, K. L. Molecular Dynamics Study of Interfacial Confinement Effects of Aqueous Nacl Brines in Nanoporous Carbon. *J. Phys. Chem. C* **2010**, *114*, 20539−20546.
(633) Nicholson, D.; Quirke, N. Ion Pairing in Confined Electrolytes. *Mol. Simul.* **2003**, *29*, 287−290.
(634) Jiang, Z.; Stein, D. Charge Regulation in Nanopore Ionic Field-Effect Transistors. *Phys. Rev. E* **2011**, *83*, 031203.
(635) Trefalt, G.; Behrens, S. H.; Borkovec, M. Charge Regulation in the Electrical Double Layer: Ion Adsorption and Surface Interactions. *Langmuir* **2016**, *32*, 380−400.
(636) Hiemstra, T.; Van Riemsdijk, W. H.; Bolt, G. H. Multisite Proton Adsorption Modeling at the Solid/Solution Interface of (Hydr) Oxides: A New Approach: I. Model Description and Evaluation of Intrinsic Reaction Constants. *J. Colloid Interface Sci.* **1989**, *133*, 91−104.
(637) Khan, S. M.; Faraezi, S.; Oya, Y.; Hata, K.; Ohba, T. Anomalous Changes of Intermolecular Distance in Aqueous Electrolytes in Narrow Pores of Carbon Nanotubes. *Adsorption* **2019**, *25*, 1067−1074.
(638) Aydin, F.; Moradzadeh, A.; Bilodeau, C. L.; Lau, E. Y.; Schwegler, E.; Aluru, N. R.; Pham, T. A. Ion Solvation and Transport in Narrow Carbon Nanotubes: Effects of Polarizability, Cation-Π Interaction, and Confinement. *J. Chem. Theory Comput.* **2021**, *17*, 1596.

https://doi.org/10.1021/acs.chemrev.2c00155
Chem. Rev. 2023, 123, 2737−2831

(639) Zhan, C.; Ceron, M.; Hawks, S.; Otani, M.; Wood, B. C.; Pham, A.; Stadermann, M.; Campbell, P. G. Specific Ion Effects at Graphitic Interfaces. *Nat. Commun.* **2019**, *10*, 4858.
(640) Zhan, C.; Aydin, F.; Schwegler, E.; Noy, A.; Pham, T. A. Understanding Cation Selectivity in Carbon Nanopores with Hybrid First-Principles/Continuum Simulations: Implications for Water Desalination and Separation Technologies. *ACS Appl. Nano Mater.* **2020**, *3*, 9740−9748.
(641) Plecis, A.; Schoch, R. B.; Renaud, P. Ionic Transport Phenomena in Nanofluidics: Experimental and Theoretical Study of the Exclusion-Enrichment Effect on a Chip. *Nano Lett.* **2005**, *5*, 1147−1155.
(642) Schoch, R. B.; Renaud, P. Ion Transport through Nanoslits Dominated by the Effective Surface Charge. *Appl. Phys. Lett.* **2005**, *86*, 253111.
(643) Pu, Q.; Yun, J.; Temkin, H.; Liu, S. Ion-Enrichment and Ion-Depletion Effect of Nanochannel Structures. *Nano Lett.* **2004**, *4*, 1099−1103.
(644) Wang, Y.-C.; Stevens, A. L.; Han, J. Million-Fold Preconcentration of Proteins and Peptides by Nanofluidic Filter. *Anal. Chem.* **2005**, *77*, 4293−4299.
(645) Karnik, R.; Duan, C.; Castelino, K.; Daiguji, H.; Majumdar, A. Rectification of Ionic Current in a Nanofluidic Diode. *Nano Lett.* **2007**, *7*, 547−551.
(646) Buchsbaum, S. F.; Nguyen, G.; Howorka, S.; Siwy, Z. S. DNA-Modified Polymer Pores Allow Ph- and Voltage-Gated Control of Channel Flux. *J. Am. Chem. Soc.* **2014**, *136*, 9902−9905.
(647) Siwy, Z.; Heins, E.; Harrell, C. C.; Kohli, P.; Martin, C. R. Conical-Nanotube Ion-Current Rectifiers: The Role of Surface Charge. *J. Am. Chem. Soc.* **2004**, *126*, 10850−10851.
(648) Experton, J.; Wu, J.; Martin, C. From Ion Current to Electroosmotic Flow Rectification in Asymmetric Nanopore Membranes. *Nanomaterials (Basel, Switzerland)* **2017**, *7*, 445.
(649) Fan, R.; Yue, M.; Karnik, R.; Majumdar, A.; Yang, P. Polarity Switching and Transient Responses in Single Nanotube Nanofluidic Transistors. *Phys. Rev. Lett.* **2005**, *95*, 086607.
(650) Nam, S.-W.; Rooks, M. J.; Kim, K.-B.; Rossnagel, S. M. Ionic Field Effect Transistors with Sub-10 Nm Multiple Nanopores. *Nano Lett.* **2009**, *9*, 2044−2048.
(651) Kalman, E. B.; Vlassiouk, I.; Siwy, Z. S. Nanofluidic Bipolar Transistors. *Adv. Mater.* **2008**, *20*, 293−297.
(652) Lucas, R. A.; Lin, C.-Y.; Baker, L. A.; Siwy, Z. S. Ionic Amplifying Circuits Inspired by Electronics and Biology. *Nat. Commun.* **2020**, *11*, 1568.
(653) Tybrandt, K.; Larsson, K. C.; Richter-Dahlfors, A.; Berggren, M. Ion Bipolar Junction Transistors. *Proc. Natl. Acad. Sci. U.S.A.* **2010**, *107*, 9929.
(654) Maglia, G.; Heron, A. J.; Hwang, W. L.; Holden, M. A.; Mikhailova, E.; Li, Q.; Cheley, S.; Bayley, H. Droplet Networks with Incorporated Protein Diodes Show Collective Properties. *Nat. Nanotechnol.* **2009**, *4*, 437−440.
(655) Ali, M.; Mafe, S.; Ramirez, P.; Neumann, R.; Ensinger, W. Logic Gates Using Nanofluidic Diodes Based on Conical Nanopores Functionalized with Polyprotic Acid Chains. *Langmuir* **2009**, *25*, 11993−11997.
(656) Tybrandt, K.; Forchheimer, R.; Berggren, M. Logic Gates Based on Ion Transistors. *Nat. Commun.* **2012**, *3*, 871.
(657) Esfandiar, A.; Radha, B.; Wang, F. C.; Yang, Q.; Hu, S.; Garaj, S.; Nair, R. R.; Geim, A. K.; Gopinadhan, K. Size Effect in Ion Transport through Angstrom-Scale Slits. *Science* **2017**, *358*, 511.
(658) Ajayan, P. M.; Ebbesen, T. W.; Ichihashi, T.; Iijima, S.; Tanigaki, K.; Hiura, H. Opening Carbon Nanotubes with Oxygen and Implications for Filling. *Nature* **1993**, *362*, 522−525.
(659) Tsang, S. C.; Harris, P. J. F.; Green, M. L. H. Thinning and Opening of Carbon Nanotubes by Oxidation Using Carbon Dioxide. *Nature* **1993**, *362*, 520−522.
(660) Ajayan, P. M.; Iijima, S. Capillarity-Induced Filling of Carbon Nanotubes. *Nature* **1993**, *361*, 333−334.
(661) Tsang, S. C.; Chen, Y. K.; Harris, P. J. F.; Green, M. L. H. A Simple Chemical Method of Opening and Filling Carbon Nanotubes. *Nature* **1994**, *372*, 159−162.
(662) Pederson, M. R.; Broughton, J. Q. Nanocapillarity in Fullerene Tubules. *Phys. Rev. Lett.* **1992**, *69*, 2689−2692.
(663) Ugarte, D.; Châtelain, A.; De Heer, W. A. Nanocapillarity and Chemistry in Carbon Nanotubes. *Science* **1996**, *274*, 1897−1899.
(664) Dujardin, E.; Ebbesen, T. W.; Hiura, H.; Tanigaki, K. Capillarity and Wetting of Carbon Nanotubes. *Science (New York, N.Y.)* **1994**, *265*, 1850−1852.
(665) Dillon, A. C.; Jones, K. M.; Bekkedahl, T. A.; Kiang, C. H.; Bethune, D. S.; Heben, M. J. Storage of Hydrogen in Single-Walled Carbon Nanotubes. *Nature* **1997**, *386*, 377−379.
(666) Kuznetsova, A.; Yates, J. T.; Liu, J.; Smalley, R. E. Physical Adsorption of Xenon in Open Single Walled Carbon Nanotubes: Observation of a Quasi-One-Dimensional Confined Xe Phase. *J. Chem. Phys.* **2000**, *112*, 9590−9598.
(667) Wang, Q.; Challa, S. R.; Sholl, D. S.; Johnson, J. K. Quantum Sieving in Carbon Nanotubes and Zeolites. *Phys. Rev. Lett.* **1999**, *82*, 956−959.
(668) Stan, G.; Bojan, M. J.; Curtarolo, S.; Gatica, S. M.; Cole, M. W. Uptake of Gases in Bundles of Carbon Nanotubes. *Phys. Rev. B* **2000**, *62*, 2173−2180.
(669) Gogotsi, Y.; Libera, J. A.; Güvenç-Yazicioglu, A.; Megaridis, C. M. In Situ Multiphase Fluid Experiments in Hydrothermal Carbon Nanotubes. *Appl. Phys. Lett.* **2001**, *79*, 1021−1023.
(670) Sun, L.; Crooks, R. M. Single Carbon Nanotube Membranes: A Well-Defined Model for Studying Mass Transport through Nanoporous Materials. *J. Am. Chem. Soc.* **2000**, *122*, 12340−12345.
(671) Kim, S.; Jinschek, J. R.; Chen, H.; Sholl, D. S.; Marand, E. Scalable Fabrication of Carbon Nanotube/Polymer Nanocomposite Membranes for High Flux Gas Transport. *Nano Lett.* **2007**, *7*, 2806−2811.
(672) Pang, P.; He, J.; Park, J. H.; Krstic, P. S.; Lindsay, S. Origin of Giant Ionic Currents in Carbon Nanotube Channels. *ACS Nano* **2011**, *5*, 7277−7283.
(673) Dekker, C. Solid-State Nanopores. *Nat. Nanotechnol.* **2007**, *2*, 209−215.
(674) Yu, C.; Shi, L.; Yao, Z.; Li, D.; Majumdar, A. Thermal Conductance and Thermopower of an Individual Single-Wall Carbon Nanotube. *Nano Lett.* **2005**, *5*, 1842−1846.
(675) Borg, M. K.; Lockerby, D. A.; Ritos, K.; Reese, J. M. Multiscale Simulation of Water Flow through Laboratory-Scale Nanotube Membranes. *J. Membr. Sci.* **2018**, *567*, 115−126.
(676) Thomas, J. A.; McGaughey, A. J. H. Water Flow in Carbon Nanotubes: Transition to Subcontinuum Transport. *Phys. Rev. Lett.* **2009**, *102*, 184502.
(677) Li, Y.; Li, Z.; Aydin, F.; Quan, J.; Chen, X.; Yao, Y. C.; Zhan, C.; Chen, Y.; Pham, T. A.; Noy, A. Water-Ion Permselectivity of Narrow-Diameter Carbon Nanotubes. *Sci. Adv.* **2020**, *6*, eaba9966.
(678) Kim, S.; Fornasiero, F.; Park, H. G.; In, J. B.; Meshot, E.; Giraldo, G.; Stadermann, M.; Fireman, M.; Shan, J.; Grigoropoulos, C. P.; et al. Fabrication of Flexible, Aligned Carbon Nanotube/Polymer Composite Membranes by in-Situ Polymerization. *J. Membr. Sci.* **2014**, *460*, 91−98.
(679) Zhang, L.; Zhao, B.; Jiang, C.; Yang, J.; Zheng, G. Preparation and Transport Performances of High-Density, Aligned Carbon Nanotube Membranes. *Nanoscale Res. Lett.* **2015**, *10*, 266.
(680) Mattia, D.; Leese, H.; Lee, K. P. Carbon Nanotube Membranes: From Flow Enhancement to Permeability. *J. Membr. Sci.* **2015**, *475*, 266−272.
(681) Bui, N.; Meshot, E. R.; Kim, S.; Peña, J.; Gibson, P. W.; Wu, K. J.; Fornasiero, F. Ultrabreathable and Protective Membranes with Sub-5 Nm Carbon Nanotube Pores. *Adv. Mater.* **2016**, *28*, 5871−5877.
(682) Jue, M. L.; Buchsbaum, S. F.; Chen, C.; Park, S. J.; Meshot, E. R.; Wu, K. J. J.; Fornasiero, F. Ultra-Permeable Single-Walled Carbon Nanotube Membranes with Exceptional Performance at Scale. *Advanced Science* **2020**, *7*, 2001670.

https://doi.org/10.1021/acs.chemrev.2c00155
Chem. Rev. 2023, 123, 2737−2831

(683) Whitby, M.; Cagnon, L.; Thanou, M.; Quirke, N. Enhanced Fluid Flow through Nanoscale Carbon Pipes. *Nano Lett.* **2008**, *8*, 2632−2637.
(684) Majumder, M.; Corry, B. Anomalous Decline of Water Transport in Covalently Modified Carbon Nanotube Membranes. *Chem. Commun.* **2011**, *47*, 7683−7685.
(685) Du, F.; Qu, L.; Xia, Z.; Feng, L.; Dai, L. Membranes of Vertically Aligned Superlong Carbon Nanotubes. *Langmuir* **2011**, *27*, 8437−8443.
(686) Baek, Y.; Kim, C.; Seo, D. K.; Kim, T.; Lee, J. S.; Kim, Y. H.; Ahn, K. H.; Bae, S. S.; Lee, S. C.; Lim, J.; et al. High Performance and Antifouling Vertically Aligned Carbon Nanotube Membrane for Water Purification. *J. Membr. Sci.* **2014**, *460*, 171−177.
(687) Thomas, J. A.; McGaughey, A. J. H. Reassessing Fast Water Transport through Carbon Nanotubes. *Nano Lett.* **2008**, *8*, 2788−2793.
(688) Majumder, M.; Chopra, N.; Hinds, B. J. Mass Transport through Carbon Nanotube Membranes in Three Different Regimes: Ionic Diffusion and Gas and Liquid Flow. *ACS Nano* **2011**, *5*, 3867−3877.
(689) Werder, T.; Walther, J. H.; Jaffe, R. L.; Halicioglu, T.; Noca, F.; Koumoutsakos, P. Molecular Dynamics Simulation of Contact Angles of Water Droplets in Carbon Nanotubes. *Nano Lett.* **2001**, *1*, 697−702.
(690) Falk, K.; Sedlmeier, F.; Joly, L.; Netz, R. R.; Bocquet, L. Molecular Origin of Fast Water Transport in Carbon Nanotube Membranes: Superlubricity Versus Curvature Dependent Friction. *Nano Lett.* **2010**, *10*, 4067−4073.
(691) Berezhkovskii, A.; Hummer, G. Single-File Transport of Water Molecules through a Carbon Nanotube. *Phys. Rev. Lett.* **2002**, *89*, 064503.
(692) Zhu, F.; Schulten, K. Water and Proton Conduction through Carbon Nanotubes as Models for Biological Channels. *Biophys. J.* **2003**, *85*, 236−244.
(693) Striolo, A. The Mechanism of Water Diffusion in Narrow Carbon Nanotubes. *Nano Lett.* **2006**, *6*, 633−639.
(694) Alexiadis, A.; Kassinos, S. Molecular Simulation of Water in Carbon Nanotubes. *Chem. Rev.* **2008**, *108*, 5014−5034.
(695) Sisan, T. B.; Lichter, S. The End of Nanochannels. *Microfluid. Nanofluid.* **2011**, *11*, 787−791.
(696) Nicholls, W. D.; Borg, M. K.; Lockerby, D. A.; Reese, J. M. Water Transport through (7,7) Carbon Nanotubes of Different Lengths Using Molecular Dynamics. *Microfluid. Nanofluid.* **2012**, *12*, 257−264.
(697) Walther, J. H.; Ritos, K.; Cruz-Chu, E. R.; Megaridis, C. M.; Koumoutsakos, P. Barriers to Superfast Water Transport in Carbon Nanotube Membranes. *Nano Lett.* **2013**, *13*, 1910−1914.
(698) Suk, M. E.; Aluru, N. R. Modeling Water Flow through Carbon Nanotube Membranes with Entrance/Exit Effects. *Nanoscale and Microscale Thermophysical Engineering* **2017**, *21*, 247−262.
(699) Weissberg, H. L. End Correction for Slow Viscous Flow through Long Tubes. *Phys. Fluids* **1962**, *5*, 1033−1036.
(700) Dagan, Z.; Weinbaum, S.; Pfeffer, R. An Infinite-Series Solution for the Creeping Motion through an Orifice of Finite Length. *J. Fluid Mech.* **1982**, *115*, 505−523.
(701) Horner, A.; Zocher, F.; Preiner, J.; Ollinger, N.; Siligan, C.; Akimov, S. A.; Pohl, P. The Mobility of Single-File Water Molecules Is Governed by the Number of H-Bonds They May Form with Channel-Lining Residues. *Sci. Adv.* **2015**, *1*, No. e1400083.
(702) Kofinger, J.; Hummer, G.; Dellago, C. Single-File Water in Nanopores. *Phys. Chem. Chem. Phys.* **2011**, *13*, 15403−15417.
(703) Agmon, N. The Grotthuss Mechanism. *Chem. Phys. Lett.* **1995**, *244*, 456−462.
(704) Cao, Z.; Peng, Y.; Yan, T.; Li, S.; Li, A.; Voth, G. A. Mechanism of Fast Proton Transport Along One-Dimensional Water Chains Confined in Carbon Nanotubes. *J. Am. Chem. Soc.* **2010**, *132*, 11395−11397.
(705) Chen, J.; Li, X. Z.; Zhang, Q.; Michaelides, A.; Wang, E. Nature of Proton Transport in a Water-Filled Carbon Nanotube and in Liquid Water. *Phys. Chem. Chem. Phys.* **2013**, *15*, 6344−6349.
(706) Marx, D.; Tuckerman, M. E.; Hutter, J.; Parrinello, M. The Nature of the Hydrated Excess Proton in Water. *Nature* **1999**, *397*, 601−604.
(707) Bankura, A.; Chandra, A. Hydroxide Ion Can Move Faster Than an Excess Proton through One-Dimensional Water Chains in Hydrophobic Narrow Pores. *J. Phys. Chem. B* **2012**, *116*, 9744−9757.
(708) Zimmerli, U.; Gonnet, P. G.; Walther, J. H.; Koumoutsakos, P. Curvature Induced L-Defects in Water Conduction in Carbon Nanotubes. *Nano Lett.* **2005**, *5*, 1017−1022.
(709) Dellago, C.; Hummer, G. Kinetics and Mechanism of Proton Transport across Membrane Nanopores. *Phys. Rev. Lett.* **2006**, *97*, 245901.
(710) Lee, S. H.; Rasaiah, J. C. Proton Transfer and the Diffusion of H + and Oh- Ions Along Water Wires. *J. Chem. Phys.* **2013**, *139*, 124507.
(711) Muñoz-Santiburcio, D.; Marx, D. Nanoconfinement in Slit Pores Enhances Water Self-Dissociation. *Phys. Rev. Lett.* **2017**, *119*, 056002.
(712) Sirkin, Y. A. P.; Hassanali, A.; Scherlis, D. A. One-Dimensional Confinement Inhibits Water Dissociation in Carbon Nanotubes. *J. Phys. Chem. Lett.* **2018**, *9*, 5029−5033.
(713) Grosjean, B.; Bocquet, M. L.; Vuilleumier, R. Versatile Electrification of Two-Dimensional Nanomaterials in Water. *Nat. Commun.* **2019**, *10*, 1656.
(714) Li, Z.; Li, Y.; Yao, Y.-C.; Aydin, F.; Zhan, C.; Chen, Y.; Elimelech, M.; Pham, T. A.; Noy, A. Strong Differential Monovalent Anion Selectivity in Narrow Diameter Carbon Nanotube Porins. *ACS Nano* **2020**, *14*, 6269−6275.
(715) Marcotte, A.; Mouterde, T.; Niguès, A.; Siria, A.; Bocquet, L. Mechanically Activated Ionic Transport across Single-Digit Carbon Nanotubes. *Nat. Mater.* **2020**, *19*, 1057−1061.
(716) Peter, C.; Hummer, G. Ion Transport through Membrane-Spanning Nanopores Studied by Molecular Dynamics Simulations and Continuum Electrostatics Calculations. *Biophys. J.* **2005**, *89*, 2222−2234.
(717) Corry, B. Designing Carbon Nanotube Membranes for Efficient Water Desalination. *J. Phys. Chem. B* **2008**, *112*, 1427−1434.
(718) Li, H.; Francisco, J. S.; Zeng, X. C. Unraveling the Mechanism of Selective Ion Transport in Hydrophobic Subnanometer Channels. *Proc. Natl. Acad. Sci. U. S. A.* **2015**, *112*, 10851−10856.
(719) Joseph, S.; Mashl, R. J.; Jakobsson, E.; Aluru, N. R. Electrolytic Transport in Modified Carbon Nanotubes. *Nano Lett.* **2003**, *3*, 1399−1403.
(720) Park, J. H.; Sinnott, S. B.; Aluru, N. R. Ion Separation Using a Y-Junction Carbon Nanotube. *Nanotechnology* **2006**, *17*, 895−900.
(721) Gong, X.; Li, J.; Xu, K.; Wang, J.; Yang, H. A Controllable Molecular Sieve for Na^+ and K^+ Ions. *J. Am. Chem. Soc.* **2010**, *132*, 1873−1877.
(722) Lokesh, M.; Youn, S. K.; Park, H. G. Osmotic Transport across Surface Functionalized Carbon Nanotube Membrane. *Nano Lett.* **2018**, *18*, 6679−6685.
(723) Qiao, R.; Aluru, N. R. Atypical Dependence of Electroosmotic Transport on Surface Charge in a Single-Wall Carbon Nanotube. *Nano Lett.* **2003**, *3*, 1013−1017.
(724) Su, J.; Huang, D. Coupling Transport of Water and Ions through a Carbon Nanotube: The Role of Ionic Condition. *J. Phys. Chem. C* **2016**, *120*, 11245−11252.
(725) Liu, H.; Murad, S.; Jameson, C. J. Ion Permeation Dynamics in Carbon Nanotubes. *J. Chem. Phys.* **2006**, *125*, 084713.
(726) Gao, X.; Zhao, T.; Li, Z. Fluid Breakup in Carbon Nanotubes: An Explanation of Ultrafast Ion Transport. *Phys. Fluids* **2017**, *29*, 092003.
(727) Beu, T. A. Molecular Dynamics Simulations of Ion Transport through Carbon Nanotubes. Iii. Influence of the Nanotube Radius, Solute Concentration, and Applied Electric Fields on the Transport Properties. *J. Chem. Phys.* **2011**, *135*, 044516.
(728) Yazda, K.; Tahir, S.; Michel, T.; Loubet, B.; Manghi, M.; Bentin, J.; Picaud, F.; Palmeri, J.; Henn, F.; Jourdain, V. Voltage-Activated Transport of Ions through Single-Walled Carbon Nanotubes. *Nanoscale* **2017**, *9*, 11976−11986.

https://doi.org/10.1021/acs.chemrev.2c00155
Chem. Rev. 2023, 123, 2737−2831

(729) Deen, W. M. Hindered Transport of Large Molecules in Liquid-Filled Pores. *AIChE J.* **1987**, *33*, 1409−1425.
(730) Renkin, E. M. Filtration, Diffusion, and Molecular Sieving through Porous Cellulose Membranes. *J. Gen. Physiol.* **1954**, *38*, 225−243.
(731) Dechadilok, P.; Deen, W. M. Hindrance Factors for Diffusion and Convection in Pores. *Ind. Eng. Chem. Res.* **2006**, *45*, 6953−6959.
(732) Liu, H.; He, J.; Tang, J.; Liu, H.; Pang, P.; Cao, D.; Krstic, P.; Joseph, S.; Lindsay, S.; Nuckolls, C. Translocation of Single-Stranded DNA through Single-Walled Carbon Nanotubes. *Science* **2010**, *327*, 64−67.
(733) Liu, L.; Yang, C.; Zhao, K.; Li, J.; Wu, H. C. Ultrashort Single-Walled Carbon Nanotubes in a Lipid Bilayer as a New Nanopore Sensor. *Nat. Commun.* **2013**, *4*, 2989.
(734) Song, W.; Pang, P.; He, J.; Lindsay, S. Optical and Electrical Detection of Single-Molecule Translocation through Carbon Nanotubes. *ACS Nano* **2013**, *7*, 689−694.
(735) Amiri, H.; Shepard, K. L.; Nuckolls, C.; Hernandez Sanchez, R. Single-Walled Carbon Nanotubes: Mimics of Biological Ion Channels. *Nano Lett.* **2017**, *17*, 1204−1211.
(736) Choi, W.; Lee, C. Y.; Ham, M. H.; Shimizu, S.; Strano, M. S. Dynamics of Simultaneous, Single Ion Transport through Two Single-Walled Carbon Nanotubes: Observation of a Three-State System. *J. Am. Chem. Soc.* **2011**, *133*, 203−205.
(737) Wu, J.; Gerstandt, K.; Zhang, H.; Liu, J.; Hinds, B. J. Electrophoretically Induced Aqueous Flow through Single-Walled Carbon Nanotube Membranes. *Nat. Nanotechnol.* **2012**, *7*, 133−139.
(738) Wu, J.; Gerstandt, K.; Majumder, M.; Zhan, X.; Hinds, B. J. Highly Efficient Electroosmotic Flow through Functionalized Carbon Nanotube Membranes. *Nanoscale* **2011**, *3*, 3321−3328.
(739) Benz, R.; Schmid, A.; Wagner, W.; Goebel, W. Pore Formation by the Escherichia Coli Hemolysin: Evidence for an Association-Dissociation Equilibrium of the Pore-Forming Aggregates. *Infect. Immun.* **1989**, *57*, 887−895.
(740) Sakmann, B.; Trube, G. Conductance Properties of Single Inwardly Rectifying Potassium Channels in Ventricular Cells from Guinea-Pig Heart. *Journal of Physiology* **1984**, *347*, 641−657.
(741) Uematsu, Y.; Netz, R. R.; Bocquet, L.; Bonthuis, D. J. Crossover of the Power-Law Exponent for Carbon Nanotube Conductivity as a Function of Salinity. *J. Phys. Chem. B* **2018**, *122*, 2992−2997.
(742) Manghi, M.; Palmeri, J.; Yazda, K.; Henn, F.; Jourdain, V. Role of Charge Regulation and Flow Slip in the Ionic Conductance of Nanopores: An Analytical Approach. *Phys. Rev. E* **2018**, *98*, 012605.
(743) Anishkin, A.; Loukin, S. H.; Teng, J.; Kung, C. Feeling the Hidden Mechanical Forces in Lipid Bilayer Is an Original Sense. *Proc. Natl. Acad. Sci. U.S.A.* **2014**, *111*, 7898−7905.
(744) Cox, C. D.; Bavi, N.; Martinac, B. Biophysical Principles of Ion-Channel-Mediated Mechanosensory Transduction. *Cell Reports* **2019**, *29*, 1−12.
(745) Donnan, F. G. Theory of Membrane Equilibria and Membrane Potentials in the Presence of Non-Dialysing Electrolytes. A Contribution to Physical-Chemical Physiology. *J. Membr. Sci.* **1995**, *100*, 45−55.
(746) Li, Y.; Li, Z.; Aydin, F.; Quan, J.; Chen, X.; Yao, Y.-C.; Zhan, C.; Chen, Y.; Pham, T. A.; Noy, A. Water-Ion Permselectivity of Narrow-Diameter Carbon Nanotubes. *Sci. Adv.* **2020**, *6*, No. eaba9966.
(747) Freger, V.; Ramon, G. Z. Polyamide Desalination Membranes: Formation, Structure, and Properties. *Prog. Polym. Sci.* **2021**, *122*, 101451.
(748) Corry, B. Mechanisms of Selective Ion Transport and Salt Rejection in Carbon Nanostructures. *MRS Bull.* **2017**, *42*, 306−310.
(749) Peters, P. B.; Van Roij, R.; Bazant, M. Z.; Biesheuvel, P. M. Analysis of Electrolyte Transport through Charged Nanopores. *Phys. Rev. E* **2016**, *93*, 053108.
(750) Gross, R. J.; Osterle, J. F. Membrane Transport Characteristics of Ultrafine Capillaries. *J. Chem. Phys.* **1968**, *49*, 228−234.
(751) Alizadeh, S.; Bazant, M. Z.; Mani, A. Impact of Network Heterogeneity on Electrokinetic Transport in Porous Media. *J. Colloid Interface Sci.* **2019**, *553*, 451−464.
(752) van der Heyden, F. H. J.; Bonthuis, D. J.; Stein, D.; Meyer, C.; Dekker, C. Electrokinetic Energy Conversion Efficiency in Nanofluidic Channels. *Nano Lett.* **2006**, *6*, 2232−2237.
(753) Ma, Y.; Yeh, L.-H.; Lin, C.-Y.; Mei, L.; Qian, S. Ph-Regulated Ionic Conductance in a Nanochannel with Overlapped Electric Double Layers. *Anal. Chem.* **2015**, *87*, 4508−4514.
(754) Tedesco, M.; Hamelers, H. V. M.; Biesheuvel, P. M. Nernst-Planck Transport Theory for (Reverse) Electrodialysis: Ii. Effect of Water Transport through Ion-Exchange Membranes. *J. Membr. Sci.* **2017**, *531*, 172−182.
(755) Cervera, J.; García-Morales, V.; Pellicer, J. Ion Size Effects on the Electrokinetic Flow in Nanoporous Membranes Caused by Concentration Gradients. *J. Phys. Chem. B* **2003**, *107*, 8300−8309.
(756) Sanders, D. E.; Smith, Z. P.; Guo, R. L.; Robeson, L. M.; McGrath, J. E.; Paul, D. R.; Freeman, B. D. Energy-Efficient Polymeric Gas Separation Membranes for a Sustainable Future: A Review. *Polymer* **2013**, *54*, 4729−4761.
(757) Landsman, M. R.; Sujanani, R.; Brodfuehrer, S. H.; Cooper, C. M.; Darr, A. G.; Davis, R. J.; Kim, K.; Kum, S.; Nalley, L. K.; Nomaan, S. M.; et al. Water Treatment: Are Membranes the Panacea? *Annu. Rev. Chem. Biomol. Eng.* **2020**, *11*, 559−585.
(758) Koros, W. J.; Fleming, G. K. Membrane-Based Gas Separation. *J. Membr. Sci.* **1993**, *83*, 1−80.
(759) Pendergast, M. M.; Hoek, E. M. V. A Review of Water Treatment Membrane Nanotechnologies. *Energy Environ. Sci.* **2011**, *4*, 1946−1971.
(760) Sarbolouki, M. N.; Miller, I. F. Pore Flow Models for Reverse-Osmosis Desalination. *Desalination* **1973**, *12*, 343−359.
(761) Nagel, C.; Gunther-Schade, K.; Fritsch, D.; Strunskus, T.; Faupel, F. Free Volume and Transport Properties in Highly Selective Polymer Membranes. *Macromolecules* **2002**, *35*, 2071−2077.
(762) Wijmans, J. G.; Baker, R. W. The Solution-Diffusion Model - a Review. *J. Membr. Sci.* **1995**, *107*, 1−21.
(763) Geise, G. M.; Park, H. B.; Sagle, A. C.; Freeman, B. D.; McGrath, J. E. Water Permeability and Water/Salt Selectivity Tradeoff in Polymers for Desalination. *J. Membr. Sci.* **2011**, *369*, 130−138.
(764) Freeman, B. D. Basis of Permeability/Selectivity Tradeoff Relations in Polymeric Gas Separation Membranes. *Macromolecules* **1999**, *32*, 375−380.
(765) Cahill, D. G.; Freger, V.; Kwak, S. Y. Microscopy and, Microanalysis of Reverse-Osmosis and Nanofiltration Membranes. *MRS Bull.* **2008**, *33*, 27−32.
(766) Jiang, Z. W.; Karan, S.; Livingston, A. G. Water Transport through Ultrathin Polyamide Nanofilms Used for Reverse Osmosis. *Adv. Mater.* **2018**, *30*, 1705973.
(767) Kamcev, J.; Paul, D. R.; Freeman, B. D. Equilibrium Ion Partitioning between Aqueous Salt Solutions and Inhomogeneous Ion Exchange Membranes. *Desalination* **2018**, *446*, 31−41.
(768) Damasceno Borges, D.; Franco, A. A.; Malek, K.; Gebel, G.; Mossa, S. Inhomogeneous Transport in Model Hydrated Polymer Electrolyte Supported Ultrathin Films. *ACS Nano* **2013**, *7*, 6767−6773.
(769) Cui, S. T.; Liu, J. W.; Selvan, M. E.; Keffer, D. J.; Edwards, B. J.; Steele, W. V. A Molecular Dynamics Study of a Nafion Polyelectrolyte Membrane and the Aqueous Phase Structure for Proton Transport. *J. Phys. Chem. B* **2007**, *111*, 2208−2218.
(770) Koros, W. J.; Zhang, C. Materials for Next-Generation Molecularly Selective Synthetic Membranes. *Nat. Mater.* **2017**, *16*, 289−297.
(771) Cahill, D. G.; Freger, V.; Kwak, S.-Y. Microscopy and Microanalysis of Reverse-Osmosis and Nanofiltration Membranes. *MRS Bull.* **2008**, *33*, 27−32.
(772) Beenakker, J. J. M.; Borman, V. D.; Krylov, S. Y. Molecular Transport in Subnanometer Pores: Zero-Point Energy, Reduced Dimensionality and Quantum Sieving. *Chem. Phys. Lett.* **1995**, *232*, 379−382.
(773) Oh, H.; Savchenko, I.; Mavrandonakis, A.; Heine, T.; Hirscher, M. Highly Effective Hydrogen Isotope Separation in Nanoporous Metal-Organic Frameworks with Open Metal Sites: Direct Measurement and Theoretical Analysis. *ACS Nano* **2014**, *8*, 761−770.

https://doi.org/10.1021/acs.chemrev.2c00155
Chem. Rev. 2023, 123, 2737−2831

(774) Savchenko, I.; Mavrandonakis, A.; Heine, T.; Oh, H.; Teufel, J.; Hirscher, M. Hydrogen Isotope Separation in Metal-Organic Frameworks: Kinetic or Chemical Affinity Quantum-Sieving? *Microporous Mesoporous Mater.* **2015**, *216*, 133−137.
(775) Jiao, Y.; Du, A.; Hankel, M.; Smith, S. C. Modelling Carbon Membranes for Gas and Isotope Separation. *Phys. Chem. Chem. Phys.* **2013**, *15*, 4832−4843.
(776) Oh, H.; Hirscher, M. Quantum Sieving for Separation of Hydrogen Isotopes Using Mofs. *Eur. J. Inorg. Chem.* **2016**, *2016*, 4278−4289.
(777) Cao, D.; Ren, J.; Gong, Y.; Huang, H.; Fu, X.; Chang, M.; Chen, X.; Xiao, C.; Liu, D.; Yang, Q.; et al. Quantum Sieving of H2/D2 in Mofs: A Study on the Correlation between the Separation Performance, Pore Size and Temperature. *J. Mater. Chem. A* **2020**, *8*, 6319−6327.
(778) Liu, M.; Zhang, L.; Little, M. A.; Kapil, V.; Ceriotti, M.; Yang, S.; Ding, L.; Holden, D. L.; Balderas-Xicohtencatl, R.; He, D.; et al. Barely Porous Organic Cages for Hydrogen Isotope Separation. *Science* **2019**, *366*, 613−620.
(779) Oh, H.; Kalidindi, S. B.; Um, Y.; Bureekaew, S.; Schmid, R.; Fischer, R. A.; Hirscher, M. A Cryogenically Flexible Covalent Organic Framework for Efficient Hydrogen Isotope Separation by Quantum Sieving. *Angew. Chem., Int. Ed. Engl.* **2013**, *52*, 13219−13222.
(780) Noguchi, D.; Tanaka, H.; Fujimori, T.; Kagita, H.; Hattori, Y.; Honda, H.; Urita, K.; Utsumi, S.; Wang, Z. M.; Ohba, T.; et al. Selective D2 Adsorption Enhanced by the Quantum Sieving Effect on Entangled Single-Wall Carbon Nanotubes. *J. Phys.: Condens. Matter* **2010**, *22*, 334207.
(781) Yu, M.; Funke, H. H.; Falconer, J. L.; Noble, R. D. High Density, Vertically-Aligned Carbon Nanotube Membranes. *Nano Lett.* **2009**, *9*, 225−229.
(782) Zhang, L.; Yang, J.; Wang, X.; Zhao, B.; Zheng, G. Temperature-Dependent Gas Transport Performance of Vertically Aligned Carbon Nanotube/Parylene Composite Membranes. *Nanoscale Res. Lett.* **2014**, *9*, 448.
(783) Wang, P.; Barnes, B.; Huang, Z.; Wang, Z.; Zheng, M.; Wang, Y. Beyond Color: The New Carbon Ink. *Adv. Mater.* **2021**, *33*, 2005890.
(784) Wang, P.; Li, Y.; Wang, L.; Klos, J.; Peng, Z.; Kim, N.; Bluhm, H.; Gaskell, K.; Liu, P.; Lee, S. B.; et al. Probing the Electrical Double Layer by Operando X-Ray Photoelectron Spectroscopy through a Graphene-Carbon Nanotube Composite Window. *EcoMat* **2020**, *2*, No. e12023.
(785) Nicholls, W. D.; Borg, M. K.; Lockerby, D. A.; Reese, J. M. Water Transport through Carbon Nanotubes with Defects. *Mol. Simul.* **2012**, *38*, 781−785.
(786) Won, C. Y.; Aluru, N. R. Water Phase Transition Induced by a Stone-Wales Defect in a Boron Nitride Nanotube. *J. Am. Chem. Soc.* **2008**, *130*, 13649−13652.
(787) Joly, L.; Tocci, G.; Merabia, S.; Michaelides, A. Strong Coupling between Nanofluidic Transport and Interfacial Chemistry: How Defect Reactivity Controls Liquid-Solid Friction through Hydrogen Bonding. *J. Phys. Chem. Lett.* **2016**, *7*, 1381−1386.
(788) Tocci, G.; Bilichenko, M.; Joly, L.; Iannuzzi, M. Ab Initio Nanofluidics: Disentangling the Role of the Energy Landscape and of Density Correlations on Liquid/Solid Friction. *Nanoscale* **2020**, *12*, 10994−11000.
(789) Tocci, G.; Joly, L.; Michaelides, A. Friction of Water on Graphene and Hexagonal Boron Nitride from Ab Initio Methods: Very Different Slippage Despite Very Similar Interface Structures. *Nano Lett.* **2014**, *14*, 6872−6877.
(790) Scalfi, L.; Dufils, T.; Reeves, K. G.; Rotenberg, B.; Salanne, M. A Semiclassical Thomas-Fermi Model to Tune the Metallicity of Electrodes in Molecular Simulations. *J. Chem. Phys.* **2020**, *153*, 174704.
(791) Schlaich, A.; Jin, D.; Bocquet, L.; Coasne, B. Electronic Screening Using a Virtual Thomas-Fermi Fluid for Predicting Wetting and Phase Transitions of Ionic Liquids at Metal Surfaces. *Nat. Mater.* **2022**, *21*, 237−245.
(792) Merlet, C.; Rotenberg, B.; Madden, P. A.; Taberna, P.-L.; Simon, P.; Gogotsi, Y.; Salanne, M. On the Molecular Origin of Supercapacitance in Nanoporous Carbon Electrodes. *Nat. Mater.* **2012**, *11*, 306−310.
(793) Behler, J.; Parrinello, M. Generalized Neural-Network Representation of High-Dimensional Potential-Energy Surfaces. *Phys. Rev. Lett.* **2007**, *98*, 146401.
(794) Zhang, L.; Han, J.; Wang, H.; Car, R.; E, W. Deep Potential Molecular Dynamics: A Scalable Model with the Accuracy of Quantum Mechanics. *Phys. Rev. Lett.* **2018**, *120*, 143001.
(795) Bartók, A. P.; Payne, M. C.; Kondor, R.; Csányi, G. Gaussian Approximation Potentials: The Accuracy of Quantum Mechanics, without the Electrons. *Phys. Rev. Lett.* **2010**, *104*, 136403.
(796) Thiemann, F. L.; Schran, C.; Rowe, P.; Müller, E. A.; Michaelides, A. Water Flow in Single-Wall Nanotubes: Oxygen Makes It Slip, Hydrogen Makes It Stick. *ACS Nano* **2022**, *16*, 10775.
(797) Schran, C.; Thiemann, F. L.; Rowe, P.; Müller, E. A.; Marsalek, O.; Michaelides, A. Machine Learning Potentials for Complex Aqueous Systems Made Simple. *Proc. Natl. Acad. Sci. U.S.A.* **2021**, *118*, e2110077118.
(798) Kapil, V.; Schran, C.; Zen, A.; Chen, J.; Pickard, C. J.; Michaelides, A. The First-Principles Phase Diagram of Monolayer Nanoconfined Water. *Nature* **2022**, *609*, 512−516.
(799) Zhao, W.; Qiu, H.; Guo, W. A Deep Neural Network Potential for Water Confined in Graphene Nanocapillaries. *J. Phys. Chem. C* **2022**, *126*, 10546−10553.
(800) Ghorbanfekr, H.; Behler, J.; Peeters, F. M. Insights into Water Permeation through Hbn Nanocapillaries by Ab Initio Machine Learning Molecular Dynamics Simulations. *J. Phys. Chem. Lett.* **2020**, *11*, 7363−7370.
(801) Joly, L.; Tocci, G.; Merabia, S.; Michaelides, A. Strong Coupling between Nanofluidic Transport and Interfacial Chemistry: How Defect Reactivity Controls Liquid-Solid Friction through Hydrogen Bonding. *J. Phys. Chem. Lett.* **2016**, *7*, 1381−1386.
(802) Piao, Y.; Meany, B.; Powell, L. R.; Valley, N.; Kwon, H.; Schatz, G. C.; Wang, Y. Brightening of Carbon Nanotube Photoluminescence through the Incorporation of Sp3 Defects. *Nat. Chem.* **2013**, *5*, 840−845.
(803) Kwon, H.; Furmanchuk, A.; Kim, M.; Meany, B.; Guo, Y.; Schatz, G. C.; Wang, Y. Molecularly Tunable Fluorescent Quantum Defects. *J. Am. Chem. Soc.* **2016**, *138*, 6878−6885.
(804) Kim, M.; Wu, X.; Ao, G.; He, X.; Kwon, H.; Hartmann, N. F.; Zheng, M.; Doorn, S. K.; Wang, Y. Mapping Structure-Property Relationships of Organic Color Centers. *Chem.* **2018**, *4*, 2180−2191.
(805) Luo, H.; Wang, P.; Wu, X.; Qu, H.; Ren, X.; Wang, Y. One-Pot, Large-Scale Synthesis of Organic Color Center-Tailored Semiconducting Carbon Nanotubes. *ACS Nano* **2019**, *13*, 8417−8424.
(806) Brozena, A. H.; Kim, M.; Powell, L. R.; Wang, Y. Controlling the Optical Properties of Carbon Nanotubes with Organic Colour-Centre Quantum Defects. *Nature Reviews Chemistry* **2019**, *3*, 375−392.
(807) Shiraki, T.; Miyauchi, Y.; Matsuda, K.; Nakashima, N. Carbon Nanotube Photoluminescence Modulation by Local Chemical and Supramolecular Chemical Functionalization. *Acc. Chem. Res.* **2020**, *53*, 1846−1859.
(808) Gifford, B. J.; Kilina, S.; Htoon, H.; Doorn, S. K.; Tretiak, S. Controlling Defect-State Photophysics in Covalently Functionalized Single-Walled Carbon Nanotubes. *Acc. Chem. Res.* **2020**, *53*, 1791−1801.
(809) Nagai, Y.; Nakamura, K.; Yudasaka, M.; Shiraki, T.; Fujigaya, T. Radical Polymer Grafting on the Surface of Single-Walled Carbon Nanotubes Enhances Photoluminescence in the near-Infrared Region: Implications for Bioimaging and Biosensing. *ACS Applied Nano Materials* **2020**, *3*, 8840−8847.
(810) Powell, L. R.; Piao, Y.; Wang, Y. Optical Excitation of Carbon Nanotubes Drives Localized Diazonium Reactions. *J. Phys. Chem. Lett.* **2016**, *7*, 3690−3694.
(811) Wu, X. J.; Kim, M.; Kwon, H.; Wang, Y. H. Photochemical Creation of Fluorescent Quantum Defects in Semiconducting Carbon Nanotube Hosts. *Angew. Chem., Int. Ed.* **2018**, *57*, 648.

https://doi.org/10.1021/acs.chemrev.2c00155
Chem. Rev. 2023, 123, 2737−2831

(812) Huang, Z.; Powell, L. R.; Wu, X.; Kim, M.; Qu, H.; Wang, P.; Fortner, J. L.; Xu, B.; Ng, A. L.; Wang, Y. Photolithographic Patterning of Organic Color-Centers. *Adv. Mater.* **2020**, *32*, 1906517.
(813) Dou, Q.; Xu, B.; Wu, X.; Mo, J.; Wang, Y. Tunable Photo-Patterning of Organic Color-Centers. *Materials & Design* **2021**, *212*, 110252.
(814) Kwon, H.; Kim, M.; Meany, B.; Piao, Y.; Powell, L. R.; Wang, Y. Optical Probing of Local Ph and Temperature in Complex Fluids with Covalently Functionalized, Semiconducting Carbon Nanotubes. *J. Phys. Chem. C* **2015**, *119*, 3733−3739.
(815) Onida, G.; Reining, L.; Rubio, A. Electronic Excitations: Density-Functional Versus Many-Body Green's-Function Approaches. *Rev. Mod. Phys.* **2002**, *74*, 601−659.
(816) Runge, E.; Gross, E. K. U. Density-Functional Theory for Time-Dependent Systems. *Phys. Rev. Lett.* **1984**, *52*, 997−1000.
(817) Deslippe, J.; Samsonidze, G.; Strubbe, D. A.; Jain, M.; Cohen, M. L.; Louie, S. G. Berkeleygw: A Massively Parallel Computer Package for the Calculation of the Quasiparticle and Optical Properties of Materials and Nanostructures. *Comput. Phys. Commun.* **2012**, *183*, 1269−1289.
(818) Rocca, D.; Gebauer, R.; Saad, Y.; Baroni, S. Turbo Charging Time-Dependent Density-Functional Theory with Lanczos Chains. *J. Chem. Phys.* **2008**, *128*, 154105.
(819) Rocca, D.; Lu, D.; Galli, G. Ab Initio Calculations of Optical Absorption Spectra: Solution of the Bethe-Salpeter Equation within Density Matrix Perturbation Theory. *J. Chem. Phys.* **2010**, *133*, 164109.
(820) Comtet, J.; Rayabharam, A.; Glushkov, E.; Zhang, M.; Avsar, A.; Watanabe, K.; Taniguchi, T.; Aluru, N. R.; Radenovic, A. Anomalous Interfacial Dynamics of Single Proton Charges in Binary Aqueous Solutions. *Sci. Adv.* **2021**, *7*, eabg8568.
(821) Baloch, K. H.; Voskanian, N.; Bronsgeest, M.; Cumings, J. Remote Joule Heating by a Carbon Nanotube. *Nat. Nanotechnol.* **2012**, *7*, 316−319.
(822) Daunheimer, S. A.; Petrova, O.; Tchernyshyov, O.; Cumings, J. Reducing Disorder in Artificial Kagome Ice. *Phys. Rev. Lett.* **2011**, *107*, 167201.
(823) Tong, T.; Majumdar, A.; Zhao, Y.; Kasham, A.; Delzeit, L.; Meyyappan, M.Indium Assisted Multiwalled Carbon Nanotube Array Thermal Interface Materials. *2006 Proceedings 10th Intersociety Conference on Thermal and Thermomechanical Phenomena in Electronics Systems*, Vols *1 and 2*2006, 1406.
(824) Weathersby, S. P.; Brown, G.; Centurion, M.; Chase, T. F.; Coffee, R.; Corbett, J.; Eichner, J. P.; Frisch, J. C.; Fry, A. R.; Gühr, M.; et al. Mega-Electron-Volt Ultrafast Electron Diffraction at Slac National Accelerator Laboratory. *Rev. Sci. Instrum.* **2015**, *86*, 073702.
(825) Guan, W. H.; Joseph, S.; Park, J. H.; Krstic, P. S.; Reed, M. A. Paul Trapping of Charged Particles in Aqueous Solution. *Proc. Natl. Acad. Sci. U.S.A.* **2011**, *108*, 9326−9330.
(826) Werber, J. R.; Deshmukh, A.; Elimelech, M. Can Batch or Semi-Batch Processes Save Energy in Reverse-Osmosis Desalination? *Desalination* **2017**, *402*, 109−122.
(827) Song, W.; Kumar, M. Artificial Water Channels: Toward and Beyond Desalination. *Curr. Opin. Chem. Eng.* **2019**, *25*, 9−17.
(828) Shen, Y. X.; Saboe, P. O.; Sines, I. T.; Erbakan, M.; Kumar, M. Biomimetic Membranes: A Review. *J. Membr. Sci.* **2014**, *454*, 359−381.
(829) Werber, J. R.; Elimelech, M. Permselectivity Limits of Biomimetic Desalination Membranes. *Sci. Adv.* **2018**, *4*, eaar8266.
(830) Ghosh, S.; Sood, A. K.; Kumar, N. Carbon Nanotube Flow Sensors. *Science* **2003**, *299*, 1042−1044.
(831) de la Escosura-Muniz, A.; Merkoci, A. Nanochannels Preparation and Application in Biosensing. *ACS Nano* **2012**, *6*, 7556−7583.
(832) Miles, B. N.; Ivanov, A. P.; Wilson, K. A.; Dogan, F.; Japrung, D.; Edel, J. B. Single Molecule Sensing with Solid-State Nanopores: Novel Materials, Methods, and Applications. *Chem. Soc. Rev.* **2013**, *42*, 15−28.
(833) Haque, F.; Li, J. H.; Wu, H. C.; Liang, X. J.; Guo, P. X. Solid-State and Biological Nanopore for Real-Time Sensing of Single Chemical and Sequencing of DNA. *Nano Today* **2013**, *8*, 56−74.
(834) Branton, D.; Deamer, D. W.; Marziali, A.; Bayley, H.; Benner, S. A.; Butler, T.; Di Ventra, M.; Garaj, S.; Hibbs, A.; Huang, X. H.; et al. The Potential and Challenges of Nanopore Sequencing. *Nat. Biotechnol.* **2008**, *26*, 1146−1153.
(835) Chinappi, M.; Cecconi, F. Protein Sequencing Via Nanopore Based Devices: A Nanofluidics Perspective. *J. Phys.: Condens. Matter* **2018**, *30*, 204002.
(836) Bell, N. A. W.; Keyser, U. F. Digitally Encoded DNA Nanostructures for Multiplexed, Single-Molecule Protein Sensing with Nanopores. *Nat. Nanotechnol.* **2016**, *11*, 645.
(837) Li, W. Z.; Wang, X.; Chen, Z. W.; Waje, M.; Yan, Y. S. Carbon Nanotube Film by Filtration as Cathode Catalyst Support for Proton-Exchange Membrane Fuel Cell. *Langmuir* **2005**, *21*, 9386−9389.
(838) Kreuer, K. D.; Paddison, S. J.; Spohr, E.; Schuster, M. Transport in Proton Conductors for Fuel-Cell Applications: Simulations, Elementary Reactions, and Phenomenology. *Chem. Rev.* **2004**, *104*, 4637−4678.
(839) Morris, R. E.; Wheatley, P. S. Gas Storage in Nanoporous Materials. *Angew. Chem., Int. Ed.* **2008**, *47*, 4966−4981.
(840) Gao, J.; Feng, Y. P.; Guo, W.; Jiang, L. Nanofluidics in Two-Dimensional Layered Materials: Inspirations from Nature. *Chem. Soc. Rev.* **2017**, *46*, 5400−5424.
(841) Zhai, Y. P.; Dou, Y. Q.; Zhao, D. Y.; Fulvio, P. F.; Mayes, R. T.; Dai, S. Carbon Materials for Chemical Capacitive Energy Storage. *Adv. Mater.* **2011**, *23*, 4828−4850.
(842) Liu, C.; Li, F.; Ma, L. P.; Cheng, H. M. Advanced Materials for Energy Storage. *Adv. Mater.* **2010**, *22*, No. E28.
(843) Park, H. G.; Jung, Y. Carbon Nanofluidics of Rapid Water Transport for Energy Applications. *Chem. Soc. Rev.* **2014**, *43*, 565−576.
(844) Heinze, S.; Wang, N. P.; Tersoff, J. Electromigration Forces on Ions in Carbon Nanotubes. *Phys. Rev. Lett.* **2005**, *95*, 186802.
(845) Cao, Y.; Fatemi, V.; Fang, S.; Watanabe, K.; Taniguchi, T.; Kaxiras, E.; Jarillo-Herrero, P. Unconventional Superconductivity in Magic-Angle Graphene Superlattices. *Nature* **2018**, *556*, 43−50.
(846) Yaroshchuk, A. E. Non-Steric Mechanisms of Nanofiltration: Superposition of Donnan and Dielectric Exclusion. *Sep. Purif. Technol.* **2001**, *22−23*, 143−158.
(847) Dimeski, G.; Badrick, T.; John, A. S. Ion Selective Electrodes (Ises) and Interferences—a Review. *Clin. Chim. Acta* **2010**, *411*, 309−317.
(848) Nieves-Cordones, M.; Al Shiblawi, F. R.; Sentenac, H.*Roles and Transport of Sodium and Potassium in Plants.*; Springer International, 2016; pp 291−324.
(849) Fang, A.; Kroenlein, K.; Riccardi, D.; Smolyanitsky, A. Highly Mechanosensitive Ion Channels from Graphene-Embedded Crown Ethers. *Nat. Mater.* **2019**, *18*, 76−81.
(850) Bhabha, G.; Lee, J.; Ekiert, D. C.; Gam, J.; Wilson, I. A.; Dyson, H. J.; Benkovic, S. J.; Wright, P. E. A Dynamic Knockout Reveals That Conformational Fluctuations Influence the Chemical Step of Enzyme Catalysis. *Science* **2011**, *332*, 234−238.
(851) Sahu, S.; Elenewski, J.; Rohmann, C.; Zwolak, M. Optimal Transport and Colossal Ionic Mechano-Conductance in Graphene Crown Ethers. *Sci. Adv.* **2019**, *5*, No. eaaw5478.
(852) Allen, T. W.; Andersen, O. S.; Roux, B. On the Importance of Atomic Fluctuations, Protein Flexibility, and Solvent in Ion Permeation. *J. Gen. Physiol.* **2004**, *124*, 679−690.
(853) Bezrukov, S. M.; Vodyanoy, I. Noise-Induced Enhancement of Signal Transduction across Voltage-Dependent Ion Channels. *Nature* **1995**, *378*, 362−364.
(854) Douglass, J. K.; Wilkens, L.; Pantazelou, E.; Moss, F. Noise Enhancement of Information Transfer in Crayfish Mechanoreceptors by Stochastic Resonance. *Nature* **1993**, *365*, 337−340.
(855) Vázquez-Rodríguez, B.; Avena-Koenigsberger, A.; Sporns, O.; Griffa, A.; Hagmann, P.; Larralde, H. Stochastic Resonance at Criticality in a Network Model of the Human Cortex. *Sci. Rep.* **2017**, *7*, 13020.
(856) Beckstein, O.; Sansom, M. S. P. The Influence of Geometry, Surface Character, and Flexibility on the Permeation of Ions and Water through Biological Pores. *Physical Biology* **2004**, *1*, 42−52.

https://doi.org/10.1021/acs.chemrev.2c00155
Chem. Rev. 2023, 123, 2737−2831

(857) Hu, S.; Lozada-Hidalgo, M.; Wang, F. C.; Mishchenko, A.; Schedin, F.; Nair, R. R.; Hill, E. W.; Boukhvalov, D. W.; Katsnelson, M. I.; Dryfe, R. A. W.; et al. Proton Transport through One-Atom-Thick Crystals. *Nature* **2014**, *516*, 227−230.
(858) Challa, S. R.; Sholl, D. S.; Johnson, J. K. Adsorption and Separation of Hydrogen Isotopes in Carbon Nanotubes: Multi-component Grand Canonical Monte Carlo Simulations. *J. Chem. Phys.* **2002**, *116*, 814−824.
(859) Ponder, J. W.; Wu, C.; Ren, P.; Pande, V. S.; Chodera, J. D.; Schnieders, M. J.; Haque, I.; Mobley, D. L.; Lambrecht, D. S.; DiStasio, R. A.; et al. Current Status of the Amoeba Polarizable Force Field. *J. Phys. Chem. B* **2010**, *114*, 2549−2564.
(860) Schran, C.; Thiemann, F. L.; Rowe, P.; Müller, E. A.; Marsalek, O.; Michaelides, A. Machine Learning Potentials for Complex Aqueous Systems Made Simple. *Proc. Natl. Acad. Sci. U. S. A.* **2021**, *118*, No. e2110077118.
(861) Babin, V.; Leforestier, C.; Paesani, F. Development of a "First Principles" Water Potential with Flexible Monomers: Dimer Potential Energy Surface, Vrt Spectrum, and Second Virial Coefficient. *J. Chem. Theory Comput.* **2013**, *9*, 5395−5403.
(862) Ceriotti, M.; Fang, W.; Kusalik, P. G.; McKenzie, R. H.; Michaelides, A.; Morales, M. A.; Markland, T. E. Nuclear Quantum Effects in Water and Aqueous Systems: Experiment, Theory, and Current Challenges. *Chem. Rev.* **2016**, *116*, 7529−7550.
(863) He, L.-L.; Li, Y.; Zhao, D.-X.; Yu, L.; Zhao, C.-L.; Lu, L.-N.; Liu, C.; Yang, Z.-Z. Structure and Phase Behavior of the Confined Water in Graphene Nanocapillaries Studied by Abeem$\sigma\pi$ Polarizable Force Field. *J. Phys. Chem. C* **2019**, *123*, 5653−5666.
(864) Zhang, L.; Han, J.; Wang, H.; Car, R.; E, W. Deep Potential Molecular Dynamics: A Scalable Model with the Accuracy of Quantum Mechanics. *Phys. Rev. Lett.* **2018**, *120*, 143001.
(865) Duan, C.; Alibakhshi, M. A.; Kim, D.-K.; Brown, C. M.; Craik, C. S.; Majumdar, A. Label-Free Electrical Detection of Enzymatic Reactions in Nanochannels. *ACS Nano* **2016**, *10*, 7476−7484.
(866) Pilling, M. J.; Seakins, P. W.*Reaction Kinetics*; Oxford University Press, 1997.
(867) Dong, B.; Pei, Y.; Mansour, N.; Lu, X.; Yang, K.; Huang, W.; Fang, N. Deciphering Nanoconfinement Effects on Molecular Orientation and Reaction Intermediate by Single Molecule Imaging. *Nat. Commun.* **2019**, *10*, 4815.
(868) Li, Z.; Misra, R. P.; Li, Y.; Yao, Y.-C.; Zhao, S.; Zhang, Y.; Chen, Y.; Blankschtein, D.; Noy, A. Breakdown of the Nernst−Einstein relation in carbon nanotube porins. *Nature Nanotechnology* **2023**, *18* (2), 177−183.

https://doi.org/10.1021/acs.chemrev.2c00155
Chem. Rev. 2023, 123, 2737−2831